ELECTROCHEMICAL STUDIES OF REDOX REACTIONS AT NANOSTRUCTURED CARBON ELECTRODES IN AQUEOUS ELECTROLYTE SOLUTIONS AND ROOM TEMPERATURE IONIC LIQUIDS

By

Fatemehsadat Parvis

A DISSERTATION

Submitted to
Michigan State University
in partial fulfillment of the requirements
for the degree of

Chemistry-Doctor of Philosophy

2023

ABSTRACT

Carbon electrodes are often used in electroanalytical chemistry. There are several reasons for this including low cost, high mechanical strength, wide usable potential range, rich surface chemistry, chemical inertness, and compatibility with a wide variety of reaction conditions.[1-3] There are different allotropes of carbon including diamond, graphite, glassy carbon, and fullerenes.[3]

Room temperature ionic liquids (RTILs) are solventless salts with a low melting point. They are liquid at room temperature and composed of pure ions. They usually contain a large asymmetric organic cation and a small symmetric inorganic anion. The physiochemical properties of these liquid salts can be manipulated based on the molecular structure of cationic and anionic parts. Their low vapor pressure, high thermal and chemical stability, moderate electrical conductivity, and non-flammability make them a unique choice for electroanalytical measurements offering huge advantages over organic solvents and aqueous electrolyte solutions.[4-7]

High viscosity and the presence of impurities limit their electrochemical applications. Their high viscosity suppresses the diffusional mass transport and slows down the heterogeneous electron-transfer kinetics.[8-12] The presence of impurities has a noticeable impact on electrochemical processes in RTILs. One of the most abundant impurities in RTILs is water. Water decreases the viscosity[13-16], density[17], working potential window[13-15, 18], and increases the electrical conductivity[13-16]. Also, the presence of water can influence the solubility of redox analytes, the structure of the electrical double-layer, and the solvent environment around a redox system. Therefore, the effective removal of water is a vital step if researchers aim to study the electron-transfer processes in RTILs.[6, 16, 17, 19]

There are fundamental differences between room-temperature ionic liquids and aqueous electrolyte solutions. RTILs contain no dielectric solvent to separate the ions. Their ionic nature makes the columbic interaction the principal force in this environment. As such, ions exist with significant ion pairing. Cations and anions in an RTIL surround the redox system with some particular organization. However, there is a solvation shell around redox systems in an aqueous electrolyte solution.[11, 17, 20] Therefore, the solvation dynamics in RTILs is distinctly different from the aqueous electrolyte environment, and consequently, the process of electron transfer in RTILs differs from that aqueous solution. Additionally, the electrode-solution interfacial region in RTILs and aqueous solutions is different. The structure of the double-layer influences electrochemical processes.

There is a large body of research on how the electronic properties, microstructure, and surface chemistry affect electron-transfer kinetics of various redox systems at sp^2 carbon electrodes in aqueous electrolyte solutions. However, more limited research is available about electron transfer kinetics at sp^2 and sp^3 carbon electrodes in room temperature ionic liquids. The dissertation research reported herein addresses this knowledge gap.

The central hypothesis of this research is that the distinct microstructure of the carbon materials studied, glassy carbon and boron-doped nanocrystalline diamond thin films will affect the capacitance, molecular adsorption, and heterogeneous electron-transfer rate constants of several soluble redox systems in RTILs in ways that are different from the trends found for the same electrodes in aqueous electrolyte solutions.

To Shahnaz, Hamid, Ali, Maedeh,
&
my love, Mohammad

ACKNOWLEDGEMENTS

I want to take this chance to thank my supervisor, family, and colleagues from the bottom of my heart for helping me finish my Ph.D. thesis.

I want to express my gratitude to my supervisor, Professor Greg Swain, for all of his help and advice during my research project. His support, helpful criticism, wise guidance, and emotional support have been crucial in helping me to get through challenging times. A better mentor to lead me through this fantastic learning experience is something I could not have hoped for.

I also want to express my gratitude to the members of my committee, Dr. Gary Blanchard, Dr. James Jackson, and Dr. Denis Proshlyakov, for their invaluable comments, wise counsel, and original ideas. My research work has been substantially enhanced by their comments and helpful critique.

To all of my coworkers - Skye, Jack, Maiyara, Isuri, Shashika, Aaron, Sarah, Romana, Shruti, Dr. Peteu, Kirti, Nick, Zack, Yufeng, Iqbal, and Simphiwe - Your friendship and assistance with my work will always be remembered. I want to thank you all for the great memories we have shared.

I want to express my gratitude to my parents, Shahnaz and Hamid, and my brother and sister, Ali and Maedeh for their everlasting love and support throughout my academic career. Their unending efforts, direction, and inspiration have given me courage and inspired me.

Finally, I would like to convey my sincere gratitude to my dear spouse, Mohammad, for his unflagging love, support, and tolerance during my academic career. His unending encouragement, support, and understanding have been a continual source of inspiration and strength.

TABLE OF CONTENTS

CHAPTER 1. INTRODUCTION

1.1. Carbon Electrodes

Carbon is one of the most abundant elements in the universe.[21] Carbon electrodes have several advantages, including low cost, wide working potential window, chemical inertness, rich surface chemistry, and chemical inertness.[3, 22-25] Because of these properties, carbon is commonly used in analytical and industrial electrochemistry.[3] They have been used for redox reactions involving organic and bio-organic molecules, energy storage, supercapacitors, batteries, and catalyst supports.[3]

Carbon electrodes exist as 1, 2 and 3D materials with sp^2 and sp^3-boned carbon including including diamond, graphite, fullerene, etc.[3] Each allotrope exists in various forms having different electrochemical properties.[3] This variety of carbon electrodes arises from the heterogeneous nature of the material.[3]

Different types of carbon electrodes are commonly used in electrochemistry, including glassy carbon, boron-doped diamond, and graphite.[3] Graphite has a hexagonal structure in which carbon atoms are in a trigonal configuration with the sp^2-hybridized bonding (Figure 1.1). Graphite has a layered structure named graphite sheets. The layer planes have a spacing of 3.354 Å. Though there is a strong covalent bonding between the atoms in each plane, the weaker van der Waals force between the layer planes is not strong enough to hold the layers together. This weak interaction allows the layer planes to slide across each other.[3, 26]

Graphite has two main microstructural sites: 1) edge plane and 2) basal plane. Edge plane sites exist where the individual graphene sheets terminate, and they generally possess high electrochemical activity because of the high density of electronic states. These sites are active for adsorption and electron transfer. The carbon atoms at these sites react with oxygen and water to

form carbon-oxygen functional groups. Unlike edge plane sites, basal plane sites possess a lower density of electronic states and lower reactivity. These sites are on the layer plane surface. They are unreactive to water and oxygen. Generally, slower electron transfer and weaker molecular adsorption occurs at these sites.[3, 27-30]

There are permutations of graphitic structures such as amorphous carbons. Amorphous carbons, such as powders and glassy carbon, have a small in-plane dimension and a large spacing between the graphene sheets.[26] It is questionable that glassy carbon be considered amorphous. According to the Jenkins and Kawamura, glassy carbon has a network structure consisting of tangled aromatic ribbon molecules that are cross-linked by highly strained carbon-carbon covalent bonds with a wide spectrum of bond energies. [31] The ribbons consist of stacks of graphene sheets with a small domain size of tens of angstroms.

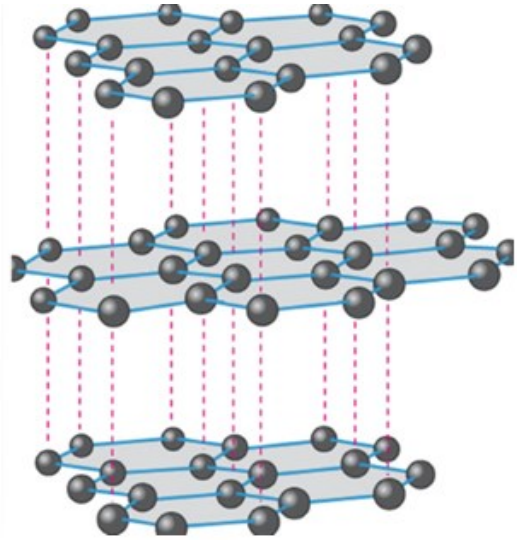

Figure 1.1. Structure of graphite. [32]

Another distinct form of carbon is diamond. Diamond has a cubic structure.[3] It has a tetrahedral configuration with sp^3 hybridized carbon-carbon bonding (Figure 1.2). The strong

covalent bonding between atoms makes this structure hard. Diamond is an electrical insulator with a large bandgap (~5.5 eV) and a low density of electronic states. [26, 33]

A dopant must be added to its microstructure for diamond to have high electrical conductivity and to function as an electrode. The dopant increases the electrical conductivity (*i.e.*, number of charge carriers) of the material. Nitrogen, boron, sulfur, and phosphorous are common dopants. Boron is the most common dopant for diamond films, which can be introduced to the gas source during film growth. The most used of these diamond electrodes are boron-doped diamond films (BDD) with various polycrystalline structures such as microcrystalline, nanocrystalline, and ultra-nanocrystalline. [3]

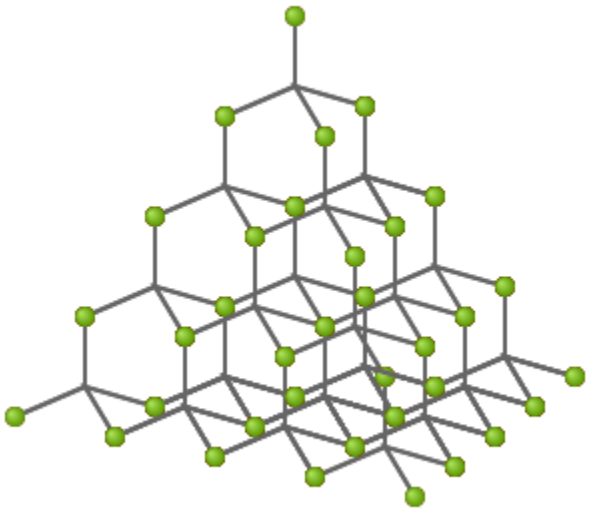

Figure 1.2. Structure of diamond. (https://www.physics-in-a-nutshell.com article/13/diamond-structure).

1.1.1. Glassy Carbon

One of the most important materials used as an electrode is glassy carbon (GC). Glassy carbon is widely used in electroanalytical chemistry.[1, 3, 34] Glassy carbon electrodes are available

in different forms including rods, disks, and plates. A polished glassy carbon electrode has a mirror-like appearance. Unlike graphite, the structure of GC is hard and brittle.

Glassy carbon is prepared through heat treatment of polymer materials (*e.g.*, polyacrylonitrile (PAN) or phenolic resin).[3] Polymers are heated at high temperatures (~1000-3000 ºC) under high pressure in an inert atmosphere to the degree that all the heteroatoms evaporate. The only remaining atom under this condition is the carbon atom. The final features of this material highly depend on the preparation conditions. The C-C bonds in the polymer backbone remain largely intact at these temperatures. So, the full graphitic structure cannot be developed.[3] The resulting sp^2-bonded structure is made of randomly intertwined ribbons of graphitic planes with L_a (layer plane width) and L_c (stacking height) values of *ca.* 50 and 15 Å, respectively (Figure 1.3).[26]

Glassy carbon is microstructurally isotropic with very small internal voids[3]. These voids are not connected so GC is impermeable to liquids and gases. Its mechanical hardness and impenetrability to liquids and gases arise from the interwoven sp^2 carbon ribbons (Figure 1.3).

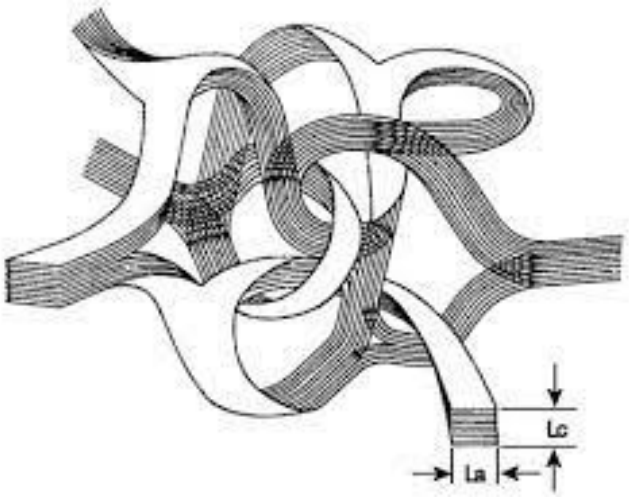

Figure 1.3. Structure of glassy carbon. (http://www.ijcambria.com/Glassy%20Carbon.htm).

Two peaks are seen in the Raman spectrum of GC at 1350 cm^{-1} (disordered D1 peak) and 1580 cm^{-1} (graphitic G peak).[35] The ratio of these two peaks demonstrates the extent of the microstructure disorder. This value is usually between 1.3-1.5.

Glassy carbon electrodes have complex surface chemistry containing different types of carbon-oxygen functional groups.[1, 2, 24, 26, 31, 34, 36] It is worth mentioning that GC has both σ and π orbitals, leading to a lower bandgap and higher density of electronic states. As a result, GC shows high background current and capacitance, a high degree of adsorption, and relatively rapid electron-transfer kinetics.[26]

Glassy carbon electrodes need pretreatment before electrochemical measurements. They are susceptible to adsorption and fouling because of the presence of carbon-oxygen functional groups at the surface of the electrode. There are various methods used for pretreatment including solvent cleaning[27], mechanical polishing[27], vacuum heat treatment[37], RF plasma pretreatment[38], electrochemical polarization[39], and laser activation[40]. Pretreatment cleans and conditions the electrode surface activating it for fast electrode transfer kinetics.[26] The electrochemical activity of glassy carbon depends on the surface pretreatment, manufacturing condition, surface roughness, and its history.[3, 26, 41, 42] This leads to the variations in the response of glassy carbon electrodes.

1.1.2. Boron-Doped Diamond

Diamond is one type of carbon allotrope that is an electrical insulator.[3] It can be doped using various elements to make it conductive and useable as an electrode.[3] Boron is one of the most common elements introduced into the diamond lattice to make a category of diamond-based electrodes known as “boron-doped diamond” or “BDD”. The boron-doped diamond film has p-type electrical properties. The typical doping boron level is $> 5 \times 10^{20}$ cm^{-3}. Boron introduces an

impurity band 0.35 eV above the valance band. The boron-doped diamond film is usually grown on a conducting substrate, such as Si, Ti, etc.[26, 43]

There are various methods to grow boron-doped diamond films, including microwave plasma, hot filament, or combustion flame-assisted CVD (chemical vapor deposition). The most common method is microwave plasma CVD.[26, 43] Microwave plasma-assisted CVD is the most common deposition process that uses a 0.5-2 % CH_4/H_2 source gas mixture with B_2H_6 added for boron doping.[44] The growth temperature is 700-850 ºC and the system pressure is generally 25-100 mTorr. The gas molecules break into radicals, ions, and electrons in the plasma. The main growth species in this technique is the methyl radical ($\cdot CH_3$) formed by hydrogen abstraction by atomic hydrogen formed in the plasma The $\cdot CH_3$ adds to carbon sites on the growing diamond surface.[45] A dopant gas of diborane (B_2H_6) is added to introduce impurities into the microstructure of the diamond.

There are three main reasons for the addition of hydrogen background:

1. Hydrogen abstraction from carbon/hydrogen source gas which generates methyl radical species.
2. Passivation of the surface through reacting with dangling bonds at the surface.
3. Gasification of the sp^2-bonded non-diamond carbon impurity.[26]

Synthetic diamond films have two main structures: 1) single crystalline and 2) polycrystalline. Polycrystalline diamond can be prepared in three different forms: 1) microcrystalline (μm grain size), 2) nanocrystalline (NCD 100-1000 nm grain size), and 3) ultrananocrystalline (UNCD <20 nm grain size.[43, 46-48] Figure 1.4 shows the SEM images of microcrystalline and nanocrystalline diamond on silicon. Micro and nanocrystalline diamond are deposited from CH_4/H_2 source gas mixtures[43, 44, 49] while ultrananocrystalline diamond is

deposited from CH_4/Ar source gas mixtures.[50-53]

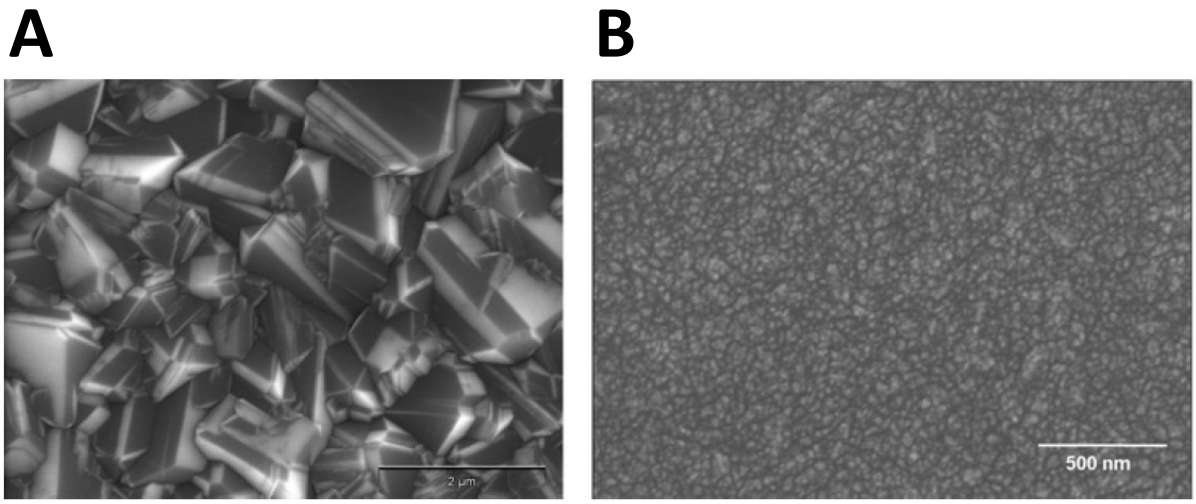

Figure 1.4. SEM images of A) a boron-doped microcrystalline (scale bar = 2 µm) and B) a boron-doped nanocrystalline (scale bar = 500 nm) diamond thin films grown on Si. [26]

Boron-doped thin-film electrodes exhibit excellent properties for electroanalytical measurements: low background current, wide working potential window, stable microstructure, relatively rapid electron transfer for multiple redox systems without conventional pretreatment, weak adsorption and resistance to fouling and optically transparency.[48, 54-59] Unlike glassy carbon, the boron-diamond films are stable at extreme positive and negative potentials. They mainly consist of sigma bonds. So, they do not possess π bonds, resulting in less adsorption compared to glassy carbon electrodes.[48, 54-58]

Factors such as the boron doping level, surface termination, sub-surface hydrogen content, and size of crystals can affect the electrochemical behavior of BDD films depending on the redox system.[58, 60-62] For example, in the case of surface termination, BDD films generally have a hydrogen-terminated surface after the growth process. Though hydrogen-terminated surfaces are known to be stable, they gradually get oxidized when they are exposed to the atmosphere. Also, the film can get oxidized using different methods, including anodic polarization, and boiling in

acid. The oxidized films show different electrochemical activity from the hydrogenated films.[63-65] In some cases, the oxidized films show higher electrochemical activity for some redox systems, which go through the adsorption.[66-71]

Additionally, the research for this dissertation has shown that the heterogeneous electron transfer rate constant for potassium ferrocyanide ($[Fe(CN)_6]^{-3/-4}$) decreases over time because of the increase in the level of oxygen at the film surface. It is due to the repulsive interaction between the oxidized films and charged redox system.

If diamond films are deposited on quartz or undoped Si, they can be used as an optically transparent electrode (OTE) for spectroelectrochemical measurements in UV/Vis and IR regions of the electromagnetic radiation spectrum.[46, 72-77] An optically transparent electrode works as a source of the electron. It is transparent to electromagnetic radiation. Making optically transparent boron-doped diamond electrodes requires a balance between the film thickness and doping level. The doping level should be enough to provide sufficient conductivity and not too high to make the film opaque. The film thickness should be thick enough to provide a continuous film across the substrate, not too thick to make the film opaque.[78]

1.2. Characterization of Carbon Electrodes

To understand the structure-function relationship of carbon electrodes, one needs to have knowledge of the electrode's morphology, microstructure, surface chemistry and electrical properties. The surface chemistry, composition, and roughness are known to affect the electrochemical behavior of carbon electrodes. For example, one study showed that the level of sp^2-bonded non-diamond carbon impurity significantly affects the working potential window, voltammetric background current, and peak separation of boron-doped polycrystalline diamond

thin-film electrodes. This study showed that the cyclic voltammetric peak potential separation, ΔE_p, for 4-*tert*-butylcatechol and $Fe^{+3/+2}$ decreases with increased sp^2-bonded carbon content.[79]

Several spectroscopic and microscopic methods can provide useful information about the carbon material properties. These methods include UV/Vis absorption spectroscopy, Raman spectroscopy, scanning electron microscopy (SEM), and atomic force microscopy (AFM).[3]

1.2.1. Raman Spectroscopy

Raman spectroscopy is a non-destructive technique that can be used to identify the chemical bonding in molecules or solids and the doping level in semiconducting materials. It is particularly useful for identifying different forms of carbon materials. Raman spectra originate when an intense light (laser) of frequency υ_0 is irradiated upon a sample, scattered light is observed in perpendicular direction to the incident light.[80] The scattered light can be categorized in two parts: (i) the Rayleigh scattering, which has the same frequency (υ_0) as the incident light, and (ii) the Raman scattering having the frequency $\upsilon_0 \pm \upsilon_R$, where υ_R is the frequency corresponding to a molecular vibration or lattice phonon in a material. The $\upsilon_0 + \upsilon_R$ and $\upsilon_0 - \upsilon_R$ lines are called the anti-Stokes and Stokes lines, respectively. Thus, in Raman spectroscopy, one measures the molecular vibration frequency (υ_R) as a shift from the incident frequency (υ_0).

Two peaks are seen at 1350 and 1580 cm^{-1} for glassy carbon electrodes.[81] The peaks at 1350 and 1580 are associated with graphitic "D-band" and "G-band", respectively. The "disorder-induced or D band" arises from a disorder-allowed A_{1g} breathing mode of sp^2 carbon atoms in six-membered rings.[82] It arises from defects and graphitic edge plane sites. The Raman intensity of this band is inversely proportional to the crystallite size and is caused by a breakdown of the k-selection rule.[83] The G-band or graphitic band arise because of the optical phonon mode with E_{2g} symmetry related to the in-plane C-C stretching of sp^2-bonded carbon atoms in rings and chains.[35]

The ratio of these two peaks demonstrates the level of microstructural disorder in the material (*i.e.*, fraction of graphitic edge plane sites). The typical value for this ratio in glassy carbon is 1.3-1.5.[26, 35]

For the case of boron-doped diamond electrodes (BDD), Raman spectroscopy is used to distinguish BDD electrodes with different crystalline structures, domain size, the level of doping, and intrinsic film stress.[78, 84, 85] Single crystal diamond shows a sharp peak at 1332 cm^{-1}. This line is inversely related to the defect density.[86, 87] The position of this line can reflect the stress within the film.[88, 89] For a heavily boron doped film, the first-order diamond phonon line shifts from 1332 cm^{-1} to lower wavenumbers, and the scattering intensity at ~ 507 cm^{-1} and 1225 cm^{-1} increases by increasing the concentration of boron.[90, 91] The 507 cm^{-1} peak is related to the vibrational modes of boron dimers [92-94] and clusters [95]. The 1225 cm^{-1} peak comes from the defects in the diamond lattice arising from a high level of boron-doping. It is probably associated with boron-carbon complexes.[90, 91] The 1127 cm^{-1} and 1468 cm^{-1} peaks have been assigned to the polymeric sp^2 carbon species in the grain boundaries.[85] The 1552 cm^{-1} peak is related to crystalline graphite.[90, 91] The carbon graphitization increases in the grain boundaries by increasing the level of boron doping. [78, 90, 91]

1.2.2. UV/Visible Spectroscopy

UV/Visible spectroscopy is one method to study the optical properties of transparent electrodes such as boron-doped diamond films deposited on quartz. Transparent electrodes can be used for spectroelectrochemical measurements. The transparency and the stability of the optically transparent electrodes are critical for their use in spectroelectrochemical studies.[78] This technique helps to understand if the optically transparent electrode provides enough transparency

for the following spectroelectrochemical studies. The transmission spectrum has peaks associated with the band gap absorption by diamond and boron dopant bands.[78]

1.2.3. Scanning Electron Microscopy

The morphology of boron-doped diamond films deposited on Si, quartz and other substrates can be studied using scanning electron microscopy (SEM). The SEM uses a focused beam of high-energy electrons to generate a variety of signals at the surface of solid specimens. The signals that derive from electron-sample interactions reveal information about the sample including external morphology (texture), chemical composition, and crystalline structure and orientation of materials making up the sample. Sample preparation can be minimal or elaborate for SEM analysis, depending on the nature of the samples and the data required. For electrically insulating specimens, a thin layer of carbon or gold can be sputtered over the surface to improve the image quality and resolution.

1.3. Room Temperature Ionic Liquids (RTILs)

Room temperature ionic liquids (RTILs) are liquid electrolytes at room temperature. They contain no dielectric solvent. They consist of two ions: 1) a bulky asymmetric organic cation, such as pyridinium and imidazolium, and 2) smaller symmetric inorganic anion, such as tetrafluoroborate, hexafluorophosphate, and triflate.[5, 13, 14] Because of the many different combinations of ions, it is possible to design an ionic liquid with controlled physicochemical properties.[8, 10, 96] Figure 1.5 shows a few common cations and anions.

RTILs have garnered the scientific community's attention in recent years because of their unique physical properties. For example, they possess low melting points, low vapor pressure, high thermal/chemical stability, nonflammability, and moderate electrical conductivity.[5, 97-100]

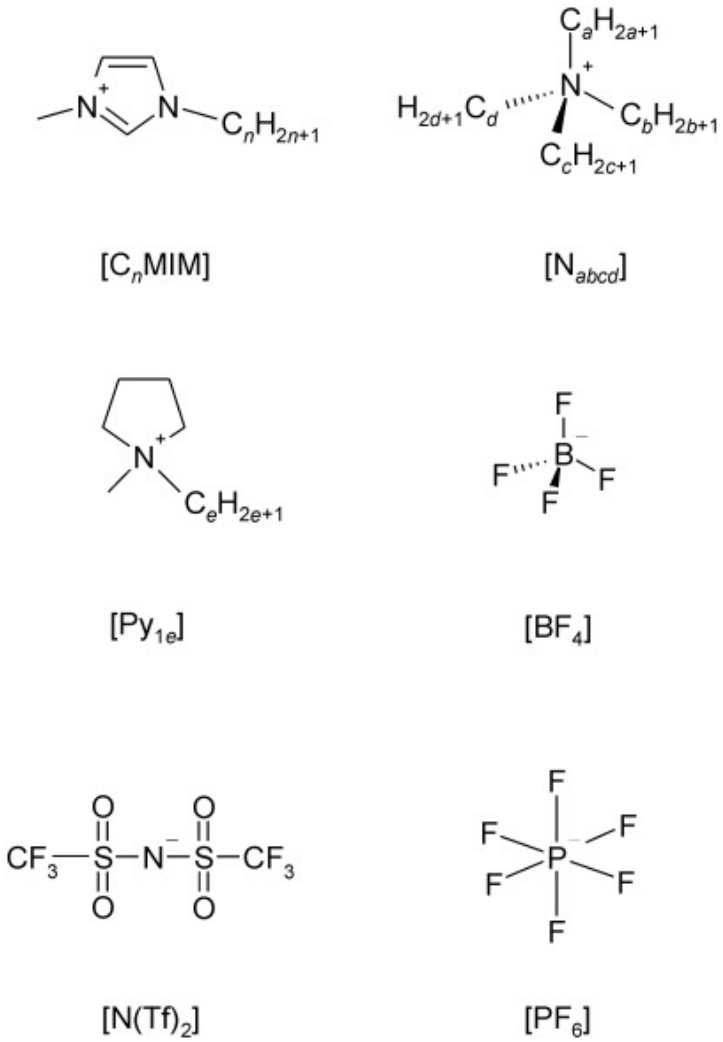

Figure 1.5. Some cations and anions used in room temperature ionic liquids.[5] [C_nMIM]: 1-alkyl-3-methylimidazolium, [Py_{1e}]: N-methyl-N-alkylpyrrolidinium, [N_{abcd}]: tetraalkylammonium, [BF_4]: tetrafluoroborate, [PF_6]: hexafluorophosphate, [$N(Tf)_2$]: bis(trifluoromethylsulfonyl)imide.

Their physicochemical properties differ greatly from the typical aqueous or organic electrolyte solutions. It is, therefore, important to consider their unique physicochemical features as they can significantly influence the electrochemical behavior:

1. RTILs exhibit a wide working potential window, making them a great choice for use in electrochemical studies. Their working potential window is wider than that for conventional organic solvents and aqueous media. A potential window between 4 to 6 V is a typical reported value for RTILs. The working potential window is highly affected by the

water impurity level, the presence of impurities from the synthesis, and the type of working electrode material. The wide working potential windows allow scientists to study a larger number of redox systems in RTILs compared to conventional solvents and aqueous environments.[8, 101]

2. RTILs have higher viscosity as compared to aqueous electrolytes. The high viscosity of RTILs slows down the diffusion and electron transfer processes in this environment.[11, 12, 20] The viscosity of ionic liquids is highly influenced by the level of water,[102, 103] temperature,[14, 104, 105] and structure of anions.[8, 10, 106]

3. The presence of impurities, especially water, has a noticeable effect on the electrochemical behavior of ionic liquids. Water can decrease the working potential window[13, 14, 18, 107], density[17], and viscosity[13, 14, 16, 107], increase conductivity[13, 14, 16, 107] and background current[108]. It introduces additional anodic and cathodic peaks to the voltammograms.[109] Additionally, it remarkably affects the kinetics parameters of redox systems under study in this environment.[108] For example, it results in a decrease in peak separation and an increase in the apparent heterogeneous electron transfer rate constant and the diffusion coefficient.[109]

4. The ionic nature of RTILs makes the columbic interaction the principal force in this environment. So, ions exist as ion pairs in RTILs rather than simple spherical charges. The ion-pairing decreases the true concentration of free ions in RTILs.

5. RTILs consist of pure ions. They do not have any solvent. So, there is no solvent to cover the surrounding of cations and anions. The asymmetry and polarizability of the ions prevent the formation of a stable lattice in these compounds. Therefore, the environment around redox systems and the double-layer structure are different from those

in conventional organic solvents and aqueous environments. It is known that the structure of the double-layer influences the electrochemical processes. Frumkin showed the effect of double-layer structure on the kinetics of electrochemical reactions. For example, the heterogeneous electron transfer rate constant depends on the nature and concentration of electrolyte ions.[7]

The structure of the double-layer in aqueous solutions is well-known. Solvent molecules surround ions in aqueous solutions.[11, 17, 20] "Gouy-Chapman-Stern" model can describe the solid-electrolyte interface. However, the "G-C-S" model cannot be used to describe the double-layer structure in RTILs because of the differences between RTILs and aqueous solutions. So, there is still a need to develop a model to fully explain the double-layer structure in the solventless environment of room temperature ionic liquids. Kornyshev developed the most well-known model to describe the double-layer structure in ionic liquids: the "Lattice Saturation Model". It is believed that there are multilayers of oscillatory charges at the interface.[13, 14] Figure 1.6. shows the proposed double-layer structure in room-temperature ionic liquids.[110]

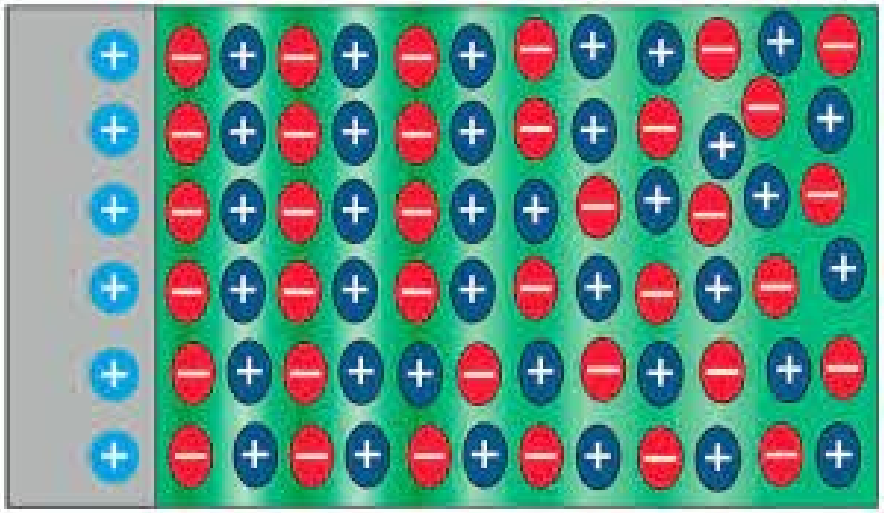

Figure 1.6. The double-layer structure in room-temperature ionic liquids. [110]

6. Several studies revealed the presence of long and short organization[111-113] of cations and anions in RTILs. So, the movement of one ion in RTILs results in the movement of all surrounding cations and anions because of the electrostatic interactions between constituent ionic parts. So, it is believed that in RTILs, redox systems should overcome a larger barrier of energy when they undergo an electron transfer process.

1.4. Research Objectives and Specific Aims

The central hypothesis of this research is that the capacitance, molecular adsorption, and heterogeneous electron- transfer rate constants of several soluble redox systems in RTILs will depend on the carbon electrode microstructure and surface chemistry in ways that are different from the trends found for the same electrodes in aqueous electrolyte solutions.

The research was conducted around three specific aims as follows:

Specific Aim 1. Detailed material characterization of boron-doped nanocrystalline diamond (BDD) thin-film electrodes, prepared by chemical vapor deposition on Si(100) and quartz substrates, will be performed to understand how the physical (texture and microstructure), chemical (B doping) and electrical properties (resistivity, carrier concentration and carrier mobility) are affected by the B incorporation and the sp^3 and sp^2 bonding in the films.

Specific Aim 2. Fundamental investigations of capacitance and heterogeneous electron-transfer rate constants for a variety of outer-sphere redox systems (ferrocene derivatives) in RTILs of different molecular composition. A goal is to learn if Marcus Theory of outer-sphere electron transfer kinetics adequately describes k^o for the different redox systems. Comparison studies will be performed using GC.

Specific Aim 3. Fundamental investigations of how the behavior of a surface confined redox-active molecule (*e.g.*, 1- and 2-anthraquinone diazonium) on BDD and GC electrodes is affected

by the molecular composition of the RTIL and how the behavior compares with that observed in aqueous elecrolyte solution.

REFERENCES

[1] R. L. McCreery, 'Carbon electrodes: structural effects on electron transfer kinetics', *Electroanal. Chem.* **1991**, *17*, 221-374.

[2] R. L. McCreery, in *Interfacial Electrochemistry*, Routledge, **2017**, 631-647.

[3] R. L. McCreery, 'Advanced carbon electrode materials for molecular electrochemistry', *Chem. Rev.* **2008**, *108*, 2646-2687.

[4] R. Khalil, N. Chaabene, M. Azar, I. B. Malham, M. Turmine, 'Effect of the chain lengthening on transport properties of imidazolium-based ionic liquids', *Fluid Ph. Equilibria.* **2020**, *503*, 112316.

[5] M. C. Buzzeo, R. G. Evans, R. G. Compton, 'Non-haloaluminate room-temperature ionic liquids in electrochemistry-A Review', *ChemPhysChem* **2004**, *5*, 1106-1120.

[6] H. Tokuda, S. Tsuzuki, M. A. Susan, K. Hayamizu, M. Watanabe, 'How ionic are room-temperature ionic liquids? An indicator of the physicochemical properties', *J Phys Chem B* **2006**, *110*, 19593-19600.

[7] A. Frumkin, 'Wasserstoffüberspanimng und Struktur der Doppelschicht', *Z. Phys. Chem. A* **1933**, *164*, 121-133.

[8] M. Galiński, A. Lewandowski, I. Stępniak, 'Ionic liquids as electrolytes', *Electrochim. Acta* **2006**, *51*, 5567-5580.

[9] M. Lozynski, J. Pernak, Z. Gdaniec, B. Gorska, F. Béguin, 'Proof of ion-pair structures in ammonium-based protic ionic liquids using combined NMR and DFT/PCM-based chemical shift calculations', *Phys. Chem. Chem. Phys.* **2017**, *19*, 25033-25043.

[10] T. L. Greaves, C. J. Drummond, 'Protic ionic liquids: properties and applications', *Chem. Rev.* **2008**, *108*, 206-237.

[11] A. A. Kornyshev, 'Double-layer in ionic liquids: paradigm change?', *J. Phys. Chem. B* **2007**, *111*, 5545-5557.

[12] J. L. Anderson, D. W. Armstrong, 'High-stability ionic liquids. A new class of stationary phases for gas chromatography', *Anal. Chem.* **2003**, *75*, 4851-4858.

[13] C. Zhao, G. Burrell, A. A. J. Torriero, F. Separovic, N. F. Dunlop, D. R. MacFarlane, A. M. Bond, 'Electrochemistry of room temperature protic ionic liquids', *J. Phys. Chem. B* **2008**, *112*, 6923-6936.

[14] D. S. Silvester, R. G. Compton, 'Electrochemistry in room temperature ionic liquids: A review and some possible applications', *Z. fur Phys. Chem.* **2006**, *220*, 1247-1274.

[15] M. Gnahm, D. M. Kolb, 'The purification of an ionic liquid', *J. Electroanal. Chem.* **2011**, *651*, 250-252.

[16] J. A. Widegren, A. Laesecke, J. W. Magee, 'The effect of dissolved water on the viscosities of hydrophobic room-temperature ionic liquids', *Chem. Commun.* **2005**, 1610-1612.

[17] J. G. Huddleston, A. E. Visser, W. M. Reichert, H. D. Willauer, G. A. Broker, R. D. Rogers, 'Characterization and comparison of hydrophilic and hydrophobic room temperature ionic liquids incorporating the imidazolium cation', *Green Chem.* **2001**, *3*, 156-164.

[18] U. Schröder, J. D. Wadhawan, R. G. Compton, F. Marken, P. A. Z. Suarez, C. S. Consorti, R. F. de Souza, J. Dupont, 'Water-induced accelerated ion diffusion: voltammetric studies in 1-methyl-3-[2,6-(S)-dimethylocten-2-yl]imidazolium tetrafluoroborate, 1-butyl-3-methylimidazolium tetrafluoroborate and hexafluorophosphate ionic liquids', *New J. Chem.* **2000**, *24*, 1009-1015.

[19] M. S. Kelkar, E. J. Maginn, 'Effect of temperature and water content on the shear viscosity of the ionic liquid 1-ethyl-3-methylimidazolium bis(trifluoromethanesulfonyl)imide as studied by atomistic simulations', *J. Phys. Chem. B* **2007**, *111*, 4867-4876.

[20] H. Weingärtner, P. Sasisanker, C. Daguenet, P. J. Dyson, I. Krossing, J. M. Slattery, T. Schubert, 'The dielectric response of room-temperature ionic liquids: effect of cation variation', *J. Phys. Chem. B* **2007**, *111*, 4775-4780.

[21] J. B. Reece, M. R. Taylor, E. J. Simon, J. L. Dickey, R. M. Liebaert, Study guide for Campbell biology: Pearson new international edition PDF ebook: concepts & connections, Pearson Higher Ed, **2013**.

[22] C. A. L. Y. Leon, L. R. Radovic, 'Interfacial chemistry and electrochemistry of carbon surfaces', *Chem. phys. carbon,* **1994**, *24*, 213-310.

[23] R. L. McCreery, A. J. Bard, 'Electroanalytical Chemistry', *Marcel Dekker, Inc., New York* **1991**, *17*, 221-374.

[24] K. Kinoshita, 'Carbon: electrochemical and physicochemical properties', **1988**.

[25] P. L. Walker, P. A. Thrower, *Chem. phys. carbon, Vol. 12*, CRC Press, **1975**.

[26] G. M. Swain, in *Handbook of Electrochemistry* (Ed.: C. G. Zoski), Elsevier, Amsterdam, **2007**, 111-153.

[27] S. Ranganathan, T.-C. Kuo, R. L. McCreery, 'Facile preparation of active glassy carbon electrodes with activated carbon and organic solvents', *Anal. Chem.* **1999**, *71*, 3574-3580.

[28] F. Barrière, A. J. Downard, 'Covalent modification of graphitic carbon substrates by non-electrochemical methods', *J. Solid State Electrochem.* **2008**, *12*, 1231-1244.

[29] H.-H. Yang, R. L. McCreery, 'Effects of surface monolayers on the electron-transfer kinetics and adsorption of methyl viologen and phenothiazine derivatives on glassy carbon electrodes', *Anal. Chem.* **1999**, *71*, 4081-4087.

[30] C. E. Banks, R. G. Compton, 'New electrodes for old: from carbon nanotubes to edge plane pyrolytic graphite', *Analyst* **2006**, *131*, 15-21.

[31] G. M. Jenkins, K. Kawamura, 'Structure of glassy carbon', *Nature* **1971**, *231*, 175-176.

[32] B. I. Kharisov, O. V. Kharissova, in *Carbon allotropes: metal-complex chemistry, properties and applications*, Springer, **2019**, 9-33.

[33] J. Asmussen, D. Reinhard, *Diamond films handbook*, CRC Press, **2002**.

[34] R. L. McCreery, in *Voltammetric methods in brain systems* (Eds.: A. A. Boulton, G. B. Baker, R. N. Adams), Humana Press, Totowa, NJ, **1995**, 1-26.

[35] K. Jurkiewicz, M. Pawlyta, D. Zygadło, D. Chrobak, S. Duber, R. Wrzalik, A. Ratuszna, A. Burian, 'Evolution of glassy carbon under heat treatment: correlation structure–mechanical properties', *J. Mater. Sci.* **2018**, *53*, 3509-3523.

[36] P. J. F. Harris †, 'Fullerene-related structure of commercial glassy carbons', *Philos Mag* **2004**, *84*, 3159-3167.

[37] D. T. Fagan, I. F. Hu, T. Kuwana, 'Vacuum heat-treatment for activation of glassy carbon electrodes', *Anal. Chem.* **1985**, *57*, 2759-2763.

[38] J. F. Evans, T. Kuwana, 'Introduction of functional groups onto carbon electrodes via treatment with radio-frequency plasmas', *Anal. Chem.* **1979**, *51*, 358-365.

[39] R. C. Engstrom, 'Electrochemical pretreatment of glassy carbon electrodes', *Anal. Chem.* **1982**, *54*, 2310-2314.

[40] M. Poon, R. L. McCreery, 'In situ laser activation of glassy carbon electrodes', *Anal. Chem.* **1986**, *58*, 2745-2750.

[41] J. Robertson, E. P. O'Reilly, 'Electronic and atomic structure of amorphous carbon', *Phys. Rev. B.* **1987**, *35*, 2946-2957.

[42] D. F. Baker, R. H. Bragg, 'The electrical conductivity and Hall effect of glassy carbon', *J. Non-Cryst* **1983**, *58*, 57-69.

[43] F. G. Celii, J. E. Butler, 'Diamond chemical vapor deposition', *Annu. Rev. Phys. Chem.* **1991**, *42*, 643-684.

[44] J. E. Butler, A. V. Sumant, 'The CVD of nanodiamond materials', *Chem. Vap. Depos.* **2008**, *14*, 145-160.

[45] P. W. May, M. N. R. Ashfold, Y. A. Mankelevich, 'Microcrystalline, nanocrystalline, and ultrananocrystalline diamond chemical vapor deposition: Experiment and modeling of the factors controlling growth rate, nucleation, and crystal size', *J. Appl. Phys.* **2007**, *101*, 053115.

[46] Y. Dai, D. A. Proshlyakov, J. K. Zak, G. M. Swain, 'Optically transparent diamond electrode for use in IR transmission spectroelectrochemical measurements', *Anal. Chem.* **2007**, *79*, 7526-7533.

[47] G. M. Swain, 'Electricity conducting diamond thin films: advanced electrode materials for electrochemical technologies', *Electroanal. chem., ser. adv.* **2003**, *22*, 181.

[48] Y. Einaga, J. S. Foord, G. M. Swain, 'Diamond electrodes: diversity and maturity', *MRS Bull.* **2014**, *39*, 525-532.

[49] M. Jiang, C. Chen, P. Wang, D. Guo, S. Han, X. Li, S. Lu, X. Hu, 'Diamond formation mechanism in chemical vapor deposition', *PNAS* **2022**, *119*, e2201451119.

[50] D. M. Gruen, 'Nanocrystalline diamond films', *Annu. Rev. Mater. Res.***1999**, *29*, 211.

[51] T. D. Corrigan, D. M. Gruen, A. R. Krauss, P. Zapol, R. P. H. Chang, 'The effect of nitrogen addition to Ar/CH_4 plasmas on the growth, morphology and field emission of ultrananocrystalline diamond', *Diam. Relat. Mater.* **2002**, *11*, 43-48.

[52] D. Zhou, D. M. Gruen, L. C. Qin, T. G. McCauley, A. R. Krauss, 'Control of diamond film microstructure by Ar additions to CH_4/H_2 microwave plasmas', *J. Appl. Phys.* **1998**, *84*, 1981-1989.

[53] D. Zhou, A. R. Krauss, T. D. Corrigan, T. G. McCauley, R. P. H. Chang, D. M. Gruen, 'Microstructure and field emission of nanocrystalline diamond prepared from C 60 precursors', *J. Electrochem. Soc.* **1997**, *144*, L224.

[54] M. Hupert, A. Muck, J. Wang, J. Stotter, Z. Cvackova, S. Haymond, Y. Show, G. M. Swain, 'Conductive diamond thin-films in electrochemistry', *Diam. Relat. Mater.* **2003**, *12*, 1940-1949.

[55] R. G. Compton, J. S. Foord, F. Marken, 'Electroanalysis at diamond-like and doped-diamond electrodes', *Electroanalysis* **2003**, *15*, 1349-1363.

[56] C. E. Nebel, B. Rezek, D. Shin, H. Uetsuka, N. Yang, 'Diamond for bio-sensor applications', *J. Phys. D: Appl. Phys* **2007**, *40*, 6443-6466.

[57] K. Pecková, J. Musilová, J. Barek, 'Boron-doped diamond film electrodes-new tool for voltammetric determination of organic substances', *Crit. Rev. Anal* **2009**, *39*, 148-172.

[58] J. V. Macpherson, 'A practical guide to using boron doped diamond in electrochemical research', *Phys. Chem. Chem. Phys.* **2015**, *17*, 2935-2949.

[59] S. J. Cobb, Z. J. Ayres, J. V. Macpherson, 'Boron doped diamond: a designer electrode material for the twenty-first century', *Annu Rev Anal Chem* **2018**, *11*, 463-484.

[60] C. I. Pakes, J. A. Garrido, H. Kawarada, 'Diamond surface conductivity: properties, devices, and sensors', *MRS Bull.* **2014**, *39*, 542-548.

[61] J. H. T. Luong, K. B. Male, J. D. Glennon, 'Boron-doped diamond electrode: synthesis, characterization, functionalization and analytical applications', *Analyst* **2009**, *134*, 1965-1979.

[62] J. Ristein, in *Semiconductors and Semimetals, Vol. 77* (Eds.: C. E. Nebel, J. Ristein), Elsevier, **2004**, 37-96.

[63] K. Bhardwaj, F. Parvis, Y. Wang, G. J. Blanchard, G. M. Swain, 'Effect of surface oxygen on the wettability and electrochemical properties of boron-doped nanocrystalline diamond electrodes in room-temperature ionic liquids', *Langmuir* **2020**, *36*, 5717-5729.

[64] M. C. Granger, G. M. Swain, 'The influence of surface interactions on the reversibility of Ferri/Ferrocyanide at boron-doped diamond thin-film electrodes', *J. Electrochem. Soc.* **1999**, *146*, 4551.

[65] I. Yagi, H. Notsu, T. Kondo, D. A. Tryk, A. Fujishima, 'Electrochemical selectivity for redox systems at oxygen-terminated diamond electrodes', *J. Electroanal. Chem.* **1999**, *473*, 173-178.

[66] F. B. Liu, B. Jing, Y. Cui, J. J. Di, M. Qu, 'Voltammetric and impedance behaviours of surface-treated nano-crystalline diamond film electrodes', *AIP Adv.* **2014**, *5*, 041306.

[67] R. Boukherroub, X. Wallart, S. Szunerits, B. Marcus, P. Bouvier, M. Mermoux, 'Photochemical oxidation of hydrogenated boron-doped diamond surfaces', *Electrochem. commun.* **2005**, *7*, 937-940.

[68] S. Wang, V. M. Swope, J. E. Butler, T. Feygelson, G. M. Swain, 'The structural and electrochemical properties of boron-doped nanocrystalline diamond thin-film electrodes grown from Ar-rich and H_2-rich source gases', *Diam. Relat. Mater.* **2009**, *18*, 669-677.

[69] P. E. Pehrsson, J. P. Long, M. J. Marchywka, J. E. Butler, 'Electrochemically induced surface chemistry and negative electron affinity on diamond (100)', *Appl. Phys. Lett.* **1995**, *67*, 3414-3416.

[70] J. Shirafuji, T. Sugino, 'Electrical properties of diamond surfaces', *Diam. Relat. Mater.* **1996**, *5*, 706-713.

[71] T. N. Rao, D. A. Tryk, K. Hashimoto, A. Fujishima, 'Band-edge movements of semiconducting diamond in aqueous electrolyte induced by anodic surface treatment', *J. Electrochem. Soc.* **1999**, *146*, 680-684.

[72] J. K. Zak, J. E. Butler, G. M. Swain, 'Diamond optically transparent electrodes: demonstration of concept with ferri/ferrocyanide and methyl viologen', *Anal Chem* **2001**, *73*, 908-914.

[73] S. Haymond, J. K. Zak, Y. Show, J. E. Butler, G. T. Babcock, G. M. Swain, 'Spectroelectrochemical responsiveness of a freestanding, boron-doped diamond, optically transparent electrode toward ferrocene', *Anal. Chim. Acta* **2003**, *500*, 137-144.

[74] J. Stotter, J. Zak, Z. Behler, Y. Show, G. M. Swain, 'Optical and electrochemical properties of optically transparent, boron-doped diamond thin films deposited on quartz', *Anal. Chem.* **2002**, *74*, 5924-5930.

[75] J. Stotter, Y. Show, S. Wang, G. Swain, 'Comparison of the electrical, optical, and electrochemical properties of diamond and indium tin oxide thin-film electrodes', *Chem. Mater.* **2005**, *17*, 4880-4888.

[76] Y. Dai, Y. Zheng, G. M. Swain, D. A. Proshlyakov, 'Equilibrium and kinetic behavior of $Fe(CN)_6^{-3/-4}$ and Cytochrome c in direct electrochemistry using a film electrode thin-layer transmission cell', *Anal. Chem.* **2011**, *83*, 542-548.

[77] H. B. Martin, P. W. Morrison, 'Application of a diamond thin film as a transparent electrode for in situ infrared spectroelectrochemistry', *Electrochem. solid-state lett.* **2001**, *4*, E17.

[78] N. Wächter, C. Munson, R. Jarošová, I. Berkun, T. Hogan, R. C. Rocha-Filho, G. M. Swain, 'Structure, electronic properties, and electrochemical behavior of a boron-Doped diamond/quartz optically transparent electrode', *ACS Appl Mater Interfaces* **2016**, *8*, 28325-28337.

[79] J. A. Bennett, J. Wang, Y. Show, G. M. Swain, 'Effect of sp^2-bonded nondiamond carbon impurity on the response of boron-doped polycrystalline diamond thin-film electrodes', *J. Electrochem. Soc.* **2004**, *151*, E306.

[80] P. Rai, S. K. Dubey, in *Handbook of Materials Characterization*, Springer, **2018**, 405-434.

[81] M. I. Nathan, J. E. Smith Jr, K.-N. Tu, 'Raman spectra of glassy carbon', *J. Appl. Phys.* **1974**, *45*, 2370-2370.

[82] M. A. Pimenta, G. Dresselhaus, M. S. Dresselhaus, L. G. Cançado, A. Jorio, R. Saito, 'Studying disorder in graphite-based systems by Raman spectroscopy', *Phys. Chem. Chem. Phys.* **2007**, *9*, 1276-1290.

[83] F. Tuinstra, J. L. Koenig, 'Raman spectrum of graphite', *J. Chem. Phys.* **1970**, *53*, 1126-1130.

[84] P. K. Chu, L. Li, 'Characterization of amorphous and nanocrystalline carbon films', *Mater. Chem. Phys.* **2006**, *96*, 253-277.

[85] A. C. Ferrari, J. Robertson, 'Origin of the 1150 - cm^{-1} Raman mode in nanocrystalline diamond', *Phys. Rev. B.* **2001**, *63*, 121405.

[86] A. C. Ferrari, J. Robertson, 'Raman spectroscopy of amorphous, nanostructured, diamond–like carbon, and nanodiamond', *Philos. Trans. Royal Soc. A* **2004**, *362*, 2477-2512.

[87] S. Prawer, R. J. Nemanich, 'Raman spectroscopy of diamond and doped diamond', *Philos. Trans. Royal Soc. A* **2004**, *362*, 2537-2565.

[88] W. A. Yarbrough, R. Messier, 'Current issues and problems in the chemical vapor deposition of diamond', *Science* **1990**, *247*, 688-696.

[89] M. Mermoux, B. Marcus, G. M. Swain, J. E. Butler, 'A Confocal Raman imaging study of an optically transparent boron-doped diamond electrode', *J. Phys. Chem. B* **2002**, *106*, 10816-10827.

[90] P. W. May, W. J. Ludlow, M. Hannaway, P. J. Heard, J. A. Smith, K. N. Rosser, 'Raman and conductivity studies of boron-doped microcrystalline diamond, facetted nanocrystalline diamond and cauliflower diamond films', *Diam. Relat. Mater.* **2008**, *17*, 105-117.

[91] P. Szirmai, T. Pichler, O. A. Williams, S. Mandal, C. Bäuerle, F. Simon, 'A detailed analysis of the Raman spectra in superconducting boron doped nanocrystalline diamond', *Phys. Status Solidi B* **2012**, *249*, 2656-2659.

[92] E. Bourgeois, E. Bustarret, P. Achatz, F. Omnès, X. Blase, 'Impurity dimers in superconducting B-doped diamond: Experiment and first-principles calculations', *Phys. Rev. B.* **2006**, *74*, 094509.

[93] M. Bernard, C. Baron, A. Deneuville, 'About the origin of the low wave number structures of the Raman spectra of heavily boron doped diamond films', *Diam. Relat. Mater.* **2004**, *13*, 896-899.

[94] V. A. Sidorov, E. A. Ekimov, 'Superconductivity in diamond', *Diam. Relat. Mater.* **2010**, *19*, 351-357.

[95] J. P. Goss, P. R. Briddon, 'Theory of boron aggregates in diamond: First-principles calculations', *Phys. Rev. B.* **2006**, *73*, 085204.

[96] T. D. Ho, C. Zhang, L. W. Hantao, J. L. Anderson, 'Ionic liquids in analytical chemistry: fundamentals, advances, and perspectives', *Anal. Chem.* **2014**, *86*, 262-285.

[97] J. Dupont, C. S. Consorti, J. Spencer, 'Room temperature molten salts: Neoteric" green" solvents for chemical reactions and processes', *J. Braz. Chem. Soc.* **2000**, *11*, 337-344.

[98] S. Passerini, G. B. Appetecchi, 'Toward more environmentally friendly routes to high purity ionic liquids', *MRS Bull.* **2013**, *38*, 540-547.

[99] N. Borisenko, R. Atkin, F. Endres, 'Influence of molecular organization of ionic liquids on electrochemical properties', *Electrochem. Soc. Interface* **2014**, *23*, 59.

[100] A. J. Greer, J. Jacquemin, C. Hardacre, 'Industrial applications of ionic liquids', *Molecules* **2020**, *25*.

[101] P. Hapiot, C. Lagrost, 'Electrochemical reactivity in room-temperature ionic liquids', *Chem. Rev.* **2008**, *108*, 2238-2264.

[102] S. Guo, F. Chen, L. Liu, Y. Li, X. Liu, K. Jiang, R. Liu, S. Zhang, 'Effects of the water content on the transport properties of ionic liquids', *Ind. Eng. Chem. Res.* **2019**, *58*, 19661-19669.

[103] S. Fendt, S. Padmanabhan, H. W. Blanch, J. M. Prausnitz, 'Viscosities of acetate or chloride-based ionic liquids and some of their mixtures with water or other common solvents', *J. Chem. Eng. Data.* **2011**, *56*, 31-34.

[104] A. B. McEwen, H. L. Ngo, K. LeCompte, J. L. Goldman, 'Electrochemical properties of imidazolium salt electrolytes for electrochemical capacitor applications', *J. Electrochem. Soc.* **1999**, *146*, 1687-1695.

[105] O. O. Okoturo, T. J. VanderNoot, 'Temperature dependence of viscosity for room temperature ionic liquids', *J. Electroanal. Chem.* **2004**, *568*, 167-181.

[106] R. S. Varma, 'Solvent-free organic syntheses . using supported reagents and microwave irradiation', *Green Chem.* **1999**, *1*, 43-55.

[107] M. Gnahm, C. Müller, R. Répánszki, T. Pajkossy, D. M. Kolb, 'The interface between Au(100) and 1-butyl-3-methyl-imidazolium-hexafluorophosphate', *Phys. Chem. Chem. Phys.* **2011**, *13*, 11627-11633.

[108] R. Jarosova, G. M. Swain, 'Rapid preparation of room temperature ionic liquids with low water content as characterized with a t*a*-C:N electrode', *J. Electrochem. Soc.* **2015**, *162*, H507-H511.

[109] R. Jarošová, K. Bhardwaj, G. M. Swain, 'Temperature dependence of the heterogeneous electron-transfer rate constant for ferrocene carboxylic acid in room temperature ionic liquids at microstructurally distinct carbon electrodes', *J. Electroanal. Chem.* **2020**, *875*, 114744.

[110] C. Rodenbücher, K. Wippermann, C. Korte, 'Atomic force dpectroscopy on ionic liquids', *Appl. Sci.* **2019**, *9*.

[111] R. S. Anaredy, S. K. Shaw, 'Long-range ordering of ionic liquid fluid films', *Langmuir* **2016**, *32*, 5147-5154.

[112] K. Ma, R. Jarosova, G. M. Swain, G. J. Blanchard, 'Charge-induced long-range order in a room-temperature ionic liquid', *Langmuir* **2016**, *32*, 9507-9512.

[113] K. Ma, R. Jarosova, G. M. Swain, G. J. Blanchard, 'Modulation of an induced charge density gradient in the room-temperature ionic liquid $BMIM^{+}BF_4^{-}$, *J. Phys. Chem. C* **2018**, *122*, 7361-7367.

CHAPTER 2. VOLTAMMETRIC AND CAPACITANCE BEHAVIOR OF OPTICALLY TRANSPARENT DIAMOND ELECTRODES IN RTILS

2.1. Abstract

The electrochemical working potential window, voltammetric background current, potential-dependent capacitance and redox activity of boron-doped diamond optically transparent electrodes (BDDOTEs) were evaluated in different room temperature ionic liquids (RTILs) using cyclic voltammetry and electrochemical impedance spectroscopy. Three alkyl imidazolium tetrafluoroborate ([EMIM][BF_4], [BMIM][BF_4], and [HMIM][BF_4]) and three alkyl imidazolium bis(trifluoromethylsulfonyl) imide ([EMIM][TFSI], [BMIM][TFSI], and [HMIM][TFSI]) RTILs were studied. Some measurements were also performed in an aqueous electrolyte solution, 1 mol L^{-1} KCl, for comparison The goal of the work was to learn about the electrochemical behavior of BDDOTEs in RTILs and how it differs from that in a conventional aqueous electrolyte solution. The working potential window was 4.5 V in all three RTILs. The potential-dependent capacitance values (C_{dl}-E) were lower in the different RTILs over the potential range probed ranging from 3 to 8 μF cm^{-2}, as compared to 9-20 μF cm^{-2} in 1 mol L^{-1} KCl. The RTIL type exhibited little effect on the working potential window, voltammetric background current, or interfacial capacitance values of the BDDOTEs. The C_{dl}-E curves were generally flat across the potential range probed or had a slight upward shift with increasing positive potential, much different from bell-shaped C_{dl}-E trends around the potential of zero charge observed for an Au disk electrode. Interestingly, the BDDOTEs exhibited both semiconducting electronic properties, as evidenced by Mott-Schottky analysis of the capacitance data with an apparent flat band potential in the 2-3 V vs. AgQRE range, and semimetallic electronic properties, as evidenced by quasi-reversible electron-transfer kinetics for ferrocene and ferrocene derivatives with the electrodes under depletion conditions. The heterogeneous behavior of the BDDOTEs is attributed to the uneven boron dopant

distribution spatially within the film. Comparison studies with glassy carbon (GC) electrodes revealed voltammetric background current and capacitance values 5-10x larger than the values for the BDDOTEs in the RTILs consistent with a lower density of electronic states in the latter.

2.2. Introduction

Optically transparent diamond electrodes are a unique type of electrode made from transparent diamond material. These electrodes are gaining popularity in various fields due to their exceptional properties, such as high transparency, chemical stability, and biocompatibility.[1-10] These electrodes are particularly useful in applications that require both electrical conductivity and optical transparency, such as in optoelectronics, bioelectronics, and electrochemical sensors (*i.e.*, spectroelectrochemistry).

Our group, and others, have made use of either free-standing diamond plates or thin films of boron-doped diamond (BDD) deposited on quartz for transmission spectroelectrochemical measurements in the UV/Vis region of the electromagnetic spectrum[1,3-6] or on undoped Si for measurements in the mid to far-IR.[2,6,7] BDD possesses attractive qualities as an optically transparent electrode: optical transparency in different regions of the electromagnetic spectrum, a wide working potential window (> 3V in aqueous media), chemical stability, low background current, microstructural stability during anodic and cathodic polarization, and resistance to molecular adsorption and fouling. [1,4-8] Depending on the doping level and film thickness, diamond films are transparent in the visible (300-700 nm) and mid to far-IR (<1100 cm^{-1}) regions. The preparation of an OTE requires a balance of film thickness (thick enough to be continuous but not too thick to significantly reduce transmission) and doping level (sufficient doping level to impart electrical conductivity but not so high to make the film opaque). In the case of diamond, one has some control over the material's optical properties through selection of the chemical vapor

deposition conditions used for thin film growth. The wide optical window coupled with the interesting electrochemical properties make BDDOTEs unique materials for transmission spectroelectrochemistry and sensor technologies in which both electrochemical and spectroscopic signal transduction is desired. A longer-term goal of our research is to use these optically transparent electrodes in spectroelectrochemical measurements for the study of redox reactions in room temperature ionic liquids (RTILs). To this end, the research reported herein was conducted to learn about how the electrochemical properties of the electrodes are influenced by RTILs of different ionic composition.

Room temperature ionic liquids (RTILs) are solventless liquid salts with a low melting point and are composed of pure ions. [11-17] They consist of a large asymmetric organic cation and a smaller, more symmetric inorganic anion. The physiochemical properties of these liquid salts can be manipulated by combining different cations and anions. Their low vapor pressure, high thermal and chemical stability, moderate electrical conductivity, and non-flammability make them interesting and attractive for electrochemical applications, affording advantages over organic and aqueous electrolyte solutions. [11-17] Their solventless nature, large breakdown voltage, high viscosity, and moderate electrical conductivity are key properties for electrochemical measurements. [11-20]

RTILs contain no dielectric solvent to separate the ions. Compositionally, RTILs are composed of a mixture of free ions, associated cation-anion pairs, and clusters of associated ion pairs. [15,17,18,21-23] Their ionic nature makes the columbic interactions the principal force controlling the ion mobility and the free ion concentration. Although weaker, dipole-dipole, ion-dipole, and Van der Waals forces are also operative. For example, Lozynski and co-workers demonstrated the formation of ion-pair complexes in triethylammonium bis

(trifluoromethylsulfonyl)imide $(C_2H_5)_3NH$ TFSI using combined NMR and DFT/PCM-based chemical shift calculations. [21] The viscous and ionic nature of RTILs impacts both electron transfer and mass transfer kinetics in electrochemical reactions. Fundamentally, the chemical environment around a soluble redox system in an RTIL is distinct from that in a typical aqueous or organic electrolyte environment. Large reorganization energy barriers can exist in RTILs to transition the ionic environment from that of the reactant to that of the product upon electron transfer, resulting in sluggish electron transfer kinetics. The viscosity of the RTIL can slow the nuclear frequency factor (or the frequency of attempts the redox analyte attempts to surmount the activation barrier) thereby slowing the electron transfer kinetics. The high viscosity of these liquids reduces diffusional flux of the redox analyte to the electrode. [15,17]

Another point to consider is that the electrode-solution interfacial region in RTILs is distinctly different from that in an aqueous or organic electrolyte solution. This can affect both the capacitance and the potential felt by the analyte at the plane of closest approach. This plane, where the electron transfer is envisioned to occur, is likely spaced further away from the electrode surface with less potential drop. Both factors would decrease the rate of electron transfer. Electrochemists employ the "Gouy-Chapman-Stern" model (Helmholtz + diffuse layers) to describe electrochemical double-layer formed in an aqueous electrolyte solution. This model predicts that as an electrode becomes more highly charged (*e.g.*, excess surface charge at a given potential increases), the diffuse layer becomes more compact, and the capacitance increases away from the potential of zero charge. The application of this model for RTILs is inappropriate for two reasons. First, there is no dielectric solvent separating the ions and the total concentration of ions is rather high at 3-6 M. However, the concentration of free ions is less than this because of significant ion-pairing. A study by the Tokuda group showed the true ionic concentration of RTILs is in the range

of 50 to 80 % of their total ionic concentration.[20] Second, the model treats ions as point charges with little occupied volume. This means the model is most accurate in dilute solutions and potentials near the potential of zero charge. A model that has been broadly applied to describe RTIL interfaces at metal electrodes is the lattice saturation model described by Kornyshev and co-workers. [17] This model predicts that at potentials away from the potential of zero charge, the capacitance decreases, rather than increases, with increasing potential. This results because a single layer of volume occupying ions is not sufficient to counterbalance the excess surface charge on the electrode, so multiple layers develop. This model predicts a bell shaped rather than a U-shaped capacitance-potential curve around the potential of zero charge. [17]

Several factors are known to influence the interfacial capacitance and heterogeneous electron-transfer kinetics for soluble redox systems at BDD electrodes, including the film microstructure, boron-doping level, hydrogen incorporation, level of sp^2 carbon impurity, and surface chemistry. [24-29, and refs. therein] This insight exists mainly for redox systems in aqueous electrolyte solutions. There has been limited literature published on the electrochemical behavior of BDD electrodes in RTILs, and no reports concerning BDDOTEs. A few examples are given here. Ernst et al. studied the electrochemical reduction of oxygen at the BDD and GC electrodes in 1-ethyl-3-methylimidazolium bis(trifluoromethylsulfonyl)imide, C_2mim NTf_2.[30] They observed more sluggish electron transfer kinetics at BDD as compared to GC electrodes, which was attributed to a lower density of electronic states in the former. Cannes et al. studied the interfacial capacitance of Pt and various carbon electrodes in [BMIM][Tf_2N] at different temperatures. [31] They studied the potential-dependent capacitance of Pt, GC, a-CNx and BDD electrodes. For BDD, Mott-Schottky plots confirmed the polycrystalline semiconducting properties of the material. Capacitance values ranged from 35-45 μF cm^{-2} for BDD, which were

higher than the values of 20-30 μF cm^{-2} observed for GC over the potential range probed. The capacitance of both electrodes increased with increasing temperature. Lucio et al. investigated the double-layer capacitance of BDD in two protic and three aprotic RTILs using large-amplitude Fourier transformed alternating current voltammetry (FT-ACV). [32] The capacitance values ranged from 3 to 8 μF cm^{-2} over the potential range probed. The potential-dependent capacitance values did not depend on RTIL composition. Li et al. studied the effect of highly localized sp^2 carbon impurity concentrated at the edge of a BDD electrode on the electrochemical behavior in 1-butyl-3-methylimidazolium hexafluorophosphate [BMIM][PF_6]. [33] The work showed that sp^2 carbon impurity can significantly affect the electrochemical behavior (ferrocene) of BDD in RTILs under conditions of slow mass transport and short time scales. The heterogeneity of the electrodes in terms of the sp^2 and sp^3 carbon domains can be evaluated individually under these conditions. Kim et al. determined the heterogeneous electron transfer rate constant for ferrocene and ferrocene carboxylic acid in 1-butyl-3-methylimidazolium tetrafluoroborate (BMIM BF_4) at boron-doped microcrystalline diamond thin-film electrodes. [34] The k^o for FCA and ferrocene were found to be 1.5 (±1.1)×10^{-3} cm s^{-1} and 5.0 (±1.2)×10^{-3} cm s^{-1} in BMIM BF_4, respectively. Comparison studies for FCA in KCl revealed a larger value of 4.6 (±1.3)×10^{-2} cm s^{-1} for the rate constant. Jarosova et al. reported on the temperature dependence of the heterogeneous electron-transfer rate constant for ferrocene carboxylic acid in EMIM BF_4 and BMIM BF_4 at boron-doped diamond (BDD), nitrogen-incorporated tetrahedral carbon thin-film (t*a*-C:N), and GC electrodes.[35] They measured capacitance values of 5-12 μF cm^{-2} in the two RTILs over the potential range probed. They also observed both the type of carbon electrodes and the type of RTILs have a noticeable effect on heterogeneous electron transfer rate constant. They reported an increase in both the diffusion coefficient and the rate constant with increasing the temperature. The apparent heterogeneous rate

constant increased in the following order BDD > t*a*-C:N > GC. The reported activation energy showed the following trend: BDD < t*a*-C: N < GC. The rate constant increases and the activation energy decreases in the less viscous medium of [EMIM][BF_4]. Another report by Swain's group on the electrochemical properties of BDD electrodes in RTILs revealed a slight effect of surface chemistry (H vs. O) on the background voltammetric current, working potential window, and potential-dependent capacitance in [BMIM][PF_6] and [HMIM] [PF_6] using cyclic voltammetry and electrochemical impedance spectroscopy. [36]

In this work, we report on the working potential window, background voltammetric current and potential dependent interfacial capacitance for BDDOTEs in multiple RTILs. We also probed the electrode activity using ferrocene and two ferrocene derivatives. The results for BDDOTEs are compared with GC in the RTILs, and the electrode behavior in the RTILs is compared with the behavior in an aqueous electrolyte solution.

2.3. Experimental

Growth of Nanocrystalline Boron-Doped Diamond Optically Transparent Electrodes (BDDOTEs). The optically transparent diamond thin films were grown on 0.2 cm-thick quartz substrates that were 2.54 × 2.54 cm^2 in area, as described previously. [1,3,8] The quartz was pretreated for diamond growth by (i) ultrasonic cleaning in acetone for 30 min, (ii) scratching the clean substrate with 100 nm diamond powder suspended in water on a felt pad, (iii) ultrasonically seeding the scratched substrate in "Opal Seed" (Adamas Technologies, Raleigh, NC) for 30 min, and (iv) rinsing with ultrapure water. Opal Seed, as purchased, consists of ~30 nm diamond particles suspended in dimethyl sulfoxide. The diamond deposition was accomplished by microwave-assisted chemical vapor deposition (Seki Diamond Systems, 1.5 kW) using 600 W, 25 torr, and a hydrogen-rich source gas mixture with a total gas flow of 200 sccm (standard cubic

centimeters per minute). A 1% (v/v) methane-to-hydrogen source gas mixture was used with 10 ppm of diborane added for boron doping. The actual ultrahigh purity gas flow rates were 2.00 sccm methane, 196 sccm hydrogen, and 2.00 sccm diborane (0.1 %, v/v) mixed with hydrogen. The deposition time was typically 4 h. These growth conditions produce a continuous film across the substrate with a thickness of 0.5-1 μm. At the end of the deposition period, the methane and diborane flows were stopped while the diamond-coated substrate remained exposed to a hydrogen plasma. The power and pressure were then gradually reduced over a 30-min period to 250 W and 10 torr to cool the coated substrates in the presence of atomic hydrogen. This step serves to preserve a hydrogen surface termination after growth and prevent reconstruction to a sp^2 carbon phase.

Chemicals and Solutions. Potassium chloride, CAS: 7447-40-7, was purchased from Sigma-Aldrich. Ferrocenecarboxaldehyde (CAS: 12093-10-6, 98%), ferrocene (CAS: 102–54-5, 98%), and ferrocenemethanol (CAS: 1273-86-5, 97%) were purchased commercially (Sigma Aldrich), and used as received. The RTILs, 1-ethyl-3-methylimidazolium tetrafluoroborate EMIM BF_4 (CAS: 143314-16-3), 1-butyl-3-methylimidazolium tetrafluoroborate BMIM BF_4 (CAS: 174501-65-6), and 1-hexyl-3-methylimidazolium tetrafluoroborate HMIM BF_4 (CAS: 244193-50-8) were purchased commercially (IoLiTec, Germany, specified as ≥ 98% purity). The physical properties of the three RTILs, as specified by the supplier, are listed in Table 2.1 The reported dielectric constants were taken from the paper by Bennett and coworkers. [37]

Table 2.1. Physical properties of water and the different RTILs at 25 °C.

Analyte	Mol. wt. (g mol^{-1})	Viscosity (mPa-s)	Conductivity (mS cm^{-1})	Dielectric Constant[37]	Density (g cm^{-3})
EMIM BF_4	197.97	34*	14.1*	12.9	1.28*
BMIM BF_4	226.02	104*	3.2*	9.7	1.30*
HMIM BF_4	254.08	288*	1.2*	8.4	1.15*
EMIM TFSI	391.31	39*	6.63*	13.8	1.52*
BMIM TFSI	419.37	49*	3.41*	9.2	1.44*
HMIM TFSI	447.42	63*	2.27*	8.5	1.37*

*Data were provided by the chemical supplier IoLiTec - Ionic Liquids Technologies (Germany).

Purification of Room Temperature Ionic Liquids (RTILs). The RTILs were purified to reduce water and other impurity content using the following steps prior to their use in electrochemical measurements[38,39]:

1. The "as-received" RTIL was stored over activated carbon for at least 14 days in a capped vial prior to use serves to remove organic impurities. The RTIL above the settled carbon black was then carefully removed using a syringe fitted with a 0.45 μm Teflon syringe filter (Millex®HA) and transferred into a clean and capped glass vial.
2. The filtered RTIL was then stored over 5Å molecular sieves (Fisher Scientific) in the capped glass vial for at least one week to remove water impurity. The molecular sieves were activated before use by heating at ~400 °C in a furnace for two weeks.

3. A small volume of the purified RTIL was then transferred to a clean and dry glass electrochemical cell in a nitrogen-purged vinyl glove box (Coy Laboratories, Grass Lake, MI). The RTIL was then heated at ~70 ºC for 50 min while being purged with ultra-high purity Ar (Airgas). This is a so-called "sweeping" pretreatment.

After this purification, the water level in selected RTILs was generally below 100 ppm, as estimated from thermogravimetric analysis mass loss data upon heating up to 300 ºC. [39] The assumption is that the weight loss that arises above 200 ºC from water evaporation. The water impurity content was measured in randomly selected RTIL samples prepared in this manner. In all cases, the water impurity level was measured before the RTIL was used in the electrochemical measurements. The ultrapure water used for solution preparation and glassware cleaning was prepared using a Barnstead E-pure System (Thermo Scientific, USA). The ultrapure water had a resistivity ≥17 MΩ-cm. All soap-cleaned glassware was rinsed with ultrapure water followed by rinsing with ultrapure isopropanol (distilled and stored over activated carbon) and then drying in the oven for at least 12 h before transferring to the glove box for use in the electrochemical experiments.

Electrochemical Measurements. All electrochemical measurements were performed in the N_2-purged vinyl glove box. The house nitrogen used for purging was blow off from a large LN_2 storage tank with a specified water content of < 0.27 ppm. The gas was passed through drierite desiccant prior to entering the glove box. The working electrode, either the BDDOTE or glassy carbon (GC), was clamped to the bottom of a single-compartment glass electrochemical cell. A Viton™ O-ring with an area of 0.2 cm^2 was placed between the bottom of the glass cell and the working electrode to define the geometric electrode area exposed to the liquid. Electrical contact with the diamond film surface was made by pressing a piece of aluminum foil along one edge of

the diamond surface outside the O-ring area, wrapping the foil to the backside of the quartz substrate, and contacting it with a clean copper plate current collector. The BDDOTEs were pretreated before use by exposure to ultraclean isopropanol (distilled and stored over activated carbon) for 20 min. The GC working electrode was pretreated before use by hand polishing with successively smaller grades of alumina powder (1.0, 0.3, and 0.05 μm diam.), slurried in ultrapure water, on separate polishing pads. After each polishing step, the electrode was rinsed with and then ultrasonically cleaned in ultrapure water for 15 min to remove polishing debris. A Pt wire (0.5 mm diam.) served as the counter electrode. An Ag wire was used as the quasi-reference electrode (Ag QRE). For all the measurements, approximately 1 mL of purified RTIL was used. Ar gas blanketed the purified RTIL in the cell during an electrochemical measurement in the glove box. This process minimized water contamination. Aqueous electrolyte solutions were deaerated with N_2 purging for at least 10 min before and blanketed with the gas during a measurement. These measurements were made outside the glove box on the laboratory bench.

The gold macro-disk electrode (3 mm diam.) was polished with an alumina power (0.3 μm)/water slurry and cleaned prior to use. The polished electrode was cleaned by thorough rinsing with ultrapure water and then ultrasonically treated for 30 s in 1 M HCl. The electrode was subjected to potential cycling in 0.5 M H_2SO_4 (scan rate: 0.5 V s^{-1}) to clean and activate the surface. A graphite rod was used as the counter electrode and a homemade Ag/AgCl electrode served as the reference in a single-compartment glass electrochemical cell. Figure 2.1 shows the stable cyclic voltammetric *i-E* curve for the activated Au electrode in 0.5 M H_2SO_4. Well defined regions of Au oxide formation (E > 1.2 V) and Au oxide reduction (E_p = 1.0 V) are seen.

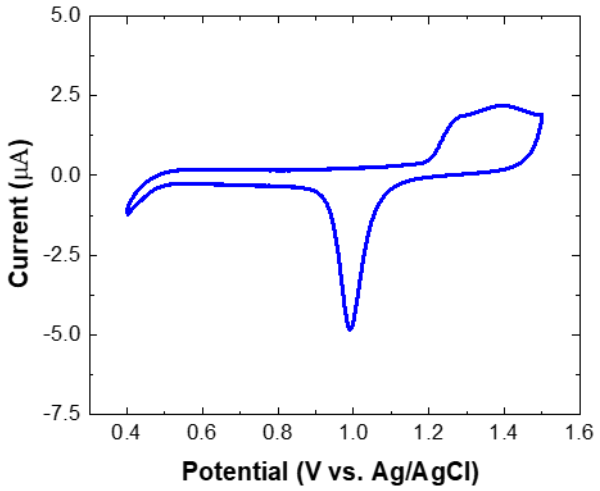

Figure 2.1. Cyclic voltammetric *i-E* curve for an activated Au electrode in 0.5 M H_2SO_4. Scan rate = 0.5 V s^{-1}.

Cyclic Voltammetry. Cyclic voltammetry (CV) was performed using a computer-controlled electrochemical workstation (Model 650B or 650A, CH Instruments Inc., Austin, TX). Voltammograms were recorded as a function of the scan rate (0.025 to 0.25 Vs^{-1}). The double-layer capacitance, C_{dl} (μF cm^{-2}), was calculated from the slope of a background current density (*j*, A cm^{-2}) *vs.* scan rate (*v*, V s^{-1}) plots at different applied potentials using the following equation.

$$j = C_{dl}\, \nu \qquad [1]$$

Electrochemical Impedance Spectroscopy. Electrochemical impedance spectroscopy (EIS) was performed using a computer-controlled potentiostat (Model 650B or 650A, CH Instruments Inc., Austin, TX). EIS was carried out at different applied dc potentials from -1.0 to 1.0 V vs. Ag QRE using a range of co-added ac frequencies from 10^6 to 10^{-1} Hz. Twelve data points were collected per decade. A sine wave (10 mV amplitude) was co-added to each dc potential. A rest time of 300 s was allotted before collecting the impedance data at each potential. The data were analyzed using the model equivalent circuit shown in Figure 2.2. The full frequency EIS experimental data were fit using the equivalent circuit below and ZView® 3.5h software.

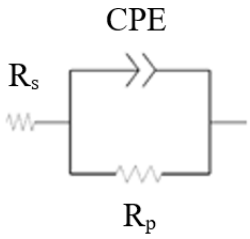

Figure 2.2. The model equivalent circuit used to fit the full frequency impedance data for the BDDOTEs in the different RTILs.

In the circuit, R_s represents the combined bulk electrolyte resistance, electrode and electrical contact ohmic resistance (so-called equivalent series resistance). R_p is the polarization resistance. A constant phase element (CPE) was used in place of a capacitor to describe the quasi-capacitive character of the electric double layer at the heterogeneous electrode surface.[40,41] The impedance of the CPE is defined in equation [2],

$$Z_{CPE} = \frac{1}{Q(j\omega)^{\alpha}} \quad [2]$$

where Q is the quasi-capacitance and is directly proportional to the active area ($(\Omega\text{-m}^2)^{-1/\alpha}\,s^{\alpha}$), α is the so-called homogeneity factor ($\alpha = 1$ for an ideal capacitor), ω is the angular frequency, and j is the imaginary number. The quasi-capacitance, Q, has no physical meaning; however, the effective capacitance, C_{eff}, in farads may be calculated from Q using the surface distribution function proposed by Hirschorn et al. shown below (Equation 3).[41] In this equation,

$$C_{eff} = \left(\frac{R_s R_p}{R_s + R_p}\right)^{\frac{1-\alpha}{\alpha}} Q^{\frac{1}{\alpha}} \quad [3]$$

α and Q represent global properties. The calculated C_{eff} is normalized to the geometric area exposed to the RTIL solution (GC and BDDOTE= 0.2 cm^2 and Au= 0.03 cm^2). All capacitance and current values reported herein are normalized to the electrodes' geometric area.

UV/Vis Spectroscopy Measurements. UV/Vis transmission spectroscopy was used to study the optical properties of the BDDOTEs. Before each measurement, films were cleaned by rinsing with deionized water and ultrapure (distilled and stored over activated carbon) isopropanol, and then dried with nitrogen. UV−Vis transmission spectra were recorded from 200-900 nm using a commercial, double-beam UV−Vis spectrophotometer (Shimadzu Model UV2401-PC). A quartz substrate used for diamond film growth served as the reference.

Statistical Data Analysis. Data are reported as mean ± standard deviation for $n \geq 3$ electrodes. The mean values were statistically compared using either a Student's t-test or one-way analysis of variance (ANOVA) to determine statistically significant differences. *p*-values ≤ 0.05 were considered statistically significant. The null hypothesis was used for testing and that is there is no significant difference between mean values.

2.4. Results

2.4.1. Material Characterization

The optical transparency of BDDOTEs in the near UV/Vis region of the electromagnetic spectrum has been reported previousl.[1-10] Figure 2.3A presents a typical transmission spectrum for a film deposited with a 1% (v/v) CH_4/H_2 ratio at a thickness of 0.5-1µm. The reduced transparency at short wavelengths, < 300 nm, is due to absorption by the diamond as the bandgap energy is approached (5.45 eV or 230 nm). Relatively constant transparency between 50-60 % is seen in the visible region from 400-700 nm. The transparency decreases at longer wavelengths due to absorption by boron dopant energy states. The optical properties of the BDDOTEs are stable in harsh chemical environments, in a variety of organic solvents, and during the application of high positive and negative potentials. [3] The optical properties reported herein are consistent with previously reported data for other BDDOTEs deposited using similar conditions. [1,3,5,8,9,10]

Reflection is the primary light loss mechanism in the visible portion of the spectrum due to the relatively high refractive index of diamond (2.41 at 590 nm).

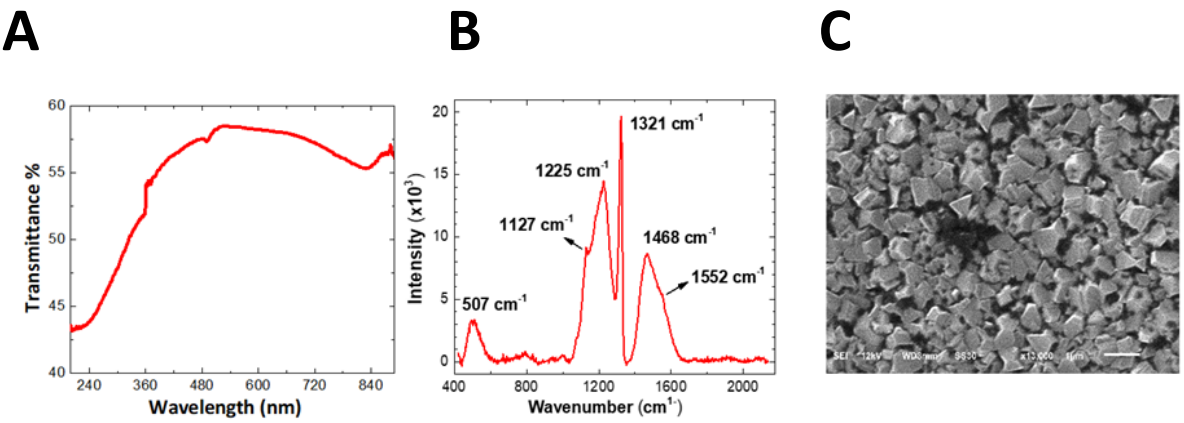

Figure 2.3. (A) Transmission spectrum for a BDDOTE with a film thickness of 0.5-1µm. (B) A representative Raman spectrum for a BDDOTE. (C) An SEM micrograph showing the polycrystalline morphology of a BDDOTE film.

Raman spectroscopy was used to study the microstructure of the BDDOTEs. A representative spectrum is shown in Figure 2.3B. Similar spectra were recorded across different regions of this and other BDDOTEs, meaning there is a similar film microstructure spatially throughout a film. The spectral features are consistent with previous reports for BDDOTEs. [8] Multiple peaks are apparent at 507, 1127, 1225, 1321, 1468, and 1552 cm^{-1}. For a heavily boron-doped film, the first-order diamond phonon line shifts from 1332 cm^{-1} to lower wavenumbers with increasing boron concentration. Here, the first-order diamond phonon line is seen at 1321 cm^{-1}. In general, the shift in the diamond phonon line is coincident with an increase in peak intensities at 507 and 1225 cm^{-1}. The peak at 507 cm^{-1} has been attributed to the vibrational modes of boron dimers, pairs, and clusters.[42-44] The peak at 1225 cm^{-1} can be assigned to the defects in the diamond lattice. These defects arise from the high boron doping level. [42,44,45] Peaks at 1127 and 1468 cm^{-1} are assigned to polymeric sp^2 carbon species in the grain boundaries. [46] Given the small crystallite size, the BDDOTEs have a relatively high fraction of exposed grain boundary.

The peak at 1552 cm^{-1} is related to more graphitic sp^2-bonded carbon impurity that forms in the grain boundaries because of the high boron-doping level. [45,47] It should be noted that the scattering cross section for sp^2-bonded carbon is larger than the cross section for sp^3-bonded carbon with visible excitation, so a relatively low level of sp^2 impurity carbon can give rise to sizeable scattering intensity in the spectrum. [48]

Figure 2.3C presents a plan-view SEM micrograph of a typical BDDOTE. A polycrystalline film morphology is evident with a nominal crystallite size on the order of 800 nm. The quartz substrate pretreatment and diamond deposition conditions generally produce a continuous film. [1,3,8] However, sometimes sites of incomplete coverage can be found. This is the case for the film in Figure 2.3C, as there is a void (dark area near the center of the micrograph) where crystallite coalescence from lateral growth across the seeded substrate has not fully occurred. These types of defects have implications on the electrical resistance as the current in the electrochemical measurements is collected laterally through the diamond thin film. If there are voids and locations where there is not good grain-to-grain contact and bonding, then the overall resistance to current flow will increase.

We previously reported on detailed material characterization of the BDDOTEs deposited similarly. [8] Temperature-dependent Hall Effect measurements revealed a room temperature resistivity of 0.06 Ω-cm that decreases by only a factor of 2 during a temperature ramp from 300 to 700 K. The carrier concentration, *ca.* 10^{21} cm^{-3}, and carrier mobility, *ca.* 0.2 cm^2 V^{-1} s^{-1} were largely temperature independent, consistent with the electronic properties of a degenerate semiconductor or semimetal. A low activation energy of conduction of 10 meV was determined. XPS revealed a surface low in carbon-oxygen functionalities, O/C = 0.03, for the OTEs as-prepared. The boron doping level was uniform with depth in the film. The boron concentration of

ca. 10^{21} cm^{-3} in the film is consistent with the high boron doping level reflected in the Raman spectra and with the carrier concentration determined from Hall Effect measurements. The boron exists in three chemical environments: B-B pairs or clusters likely in grain boundaries, B-C groups due to the substitutionally inserted boron dopant atoms and B-O groups at the film surface.

2.4.2. Cyclic Voltammetric Behavior

Figure 2.4 shows cyclic voltammetric *i-E* curves over the full potential window for a BDDOTE in [EMIM] [BF_4], [BMIM] [BF_4], and [HMIM] [BF_4]. The potential window in all three RTILs is *ca.* 4.5 V, independent of the ionic composition (cation type). The working potential window is defined as the difference between the anodic and cathodic potentials at which the current reaches ± 0.01 mA. The relatively wide working potential window means extreme positive and negative potentials are required to electrochemically oxidize and reduce the RTIL ions. This window is slightly narrower than what has been previously reported for these and other RTILs at BDD and tetrahedral amorphous carbon electrodes prepared in our laboratory (5-6 V). [35,36,39] The identities of the breakdown products are unknown at this time. Importantly, this large working potential window allows for the study of redox systems with standard reduction potentials over a wider potential range than is possible in aqueous electrolyte solutions. On the positive-going sweep, a small anodic peak is seen between 1 to 2 V. This peak is associated with the oxidation of residual water impurity.[35,36,38,49] For example, one can spike the RTIL with water and the peak will develop at these potentials. As the level of water impurity in the RTIL increases, the magnitude of this water oxidation peak will increase. [38,49] We typically do not detect any redox activity with the low background current BDDOTE in this potential range, although in this particular [EMIM][BF_4] liquid, some water impurity was detected. No efforts were made to quantify this level of water impurity from the measured peak current.

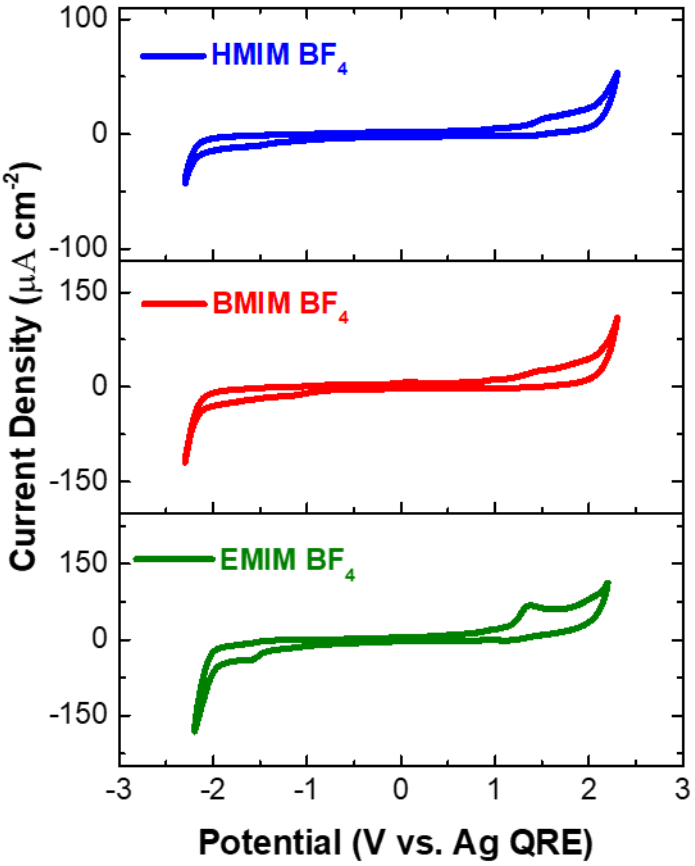

Figure 2.4. Cyclic voltammetric $i-E$ curves for a BDDOTE in [EMIM][BF_4], [BMIM][BF_4], and [HMIM] [BF_4]. Scan rate = 0.1 V s^{-1}. Geometric area = 0.2 cm^2.

2.4.3. Capacitance-Potential (C_{dl}−E) Trends in RTILs

Figures 2.5A, C, and E show background cyclic voltammetric *i-E* curves for a BDDOTE in the three alkyl imidazolium tetrafluoroborate RTILs over a smaller potential range as a function of the scan rate from 0.025 to 0.25 V s^{-1}. The curve shapes were unchanging with cycle number from 2 to 10 at a given scan rate. Furthermore, the rectangular shape of the voltammetric curves is symmetrical about the zero-current line. The magnitude of background current in all three RTILs is low (0.01−0.5 μA cm^{-2}). The current in all three RTILs increases with the scan rate, and all curves are devoid of any defined peaks within this potential range that might otherwise be associated with parasitic redox reactions. The background current at potentials within this range increased linearly with the scan rate indicating the current is capacitive in nature (see Equation [1]). The one-way analysis of variance (ANOVA) revealed there is no statistical difference in the mean current at the measured potentials for the three RTILs ($p > 0.05$).

Figure 2.5B, D, and F show plots of the background current versus scan rate in all three RTILs at 0.2 V. The current increases with the scan rate, at least up to up to 0.250 V s^{-1}, in a linear manner ($R^2 > 0.99$). This is expected for capacitive charging current. As the rate of excess surface charge accumulation at each potential is increased with scan rate, the RTIL ions and polar ion pairs on the solution side of the interface can achieve their counterbalancing excesses as fast as the rate of potential change. One would anticipate that at higher scan rates than these, the current would no longer increase linearly with the scan rate as the viscous nature of the RTIL would limit how fast ions can migrate to achieve the counterbalancing excesses in the interfacial region.

The current versus scan rate plot slopes can be used to calculate the double-layer capacitance (C_{dl}). Table 2.2 shows the calculated C_{dl} values for BDDOTEs in the three RTILs. C_{dl}

trends toward increasing values with increasing positive potential in all three RTILs. The values range from 5-10 μF cm^{-2}.

Table 2.2. Capacitance values for BDDOTEs in different RTILs as calculated from cyclic voltammetric background current data as a function of scan rate.

RTILs	C_{dl} (μF cm^{-2})		
	E= -0.2 (V)	**E= 0.2 (V)**	**E= 0.4 (V)**
[EMIM] [BF_4]	3.4 ± 0.4	5.2 ± 1.0	6.4 ± 1.7
[BMIM] [BF_4]	5.1 ± 0.9	7.2 ± 1.1	8.0 ± 1.2
[HMIM] [BF_4]	5.2 ± 0.7	7.0 ± 1.1	7.8 ± 1.2
[EMIM][TFSI]	6.2 ± 1.7	10.0 ± 3.1	12.2 ± 3.9
[BMIM][TFSI]	5.9 ± 1.2	8.5 ± 1.7	9.8 ± 1.7
[HMIM][TFSI]	5.5 ± 1.1	7.8 ± 2.4	9.4 ± 3.3

Values are presented as mean ± std. dev. for n=3 different BDDOTEs. There is no significant ($p > 0.05$) statistical difference in the mean values of capacitance in the different RTILs at 0.2 V, as assessed from the one-way analysis of variance (ANOVA).

These capacitance values are smaller in magnitude than the values for this electrode in an aqueous electrolyte solution, e.g., 1 M KCl, by a factor of 3-4x (see Figure 2.12 below). One-way analysis of variance (ANOVA) revealed there are no statistical differences in the mean C_{dl} values at 0.2 V for the different RTILs given the response variability ($p > 0.05$). The variability for the BDDOTEs is somewhat high at ~15% and is like the variability seen in similar measurements with GC in the same RTILs at ~11% (see Table

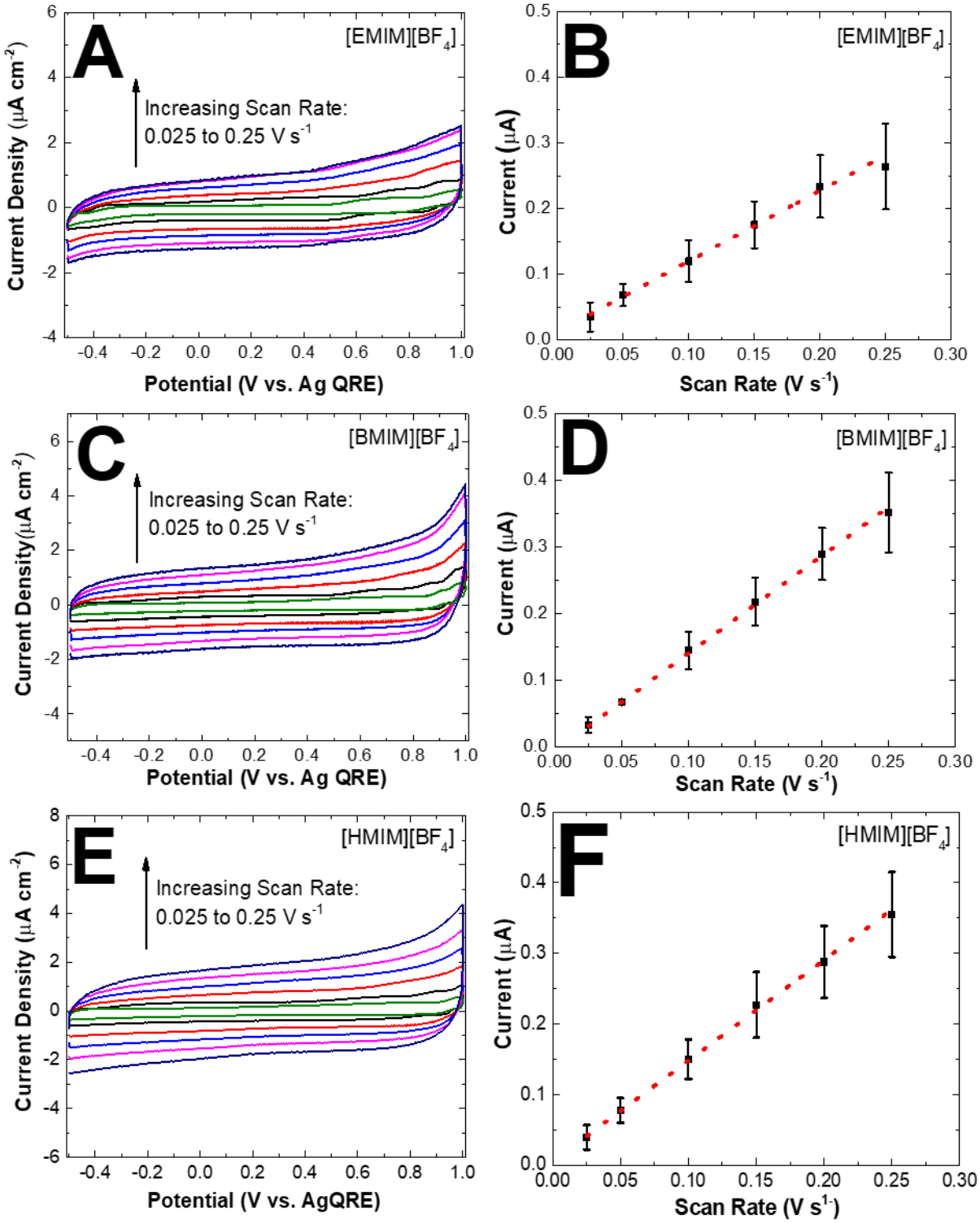

Figure 2.5. Cyclic voltammetric *i*−*E* curves recorded as a function of the scan rate (0.025-0.25 V s^{-1}) for BDDOTEs in (A) [EMIM][BF_4], (C) [BMIM] [BF_4], and (E) [HMIM] [BF_4]. Plots of the background current versus scan rate at 0.2 V for BDDOTEs in (B) [EMIM] [BF_4], (D) [BMIM] [BF_4], and (F) [HMIM] [BF_4] are also presented. Current values are presented as mean ± std. dev. for n = 3 electrodes.

2.3 below). Therefore, the variability in the measured C_{dl} values appears to mainly arise from the properties of the RTILs and the instrument used for the measurements in the glove box.

Background cyclic voltammetric *i–E* curves recorded for GC at different scan rates in [BMIM] [BF_4] are presented in Figure 2.6A. GC serves as a useful comparison electrode for the BDDOTE measurements. The curve shapes were unchanged with cycle numbers from 2 to 10 at a given scan rate. The background current for GC is larger than the current for the BDDOTEs in the potential range probed by a factor of 4-8x. The presence of electrochemically active carbon-oxygen functional groups on the surface and the larger density of electronic states are two reasons for the larger background current.[50-53] These redox-active functional groups

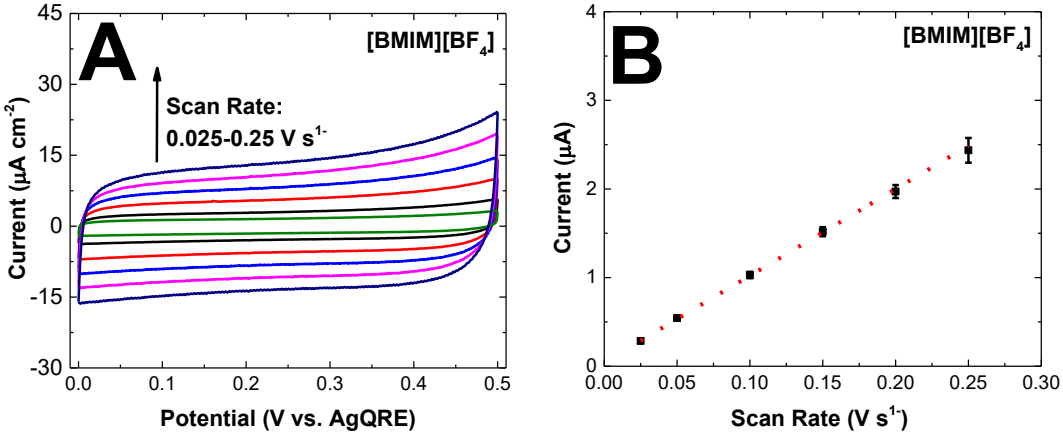

Figure 2.6. Cyclic voltammetric *i*−*E* curves recorded as a function of the scan rate (0.025−0.25 V s^{-1}) for GC in (A) [BMIM] [BF_4]. The plot of the background current versus scan rate at 0.2 V for GC in [BMIM] [BF_4] is also presented. Current values are presented as mean ± std. dev. for n = 3 GC electrodes.

are mostly absent on the BDDOTEs. The current increases proportionally with the scan rate in the probed potential range. For example, the positive-going background current at 0.2 V increases linearly with the scan rate for GC with a linear regression correlation coefficient of 0.9994. The plot of current vs. scan rate at 0.2 V is linear, indicating the current is capacitive in nature. From the plot slope in different RTILs, the electrode capacitance at 0.2 V was calculated and the results

are presented in Table 2.3 The values are 5-10x larger for GC than for the BDDOTEs. The C_{dl} values at 0.2 V in the different RTILs are not statistically different ($p > 0.05$) according to the one-way analysis of variance (ANOVA).

Table 2.3. Capacitance values for GC electrodes in [EMIM][BF_4], [BMIM][BF_4] and [HMIM][BF_4] as calculated from cyclic voltammetric background current data.

RTILs	**C_{dl} (μF cm^{-2})**
	E = 0.2 (V)
[EMIM] [BF_4]	46 ± 5
[BMIM] [BF_4]	48 ± 3
[HMIM] [BF_4]	38 ± 6

Values are presented as mean ± std. dev. for n=3 different GC electrodes. There is no significant (p = 0.11) statistical difference in the mean capacitance values in the different RTILs at each of the three potentials, as assessed by one-way analysis of variance (ANOVA).

Figure 2.7A-C shows Nyquist plots of the impedance-frequency data for a BDDOTE in [EMIM][BF_4], [BMIM][BF_4], and [HMIM][BF_4] as a function of the applied potential from -0.9 to 0.9 V vs. AgQRE. Both experimental and computer-fitted data are presented; the latter generated using the circuit model shown in Figure 2.2. Data are presented for frequencies from 10^6 to 10^{-1} Hz. The plots of the real (Z′) vs. imaginary (Z″) impedance component data at multiple potentials are approaching straight vertical lines, as expected for a pure capacitance. The data at multiple potentials have similar vector angles with the Z′ axis reflecting the close capacitance values at these potentials. At the highest frequencies, the curves intercept the Z′ axis at a value that indicates the equivalent series resistance, R_s. This resistance is the sum of the electrode, RTIL, and electrical contact ohmic resistances. The R_s values range between 0.1-1 kohm for [EMIM][BF_4], 3-4 kohm for [BMIM][BF_4], and 4-5 kohm for [HMIM][BF_4]. Clearly, the RTIL resistance dominates R_s.

The values increase with increasing cation size and viscosity of the RTIL. With careful purification of the RTIL and no Faradaic reactions occurring at the electrode surface, then the Nyquist plots of the impedance data in the RTILs is a near straight vertical line with some curvature at lower frequencies.[54,55] In the absence of Faradaic reactions, the Randle's-like equivalent circuit shown in Figure 2.2 collapses to a single R_e-*CPE* circuit. We attribute the curvature seen at the more

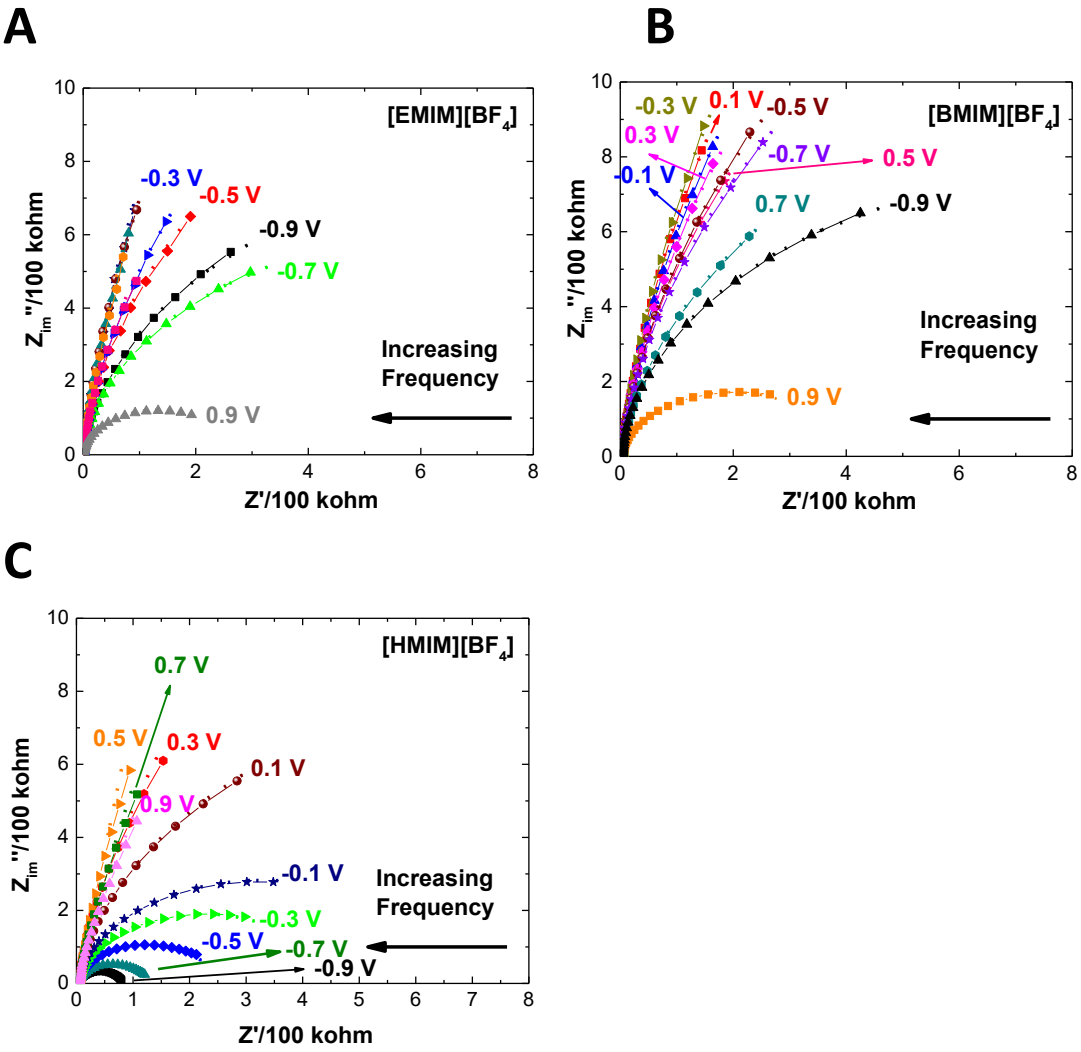

Figure 2.7. Nyquist plots of the real (Z′) vs. imaginary (Z″) components of the total impedance for a BDDOTE as a function of frequency in (A) [EMIM] [BF_4], (B) [BMIM] [BF_4], and (C) [HMIM] [BF_4] at applied potentials from -0.9 to 0.9 V vs. Ag QRE. The impedance data were obtained at frequencies from 10^6 to 10^{-1} Hz.

negative and positive potentials to current flow associated with Faradaic processes, possibly residual dissolved O_2 reduction at the negative potentials, and or the slow ion transport within the bulk RTIL.[56]

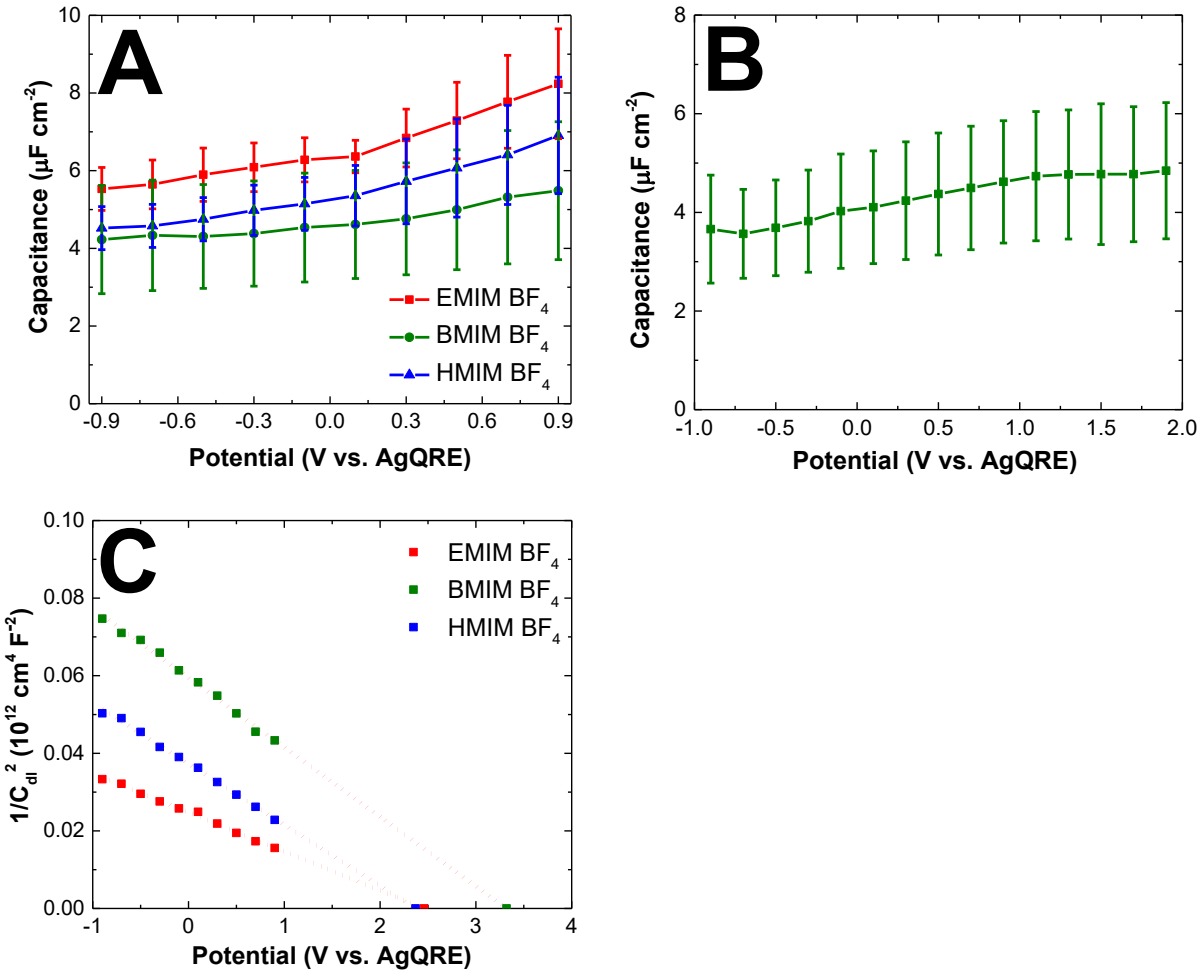

Figure 2.8. (A) Potential-dependent capacitance (C_{eff}) data for BDDOTE in [EMIM] [BF_4] (red squares), [BMIM] [BF_4] (green squares), [HMIM] [BF_4] (blue squares). The capacitance values were calculated from curve-fitting the EIS data. Data are presented as mean ± std. dev. for n = 3 electrodes. (B) Potential-dependent capacitance data for BDDOTE in [BMIM] [BF_4] over a wider potential range (-1.0 V to 2.0 V. (C) Mott–Schottky plots of $1/C_{dl}^2$ vs. potential were obtained for BDDOTE in [EMIM] [BF_4] (red squares), [BMIM] [BF_4] (green squares), and [HMIM] [BF_4] (blue squares).

The full frequency EIS data were fit using the model equivalent circuit in Figure 2.2 to determine the effective capacitance (C_{eff} or C_{dl}) at each potential. C_{eff} was calculated from the

fitting parameters as indicated in equation 3 above. Figure 2.8A shows C_{dl}-E data for BDDOTEs in [EMIM] [BF_4], [BMIM] [BF_4], and [HMIM] [BF_4]. The values are presented as mean ± std. dev. for n=3 different electrodes. The capacitance values vary minimally from 5-9 μF cm^{-2} in [EMIM][BF_4], 4-6 μF cm^{-2} in [BMIM][BF_4], and 4-7 μF cm^{-2} in [HMIM][BF_4] over the 2V potential range probed. Furthermore, the capacitance values determined from the EIS data agree with the values obtained from the cyclic voltametric measurements (see Table 2.2). Given the standard deviations, there is not a statistically significant ($p > 0.05$) difference in the mean capacitance values in the three RTILs at any of the potentials. There is a slight trend of increasing capacitance with increasing positive potential in all three RTILs. Such a trend is expected for a *p-type* semiconducting electrode. This sort of C_{dl}-E shape has been reported for BDD electrodes dating back to the earliest days of their study[57,58] and has been observed for BDD electrodes in RTILs.[32,54,55] Figure 2.8B shows C_{dl}-E data recorded for BDDOTE in [BMIM] [BF_4] over a wider potential range from -1 to 2 V. Even over this wider range, the capacitance values range from 3-6 μF cm^{-2}. There is an indication of a capacitance minimum near -0.7 V.

The capacitance values of 3-9 μF cm^{-2} are similar to values reported for other BDD electrodes in these and other RTILs. [31,32,35,36,54,55] For the BDDOTEs used in this work, the cation type of the RTIL did not have a significant effect on the measured capacitance. Nominally at the different potentials, the capacitance decreases in order of [EMIM][BF_4] > [BMIM][BF_4] ~ [HMIM][BF_4]. However, given the magnitude of the standard deviations, no significant differences were found in the capacitance at any of the potentials in the three RTILs ($p > 0.05$).

To assess whether the low and relatively unchanging capacitance with potential in the different RTILs might be due to the BDDOTEs possessing more semiconducting rather than semimetal electronic properties, Mott-Schottky plots of the C_{dl}-E data were made. Figure 2.8C

presents $1/C_{dl}^2$ vs. E plots obtained for BDDOTE in the three different RTILs. Rather unexpectedly, the plots are linear over a wide potential range of 2 V. The negative slope of the plots indicates *p*-type electrical conduction consistent with the boron acceptor doping. The potential axis intercept of the plots is the apparent flat band potential, E_{fb}. [59] In [BMIM][BF_4], the apparent E_{fb} is 3.32 V, while in [EMIM][BF_4] and [HMIM][BF_4], the apparent E_{fb} is 2.46 and 2.37 V, respectively. Mean capacitance values from one set of measurements are plotted so it is unclear if these differences in E_{fb} are significant. The fact that Mott-Schottky behavior is seen for these electrodes indicates that there is some potential drop internally in the electrode and across the solution interface. [32,59] This means that there is an internal or space charge capacitance, C_{sc}, at least at some sites across the electrically heterogeneous thin-film electrode, and an interfacial capacitance, C_H. In other words, a portion of the applied potential is distributed internally across the space charge layer with the remaining portion distributed across the Helmholtz layer on the solution-side of the interface. The slope of the plots can be used to estimate the charge carrier concentration. The linear regression equations for the plots are as follows: (i) [EMIM][BF_4] $y = -0.01005x + 0.02476$, (ii) [BMIM][BF_4] $y = -0.01792x + 0.05945$, and (iii) [HMIM][BF_4] $y = -0.01571x + 0.03728$ (all $R^2 > 0.99$). Using a dielectric constant for diamond of 5.6, the slopes were used to calculate the carrier concentration. A nominal value of 1.8×10^{21} cm^{-3} was calculated (range 1.4 to 2.5×10^{21} cm^{-3}) from the data in all three RTILs and this is consistent with the carrier concentration determined from Hall Effect measurements.[8] Lucio et al. reported an E_{fb} of 1.3 ± 0.4 V vs Fc/Fc^+ in [BMIM][BF_4] for a highly boron-doped diamond electrode.[32] This corresponds to ~1.8 V vs. AgQRE, which is positive but slightly lower than the values reported herein. They observed linearity of the $1/C_{dl}^2$ vs. E plots over a 1.5 V potential range similar to the 2V range seen in the data above. It is interesting and somewhat unexpected that the Mott-Schottky analysis

reveals linear $1/C_{dl}^2$ vs. E plots given the BDDOTEs are highly boron doped, $>10^{20}$ cm^{-3}. The doping of diamond occurs inhomogeneously, so there are likely highly doped regions surrounded by lower doped areas. [60,61] In other words, the electrode material is heterogeneous in electrical and electrochemical properties with both semiconducting and semimetallic electronic properties exhibited. [60-65]

If the Mott-Schottky analysis is correct and E_{fb} is the range of 2-3 V vs. AgQRE in the RTILs, then the material is in a state of charge carrier depletion at potentials negative of E_{fb} for a *p-type* semiconducting material. As such, the electron-transfer kinetics for soluble redox systems with formal potentials negative of E_{fb} should, in theory, be kinetically inhibited due to a limited number of available charge carriers. This behavior, in fact, is not observed. As an example, Figure 2.9A presents cyclic voltammetric *i-E* curves for 0.1 mM ferrocene (Fc) in [EMIM][TFSI] as a function of scan rate. The average peak potential ($(E_p^{ox} + E_p^{red})/2$) of 0.48 V is well into the depletion region and yet quasi-reversible electron-transfer kinetics are observed with well-defined oxidation and reduction peak currents. Similar peak-shaped voltammograms were observed for Fc in both [BMIM][TFSI] and [HMIM][TFSI], as presented in Figure 2.9B and C. The ΔE_p increases with viscosity of the RTILs and the current past both peaks decreases more slowly with time, especially for the reduction peak, than is seen in the less viscous [EMIM][TFSI]. Even though Fc is undergoing electron transfer quasi-reversibly, both the oxidation and reduction peak currents increase linearly with the scan rate$^{1/2}$, as seen in the plots in Figure 2.9D ($R^2 > 0.98$). The slopes decrease in order of [EMIM][TFSI] > [BMIM][TFSI] > [HMIM][TFSI] due to the decreasing values of D_{Fc} and D_{Fc+} with increasing RTIL viscosity. Table 2.4 summarizes the cyclic voltammetric data for Fc, ferrocene methanol (FcMeOH), and ferrocene carboxaldehyde (FcCHO) all at a scan rate of 0.025 V s^{-1}. The data indicate that all three redox systems undergo relatively

rapid electron transfer with the BDDOTEs under depletion conditions. ΔE_p values range from 70-90 mV in the least viscous [EMIM][TFSI] and increase in the more viscous [BMIM][TFSI] and [HMIM][TFSI]. It should be noted that the ΔE_p have not been corrected for potential error or *iR* effects. Apparent values of D_{red} or D_{Fc} are also presented and range from 10^{-8} to 10^{-7} cm^2 s^{-1}.

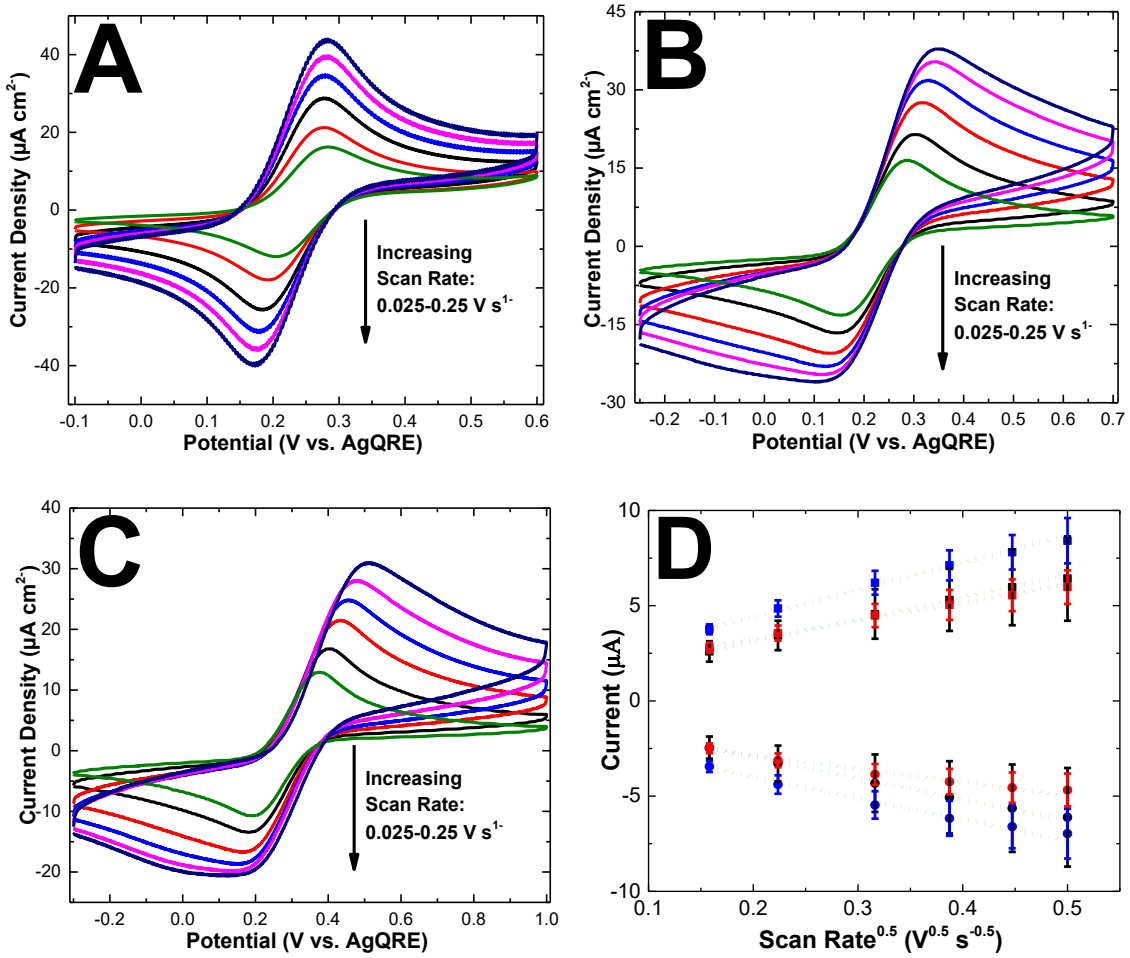

Figure 2.9. Cyclic voltammetric *i-E* curves for 1 mmol L^{-1} Fc at a BDDOTE in (A) [EMIM][TFSI], (B) [BMIM][TFSI], and (C) [HMIM][TFSI] at scan rates from 0.025-0.25 V s^{-1}. (D) Randles−Sevcik plots of i_p^{ox} and i_p^{red} vs. $v^{1/2}$ for 1 mmol L^{-1} Fc in [EMIM][TFSI] (Black), [BMIM][TFSI] (Blue), [HMIM][TFSI] (Red) at a BDDOTE. (■) Oxidation peak current (i_p^{ox}), (●) reduction peak current (i_p^{red}). Data are presented as mean ± std. dev. for n=3 BDDOTEs.

Table 2.4. Peak separations (ΔE_p), and oxidation peak current (i_p^{ox}), and diffusion coefficients (D_{red}) for ferrocene derivatives in [EMIM][TFSI], [BMIM][TFSI], and [HMIM][TFSI] at BDDOTEs.

Analyte	RTIL	ΔE_p (mV)	i_p^{ox} (µA)	$D_{red} \times 10^{-7}$ ($cm^2\ s^{-1}$)
Fc	**[EMIM] [TFSI]**	91 ± 21	2.60 ± 0.53	0.50 ± 0.40
	[BMIM] [TFSI]	109 ± 18	3.76 ± 0.26	0.65 ± 0.24
	[HMIM] [TFSI]	146 ± 33	2.80 ± 0.26	0.30 ± 0.13
FcCHO	**[EMIM] [TFSI]**	81 ± 10	3.34 ± 0.14	0.95 ± 0.11
	[BMIM] [TFSI]	76 ± 7	1.91 ± 0.30	0.36 ± 0.07
	[HMIM] [TFSI]	85 ± 25	0.79 ± 0.14	0.05 ± 0.04
FcMeOH	**[EMIM] [TFSI]**	78 ± 5	2.83 ± 0.15	0.64 ± 0.13
	[BMIM] [TFSI]	94 ± 33	1.57 ± 0.32	0.21 ± 0.16
	[HMIM] [TFSI]	127 ± 16	1.83 ± 0.10	0.13 ± 0.03

Data are reported as a mean ± std. dev. for n=3 BDDOTEs at a scan rate of 0.025 V s^{-1}. ΔE_p values are uncorrected for potential error or *iR* effects. FcCHO = ferrocene carboxaldehyde. FcMeOH = ferrocene methanol. Fc = ferrocene.

Comparison experiments were performed with glassy carbon (GC). Figure 2.10A shows C_{dl}-*E* data for GC in [EMIM] [BF_4], [BMIM] [BF_4], and [HMIM] [BF_4]. The capacitance values were determined from the full frequency EIS data fit to the equivalent circuit shown in Figure 2.2. The capacitance values in all three RTILs are larger than the values for the BDDOTEs ranging from 19 - 28 µF cm^{-2} in [EMIM] [BF_4], 28 - 33 µF cm^{-2} in [BMIM] [BF_4], and 26 - 36 µF cm^{-2} in [HMIM] [BF_4] over the potential range probed. Given the standard deviation values at each potential, there is no significant difference ($p > 0.05$) in the mean values at any of potentials in the

three RTILs. Importantly, though, the capacitance values for GC are 3-7x larger than the values for the BDDOTEs in the same RTILs and the same potentials. Additionally, the capacitance values for GC determined from EIS data are lower than the values determined from cyclic voltammetric data (see Table 2.3). This is attributed to the presence of electrochemically active surface carbon-oxygen functional groups on the GC surface that give rise to a pseudo-capacitance in the voltammetric measurements (*i.e.*, extra current above the double layer charging current).[50,51] This leads to increased voltammetric background current and a larger calculated capacitance. Finally, the C_{dl}-E curves have a distinct minimum near -0.1 V vs. Ag QRE, which is different from the shape seen for the BDDOTEs.

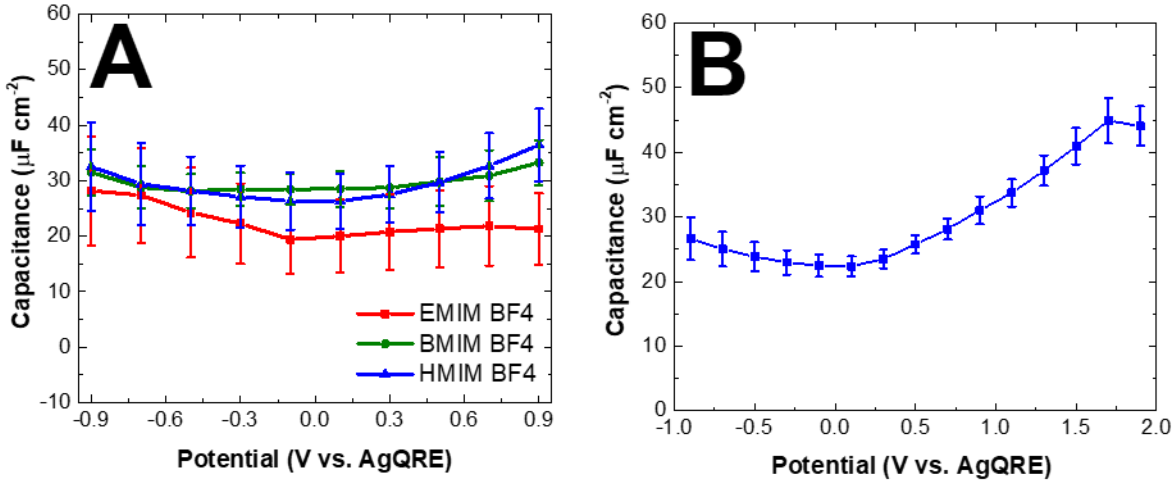

Figure 2.10. (A) Potential-dependent capacitance (C_{eff}) data for GC in [EMIM][BF_4] (red squares), [BMIM] [BF_4] (green squares), and [HMIM] [BF_4] (blue squares). (B) Potential-dependent capacitance data for GC in [HMIM] [BF_4] (blue squares) over a wider potential range from -1 to 2 V. The capacitance values were calculated from fitting the EIS data according to the equivalent circuit presented in Fig. 2.2. Data are presented as mean ± std. dev. for n = 3 GC electrodes in each electrolyte.

The shape is inconsistent with the bell-shaped curves observed for metal electrodes in RTILs.[17,31,54,55,66-72] The capacitance minimum is reflective of the potential of zero charge. Similar capacitance-potential data has been reported for GC in RTILs.[31,54,55,65]

Figure 2.10B shows C_{dl}-E data for GC in [HMIM] [BF_4] over a wider potential range from -1 to 2 V. The capacitance values range from 22 to 45 μF cm^{-2}. There is a distinct minimum seen near 0 V with the capacitance increasing with potential on either flank of the minimum. These capacitance values are lower than the values observed for GC in concentrated aqueous electrolyte solution (see Fig. 2.13 below). The U-shaped C_{dl}-E profile and the minimum near 0 V are more apparent over this larger potential range.

Capacitance-potential data for metal electrodes in RTILs generally exhibit a bell-shaped, rather than U-shaped profile. In contrast, more U-shaped profiles are typically seen for various carbon electrodes. [17,31,54,55,66-70] Therefore, as a control experiment, data were acquired for a polished polycrystalline Au disk electrode in BMIM BF_4. Figure 2.11 shows the C_{dl}-E data with values ranging from 8 - 14 μF cm^{-2} over the potential range and, importantly, a bell-shaped curve is seen, as expected.[17,31,54,55,66-73] A well-defined capacitance maximum is observed at 1.1 V (13.8 μF cm^{-2}).

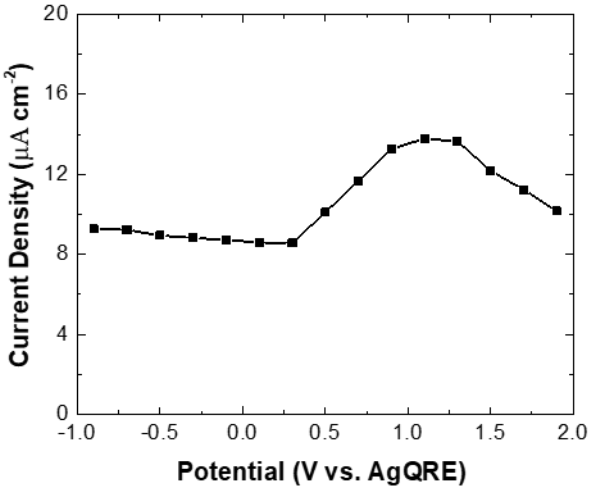

Figure 2.11. C_{dl}-E data for an Au disk electrode in [BMIM] [BF_4]. Capacitance values were calculated from fitting the EIS experimental data to the equivalent circuit shown in Figure 2.2. Data are presented for one Au electrode.

The capacitance values are slightly larger than those observed for BDDOTEs, but less than the values for GC. It is expected that the GC electrode used in this work had some surface roughness meaning the true area is larger than the geometric area. As such, the true C_{dl} values for GC are likely lower than those reported. These data indicate that our measurement protocol produces data expected for a metal electrode in RTILs in agreement with the predictions from mean field theory put forward by Kornyshev and coworkers.[17,71,72,73]

2.4.4. Capacitanc-Potential (C_{dl}–E) Trends in Aqueous Electrolyte

Comparison voltammetric and capacitance measurements were made in 1 mol L^{-1} KCl using both electrodes. Figure 2.12A and B show cyclic voltammetric *i-E* curves for BDDOTE and GC, respectively, recorded over a 1.0 V potential range as a function of scan rate from 0.025 to 0.25 V s^{-1}. The current increases with the scan rate, and the curves are generally symmetric about the zero-current line, as was the case in the RTILs. The main difference is that the currents in KCl are 5-10x larger than those in the RTILs for both electrodes. Also, the voltammetric background current is larger for GC, as compared to BDDOTE over the entire potential range by a factor of 3-5x.

Figures 2.12 C and E (BDDOTE) and D and F (GC) show plots of the background at 0.2 and 0.4 V vs. scan rate for two electrodes. The background current in KCl for both electrodes increases linearly with the scan rate indicating the current is capacitive in nature. The slope of the plots was used to calculate the capacitance. Mean values of capacitance for BDDOTE and GC are presented in Table 2.5. The capacitance values for both electrodes are larger in KCl than in the RTILs. The larger double-layer capacitance is consistent with previous reports for BDD in aqueous media.[57,58,74-77] The capacitance value of 78.5 μF cm^{-2} for GC is larger than what is typically observed for a clean and smooth GC electrode.[50,51] This is attributed to the pseudo-capacitance

arising from redox-active and ionizable carbon-oxygen functional groups on the GC surface. Additionally, the GC disk electrode likely possessed some roughness or porosity even after polishing such that the geometric area was less than the true area. The larger capacitance in 1 mol L^{-1} KCl is likely due to a combination of two factors: the smaller-sized ions such that the volumetric charge density accumulated in the interfacial region is greater and the larger dielectric constant of water. Additionally, ion-pairing would be expected to decrease the capacitance values in RTILs, as compared to aqueous electrolyte solutions, because of the increased size and smaller volumetric density.

Figure 2.13 shows the corresponding C_{dl}–E profiles for (A) BDDOTE and (B) GC in 1 M KCl constructed from the EIS data. The capacitance for a BDDOTE increases with increasing positive potential, ranging from 9 μF cm^{-2} at −0.9 V to 16 μF cm^{-2} at 0.9 V. The capacitance for GC ranges from 46 to 62 μF cm^{-2} over the same 1.8 V potential range. The capacitance values are larger for GC, as compared to the BDDOTE as was the case in the RTILs.

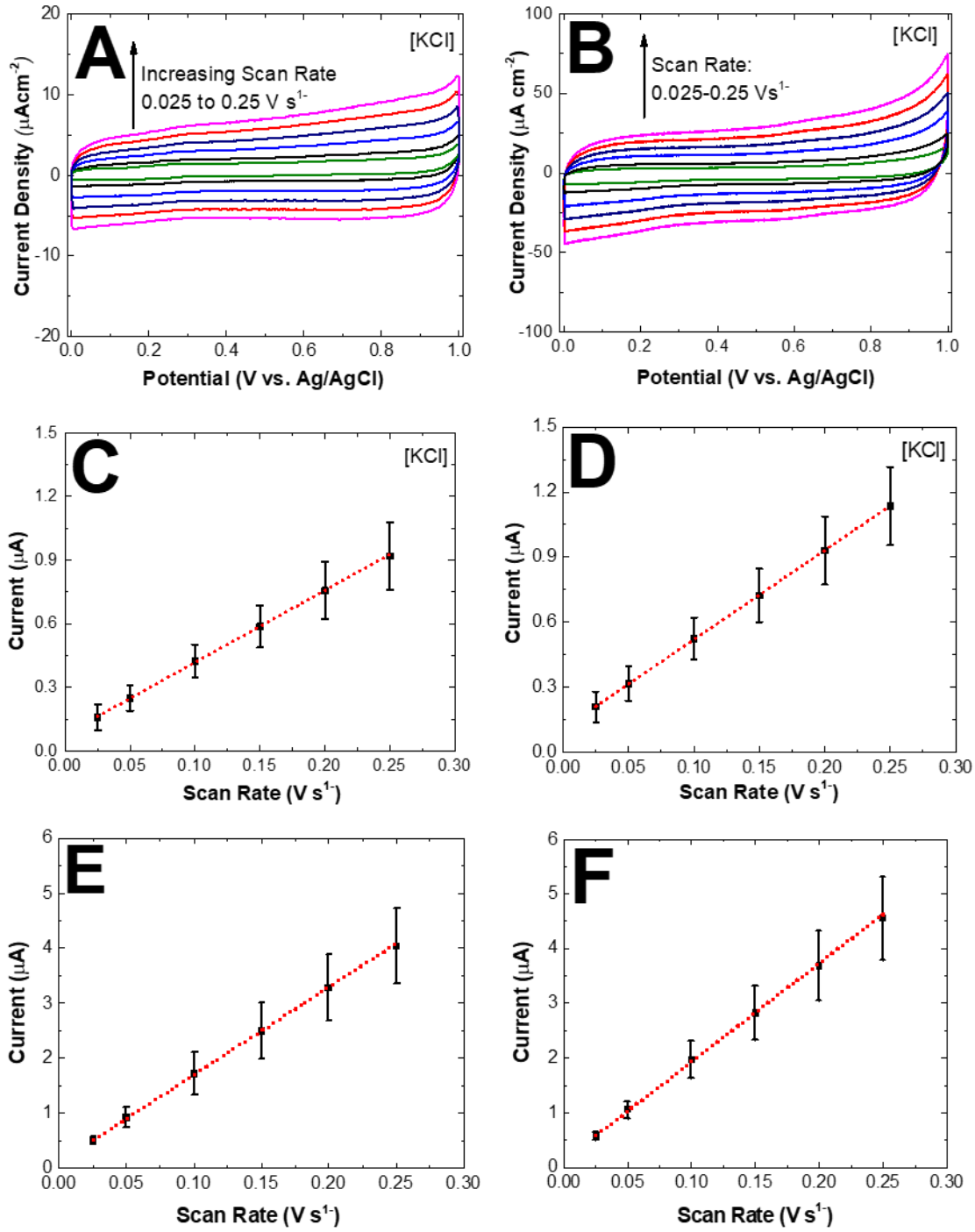

Figure 2.12. Cyclic voltammetric *i–E* curves recorded for (A) BDDOTE and (B) GC as a function of scan rate in 1 mol L^{-1} KCl from 0.025 to 0.25 V s^{-1}. The background current at 0.2 and 0.4 V is plotted versus scan rate for (C, E) BDDOTE and (D,F) GC electrodes.

Table 2.5. Capacitance values for BDDOTE and GC in 1 mol L^{-1} KCl as determined from cyclic voltammetric data as a function of the scan rate.

Type of Electrode	Capacitance (μF cm^{-2})	
	E= 0.2 (V)	E= 0.4 (V)
BDDOTE	16.9 ± 2.7	20.5 ± 2.9
GC	78.5 ± 13.6	88.0 ± 15.5

Values are presented as mean ± std. dev. for n=3 BDDOTEs and n=3 GC electrodes.

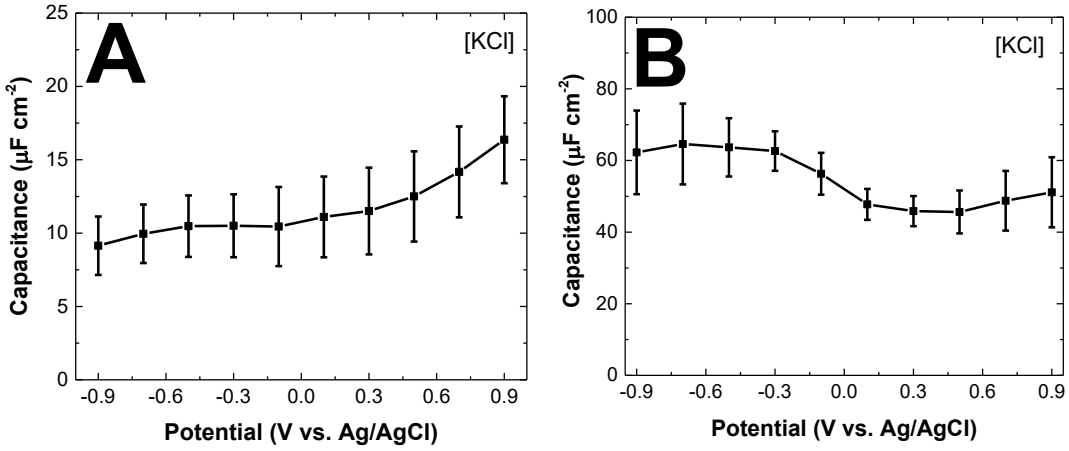

Figure 2.13. Capacitance-potential ($C-E$) profiles for a (A) BDDOTE and (B) GC in 1 mol L^{-1} KCl. The capacitance (C_{eff}) values were calculated from EIS data and are presented as mean ± std. dev. for n = 3 BDDOTEs and n=3 GC electrodes.

2.5. Discussion

The research provides new insights into the electrochemical behavior of boron-doped optically transparent electrodes in room temperature ionic liquids. Specifically work for the first time shows how the voltammetric background current, working potential window, potential dependent capacitance, and the electron transfer kinetics for ferrocene and two ferrocene derivatives depend on the RTIL type at the structurally and electronically heterogeneous BDDOTEs. More specifically, the results convey information on behavior difference of these

electrodes in RTILs and aqueous electrolyte solutions. Three imidazolium based RTILs with two different anions (BF_4 and TFSI) were studied with the main differences being the viscosity and cation type/size: EMIM, BMIM, and HMIM (n=2,4, and 6).

The working potential window was similar for the BDDOTEs in all three imidazolium tetrafluoroborate RTILs at *ca.* 4.5 V. This indicates that the breakdown voltage does not depend significantly on the molecular structure of these three RTILs. The voltammetric background current for the BDDOTEs also showed little dependence on the RTIL cation type. The background current at a given potential scaled linearly with the scan rate at least up to 0.250 V s^{-1} in all three RTILs, even the most viscous [HMIM][BF_4]. This is significant because it means that the interfacial ion excesses can be achieved in the viscous RTILs as quickly as the excess surface charge is being changed on the electrode with scan rate. This is unlikely to be the case at higher scan rates because some point would be reached when the background current would cease increasing linearly with the scan rate resulting from the limited mobility of the ions because of viscosity. Slow charging of the solution side of the electrified interface would constitute a limitation on the voltammetric scan rates or measurement time scale that could be achieved to investigate redox reaction kinetics.

The capacitance-potential data for the BDDOTEs, as determined by cyclic voltammetry and EIS, were similar in magnitude and profile. Over a wide potential range from -1 to 1 V vs. AgQRE, the capacitance values ranged from 3-12 μF cm^{-2} in the six different BF_4 and TFSI RTILs. The mean values at each potential showed a slight decrease with cation size: [EMIM] > [BMIM] > [HMIM].[36] However, given the magnitude of the relative standard deviation values, which were unexpectedly high, ranged from 10-30 %, there was no significant difference in the capacitance at any of the potentials with RTIL type. Capacitance values for the BDDOTEs in 1 M KCl were 3-

4x higher than in the RTILs. The general trend in both the RTILs and the aqueous electrolyte solution was a flat capacitance-potential profile or a slightly upward shifting profile with increasing positive potential characteristic of a *p-type* semiconductor.

The difference in capacitance values is due to differences in the organization and volumetric charge density on the solution side of the interface. The lower C_{dl} values in the RTILs is attributed to the absence of a dielectric solvent, the larger size of the free ions and ion pairs, and a lower volumetric charge density (ions cm^{-3}). By comparison, capacitance data for GC were 4-8x larger in [BMIM][BF_4] than the values for the BDDOTEs at a given potential, such as 0.2 V. Furthermore, the capacitance values for GC are larger in the aqueous electrolyte solution than in the RTILs for the reasons stated above. The differences in capacitance magnitude for the BDDOTEs and GC in a given medium is attributed to a lower density of electronic states for the former.[31,32,35,36,52,53,77]

The shape of the capacitance-potential profiles in the RTILs for both the BDDOTE and GC electrodes differs considerably from what is observed for an Au disk electrode, or metal electrodes in general.[17,31,66-73] Interestingly, the capacitance values for Au from -1.0 to 2.5 V vs. AgQRE are slightly larger than the values for the BDDOTEs, but smaller than the values for GC. In contrast with the BDDOTEs, a capacitance maximum is seen for Au in [BMIM][BF_4] at *ca.* 1.1 V vs. AgQRE with decreasing capacitance on the flanks of the peak. This capacitance-potential shape is predicted from mean field theory, which suggests a bell- or camel-shaped curvature.[17,31,32,71,72,73] The capacitance maximum represents the potential of zero charge. According to the theory, the bell-shaped curve is proposed to arise from the very concentrated ionic liquids such that a limited number of ions and or ion clusters can accumulate in the interface due to size or steric limitations. At the potential of zero charge, the thickness of the excess charge

layer in the RTIL is relatively thin. The thickness of the counterbalancing charge layer increases with increasing potential away from the maximum resulting in a decreased capacitance. Carbon electrodes behave differently from metals in terms of their capacitance-potential behavior. Parabolic U-shaped curvature is typically seen for sp^2-bonded carbon electrodes.[17,31,32,35,36,54,55,66-72,76] The reason the divergent capacitance-potential data in the same chemical environments must be due to differences in the electronic properties or magnitude of the excess charge density at a given potential on the carbon electrodes. The C_{dl}-E profiles for the BBDOTEs are flat or have a slightly upward shift with increasing potential because (i) the excess surface charge density at the potentials probed does not change much and or (ii) the applied potential is distributed across both the electrode-solution interface and internally within the space charge layer.

One of the most important findings from this work, and consistent with reason (ii) above, is that the BDDOTEs exhibit both semiconducting and semimetallic electronic properties in the RTILs. The evidence for semiconducting behavior comes from the linear Mott-Schottky plots of $\frac{1}{C_{dl}^2}$ vs. E seen in all three RTILs. The linearity of the plots was very wide, *ca.* 2 V, with potential axis intercepts in the 2-3 V vs. AgQRE range. The plots are consistent with *p-type* conduction (acceptor mediated) as expected for the boron doping. Linear Mott-Schottky plots have been reported by others for BDD electrodes in contact with RTILs.[31,32] The number of charge carriers, as determined from the slope of the linear regions of the curves, is on the order of 2×10^{21} cm^{-3}, which is consistent with the carrier concentration as determined from Hall Effect measurements.[8] These data suggest that in these RTILs, the applied potential is dropped across both the solution (Helmholtz layer) and within the near surface of the electrode in the space charge layer. As a result, the measured interfacial double layer capacitance, C_{dl}, arises from the semiconductor capacitance, C_{SC}, and the capacitance of the Helmholtz layer, C_H, in the RTIL. These are in series with one

another and add in the reciprocal with the smaller of the two dominating. The surprising observation is that this semiconducting behavior is seen for such high boron-doping or charge carrier levels.

The semimetallic behavior is evidenced by the quasi-reversible electron transfer kinetics seen for ferrocene, ferrocene carboxaldehyde and ferrocene methanol. All redox systems undergo relatively rapid electron transfer kinetics at the BDDOTEs even though all have formal potentials that are well negative of the apparent E_{fb} with the electrode under depletion conditions. The data indicate that for these concentrations, 0.1 mM, there are sufficient electronic states, holes, and electrons, at these formal potentials to support the electron transfer reactions. Therefore, these BDDOTEs exhibit both semiconducting and semimetallic electronic behavior in RTILs; an observation made by others as well.[31,32] We suppose that the reason for this dual behavior is that the BDD electrodes are not uniform electronically across a film. It is well known that polycrystalline diamond films are not uniformly doped, and boron incorporation can vary with the growth sectors.[60,61] SECM and CP-AFM measurements have revealed regions on diamond film electrodes with high electrical conductivity and high electrochemical activity surrounded by regions of lower electrical conductivity and electrochemical activity.[62-64] In the RTILs, the interfacial capacitance appears dominated by the more semiconducting regions of the electrode while the redox chemistry is occurring primarily on the more semimetallic regions of the film.

2.6. Conclusions

The electrochemical working potential window, voltammetric background current, and potential-dependent capacitance of boron-doped diamond optically transparent electrodes (BDDOTEs) were evaluated in different room temperature ionic liquids (RTILs) using cyclic voltammetry and electrochemical impedance spectroscopy. The electrode properties were studied

in three homologous RTILs ([EMIM] [BF_4], [BMIM] [BF_4], and [HMIM] [BF_4]) and in 1 M KCl, for comparison. In parallel, studies were performed with glassy carbon (GC) to enable the comparison of the properties of the BDDOTEs. One of the most important findings from this work is that the BDDOTEs exhibit both semiconducting and semimetallic electronic properties in the RTILs. The evidence for semiconducting behavior comes from the linear Mott-Schottky plots of $1/(C_{dl}^2)$ vs. E seen in all three RTILs. The linearity of the plots was very wide, *ca.* 2 V, with potential axis intercepts in the 2-3 V vs. AgQRE range. The plots are consistent with *p*-type conduction (acceptor mediated) as expected for the boron doping. The semimetallic behavior is evidenced by the quasi-reversible electron transfer kinetics seen for ferrocene, ferrocene carboxaldehyde and ferrocene methanol. All redox systems undergo relatively rapid electron transfer kinetics at the BDDOTEs even though all have formal potentials that are well negative of the apparent E_{fb} with the electrode under depletion conditions. We suppose that the reason for this dual behavior is that the electronic properties of the BDDOTEs are not uniform spatially across a film.

The key findings from the work can be summarized as follows:

1. The working potential window for the BDDOTEs is *ca.* 4.5 V and independent of the tetrafluoroborate RTIL type.

2. Voltammetric background currents increase linearly with the scan rate up to 0.250 V s^{-1} in all the viscous RTILs, consistent with the currents being capacitive in nature. Capacitance values are flat with potential or exhibit a slightly upward shift with increasing potential. From -1 to 1 V vs. AgQRE, capacitance values range from 3 to 8 μF cm^{-2} and are independent of the RTIL composition. In 1 M KCl, the capacitance values are 3-4x larger ranging from 9 to 20 μF cm^{-2}.

3. Voltammetric background currents in the RTILs also increase linearly with the scan rate for GC up to 0.250 V s^{-1}. Capacitance values exhibit a U-shaped profile with potential with values ranging from 20 to 40 μF cm^{-2} from -1 to 1 V vs. AgQRE. The values are 3-7x larger for GC than for BDDOTE in the same RTILs. Capacitance values for GC obtained from cyclic voltammetric data are larger than values from electrochemical impedance spectroscopy. A capacitance minimum is observed at -0.1 V vs. AgQRE. In 1 M KCl, the capacitance values range from 40-65 μF cm^{-2}.

4. The difference in capacitance values for GC and BDDOTE in a given medium is attributed to a higher density of electronic states in the former. The larger capacitance values for both carbon electrodes in KCl, as compared to the RTILs, is attributed to a combination of the (i) smaller size of the aqueous ions, (ii) the larger dielectric constant of water, and (iii) ion paring that exists in the RTIL that serves to increases the size of the counterbalancing "ions" and to decrease the volumetric charge density.

5. Even with the semiconducting behavior of the BDDOTEs, as exemplified by the Mott-Schottky analysis, the electrodes exhibit semimetallic behavior based on the quasi-reversible electron transfer kinetics for ferrocene and two ferrocene derivatives with the electrode under depletion conditions.

REFERENCES

[1] J. Stotter, J. Zak, Z. Behler, Y. Show, G. M. Swain, 'Optical and electrochemical properties of optically transparent, boron-doped diamond thin films deposited on quartz', *Anal. Chem.* **2002**, *74*, 5924-5930.

[2] J. Stotter, S. Haymond, J. Zak, Y. Show, Z. Cvackova, G. Swain, 'Optically transparent diamond electrodes for UV-Vis and IR spectroelectrochemistry', *Electrochem. Soc. Interface* **2003**, *12*, 33-38.

[3] J. Stotter, Y. Show, S. Wang, G. Swain, 'Comparison of the electrical, optical, and electrochemical properties of diamond and indium tin oxide thin-film electrodes', *Chem. Mater.* **2005**, *17*, 4880-4888.

[4] S. Haymond, J. K. Zak, Y. Show, J. E. Butler, G. T. Babcock, G. M. Swain, 'Spectroelectrochemical responsiveness of a freestanding, boron-doped diamond, optically transparent electrode toward ferrocene', *Anal. Chim. Acta* **2003**, *500*, 137-144.

[5] Y. Dai, G. M Swain, M. D. Porter, Jerzy Zak, 'New horizons in spectroelectrochemical measurements: optically transparent carbon electrodes', *Anal. Chem.* **2008**, *80*, 14-22.

[6] Y. Dai, D. A. Proshlyakov, J. K. Zak, G. M. Swain, Optically transparent diamond electrode for IR transmission spectroelectrochemical measurements, *Anal. Chem.* **2007**, *79*, 7526-7533.

[7] H. B. Martin, P. W. Morrison, Application of a diamond thin film as a transparent electrode for in situ infrared spectroelectrochemistry, *Electrochem Solid-State Lett.* **2001**, *4*, E17.

[8] N. Wächter, C. Munson, R. Jarošová, I. Berkun, T. Hogan, R. C. Rocha-Filho, G. M. Swain, 'Structure, electronic properties, and electrochemical behavior of a boron-Doped diamond/quartz optically transparent electrode', *ACS Appl Mater Interfaces* **2016**, *8*, 28325-28337.

[9] Sobaszek M, Skowroński Ł, Bogdanowicz R, Siuzdak K, Cirocka A, Zięba P, Gnyba M, Naparty M, Gołuński Ł and Płotka P, Optical and electrical properties of ultrathin transparent nanocrystalline boron-doped diamond electrodes, *Opt. Mater.* **2015**, *42*, 24-34.

[10] M Ficek, M Sobaszek, M Gnyba, J Ryl, M Smietana, Optical and electrical properties of boron doped diamond thin conductive films deposited on fused silica glass substrates, *Appl. Surf. Sci.* **2016**, *387*, 846-856.

[11] M. C. Buzzeo, R. G. Evans, R. G. Compton, 'Non-haloaluminate room-temperature ionic liquids in electrochemistry-a review', *ChemPhysChem* **2004**, *5*, 1106-1120.

[12] C. Zhao, G. Burrell, A. A. J. Torriero, F. Separovic, N. F. Dunlop, D. R. MacFarlane, A. M. Bond, 'Electrochemistry of room temperature protic ionic liquids', *J. Phys. Chem. B* **2008**, *112*, 6923-6936.

[13] D. S. Silvester, R. G. Compton, 'Electrochemistry in room temperature ionic liquids: A review and some possible applications', *Z. fur Phys. Chem.* **2006**, *220*, 1247-1274.

[14] M. Galiński, A. Lewandowski, I. Stępniak, 'Ionic liquids as electrolytes', *Electrochim. Acta* **2006**, *51*, 5567-5580.

[15] P. Hapiot, C. Logrost, Electrochemical reactivity in room temperature ionic liquids, *Chem. Rev.* **2008**, *108*, 2238-2264.

[16] T. L. Greaves, C. J. Drummond, 'Protic ionic liquids: properties and applications', *Chem. Rev.* **2008**, *108*, 206-237.

[17] M. V. Fedorov, A. A. Kornyshev, 'Ionic liquids at electrified interfaces', *Chem. Rev.* **2014**, *114*, 2978-3036.

[18] J. G. Huddleston, A. E. Visser, W. M. Reichert, H. D. Willauer, G. A. Broker, R. D. Rogers, 'Characterization and comparison of hydrophilic and hydrophobic room temperature ionic liquids incorporating the imidazolium cation', *Green Chem.* **2001**, *3*, 156-164.

[19] H. Weingärtner, P. Sasisanker, C. Daguenet, P. J. Dyson, I. Krossing, J. M. Slattery, T. Schubert, 'The dielectric response of room-temperature ionic liquids: effect of cation variation', *J. Phys. Chem. B* **2007**, *111*, 4775-4780.

[20] H. Tokuda, S. Tsuzuki, M. A. Susan, K. Hayamizu, M. Watanabe, 'How ionic are room-temperature ionic liquids? An indicator of the physicochemical properties', *J. Phys. Chem. B* **2006**, *110*, 19593-19600.

[21] M. Lozynski, J. Pernak, Z. Gdaniec, B. Gorska, F. Béguin, 'Proof of ion-pair structures in ammonium-based protic ionic liquids using combined NMR and DFT/PCM-based chemical shift calculations', *Phys. Chem. Chem. Phys.* **2017**, *19*, 25033-25043.

[22] R. Matsumoto, M. W. Thompson, P. T. Cummings, Ion pairing controls physical properties of ionic liquid-solvent mixtures, *J. Phys. Chem. B* **2019**, *123*, 9944–9955.

[23] K. Ma, J. Forsman, C. E. Woodward, Influence of ion pairing in ionic liquids on electrical double layer structures and surface force using classical density functional approach, *J. Chem. Phys.* **2015**, *142*, 174704.

[24] M. Hupert, A. Muck, J. Wang, J. Stotter, Z. Cvackova, S. Haymond, Y. Show, G. M. Swain, 'Conductive diamond thin-films in electrochemistry', *Diam. Relat. Mater.* **2003**, *12*, 1940-1949.

[25] R. G. Compton, J. S. Foord, F. Marken, 'Electroanalysis at diamond-like and doped-diamond electrodes', *Electroanalysis* **2003**, *15*, 1349-1363.

[26] J. A. Bennett, J. Wang, Y. Show, G. M. Swain, 'Effect of sp^2-bonded nondiamond carbon impurity on the response of boron-doped polycrystalline diamond thin-film electrodes', *J. Electrochem. Soc.* **2004**, *151*, E306.

[27] K. Pecková, J. Musilová, J. Barek, 'Boron-doped diamond film electrodes-new tool for voltammetric determination of organic substances', *Crit. Rev. Anal* **2009**, *39*, 148-172.

[28] Y. Einaga, J. S. Foord, G. M. Swain, 'Diamond electrodes: diversity and maturity', *MRS Bull.* **2014**, *39*, 525-532.

[29] N. Yang, G. M. Swain, X. Jiang, 'Nanocarbon electrochemistry and electroanalysis: current status and future perspectives', *Electroanal.* **2016**, *28*, 27-34.

[30] S. Ernst, L. Aldous, R. G. Compton, 'The electrochemical reduction of oxygen at boron-doped diamond and glassy carbon electrodes: A comparative study in a room-temperature ionic liquid', *J. Electroanal. Chem.* **2011**, *663*, 108-112.

[31] C. Cannes, H. Cachet, C. Debiemme-Chouvy, C. Deslouis, J. de Sanoit, C. Le Naour, V. A. Zinovyeva, 'Double layer at [BuMeIm][Tf_2N] ionic liquid–Pt or −C material interfaces', *J. Phys. Chem. C* **2013**, *117*, 22915-22925.

[32] A. J. Lucio, S. K. Shaw, J. Zhang, A. M. Bond, 'Double-layer capacitance at ionic liquid–boron-doped diamond electrode interfaces studied by fourier transformed alternating current voltammetry', *J. Phys. Chem. C* **2018**, *122*, 11777-11788.

[33] J. Li, C. L. Bentley, S.-y. Tan, V. S. S. Mosali, M. A. Rahman, S. J. Cobb, S.-X. Guo, J. V. Macpherson, P. R. Unwin, A. M. Bond, J. Zhang, 'Impact of sp^2 carbon edge effects on the electron-transfer kinetics of the ferrocene/ferricenium process at a Boron-doped diamond electrode in an ionic liquid', *J. Phys. Chem. C* **2019**, *123*, 17397-17406.

[34] D. Y. Kim, J. C. Yang, H. W. Kim, G. M. Swain, 'Heterogeneous electron-transfer rate constants for ferrocene and ferrocene carboxylic acid at boron-doped diamond electrodes in a room temperature ionic liquid', *Electrochim. Acta* **2013**, *94*, 49-56.

[35] R. Jarošová, K. Bhardwaj, G. M. Swain, 'Temperature dependence of the heterogeneous electron-transfer rate constant for ferrocene carboxylic acid in room temperature ionic liquids at microstructurally distinct carbon electrodes', *J. Electroanal. Chem.* **2020**, *875*, 114744.

[36] K. Bhardwaj, F. Parvis, Y. Wang, G. J. Blanchard, G. M. Swain, 'Effect of surface oxygen on the wettability and electrochemical properties of boron-doped nanocrystalline diamond electrodes in room-temperature ionic liquids', *Langmuir* **2020**, *36*, 5717-5729.

[37] E. L. Bennett, C. Song, Y. Huang, J. Xiao, , Measured relative complex permittivities for multiple series of ionic liquids, *J. Mol. Liq.* **2019**, *294*, 111571.

[38] S. Ren, Y. Hou, W. Wu, W. Liu, 'Purification of ionic liquids: sweeping solvents by nitrogen', *J. Chem. Eng. Data.* **2010**, 55, 5074-5077.

[39] R. Jarosova, G. M. Swain, 'Rapid preparation of room temperature ionic liquids with low water content as characterized with a t*a*-C:N electrode', *J. Electrochem. Soc.* **2015**, *162*, H507-H511.

[40] T. Jänsch, J. Wallauer, B. Roling, 'Influence of electrode roughness on double layer formation in ionic liquids', *J. Phys. Chem. C* **2015**, *119*, 4620-4626.

[41] B. Hirschorn, M. E. Orazem, B. Tribollet, V. Vivier, I. Frateur, M. Musiani, 'Determination of effective capacitance and film thickness from constant-phase-element parameters', *Electrochim. Acta* **2010**, *55*, 6218-6227.

[42] E. Bourgeois, E. Bustarret, P. Achatz, F. Omnès, X. Blase, 'Impurity dimers in superconducting B-doped diamond: Experiment and first-principles calculations', *Phys. Rev. B.* **2006**, *74*, 094509.

[43] M. Bernard, C. Baron, A. Deneuville, 'About the origin of the low wave number structures of the Raman spectra of heavily boron doped diamond films', *Diam. Relat. Mater.* **2004**, *13*, 896-899.

[44] V. A. Sidorov, E. A. Ekimov, 'Superconductivity in diamond', *Diam. Relat. Mater.* **2010**, *19*, 351-357.

[45] P. W. May, W. J. Ludlow, M. Hannaway, P. J. Heard, J. A. Smith, K. N. Rosser, 'Raman and conductivity studies of boron-doped microcrystalline diamond, facetted nanocrystalline diamond and cauliflower diamond films', *Diam. Relat. Mater.* **2008**, *17*, 105-117.

[46] A. C. Ferrari, J. Robertson, 'Origin of the 1150-cm^{-1} Raman mode in nanocrystalline diamond', *Phys. Rev. B.* **2001**, *63*, 121405.

[47] P. Szirmai, T. Pichler, O. A. Williams, S. Mandal, C. Bäuerle, F. Simon, 'A detailed analysis of the Raman spectra in superconducting boron doped nanocrystalline diamond', *Phys. Status Solidi B* **2012**, *249*, 2656-2659.

[48] D. S. Knight, W. B. White, Characterization of diamond films by Raman spectroscopy, *J. Mater. Res.* **1989**, *4*, 385-393.

[49] C. Zhao, A. M. Bond, X. Lu, Determination of water in room temperature ionic liquids by cathodic stripping voltammetry at a gold electrode, *Anal. Chem.* **2012**, *84*, 2784−2791.

[50] J. Xu, Q. Chen, G. M. Swain, 'Anthraquinonedisulfonate electrochemistry: A comparison of glassy carbon, hydrogenated glassy carbon, highly oriented pyrolytic graphite, and diamond electrodes', *Anal. Chem.* **1998**, *70*, 3146-3154.

[51] Q. Chen, G. M. Swain, 'Structural characterization, electrochemical reactivity, and response stability of hydrogenated glassy carbon electrodes', *Langmuir* **1998**, *14*, 7017-7026.

[52] K. K. Cline, M. T. McDermott, R. L. McCreery, Anomalously slow electron transfer at ordered graphite electrodes: influence of electronic factors and reactive sites, *J. Phys. Chem.* **1994**, *98*, 5314–5319.

[53] R. L. McCreery, Advanced carbon electrode materials for molecular electrochemistry, *Chem. Rev.* **2008**, *108*, 2646-2687.

[54] V. Lockett, R. Sedev, J. Ralston, M. Horne, T. Rodopoulos, 'Differential capacitance of the electrical double layer in imidazolium-based ionic liquids: Influence of potential, cation size, and temperature', *J. Phys. Chem. C* **2008**, *112*, 7486-7495.

[55] V. Lockett, M. Horne, R. Sedev, T. Rodopoulos, J. Ralston, 'Differential capacitance of the double layer at the electrode/ionic liquids interface', *Phys. Chem. Chem. Phys.* **2010**, *12*, 12499-12512.

[56] B-A. Mei, O. Munteshari, J. Lau, B. Dunn, L. Pilon, Physical interpretations of Nyquist plots for EDLC electrodes and devices, *J. Phys. Chem. C* **2018**, *122*, 194-206.

[57] G. M. Swain, The use of CVD diamond thin films in electrochemical systems, *Adv. Mater.* **1994**, *6*, 388-392.

[58] S. Alehashem, F. Chambers, J. W. Strojek, G. M. Swain, R. Ramesham, Cyclic voltammetric studies of charge transfer reactions at highly boron-doped polycrystalline diamond electrodes, *Anal. Chem.* **1995**, *67*, 2812-2821.

[59] A. Hankin, F. E. Bedoya-Lora, J. C. Alexander, A. Regoutz, G. H. Kelsall, Flat band potential determination: avoiding the pitfalls, *J. Mater. Chem. A* **2019**, *7*, 26162-26176.

[60] K. Ushizawa, K. Watanabe, T. Ando, I. Sakaguchi, M. Nishitani-Gamo, Y. Sato, H. Kanda, Boron concentration dependence of Raman spectra on {100} and {111} facets of B-doped CVD diamond, *Diam. Relat. Mater.* **1998**, *7*, 1719-1722.

[61] T. Kolber, K. Piplits, R. Haubner, H. Hutter, Quantitative investigation of boron incorporation in polycrystalline CVD diamond films by SIMS, *Fresenius J. Anal. Chem.* **1999**, *365*, 636–641.

[62] K. B. Holt, A. J. Bard, Y, Show, G. M. Swain, Scanning electrochemical microscopy and conductive probe atomic force microscopy studies of hydrogen-terminated boron-doped

diamond electrodes with different doping levels, *J. Phys. Chem. B* **2004**, *108*, 15117-15127.

[63] S. Wang, G. M. Swain, Spatially heterogeneous electrical and electrochemical properties of hydrogen-terminated boron-doped nanocrystalline diamond thin film deposited from an argon-rich $CH_4/H_2/Ar/B_2H_6$ source gas mixture, *J. Phys. Chem. C* **2007**, *111*, 10, 3986–3995.

[64] N. R. Wilson, S. L. Clewes, M. E. Newton, P. R. Unwin, J. V. Macpherson, Impact of grain-dependent boron uptake on the electrochemical and electrical properties of polycrystalline boron doped diamond electrodes, *J. Phys. Chem. B* **2006**, *110*, 5639–5646.

[65] M. M. Islam, M. T. Alam, T. Okajima, T. Ohsaka, 'Electrical double layer structure in ionic liquids: an understanding of the unusual capacitance-potential curve at a nonmetallic electrode', *J. Phys. Chem. C* **2009**, *113*, 3386-3389.

[66] M. T. Alam, M. M. Islam, T. Okajima, T. Ohsaka, 'Capacitance measurements in a series of room-temperature ionic liquids at glassy carbon and gold electrode interfaces', *J. Phys. Chem. C* **2008**, *112*, 16600-16608.

[67] Y. Lauw, M. D. Horne, T. Rodopoulos, A. Nelson, F. A. M. Leermakers, 'Electrical Double-Layer Capacitance in Room Temperature Ionic Liquids: Ion-Size and Specific Adsorption Effects', *J. Phys. Chem B* **2010**, *114*, 11149-11154.

[68] C. Gomes, R. Costa, C. M. Pereira, A. F. Silva, 'The electrical double layer at the ionic liquid/Au and Pt electrode interface', *RSC Adv.* **2014**, *4*, 28914-28921.

[69] M. T. Alam, J. Masud, M. M. Islam, T. Okajima, T. Ohsaka, 'Differential capacitance at Au(111) in 1-alkyl-3-methylimidazolium tetrafluoroborate based room-temperature ionic liquids', *J. Phys. Chem. C* **2011**, *115*, 19797-19804.

[70] L. J. Small, D. R. Wheeler, 'Influence of analysis method on the experimentally observed capacitance at the gold-ionic liquid interface', *J. Electrochem. Soc.* **2014**, *161*, H260-H263.

[71] M. V. Fedorov, N. Georgi, A. A. Kornyshev, 'Double layer in ionic liquids: The nature of the camel shape of capacitance', *Electrochem. commun.* **2010**, *12*, 296-299.

[72] A. A. Kornyshev, N. B. Luque, W. Schmickler, 'Differential capacitance of ionic liquid interface with graphite: the story of two double layers', *J. Solid State Electrochem.* **2014**, *18*, 1345-1349.

[73] A. A. Kornyshev, 'Double-layer in ionic liquids: paradigm change?', *J. Phys. Chem. B* **2007**, *111*, 5545-5557.

[74] Y. Show, M. A. Witek, P. Sonthalia, G. M. Swain, 'Characterization and electrochemical responsiveness of boron-doped nanocrystalline diamond thin-film electrodes', *Chem. Mater.* **2003**, *15*, 879-888.

[75] A. E. Fischer, Y. Show, G. M. Swain, 'Electrochemical performance of diamond thin-film electrodes from different commercial sources', *Anal. Chem.* **2004**, *76*, 2553-2560.

[76] S. Wang, V. M. Swope, J. E. Butler, T. Feygelson, G. M. Swain, 'The structural and electrochemical properties of boron-doped nanocrystalline diamond thin-film electrodes grown from Ar-rich and H_2-rich source gases', *Diam. Relat. Mater.* **2009**, *18*, 669-677.

[77] R. Jarošová, P. M. De Sousa Bezerra, C. Munson, G. M. Swain, 'Assessment of heterogeneous electron-transfer rate constants for soluble redox analytes at tetrahedral amorphous carbon, boron-doped diamond, and glassy carbon electrodes', *Phys. Status Solidi A* **2016**, *213*, 2087-2098.

CHAPTER 3. ELECTROCHEMICAL ACTIVITY OF FERROCENE DERIVATIVES IN [EMIM][BF_4], [BMIM][BF_4], AND [HMIM][BF_4] AT BORON-DOPED DIAMOND OPTICALLY TRANSPARENT ELECTRODES

3.1. Abstract

The working potential window, voltammetric background current, and potential-dependent double-layer capacitance of optically transparent boron-doped diamond electrodes (OTEs) were investigated in [EMIM][BF_4], [BMIM][BF_4], and [HMIM][BF_4] room temperature ionic liquids (RTILs). The diamond OTEs were prepared by depositing a thin film of boron-doped nanocrystalline diamond on a quartz substrate. Cyclic voltammetry was used to study the redox behavior of ferrocene and two ferrocene derivatives in the same RTILs. The apparent heterogeneous electron-transfer rate constant (k^o_{app}) for ferrocene, ferrocene methanol, and ferrocene carboxylic acid in different RTILs was estimated from cyclic voltammetry ΔE_p-scan rate trends and digital simulation. Comparison measurements were made in aqueous electrolyte solution. The goal was to determine if k^o_{app} for the ferrocene derivatives depends on the reorientation dynamics of the RTILs and the hydrodynamic radius of the redox probe molecules. It was found that the electron- transfer rate constant for the redox systems does not depend on the hydrodynamic radius of the molecules but does depend on the reorientation dynamics which is controlled by the viscosity (η) in three RTILs. Double-layer capacitance values were below 10 μF cm^{-2} in all three RTILs at potentials from -1 to 1 V vs. Ag QRE. The results indicate that OTEs exhibit good electrochemical activity for all the redox systems in both aqueous and RTIL media, but the mass transfer and electron-transfer kinetics are slower in the more viscous RTIL media. The diffusion coefficients and apparent heterogeneous electron-transfer rate constants (k^o_{app}) for ferrocene and ferrocene derivatives were on the order of 10^{-7} to 10^{-9} cm^2 s^{-1} and 10^{-4} to 10^{-5} cm s^{-1}, respectively, and scaled inversely with the viscosity of the RTIL. The results indicate that at least for these three RTILs, the ferrocene derivatives undergo adiabatic outer sphere electron

transfer at the BDDOTEs and that solvent relaxation dynamics control the electron transfer rate. The k^o_{app} values are largely independent of the RTIL molecular structure, but rather are controlled by the macroscopic viscosity.

3.2. Introduction

Marcus theory is the basis through which electron transfer chemistry and reactivity are understood.[1-4] It enables the electron transfer rate constant, k^o, to be calculated through the semiclassical expression [1]. Marcus theory of electron transfer [1] explains the standard heterogeneous electron-transfer rate constant (k^o_{app}) for a soluble redox system according to the following equation:[2, 5-11]

$$k^o = K_p \kappa_{el} v_n e^{\left(\frac{-\Delta G^{\ddagger}}{RT}\right)} \quad [1]$$

In this equation, K_p is the equilibrium constant for reaction precursor formation, $\Delta G^{\ddagger}$ is the free energy of activation, v_n (s^{-1}) is the nuclear frequency factor or the frequency of crossing the activation barrier, and κ_{el} is the electron transmission coefficient or the probability of electron tunneling in the transition state.[6, 7, 12, 13] R and T are the ideal gas constant and temperature, respectively. RTILs are known to form organized layers on a charged surface. RTILs are also expected to form specific organized structures around a redox analyte. Therefore, the physical and chemical properties are expected to exert a significant effect on the dynamic solvation and solvent reorganization around as well as the distance of closest approach of a redox analyte.[14]

For outer sphere electron transfer, Marcus theory predicts that v_n is proportional to the inverse of the longitudinal relaxation time of the solvent (i.e., RTIL), τ_L as shown in equation [2],

$$v_n = \tau_L^{-1}\left(\frac{-\Delta G^{\ddagger}}{4\pi RT}\right)^{\frac{1}{2}} \quad [2]$$

where τ_L is defined as

$$\tau_L = \tau_D \frac{\epsilon_\infty}{\epsilon_s} \qquad [3]$$

in which τ_D, ϵ_∞, ϵ_∞ are the experimental Debye relaxation time, the high frequency and static dielectric permittivities, respectively.[15] τ_L is proportional to the viscosity of the solvent or RTIL. For outer sphere electron transfer where $\Delta G^\ddagger$ is dominated by the outer shell ($\Delta G_{os}^\ddagger$) activation energy, this energy is related to changes in the solvent organization during electron transfer.[16] If it is assumed that parameters ($\kappa_{el}, K_P, \Delta G^\ddagger$) in equation [1] are constant or their changes are small to compensate each other in a series of homologous solvents. Therefore,

$$k^o = \tau_L^{-1} A \qquad [4]$$

There are several studies reporting a linear relationship between k^o and τ_L^{-1} for molecules that follow an outer-sphere pathway.[12, 13, 17-19] In the Marcus theory, the main factor affecting the reorganization energy ($\Delta G^\ddagger$) is the outer sphere free energy of activation ($\Delta G_{os}^\ddagger$):

$$\Delta G_{os}^\ddagger = \frac{N_A e^2}{32\pi\varepsilon_0}\left(\frac{1}{r} - \frac{1}{2d}\right)\left(\frac{1}{\varepsilon_{op}} - \frac{1}{\varepsilon_s}\right) \quad [5]$$

In equation [5], *e*, *d*, ε_{op}, ε_s, and *r* are the electronic charge, the distance from the reactant to the electrode, the optical permittivity, the static permittivity, and the hydrodynamic radius of the molecule. The molecule's hydrodynamic radius can be deduced using different methods such as crystallographic measurements or by calculations using ellipsoidal or mean spherical approximations.[13, 20, 21] Here, we used a method developed by Clegg and coworker[13] in which "*r*" is assumed to be the hydrodynamic radius and can be calculated using the Stokes-Einstein equation [6],

$$D = \frac{k_B T}{P\pi r\eta} \quad [6]$$

in which k_B represents the Boltzmann constant, T is temperature, and η is the viscosity. P is either 4 or 6 depending on whether the "stick" limit or the "slip" limit is assumed for the equation [6].[22] The main advantage of this method is that the hydrodynamic radius is directly related to the experimentally obtained diffusion coefficient.

A plot of ln k^o vs. ln τ_L is expected to have a linear trend if the redox reaction is proceeding adiabatically (without heat loss or gain) and dominated by $\Delta G_{os}^{\ddagger}$. A slope of -1.0 is expected. A slope near -1 indicates that the redox reaction mechanism is adiabatic and that the solvent relaxation dynamics control the electron transfer rate. The linear relationship also implies that ion-pairing and double layer effects on k^o are invariant with the RTIL molecular structure.[16]

Several studies provide experimental evidence to confirm the Marcus relationship for redox systems in organic and aqueous electrolyte solutions. For example, Clegg et al. used a high-speed channel electrode to estimate the heterogeneous electron transfer rate constants under the steady-state condition for the electrooxidation of a range of anthracene derivatives in alkyl cyanide solvents. Their experimental results revealed the dependence of rate constant (k^o) on the longitudinal dielectric relaxation time constant (τ_L).[12] Another study from Compton's group used hydrodynamic and stationary electrodes to measure the rate constant (k^o) for 1,4-phenylenediamines dihydrochloride in a series of alkyl cyanide solvents (acetonitrile (MeCN), propionitrile (EtCN), butyronitrile (PrCN), and valeronitrile (BuCN)) under steady-state conditions. They examined the dependence of k^o on the solvent longitudinal dielectric relaxation (τ_L) for N,N,N',N'-tetramethyl-1,4-phenylenediamine (TMPD). A minor departure from the theoretical τ_L^{-1} relationship was seen because of the solvation of the amino groups by RCN molecules causing additional solvent inertial effects. The dependence of k^o on the hydrodynamic radius (r) has been investigated over the range of $3 \leq r \leq 9$Å. The experimental data were in

excellent agreement with the theoretically calculated rate constant.[23] It validates the dependence of k^o on the hydrodynamic radius for the system under study.

Room temperature ionic liquids (RTILs) have received the attention of the scientific community in multiple research fields including electrochemistry, fuel cells, batteries, capacitors, metal surface finishing, organic and inorganic synthesis, catalysis, polymerization, and nuclear waste treatment.[24-32] RTILs are solventless salts consisting of a large asymmetric organic cation and a smaller inorganic anion. They are liquids at or below room temperature.[25, 28, 33] Columbic interactions are the principal force between the ions that affect the ion mobility and electrical conductivity. RTILs possess several properties that make them an ideal electrolyte for electrochemical applications, such as good solvating power, wide working potential window, non-flammability, chemical and thermal stability, and low vapor pressure.[24, 34-37]

One of the challenges working with RTILs is measuring the water impurity level. Adventitious water impurity has a significant effect on electrochemical reactions in RTILs. Water decreases the working potential window of the RTIL. The impurity also increases the voltammetric background current, rate of heterogeneous electron-transfer, and the diffusion coefficient of a redox analyte.[28, 33, 38-41] A rapid and effective method for reducing water impurity in RTILs is essential. In the present work, RTILs were purified using a so-called "sweeping method" developed by our group[38]. This method involves three steps: 1) storage of the as-received RTIL over activated carbon for at least 7 days, 2) storage of the purified RTIL over activated molecular sieves, and 3) heating the purified RTIL at ~70 ^{o}C while purging with argon gas for 50 min at the time of use. Activated carbon serves to remove organic impurities while the molecular sieves and argon gas purge remove water impurity.[38]

The chemical environment of an RTIL differs greatly from traditional aqueous and organic electrolyte solutions. Unlike aqueous or organic electrolyte solutions, there is no dielectric solvent to shield and separate the positive and negative ions in the RTIL. Therefore, a large fraction of the ions exist as ion pairs or clusters rather than individual solvated spherical charges. As a result, the concentration of free ions is smaller than the total concentration.[42-44] Additionally, the interfacial double-layer structure is different in RTILs from aqueous or organic electrolyte solutions. The "Gouy-Chapman-Stern" model satisfactorily describes the interfacial excesses at an electrode surface in aqueous organic electrolyte solutions, but it is questionable whether this model accurately describes the structure of the electrode-electrolyte interface in RTILs. It is believed that there are several layers of oscillatory charges at a charged electrode-RTIL interface.[28, 45] RTILs are viscous liquids; a property that suppresses the rates of diffusional mass transport and electron transfer.[5, 38, 46-49]

Carbon electrodes are widely used in electrochemical studies because of their low cost, rich surface chemistry, compatibility with a variety of reaction conditions, wide usable potential range, and chemical inertness.[50-55] There are different types of carbon electrodes, including sp^2-bond carbon materials (graphite, glassy carbon, carbon nanotubes and graphene), sp^3-bonded materials (boron-doped diamond), and the hybrid of sp^2 and sp^3-bonded carbons (diamond-like carbon specifically nitrogen-incorporated tetrahedral amorphous carbon). The electrochemical properties of carbon electrodes are governed by the microstructure exposed, surface chemistry, and the pretreatment method used to activate the electrode for electron transfer.[50,56-60] To maximize the application of carbon electrodes in electrochemical applications, it is critical to understand the variables that affect the voltammetric background current, double-layer capacitance, working potential window, and heterogeneous electron- transfer rate constant (k^o_{app}).

Over the last two decades, our group put a great effort into studying the electrochemical behavior of different types of boron-doped diamond electrodes with various crystalline structures, including microcrystalline, nanocrystalline, and ultra-nanocrystalline.[61-64] Boron-doped diamond (BDD) electrodes possess several advantages for electrochemical measurements. They exhibit low background current, wide working potential and optical window, relatively rapid electron transfer kinetics, resistivity to molecular adsorption, high stability in extreme reaction conditions, no need for conventional pretreatment, and rich surface chemistry.[65-72] BDDs are available in various architectures, including BDD films, optically transparent electrodes, powders, etc.[73-77] They can be prepared using chemical vapor deposition (CVD) methods in which a source gas mixture of CH_4/H_2 and B_2H_6 is used.[65, 78] Diborane, B_2H_6, serves as the source for boron dopant atoms to substitutionally insert into the growing diamond lattice and provide charge carriers to the material. Typical doping levels are in the low 10^{21} cm^{-3} range and electrical conductivities are < 0.01 ohm-cm. It is understood now that several factors influence the electrochemical behavior of boron-doped diamond electrodes including the surface chemistry,[78] boron doping level, adventitious sp^2-carbon impurity, and sub-surface H-content.[76, 79-86] BDD films deposited on quartz, known as boron-doped diamond optically transparent electrodes (BDDOTEs), can be used in spectroelectrochemical studies in the UV/Visible region of electromagnetic radiation.[65-68, 70, 87] A key issue with preparing BDDOTEs is the balancing needed between the doping level and the optical transparency. The boron-doping level should provide sufficient conductivity for the electrode to support rapid rates of electron transfer, but not make the film opaque and poorly transmissive to electromagnetic radiation. The BDD film should be thick enough to provide a continuous film across the quartz, but not too thick to reduce the optical transparency.[65, 67]

Herein, we report how the molecular composition and viscosity of the RTIL affects the working potential window, the double-layer capacitance, redox analyte diffusion coefficient, and heterogeneous electron-transfer rate constant for three ferrocene derivatives at boron-doped diamond optically transparent electrodes (BDDOTEs). We investigated the validity of Marcus theory to describe the heterogeneous electron transfer-rate constant for the three derivatives. The RTILs were used: 1-ethyl-3-methylimidazolium tetrafluoroborate [EMIM][BF_4], 1-butyl-3-methylimidazolium tetrafluoroborate [BMIM][BF_4], and 1-hexyl-3-methylimidazolium tetrafluoroborate [HMIM][BF_4]. The RTILs have the same anion but different alkyl imidazolium cations. The cations differ in the number of carbon atoms in the alkyl side chain. The viscosity of RTILs is mainly influenced by the molecular structure of the cation.[72] The viscosity of the RTILs increases with the length of the alkyl side chain because of the strengthened van der Waals interactions between neighboring cations.[88] The three redox systems were: ferrocene (Fc), ferrocene methanol (FcMeOH), and ferrocene carboxylic acid (FCA).[46]

Cyclic voltammetry was used to study the working potential window, the double-layer capacitance, and electron transfer kinetics. Electrochemical impedance spectroscopy was applied to measure the double-layer capacitance of the electrodes in three different RTILs. The apparent heterogeneous electron- transfer rate constant (k^o_{app}) was calculated using the Nicholson method from cyclic voltammetric ΔE_p-scan rate trends[89]. Digital simulation was also employed (Digisim® 3.30 software) to determine k^o_{app}. Chronoamperometry and cyclic voltammetry were used to calculate the diffusion coefficients for the redox systems in the different RTILs. The hydrodynamic radius of ferrocene derivatives were calculated using the experimentally obtained diffusion coefficients through the Stokes-Einstein equation. Finally, we investigated the dependence of k^o_{app} on the ferrocene derivatives hydrodynamic radius (r) and the reorientation dynamics.

3.3. Experimental

Boron-Doped Diamond Optically Transparent Electrodes (BDDOTE). The diamond OTEs were deposited on 0.2 cm-thick quartz substrates that were 2.54 × 2.54 cm^2 in area. The quartz was pretreated for diamond growth by (i) ultrasonically cleaning in acetone for 30 min, (ii) scratching the clean substrate using 100 nm diamond powder suspended in water on a felt pad, and (iii) ultrasonically seeding the scratched substrate in "Opal Seed" (Adamas Technologies, NC) for 30 min, and (iv) rinsing with ultrapure water. The Opal Seed consists of nominally 30 nm diamond particles suspended in dimethyl sulfoxide.

The diamond deposition was accomplished by microwave-assisted chemical vapor deposition (Seki Diamond Systems, 1.5 kW) using 600 W, 25 torr, and a hydrogen-rich source gas mixture at a total gas flow of 200 sccm. A 1% (V/V) methane-to-hydrogen source gas mixture was used with 10 ppm of diborane added for boron doping. The actual ultrahigh purity gas flows were 2.00 sccm methane, 196 sccm hydrogen, and 2.00 sccm diborane (0.1% (V/V)) mixed with hydrogen. The deposition time was typically 5-6 h. This produced a film thickness of 0.5-1 μm. At the end of the deposition period, the methane and diborane flows were stopped while the coated substrate remained exposed to hydrogen plasma. The power and pressure were gradually reduced over a 30-min period to 250 W and 10 torr min to cool the coated substrate in the presence of atomic hydrogen.

Statistical Data Analysis. Electrochemical experiments were performed using three different electrodes. The results are reported as mean ± standard deviation. The Student's t-test and one-way analysis of variance (ANOVA) [90] were used to verify statistically significant differences among the mean values. *P*-values ≤ 0.05 were considered statistically significant.

Electrochemical Measurements in Aqueous Electrolyte Solutions and Room Temperature Ionic Liquids.

Room Temperature Ionic Liquids (RTILs). All electrochemical measurements in RTILs were performed in a nitrogen-purged vinyl glove box (Coy Laboratory Products, MI). The relative humidity in the box was measured to be ≤ 0.1% using a digital hygrometer. The working electrode (BDDOTE) was clamped to the bottom of a single compartment glass electrochemical cell. A Viton^{TM} O-ring with an area of 0.2 cm^2 was placed between the bottom of the glass cell and the working electrode to define the geometric electrode area exposed to the solution. Electrical contact with the OTE surface was made by pressing a piece of aluminum foil along one edge of the electrode, wrapping the foil to the backside of the quartz substrate, and then contacting it with a copper plate current collector.[65] The BDDOTEs were pretreated before each use by exposure to ultraclean isopropanol (distilled and stored over activated carbon) for 20-30 min.

In the case of the Pt macro-disk electrode, the electrode was first polished with an alumina powder (0.3 μm)/ultrapure water slurry on a felt pad. The polished electrode was then ultrasonically cleaned for 30 s in 1.0 mol L^{-1} HCl and rinsed thoroughly with ultrapure water. The electrode was subjected to potential cycling in 0.5 mol L^{-1} H_2SO_4 solution (scan rate: 0.5 V s^{-1}) from -0.2 V to 1.2 V.[91] A graphite rod was used as the counter electrode. A homemade Ag/AgCl electrode served as the reference. The Pt macro-disk electrode's electrochemical active surface area (EAS) was calculated from the H-adsorption charge in the cyclic voltammetric potential range from -0.2 V to 0.1 V. A value of 210 C cm^{-2} was used as the charge density for a monolayer of adsorbed hydrogen on Pt.[91]

For all electrochemical measurements in RTILs, a Pt wire was used as the counter electrode and an Ag wire was used as the quasi-reference electrode (Ag QRE). Approximately 1 mL of

purified RTIL was used in an electrochemical measurement. The purified (as described before) was deaerated with Ar gas purging for 10 min in the electrochemical cell before a series of measurements were made. Ar gas blanketed the RTIL during an electrochemical measurement. All measurements in RTILs were prepared in an N_2-filled vinyl glove box (Coy laboratories, MI).

Aqueous Electrolyte Solutions. A graphite rod was used as the counter electrode. A homemade Ag/AgCl electrode (1M KCl) served as the reference. Aqueous electrolyte solutions were deaerated with N_2 gas purging for 10-20 min before each measurement. The same single compartment, glass electrochemical cell was used for these measurements as used with the RTILs. The only difference was that the measurements in aqueous solution were made outside the glove box on the laboratory bench.

Cyclic Voltammetry. Cyclic voltammetry (CV) was performed using a computer-controlled potentiostat (Model 650B or 650A, CH Instruments Inc., TX). Voltammograms were recorded as a function of the scan rate (0.025 to 0.25 V s^{-1}). The current data were plotted as a function of applied potential. The double-layer capacitance, C_{dl} (μF cm^{-2}), was calculated from the slope of background current density (j, A cm^{-2}) *vs.* scan rate (v, V s^{-1}) plots for different applied potentials using the following equation,[92]

$$j = C_{dl} v \qquad [7]$$

The apparent heterogeneous electron-transfer rate constant (k^o_{app}) was calculated from cyclic voltammetric ΔE_p-v data using the Nicholson method.[89] The following equation relates k^o to the Nicholson parameter (dimensionless), ψ,

$$k^o = \psi \frac{[\pi D_{ox} v (nF/RT)]^{1/2}}{(D_{ox}/D_{red})^{\alpha/2}} \qquad [8]$$

in which D_{ox}, D_{red}, v, n, R, T, F, α are diffusion coefficients of the oxidized and reduced species (cm^2 s^{-1}), scan rate (V s^{-1}), number of electrons transferred per molecule, ideal gas constant, temperature (K), Faraday's constant, and the transfer coefficient, respectively. ψ is the transfer parameter calculated by equation [9][93]. X represents the cyclic voltametric peak potential separation (ΔE_p) that is used to calculate the Nicholson parameter.

$$\psi = \frac{(-0.6288+0.0021\,X)}{(1-0.017\,X)} \quad [9]$$

Digisim® (version3.03) software was used to calculate the simulated rate constant (k^o_{sim}). This was accomplished by fitting the experimental voltammetric curves to simulated ones, adjustments in k^o and α were preformed to match the peak currents and peak potential separation. The software required inputs of k^o, α, D_{red}, and D_{ox} values. The goodness of the fits was judged based on matching the peak currents and ΔE_p values.

Electrochemical Impedance Spectroscopy (EIS). Electrochemical impedance spectroscopy (EIS) was performed using a computer-controlled potentiostat (Model 650B or 650 A, CH Instruments Inc., TX). EIS was carried out at different applied dc potentials from -1.0 to 1.0 V vs. Ag QRE using a range of ac frequencies from 10^5 to 10^{-1} Hz. Twelve data points were collected per decade. A sine wave (10 mV amplitude) was co-added to each DC potential. An equilibration time of 300 s was allotted before collecting the impedance data at each potential. The data were analyzed in the Nyquist plane using the equivalent circuit shown in Figure 3.1. The full frequency EIS data were fit using ZView® 3.5h software.

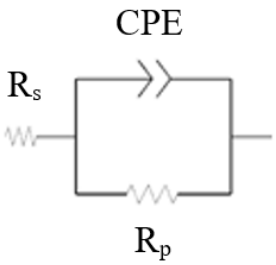

Figure 3.1. The representative equivalent circuit used to fit the full frequency electrochemical impedance spectroscopic (EIS) data in the RTILs.

R_s represents the combined bulk electrolyte resistance and electrode ohmic resistance. A constant phase element (CPE) was used in place of a pure capacitor to represent the double-layer capacitance.[94] R_p is the polarization resistance, which is the resistance to current flow at the interface between the electrode and electrolyte. The capacitance for a real capacitor does not depend on the frequency. Therefore, in the Nyquist format, a plot of Z'' (imaginary component) *vs.* Z' (real component) gives a vertical line parallel to the Z'' axis. As seen in results presented below, the plots of $Z''-Z'$ at different potentials were not always a straight vertical line. This behavior was reported for boron-doped diamond electrodes previously.[72] The impedance of CPE is given by equation [10],

$$Z_{CPE} = \frac{1}{Q(j\omega)^n} \quad [10]$$

in which Q is the quasi-capacitance, n is the so-called homogeneity factor (n = 1 for an ideal capacitor), ω is the angular frequency, and j is the imaginary number. The quasi-capacitance, Q, has no physical meaning; however, equation [11], described by Hirschorn[95] et al., was used to calculate the effective capacitance, C_{eff}, at a given potential using parameter values returned from the fits of the experimental data.

$$C_{eff} = \left(\frac{R_s R_p}{R_s + R_p}\right)^{\frac{1-n}{n}} Q^{\frac{1}{n}} \quad [11]$$

The calculated C_{eff} is divided by the area of the o-ring (for BDDs and GCs: area: 0.2 cm^2) to obtain the normalized capacitance. For the Pt mini-electrode, the area was 0.03 cm^2.

Chronoamperometry. Chronoamperometric measurements were performed in the glove box using a computer-controlled potentiostat (Model 650B, CH Instruments Inc., TX). A Pt macro-disk electrode was used as the working electrode, counter and reference electrode. The purpose for these measurements was to analyze the *i-t* curves to determine the diffusion coefficient for each ferrocene derivative in the three RTILs used.

The step width and quiet time were 2 s. Before each chronoamperometric measurement, a cyclic voltammogram was recorded to determine the potential at which the current for the oxidation reaction was diffusion-limited. Counter and reference electrodes were a Pt wire and a Ag QRE, respectively. The diffusion coefficient was determined from the Cottrell equation [12][63] by assessment of the $it^{1/2}$ vs t and i vs. $t^{-1/2}$ relationships,

$$i = \frac{nFACD^{0.5}}{\pi t^{0.5}} \quad [12]$$

In the equation [12], i, n, F, A are the current (A), the number of electrons transferred per molecule, Faraday's constant (C mol^{-1}) , and electrode area (cm^2). C, D, and t are concentration (mol cm^{-3}), diffusion coefficient (cm^2 s^{-1}), and time (s), respectively.

Reagents for Electrochemical Measurements in Aqueous Electrolytes. Potassium chloride, CAS: 7447-40-7 and potassium hexacyanoferrate(II) trihydrate ($K_4Fe(CN)_6 \cdot 3H_2O$), CAS No. 14459-95-1 were obtained from Sigma-Aldrich and used without additional purification.

Reagents for Electrochemical Measurements in RTILs. The RTILs, 1-ethyl-3-methylimidazolium tetrafluoroborate ([EMIM][BF_4]), CAS: 143314-16-3, 1-butyl-3-

methylimidazolium tetrafluoroborate ([BMIM][BF_4]), CAS: 174501-65-6, and 1-hexyl-3-methylimidazolium tetrafluoroborate ([HMIM][BF_4]), CAS: 244193-50-8) were purchased commercially from Iolitec (Tuscaloosa, AL, specified as ≥ 98% purity). Ferrocenecarboxylic acid (CAS: 1271-42-7, 97%), ferrocene (CAS: 102–54-5, 98%), and ferrocenemethanol (CAS: 1273-86-5, 97%) were purchased commercially (Sigma Aldrich), and used as received.

Purification of the RTILs. The RTILs were purified to remove water and other impurities using a so-called "sweeping method" pretreatment.[38, 96]

1. The "as-received" RTIL was stored over activated carbon for at least 14 days. This step removes organic impurities. Then, the RTIL was removed through a 0.45 μm Teflon syringe filter (Millex®HA) and transferred into a clean glass vial.
2. The filtered RTIL was then stored over molecular sieves (5Å) (Fisher Scientific Company) in the glass vial for at least one week to remove water impurity. The molecular sieves were activated before use by heating at ~400 ºC in a furnace for two weeks.
3. A small volume of the purified RTIL was then transferred to a clean and dry glass vial in a nitrogen-purged vinyl glove box (Coy Laboratories, MI) and then was heated at ~70 ºC for 50 min while being purged with ultra-high purity argon gas (Airgas).

After the sweeping method, the water level in the selected purified RTILs was found to generally be below 100 ppm, as measured by thermogravimetric analysis (TGA).[38] All cleaned glassware was rinsed with ultrapure water, rinsed with ultrapure isopropanol, and dried in the oven overnight before transferring to the glove box for use in the RTIL experiments. The ultrapure water used for glassware cleaning was prepared using a Barnstead E-pure System (Thermo Scientific, USA). The ultrapure water had a resistivity ≥17 MΩ-cm.

Solutions containing a dissolved redox system in an RTIL were prepared according to the following steps:[38, 72]

1. An appropriate mass of analyte was weighed out and dissolved quantitatively in ultraclean isopropanol (distilled and stored over activated carbon) (≥ 99.5, CAS No. 67-63-0, purchased from Sigma Aldrich) to yield the desired concentration.
2. A quantitative volume of this analyte solution was then transferred to a clean 1 mL volumetric flask.
3. The flask was placed in an oven to evaporate the isopropanol completely (~1h, 100 ^{o}C).
4. The volumetric flask with the residual analytes was then transferred back to the glove box and the desired RTIL was added to the mark.
5. The solution with the reconstituted ferrocene derivative was stirred for at least 12 h to ensure full dissolution and mixing before an electrochemical measurement.

Physical Properties of the RTILs. Figure 3.2 shows the chemical structure of three RTILs used. The physical properties of the RTILs, as specified by the supplier, are given in Table 3.1.

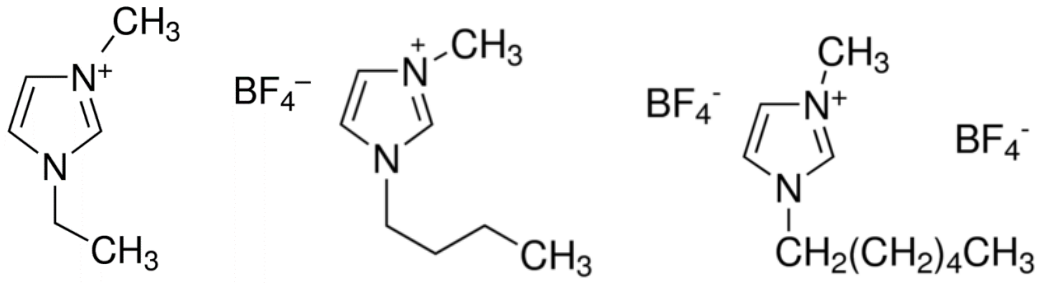

[EMIM][BF4] **[BMIM][BF4]** **[HMIM][BF4]**

Figure 3.2. Anion and cation molecular structures of three RTILs used: ([EMIM][BF_4], [BMIM][BF_4], and [HMIM][BF_4]).

Table 3.1. Physical properties of water, [EMIM][BF_4], [BMIM][BF_4], and [HMIM][BF_4] at 25 °C.

Analyte	Mol. Wt. (g mol^{-1})	Viscosity (cP)	Conductivity (mS cm^{-1})	Dielectric Constant	Density (g cm^{-3})
[EMIM][BF_4]	197.97	34*	14.1*	12.9[97]	1.28*
[BMIM][BF_4]	226.02	104*	3.2*	9.7[97]	1.30*
[HMIM][BF_4]	254.08	288*	1.2*	8.4[97]	1.15*

*Data were provided by the chemical supplier, IoLiTec Technologies.

3.4. Results

Table 3.1 compares the physical properties of three RTILs used. All have alkyl imidazolium cations with the same core structure (3-methylimidazolium), but with substituent alkyl groups containing different numbers of carbon atoms (n= 2, 4, 6). [HMIM][BF_4], [BMIM][BF_4], and [EMIM][BF_4] are about 300x, 100x, and 30x more viscous than water, respectively. The dielectric constant for [EMIM][BF_4] is slightly larger than [BMIM][BF_4] and [HMIM][BF_4], and all are at least 5x lower than water. All RTILs are slightly more dense than water. [EMIM][BF_4] is the most conducting electrolyte among three ionic liquids due to the higher mobility of the smaller [EMIM] cation.[25] The RTILs are more electrically conducting than deionized water.[72]

3.4.1. Potential Window and Capacitance Studies

The working potential window for BDDOTEs in the three RTILs was approximately 4.5 V using the limits of ± 0.01 mA. The window was the same for all three RTILs, so the molecular composition has little effect on the breakdown potentials. The wide working potential window enables the study of a larger number of redox systems than can be studied in aqueous electrolyte solution with a potential window of ~2 V. The 4.5 V potential window for the three RTILs is

smaller than the previously reported values for BDD electrodes in these and other RTILs.[33, 38, 63, 72, 98, 99]

A representative background cyclic voltammetric *i-E* curve for a BDDOTE in [HMIM][BF_4] is presented in Figure 3.3A. Voltammetric curves were recorded as a function of the scan rate (0.025-0.25 V s^{-1}) in the three RTILs over a potential range between -0.5 to 1.0 V vs. Ag QRE. There are no oxidation and reduction peaks within this potential range. As can be seen, the voltammetric background current increases with the scan rate. A plot of voltammetric background current at 0.2 V vs. scan rate is provided in Figure 3.3B. The plot is linear and the linearity indicates that the current is capacitive in nature. At all the scan rates, at least up to 0.250 V s^{-1}, the ions in the viscous RTILs can assemble their excesses in the interfacial region as fast as the excess surface charge on the electrode is being changed at each potential. It is expected that departure from linearity would occur at higher scan rates in the viscose RTILs.

According to equation [7], the slope of a plot of the voltammetric background current vs. scan rate can be used to calculate the double-layer capacitance (C_{dl}). The assumption in this measurement is that all the voltammetric current is capacitive in nature and not faradic. The calculated double-layer capacitance at 0.2 V in the three RTILs is presented in Table 3.2.

Table 3.2. The calculated double-layer capacitance for BDDOTEs in [EMIM][BF_4], [BMIM][BF_4] , and [HMIM][BF_4] at 0.2 V vs. Ag QRE.

Electrolyte	**Capacitance (μF cm^{-2})**
[EMIM][BF_4]	5.20 ± 0.97
[BMIM][BF_4]	7.17 ± 1.13
[HMIM][BF_4]	7.02 ± 1.12

Data are presented as mean ± std. dev. for n=3 BDDOTEs.

The low double-layer capacitance obtained from cyclic voltammetry for BDDOTEs is consistent with previous reports for BDD electrodes in RTILs with the same composition and similar viscosity.[63, 65, 72, 78, 99] ANOVA analysis indicated no significant differences among the mean values. In other words, the background current at each scan rate and, therefore the capacitance at each potential, is the same for these electrodes regardless of the molecular composition and viscosity of the RTIL.

Full frequency electrochemical impedance spectroscopy (EIS) was also used to measure the potential-dependence capacitance in the three RTILs. Figure 3.4 shows C_{dl}-E or C_{eff}-E curves recorded for BDDOTEs in [EMIM] [BF_4], [BMIM] [BF_4], and [HMIM] [BF_4]. Data are presented as mean ± std. dev. for n=3 different electrodes. The capacitance was recorded between -1.0 to 1.0 V vs. Ag QRE. The data were analyzed in the Nyquist plane using the equivalent circuit shown in Figure 3.1. The full frequency EIS data were fit using ZView® 3.5h software. The fitting errors (chi-squared) were in the range of 0.001-0.006, 0.0002-0.006, and 0.001-0.002 for [EMIM] [BF_4], [BMIM] [BF_4], and [HMIM] [BF_4], respectively. The equation [11], described by Hirschorn[95] et al., was used to calculate the effective capacitance, C_{eff}. The nominal capacitance values over the potential range are 5.5 - 8.2 μF cm^{-2} in [EMIM] [BF_4], 4.2 - 5.5 μF cm^{-2} in [BMIM] [BF_4], and 4.5 - 6.9 μF cm^{-2} in [HMIM] [BF_4]. These values are similar to those determined from the cyclic voltametric data. There is generally a slight upward trend in the capacitance with increasing positive potential. ANOVA analysis revealed no significant difference between the mean values in any of the RTILs at each potential. In other words, the molecular composition and viscosity of the RTILs does not have a significant effect on the capacitance values. The capacitance-potential profiles as measured by EIS are presented in Figure 3.4. As can be seen, the capacitance values are unchanging with potential or have a slightly increasing trend with increasing positive potential.

The flat or slightly U-shaped capacitance-potential curves have been reported for other carbon electrodes.[72,78] The capacitance values collected by EIS are in good agreement with literature values for BDD electrodes in RTILs with the same or similar viscosity.[72, 78] Therefore, EIS and CV are reliable techniques for measuring the capacitance of BDDOTEs in RTILs.

Capacitance data for the BDDOTEs was also measured in an aqueous electrolyte solution, for comparison. The capacitance value in 1 mol L^{-1} KCl calculated from cyclic voltametric background current data was 16.86 ± 2.73 µF cm^{-2} at 0.2 V for three BDDOTEs. The capacitance data obtained from EIS ranged from 9.14 to 16.37 µF cm^{-2} over a potential range from -1.0 to 1.0 V vs. Ag/AgCl. Clearly, the capacitance values are ~2x higher aqueous electrolyte solution than in the RTILs. The fact that the capacitance changes with the ionic composition and solvent suggests that macroscopically the capacitance is governed by the excess charge accumulation on the solution side of the interface and not by an internal space charge layer within the electrode.

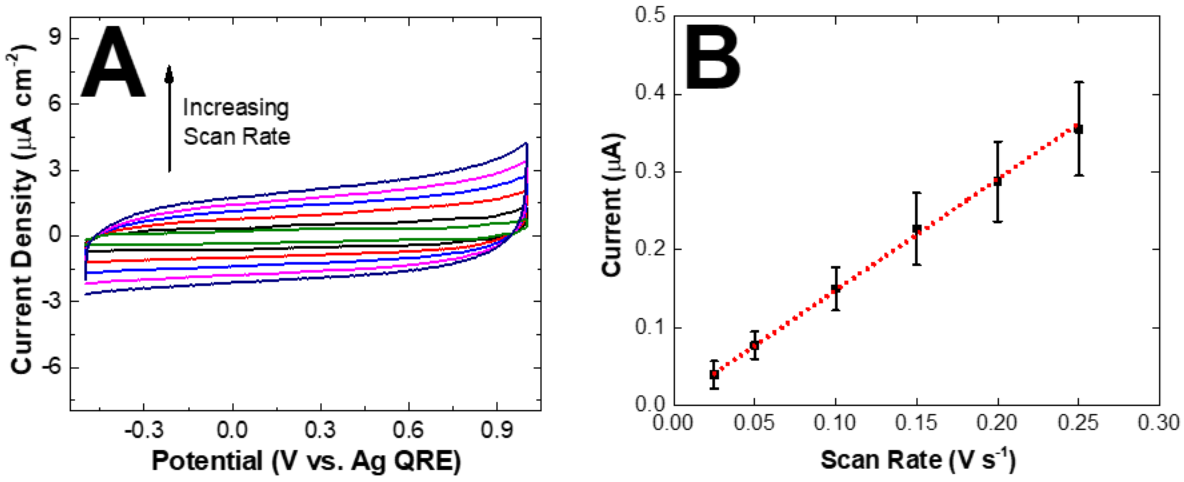

Figure 3.3. (A) Background cyclic voltammetric *i*−*E* curves as a function of increasing scan rate and (B) a plot of background current (anodic) vs. scan rate for BDDOTEs in [HMIM][BF_4]. Scan rates = 0.025-0.25 V s^{-1}. Data are reported as mean ± std. dev. for n=3 electrodes. Data are normalized to the geometric area, 0.2 cm^2.

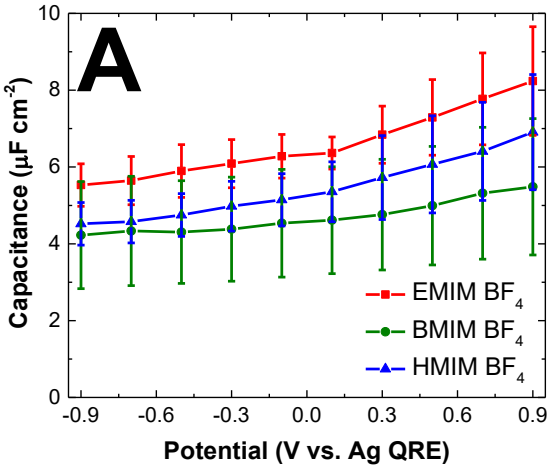

Figure 3.4. (A) Potential-dependent capacitance data for BDDOTEs in [EMIM] [BF_4] (Red), [BMIM] [BF_4] (Green), [HMIM] [BF_4] (Blue). The capacitance values were calculated from curve-fitting EIS data. Data are presented as mean ± std. dev. for n = 3 electrodes. Data are normalized to the geometric area, 0.2 cm^2.

The larger capacitance in the aqueous electrolyte solution is attributed to the larger dielectric constant of water and the larger volumetric charge density (smaller size of the solvated ions) of the counterbalancing ions on the solution side of the interface.

3.4.2. Cyclic Voltammetric Studies of Potassium Ferrocyanide in KCl as a Function of Scan Rate

Figure 3.5A provides the representative cyclic voltammetric *i-E* curves for 0.1 mmol L^{-1} potassium ferrocyanide in 1 mol L^{-1} KCl at a BDDOTE. Curves recorded at scan rates from 0.025 to 0.25 V s^{-1} are shown. Well-defined oxidation and reduction peaks are seen at 0.324 and 0.218 V vs. Ag/AgCl, respectively, at 0.025 V s^{-1}. The peak splitting (ΔE_p) and the average peak potential ($E_{p/2}$) are 0.106 V and 0.271 V vs. Ag/AgCl, respectively. The average peak potential is defined as ($E_p^{ox} + E_p^{red}$)/2. The oxidation and reduction peak currents are 3.07 × 10^{-6} and -3.27 × 10^{-6} A yielding an oxidation-to-reduction peak current ratio (i_p^{ox}/i_p^{red}) of slightly smaller than 1.The oxidation and reduction peak currents increase with the square root of the scan rate. Plots of the oxidation and reduction peak currents vs. scan rate$^{1/2}$ are shown in Figure 3.5B. There is a linear

trendline between both peak currents and scan rate$^{1/2}$ ($R^2 > 0.99$). The linearity indicates that the rate of the redox reaction is limited by the semi-infinite linear diffusion of the analyte to the electrode surface.

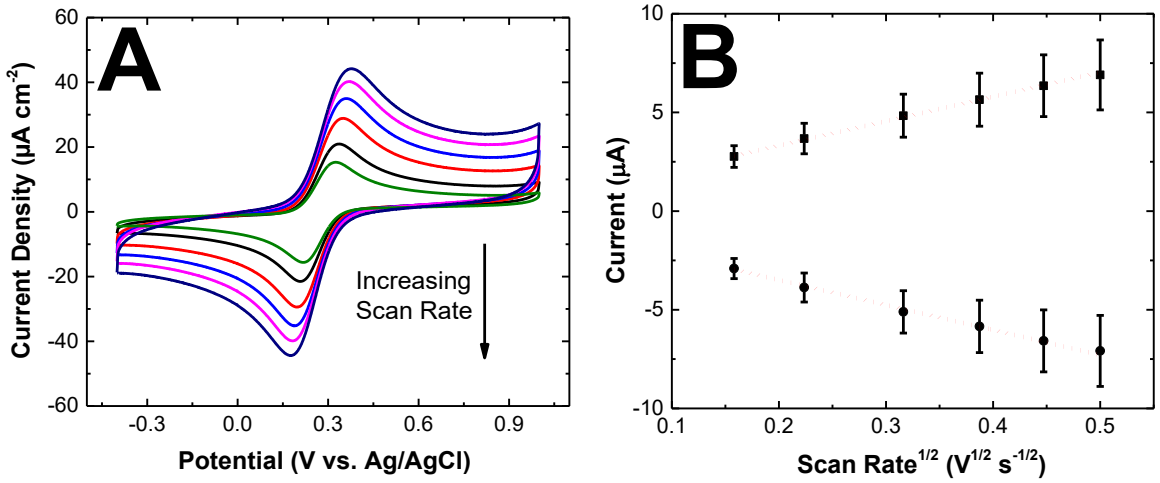

Figure 3.5. (A) Cyclic voltammetric *i-E* curves for 0.1 mmol L^{-1} potassium ferrocyanide in 1 mol L^{-1} KCl at a BDDOTE. Curves were recorded at scan rates from 0.025 to 0.25 V s^{-1}. (B) Plots of i_p^{ox} (oxidation peak current) and i_p^{red} (reduction peak current) vs. scan rate$^{1/2}$ for 0.1 mmol L^{-1} potassium ferrocyanide in 1 mol L^{-1} KCl. Values are reported as mean ± std. dev. for n=3 electrodes.

The slope of the peak current vs. scan rate$^{1/2}$ plots can be used to calculate the diffusion coefficient according the Randles–Sevcik equation,

$$i_p = 2.69 \times 10^5 \, A \, C \, n^{\frac{3}{2}} D^{\frac{1}{2}} v^{\frac{1}{2}} \quad [13]$$

in which, i_p, A, C, n, D, and v represent the peak current (A), area (cm^2), concentration (mol cm^{-3}), number of electrons transferred per molecule (n=1), diffusion coefficient (cm^2 s^{-1}), and scan rate (V s^{-1}). From the data, the diffusion coefficient (D_{red}) for potassium ferrocyanide was calculated to be 6.60 × 10^{-6} cm^2 s^{-1}. This is close to the generally accepted value of 6.3 × 10^{-6} cm^2 s^{-1}.[100]

3.4.3. Cyclic Voltammetric Studies of Potassium Ferrocyanide in KCl as a Function of Concentration

Figure 3.6A shows the cyclic voltammetric *i-E* curves for increasing concentrations from 0.1 to 1.5 mmol L^{-1} of potassium ferrocyanide in 1 mol L^{-1} KCl at a BDDOTE. The scan rate was 0.025 V s^{-1}. The oxidation and reduction peak currents increase with the concentration as expected according to the Randles–Sevcik equation shown above. The oxidation and reduction peak potentials shift positive and negative, respectively, with increasing concentration. In other words, the peak separation (ΔE_p) increases with the analyte concentration. This indicates the voltammetric data are affected by ohmic resistance effects (or *iR*-drop) within the electrode. Were there no significant *iR* distortion of the curves, ΔE_p would be unchanging with concentration.

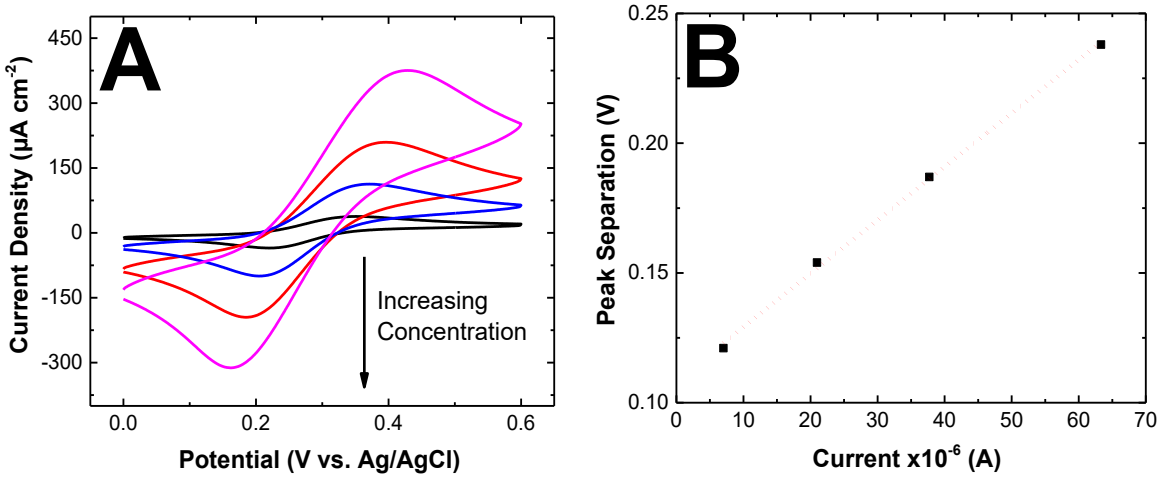

Figure 3.6. (A) Cyclic voltammetry *i-E* curves for different concentrations of potassium ferrocyanide in 1 mol L^{-1} KCl at a BDDOTE. Curves are shown for concentrations from 0.1 to 1.5 mmol L^{-1}. The curves were recorded at a scan rate of 0.025 V s^{-1}. (B) Plot of peak potential separation (ΔE_p) vs. the anodic peak current (i_p^{ox}) for different concentrations of potassium ferrocyanide in 1 mol L^{-1} KCl. The slope of this curve is *R*, the uncompensated series resistance mainly within the electrode.

In order to use cyclic voltametric ΔE_p - υ trends to extract electron-transfer kinetic information, the measured ΔE_p needs to be corrected for *iR* distortion. The plot of ΔE_p vs. i_p^{ox} for

the different concentrations of analyte shown in Figure 3.6B can be used for this correction. The plot is linear, and the slope is the uncompensated series resistance assumed to mainly be in the BDDOTE electrode. The *R* value for this BDDOTE was found to be 1737 (Ω). The original peak potential separation ($\Delta E_{p,\,org}$) can be corrected for the *iR* distortion using the following equations,

$$\mathrm{E}^{\mathrm{ox}}_{\mathrm{p,cor.}} = \mathrm{E}^{\mathrm{ox}}_{\mathrm{p,org.}} - \mathrm{iR} \quad [14]$$

$$\mathrm{E}^{\mathrm{red}}_{\mathrm{p,cor.}} = \mathrm{E}^{\mathrm{red}}_{\mathrm{p,org.}} - \mathrm{iR} \quad [15]$$

Using these equations, the oxidation and reduction potentials can be corrected for *iR* effects. $E_{p,cor.}$, $E_{p,org.}$, *i, R* represent corrected and original peak potentials (V), the peak currents (A), and electrode resistance (Ω), respectively. For example, the corrected ΔE_p values for 0.1 mmol L^{-1} potassium ferrocyanide in 1 mol L^{-1} KCl are 0.095, 0.112, 0.125, 0.143, 0.154, 0.169 V at scan rates of 0.025, 0.05, 0.10, 0.15, 0.20, and 0.25 V s^{-1}. This observation confirms that potassium ferrocyanide undergoes quasi-reversible electron-transfer kinetics at the BDDOTEs.

3.4.4. Cyclic Voltammetric Studies of Ferrocene Derivatives in RTILs as a Function of Scan Rate

Cyclic voltammetric *i-E* curves for 1 mmol L^{-1} ferrocene carboxylic acid (FCA) in [EMIM][BF_4], [BMIM][BF_4], and [HMIM][BF_4] at a BDDOTE are shown in Figure 3.7 A-C. The curves presented are the second and unchanging recorded cycle at each scan rate. The scan rates ranged from 0.025 to 0.25 V s^{-1}. Well-defined anodic and cathodic peaks are observed for FCA in all three RTILs. The oxidation peak potential (E_p^{ox}) and reduction peak potential (E_p^{red}) for FCA in [EMIM][BF_4] are 0.741 and 0.628 V vs. Ag QRE, respectively, at 0.025 V s^{-1} yielding a ΔE_p of 0.113 V. The average peak potential ($E_{p/2}$) is 0.685 V. The oxidation and reduction peak potentials were corrected for ohmic resistance yielding a ΔE_p of 0.098 V. The oxidation and reduction peak currents are 3.74×10^{-6} and -3.56×10^{-6} A, respectively, yielding a i_p^{ox}/i_p^{red} ratio of slightly larger

than 1. The corrected ΔE_p for FCA increases with the scan rate in [EMIM][BF_4] with values of 0.098, 0.107, 0.103, 0.112, 0.113, 0.118 V at scan rates of 0.025, 0.05, 0.10, 0.15, 0.20, and 0.25 V s^{-1}.This observation confirms that FCA undergoes quasi-reversible electron-transfer kinetics at the BDDOTE in [EMIM][BF_4].

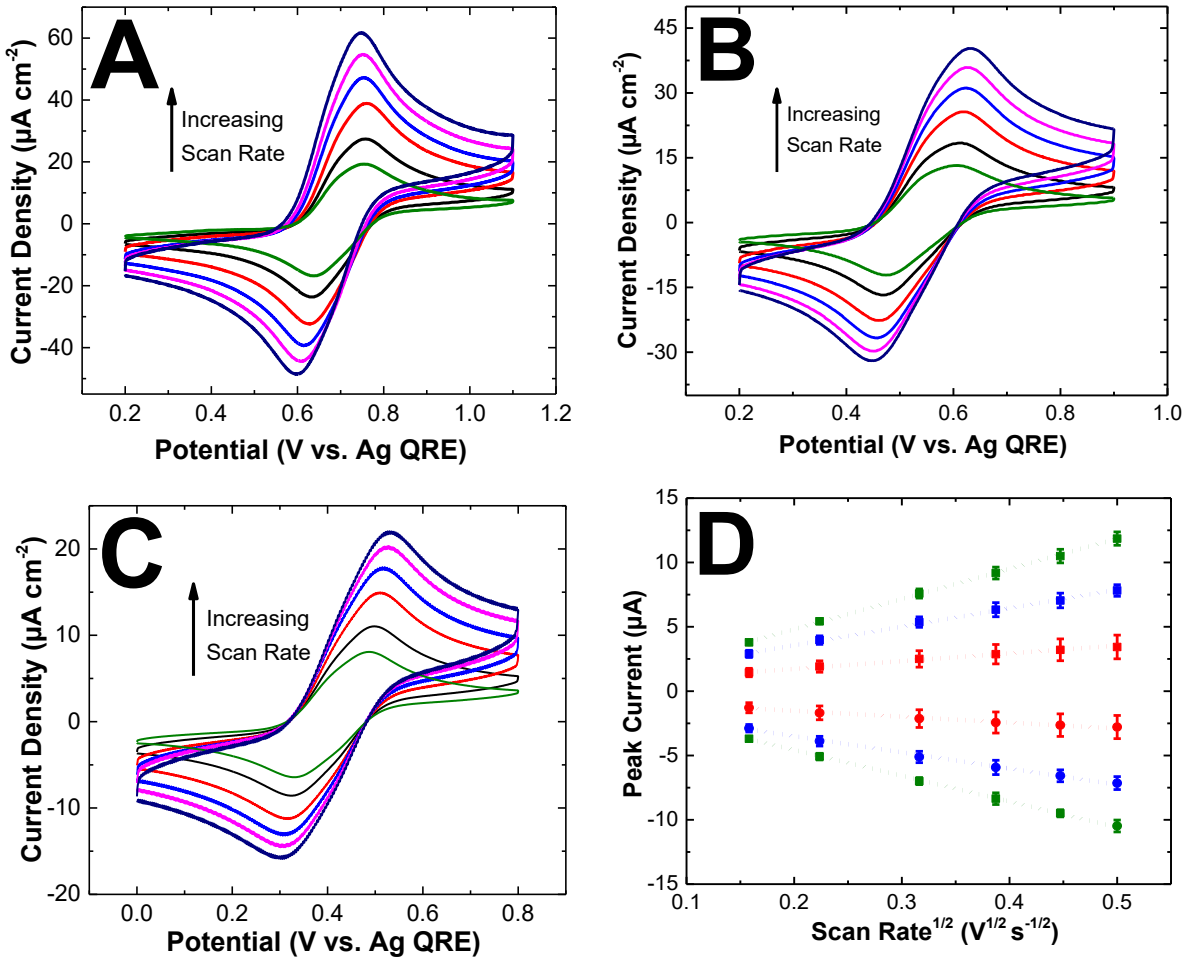

Figure 3.7. Cyclic voltammetric *i-E* curves for 1 mmol L^{-1} FCA at a BDDOTE in (A) [EMIM][BF_4], (B) [BMIM][BF_4], and (C) [HMIM][BF_4] at scan rates from 0.025-0.25 V s^{-1}. (D) Randles−Sevcik plots of i_p^{ox} and i_p^{red} vs. $v^{1/2}$ for 1 mmol L^{-1} FCA in [EMIM][BF_4] (Green), [BMIM][BF_4] (Blue), [HMIM][BF_4] (Red) at a BDDOTE. (■) Oxidation peak current (i_p^{ox}), (●) reduction peak current (i_p^{red}). Data are presented for mean ± std. dev. for n=3 electrodes.

The oxidation peak (E_p^{ox}) and reduction peak (E_p^{red}) potential values for FCA in [BMIM][BF_4] are at 0.610 and 0.477 V vs. Ag QRE, respectively, at 0.025 V s^{-1} yielding a ΔE_p of 0.133 V. The average peak potential ($E_{p/2}$) is 0.544 V. The *iR*-corrected ΔE_p is 0.125 V. The

oxidation and reduction peak currents are 2.74×10^{-6} and -2.69×10^{-6} A, respectively, yielding a i_p^{ox}/i_p^{red} ratio slightly greater than 1.

The *iR*-corrected ΔE_p for FCA increases with the scan rate in [BMIM][BF_4] with values of 0.125, 0.136, 0.150, 0.162, 0.167, and 0.176 V at scan rates of 0.025, 0.05, 0.10, 0.15, 0.20 to 0.25 V s^{-1}. This observation confirms that FCA undergoes quasi-reversible electron-transfer kinetics at the BDDOTE in [BMIM][BF_4]. Furthermore, the larger *iR*-corrected ΔE_p values in the more viscous [BMIM][BF_4] than in [EMIM][BF_4] indicate slower electron-transfer kinetics in the former.

The oxidation peak (E_p^{ox}) and reduction peak (E_p^{red}) potential values for FCA in [HMIM][BF_4] are at 0.539 and 0.380 V vs. Ag QRE, respectively, at 0.025 V s^{-1} yielding a ΔE_p of 0.159 V. The average peak potential ($E_{p/2}$) is 0.460 V vs. Ag QRE and the *iR*-corrected ΔE_p is 0.154 V. The oxidation and reduction peak currents are 1.60×10^{-6} and -1.54×10^{-6} A yielding an i_p^{ox}/i_p^{red} ratio of slightly greater than 1. The corrected ΔE_p increases with the scan rate in [HMIM][BF_4] with values of 0.154, 0.176, 0.194, 0.208, 0.217, and 0.226 V at scan rates of 0.025, 0.05, 0.10, 0.15, 0.20, and 0.25 V s^{-1}. This trend indicates that FCA undergoes quasi-reversible electron-transfer kinetics at the BDDOTE in [HMIM][BF_4]. Furthermore, the larger *iR*-corrected ΔE_p values in the more viscous [HMIM][BF_4] than in [EMIM][BF_4] or [BMIM][BF_4] indicate slower electron-transfer kinetics in the former.

Plots of oxidation and reduction peak currents vs. scan rate$^{1/2}$ for FCA in the three RTILs are provided in Figure 3.7D. These plots have linear trendline indicating the current is limited by semi-infinite linear diffusion of the analyte to the electrode surface. The diffusion coefficients for FCA, D_{red}, are calculated as $1.88 (\pm 0.17) \times 10^{-7}$, $0.70 (\pm 0.07) \times 10^{-7}$, and $0.12 (\pm 0.07) \times 10^{-7}$ cm^2 s^{-1}, respectively, in [EMIM][BF_4], [BMIM][BF_4], [HMIM][BF_4]. The diffusion coefficients

for FCA are similar to previously reported values in these and other RTILs with similar viscosity.[46, 63, 72, 101, 102] Table 3.3 provides the summary of experimental and calculated kinetic parameters for the three ferrocene derivatives (ferrocene (Fc), ferrocene methanol (FcMeOH), and ferrocene carboxylic acid (FCA)) in three RTILs.

The average peak potentials ($E_{p/2}$) for FCA are 0.685, 0.544, and 0.460 V vs. Ag QRE in [EMIM][BF_4], [BMIM][BF_4], [HMIM][BF_4], respectively. The less positive midpoint potential can be due to the lower activity of FCA^+ in RTILs with higher viscosity and the larger alkyl side chain length on the imidazolium cation. The diffusion coefficients of ferrocene derivatives (FCA, Fc, FcMeOH) were also calculated from chronoamperometric *i-t* curves using the Cottrell equation. The working electrode was a platinum disc electrode. The reference electrode was Ag QRE. In chronoamperometry, a potential step is applied to the working electrode, and a time-dependent current is measured. The diffusion coefficient can be calculated from a plot of *i* vs. $t^{-1/2}$.[63] The plot of peak currents vs. $time^{-1/2}$ for FCA in the [EMIM][BF_4] is provided in Figure 3.8D. The linearity ($R^2 > 0.99$) indicates that the rate of reaction is limited by semi-infinite linear diffusion of the analyte to the electrode surface.

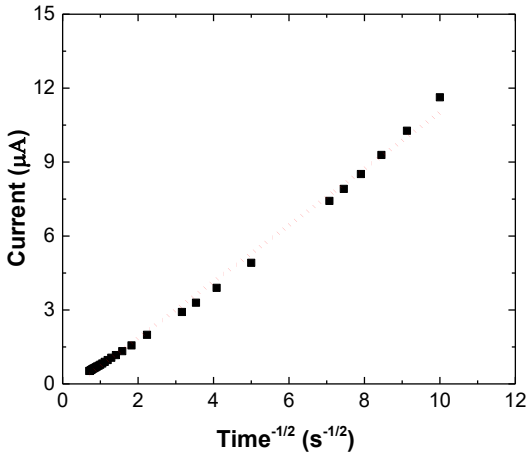

Figure 3.8. Plot of *i* vs. $t^{-1/2}$ for 1 mmol L^{-1} FCA in [EMIM][BF_4] at a Pt electrode. Data are presented for n=1 electrode.

Table 3.3 provides a summary of the diffusion coefficients for ferrocene derivatives (ferrocene, ferrocene carboxylic, and ferrocene methanol) in three used RTILs calculated from simple chronoamperometric measurement. The diffusion coefficients for FCA are calculated to be 4.59×10^{-7}, 1.15×10^{-7}, and 0.61×10^{-7} cm^2 s^{-1} in [EMIM][BF_4], [BMIM][BF_4], [HMIM][BF_4], respectively.

Table 3.3. Original and corrected peak potential separations (ΔE_p), diffusion coefficients (D), and experimental apparent heterogeneous electron transfer rate constant (k^o_{app}), simulated heterogeneous electron transfer rate constant (k^o_{sim}) for ferrocene derivatives in [EMIM][BF_4], [BMIM][BF_4], and [HMIM][BF_4] at BDDOTEs.

Analyte	**RTIL**	$\Delta E_{p,\,org}$ **(mV)**	$\Delta E_{p,\,cor.}$ **(mV)**	i_p^{ox} **(μA)**	D_{red} **(CV)** $\times 10^{-7}$ **(cm^2 s^{-1})**	D_{red} **(CA)** $\times 10^{-7}$ **(cm^2 s^{-1})**	k^o_{app} $\times 10^{-4}$ **(cm s^{-1})**	k^o_{sim} $\times 10^{-4}$ **(cm s^{-1})**
FCA	EMIM BF_4	112 ± 3	99 ± 1	3.79 ± 0.19	1.88 ± 0.17	4.59	4.32 ± 0.01	4.60 ± 0.53
	BMIM BF_4	125 ± 7	114 ± 9	2.90 ± 0.28	0.70 ± 0.07	1.15	1.82 ± 0.42	2.85 ± 0.74
	HMIM BF_4	158 ± 6	153 ± 6	1.45 ± 0.33	0.12 ± 0.07	0.61	0.32 ± 0.14	0.45 ± 0.08
FcMeOH	EMIM BF_4	105 ± 4	90 ± 8	4.13 ± 1.03	1.14 ± 0.90	3.34	4.81 ± 3.13	6.00 ± 2.65
	BMIM BF_4	111 ± 5	99 ± 5	2.65 ± 0.56	0.44 ± 0.31	2.11	2.00 ± 1.17	1.93 ± 1.21
	HMIM BF_4	129 ± 2	124 ± 1	1.52 ± 0.21	0.12 ± 0.06	0.09	0.55 ± 0.15	0.77 ± 0.21
Fc	EMIM BF_4	105 ± 4	89 ± 6	4.72 ± 0.11	0.86 ± 0.32	4.11	4.13 ± 1.26	4.83 ± 1.04
	BMIM BF_4	125 ± 19	113 ± 21	3.48 ± 0.07	0.49 ± 0.20	1.16	1.98 ± 1.66	2.83 ± 2.36
	HMIM BF_4	153 ± 6	149 ± 6	1.34 ± 0.04	0.06 ± 0.01	0.43	0.23 ± 0.03	0.48 ± 0.11

Data are reported as a mean ± std. dev. for n=3 BDDOTEs at a scan rate of 0.025 V s^{-1}. Nicholson method (corrected peak separation-scan rate trends ($\Delta E_{p,cor}$ -υ) were used to calculate the apparent heterogeneous electron transfer rate constant (k^o_{app}). Simulated rate constants were obtained using Digisim® 3.03 software.

The viscosity of RTILs increases in the following order: [EMIM][BF_4] < [BMIM] [BF_4] < [HMIM][BF_4]. In other words, the viscosity of RTILs increases with increasing the size of the alkyl side chain.[88] The diffusion coefficient for the ferrocene derivatives, D_{red}, and oxidation and reduction peak currents, i^x, decreases in the following order: [EMIM] > [BMIM] > [HMIM].

The diffusion coefficients for the ferrocene derivatives calculated from cyclic voltammetric and chronoamperometric data in three RTILs are in the range of 10^{-7} to 10^{-9} cm^2 s^{-1} which is consistent with the previous reports in RTILs with the same or similar viscosity.[16, 46, 72, 101] The diffusion coefficients in RTILs are smaller than values in aqueous solutions (10^{-5} to 10^{-6} cm^2 s^{-1}) because of the lower viscosity of water compared to the RTILs.

The *iR*-corrected ΔE_p for FCA increases in the following order: [EMIM][BF_4] < [BMIM][BF_4] < [HMIM][BF_4]. Similar trends are seen for FcMeOH and Fc. The increase in peak separation ($\Delta E_{p,\ cor.}$) is due to a decrease in the apparent heterogeneous electron-transfer rate constant (k^o_{app}) with increasing RTIL viscosity (see section 3.4.5).

3.4.5. Apparent Heterogeneous Electron-Transfer Rate Constant for Ferrocene Derivatives in RTILs

Table 3.3 provides the experimental and simulated apparent heterogeneous electron-transfer rate constant values, k^o_{app}, for FCA, FcMeOH and Fc in the three RTILs. The experimental rate constants (k^o_{app}) in Table 3.3 were determined from the *iR*-corrected cyclic voltammetric $\Delta E_{p,cor}$ -υ data using the Nicholson method.[89] The experimental k^o_{app} values for FCA are 4.32 (± 0.01) × 10^{-4}, 1.82 (± 0.42) × 10^{-4}, and 0.32 (± 0.14) × 10^{-4} cm s^{-1} in [EMIM][BF_4], [BMIM][BF_4], and [HMIM][BF_4], respectively. k^o_{app} decreases with increasing the viscosity of the RTIL. The same trends in k^o_{app} were observed for FcMeOH and Fc in the three RTILs.

The cyclic voltammetric curves were fit by digital simulation (Digisim® 3.03) as a second method for determining k^o_{app}. Figure 3.9 A-C presents the examples of the experimental and simulated voltammetric *i-E* curves for FCA in the three RTILs. In terms of the peak currents and ΔE_p values, there is a good fit between the experimental and simulated data. The best-fitting was observed using an α value of 0.5. Similar matches between the experimental and simulated voltammetric curves were also observed for FcMeOH and Fc (curves are not shown). The main difference in the curves is that the experimental values of the current at the tail end of the oxidation peak are slightly larger than the current predicted from the simulation.

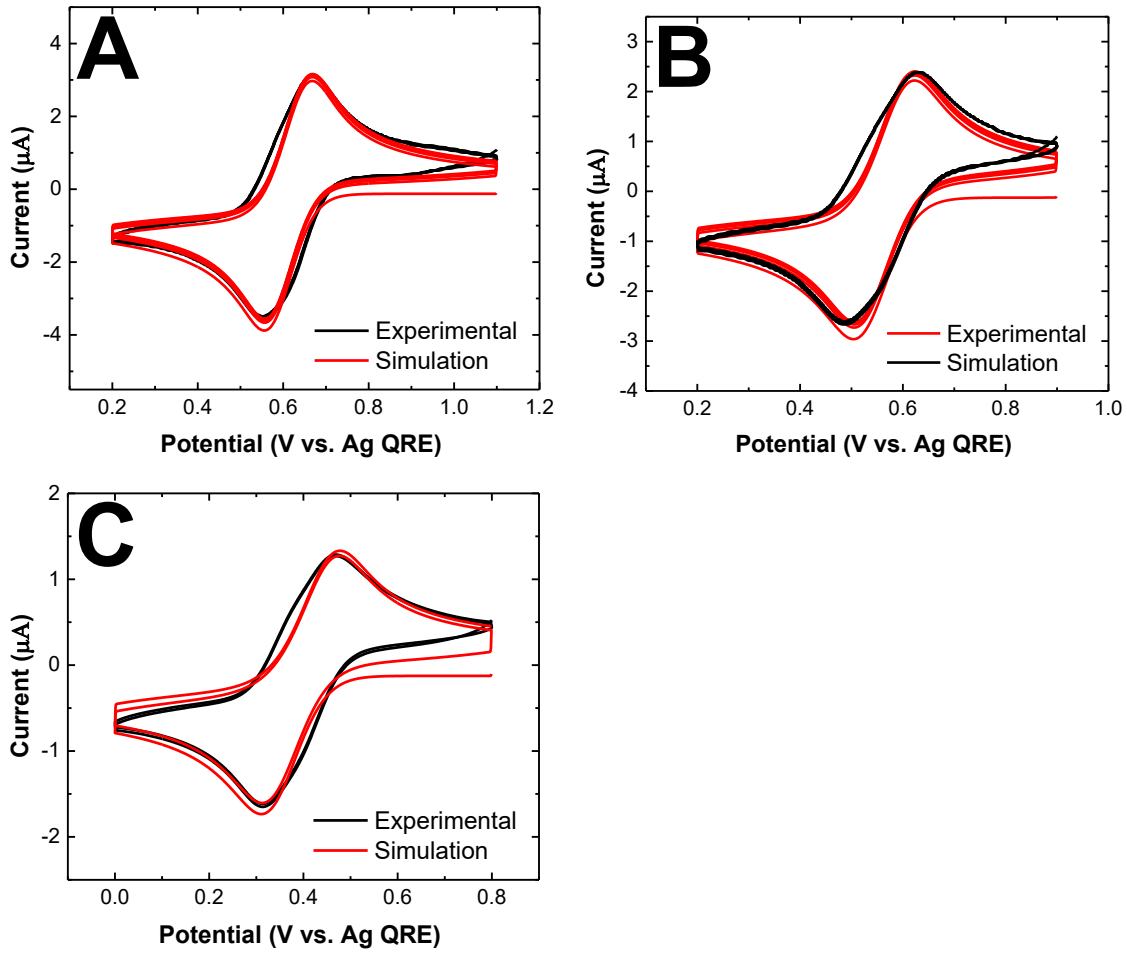

Figure 3.9. Experimental (black) and simulated (red) cyclic voltammetric *i*−*E* curves for FCA in (A) [EMIM][BF_4], (B) [BMIM][BF_4], and (C) [HMIM][BF_4] at a BDDOTE. Scan rate = 0.025 V s^{-1}, and area = 0.2 cm^2. Simulation parameters used were α = 0.5 and C_{dl} = 5µF.

The simulated apparent heterogeneous electron-transfer rate constant, k^o_{sim}, follows the same trend as seen for experimental values decreasing in the order of [EMIM][BF_4] > [BMIM][BF_4] > [HMIM][BF_4]. For example, k^o_{sim} for FCA is 4.60 (± 0.53) × 10^{-4}, 2.85 (± 0.74) × 10^{-4}, and 0.45 (± 0.08) × 10^{-4} cm s^{-1} in [EMIM][BF_4], [BMIM][BF_4], and [HMIM][BF_4], respectively. The simulated rate constants are generally in good agreement with the experimental values.

3.4.6. Dependence of Heterogeneous Electron Transfer Rate Constant on Hydrodynamic Radius

Table 3.4 shows the calculated hydrodynamic radius for the ferrocene derivatives in the three RTILs. These values were calculated using the Stokes-Einstein equation using *D* values obtained from cyclic voltammetric data analysis (see Table 3.3). In the Stokes-Einstein equation [6],

$$D = \frac{k_B T}{P \pi r \eta} \quad [6]$$

k_B represents the Boltzmann constant, *T* is temperature, r is the hydrodynamic radius, and η is the viscosity. *P* is either 4 or 6 depending on whether the "stick" or the "slip" is assumed. The plots of the heterogeneous electron transfer rate constant versus the hydrodynamic radius for the ferrocene derivatives in the three RTILs are shown in Figure 3.10.

In general, the calculated hydrodynamic radii are larger in these RTILs than reported values for ferrocene derivatives in organic solutions.[13] In Marcus theory, the main factor which affects the reorganization energy ($\Delta G^{\ddagger}$) is the outer sphere free energy of activation ($\Delta G^{\ddagger}_{os}$) (see eq. [5]). The theory suggests a plot of k^o versus *r*, the hydrodynamic radius of the molecule, would be meaningful. If the hydrodynamic radius increases with [EMIM][BF_4] < [BMIM][BF_4]

Table 3.4. Calculated hydrodynamic radius for the ferrocene derivatives in [EMIM][BF_4], [BMIM][BF_4], and [HMIM][BF_4].

Redox System	RTILs	*P*	*r* (Å) (CV)
FCA	**[EMIM][BF_4]**	4	5.19 ± 0.45
	[EMIM][BF_4]	6	3.46 ± 0.30
	[BMIM][BF_4]	4	4.52 ± 0.45
	[BMIM][BF_4]	6	3.01 ± 0.30
	[HMIM][BF_4]	4	8.13 ± 8.84
	[HMIM][BF_4]	6	8.19 ± 5.89
FcMeOH	**[EMIM][BF_4]**	4	12.09 ± 7.16
	[EMIM][BF_4]	6	8.06 ± 4.77
	[BMIM][BF_4]	4	9.80 ± 5.86
	[BMIM][BF_4]	6	6.54 ± 3.91
	[HMIM][BF_4]	4	11.32 ± 5.06
	[HMIM][BF_4]	6	7.55 ± 3.37
Fc	**[EMIM][BF_4]**	4	12.89 ± 6.20
	[EMIM][BF_4]	6	8.59 ± 4.13
	[BMIM][BF_4]	4	7.08 ± 2.38
	[BMIM][BF_4]	6	4.72 ± 1.59
	[HMIM][BF_4]	4	19.75 ± 4.45
	[HMIM][BF_4]	6	13.17 ± 2.96

* Hydrodynamic radius was calculated using the Stokes-Einstein equation.
* P was either 4 or 6. Data are presented as mean ± std. dev. for n=3 measurement values.

< [HMIM][BF_4], then the distance of closest approach should increase and k^o decrease. However, the expected trend is not observed between k^o_{app} and the hydrodynamic radius. This probably means that the electron transfer is orientation independent.

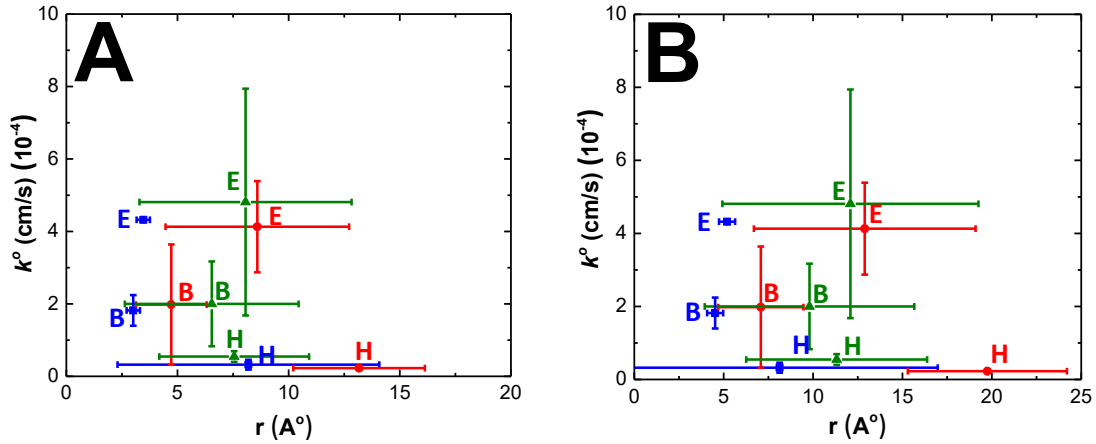

Figure 3.10. Plots of k^o vs. calculated hydrodynamic radius, r , for the ferrocene derivatives in [EMIM][BF_4], [BMIM][BF_4], and [HMIM][BF_4] at BDDOTEs for P = 4 (A) and 6 (B). Hydrodynamic radius was calculated from diffusion coefficients collected from cyclic voltammetry, A) P=6, B) P=4. E: [EMIM][BF_4], B: [BMIM][BF_4], H: [HMIM] [BF_4], Blue square: FCA, Red circle: Fc, Green triangle: FcMeOH. Data are presented as mean ± std. dev. for n=3 measurement values.

3.4.7. Dependence of Heterogeneous Electron Transfer Rate Constant on Reorientation Dynamics of RTILs

A more definitive relationship was observed between k^o_{app} and the RTIL viscosity. Figure 3.11 shows plots of the natural log of k^o_{app} versus the natural log of the RTIL viscosity (η). The plots are linear with a slope near -1.0. The Gibbs activation energy has two main contributors, inner and outer shell Gibbs activation energies. The former is associated with bond formation and breakage. The latter one is ascribed to the reorganization of solvent molecules surrounding the redox species following electron transfer. The inverse relationship between ln k^o_{app} and ln η indicates that the reorientation dynamics in the RTILs dominates k^o_{app}.

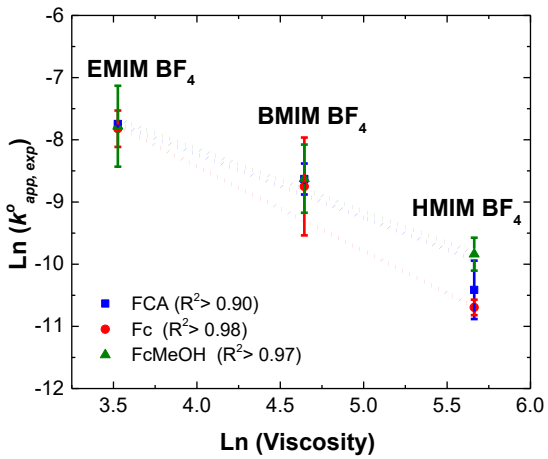

Figure 3.11. Plots of the natural log of $k^o_{app,exp}$ versus the natural log of the RTIL viscosity (η) for the three different ferrocene derivatives: Fc, FCA and FcMeOH in the three RTILs. Data are presented as mean ± std. dev. for n=3 diamond electrodes.

3.5. Discussion

This research was focused on gaining a better understanding of how the RTIL ionic composition and viscosity affect the working potential window, double-layer capacitance, and electron-transfer kinetics for three ferrocene derivatives at BDDOTEs. There is limited published research on the electrochemical behavior of sp^3-bonded carbon electrodes, like BDD, in RTILs.[33, 38, 63, 72, 78, 98, 99], so this work addressed the knowledge gap.

In summary, the voltammetric background currents increase linearly with the scan rate in the three RTILs at scan rates from 0.025 to 0.25 V s^{-1}. The double-layer capacitance, calculated from cyclic voltammetric data, revealed values from 3-8 μF cm^{-2} over the potential range probed independent of the RTIL's ionic composition or viscosity. Capacitance-potential trends were also collected from EIS data over a wide potential range from -1 to +1 V vs. Ag QRE. Over the potential range, the values ranged from 4 to 10 μF cm^{-2} independent of the RTIL's ionic composition and viscosity. The C_{dl}-E profiles were flat or showed a very slight upward trend with increasing positive potential. The capacitance magnitudes calculated from the cyclic voltametric data were in

agreement with the values determined from EIS data. Furthermore, the C_{dl}-E data are consistent with values in the literature for BDD electrodes in RTILs.[72, 78, 103-105] The capacitance values for BDDOTEs were larger in KCl [1M] by 2x. The larger capacitance in the aqueous electrolyte solution is attributed to the larger dielectric constant of water and to the smaller size and more spherical shape of the solvated ions, as compared to the dielectric constants of the RTILs and the non-spherically shaped cations. The larger size and asymmetric shape of the RTIL cations result in reduced packing density (voltammetric charge density) on the solution side of the interface.[106] The absence of close packing means the volumetric charge density of the RTILs is lower than the aqueous electrolyte solution. This means the counterbalancing charge densities on the solution side of the interface will extend a further distance away from the electrode in the RTIL leading to a lower interfacial capacitance. Additionally, ion-pairing can decrease the capacitance values in RTILs, as compared to aqueous electrolyte solution, because of a smaller number of the free ions at the carbon electrode/RTIL interface.[107]

Given that there is no dielectric solvent, the traditional Gouy-Chapman-Stern model of the electric double used to describe the organization of aqueous electrolyte solutions is not appropriate for RTILs. How the RTIL ion excesses arrange themselves in the interfacial region is important to consider. The most tested model for RTILs is the mean field theory put forward by the Kornyshev group.[45] This model predicts an interfacial capacitance maximum near the potential-of-zero charge with decreasing capacitance on either flank at potentials more positive and negative. This is because at the more positive and negative potentials, the excess surface charge on the electrode increases and therefore the thickness of the counterbalancing excess charge on the liquid side of the interface extends further away from the electrode. Metal electrodes exhibit the bell or camel-

shaped interfacial capacitance-potential profiles, as predicted by the model. An example of Au was presented in Chapter 2. However, carbon electrodes, including BDD, generally do not.[72, 78, 103, 104]

One possible reason that the BDDOTEs do not exhibit the behavior predicted by the model is because the potential range used for the capacitance measurements does not span the potential-of-zero charge. An alternate reason is that the BDDOTEs possess at least some sites across the surface that behave more like a semiconductor, as was demonstrated in the Mott-Schottky analysis in Chapter 2. In other words, the electrode may consist of regions that behave electronically as a metal and other region that behave more like a semiconductor. This is not an unreasonable expectation as SECM and CP-AFM data have revealed BDD electrodes are unevenly boron doped and consist of regions of relatively high electrochemical activity surrounded by regions of lower activity.[108-113]

The capacitance-potential data indicate that at least macroscopically the BDDOTE capacitance is controlled by the ionic organization of the counteracting liquid electrolyte solution in both aqueous and RTIL media. Microscopically, there may be regions of the electrode that have an internal space charge layer. Such, the interfaces in these regions might best be modeled as two capacitors in series: (i) the internal space charge layer capacitance and (ii) the interfacial capacitance across the solution layer. Kornyshev[103] and co-workers have suggested that the presence of the space charge layer capacitance is a possible explanation for the deviation of the experimental results with theory. A third possible reason is that the excess surface charge on the BDDOTEs is low enough at the potentials probed that the full counterbalancing excess charge can be accumulated in the layer adjacent to the electrode, much like the Helmholtz model. Any slight variations in C_{dl} with potential would be attributed to slight changes in the interfacial dielectric or spacing between the electrode surface and the plane through the adjacent layer of counterbalancing

ions according to the equation, $C_{dl} = \frac{\varepsilon_o \varepsilon}{d}$, in which ε is the dielectric constant of the RTIL, ε_o is the permittivity of free space, and d is the spacing of the counterbalancing charge layer from the electrode surface.

If the space charge layer capacitance is largest, and therefore dominating the complex interfacial capacitance, then one would expect to observe little dependence of the measured interfacial capacitance on the composition and concentration of ions in the liquid. Our work revealed a larger interfacial capacitance in aqueous electrolyte solution than in the RTILs. Therefore, we are leaning toward the Helmholtz model as an explanation for the low and relatively potential-independent capacitance at the BDDOTEs. As was discussed in Chapter 2, these electrodes are heterogeneous in that the boron-doping is inhomogeneous across the film surface meaning that one has an electrode with highly doped regions or electron-transfer hot spots surrounded by lower doped regions that might exhibit more semiconductor interfacial behavior.

The research revealed that the diffusion coefficients, and therefore cyclic voltammetric peak currents for the ferrocene derivatives, decrease with increasing the viscosity of the RTIL ($D \propto \eta^{-1}$). The highest and lowest diffusion coefficients and peak currents in three RTILs are seen for [EMIM][BF_4] (lowest viscosity) and [HMIM][BF_4] (highest viscosity), respectively. The peak currents also decrease with increasing the viscosity of RTILs as the voltametric peak current is proportional to $D^{1/2}$ according to the Randles-Sevcik equation. The ferrocene derivative diffusion coefficients calculated from the chronoamperometric and cyclic voltametric data are 10^{-7} to 10^{-9} cm^2 s^{-1} in the three RTILs, and all are lower than the values of 10^{-5} to 10^{-6} cm^2 s^{-1} in aqueous electrolyte solution.

It is known that the boron-doped diamond optically transparent electrodes possess some electrical resistance by their nature. The resistance arises from the low carrier mobility when the

current is collected laterally through the grains and grain boundaries of the film.[67] Cyclic voltammetric *i-E* curves were distorted by *iR* ohmic effects. For electron-transfer kinetic studies using voltametric methods, it is critical to correct for any ohmic distortion. The *iR*-corrected peak separation-scan rate (ΔE_p-v) trends were used to determine the apparent heterogeneous electron-transfer rate constant k^o_{app} for the ferrocene derivatives. The k^o_{app} values for each derivative decreases in the order of [EMIM][BF_4] > [BMIM][BF_4] > [HMIM][BF_4]. Furthermore, the k^o_{app} values were similar for the three ferrocene redox systems independent the molecular composition of the RTIL.

Digital simulation (Butler-Volmer theory) of cyclic voltametric *i-E* curves to fit experimental ones was used to determine the transfer coefficient, α, and k^o. was also used to determine k^o_{app}. The digital simulation produced good fits with experimental data based on matching the peak currents and peak potentials. A mismatch can be seen in the rising portion before each peak, where the electron transfer controls the rate of electron transfer. A greater mismatch is seen for [HMIM][BF_4] with the highest viscosity among probed RTILs. The greater mismatch is probably due to the viscose nature of room temperature ionic liquids, not the electrode itself. This means that heterogeneities in the electrode surface (surface roughness and active area density and spacing)[114] will influence the voltametric curve shapes more in an RTIL with higher viscosity. Our group previously reported this mismatch between the experimental and simulated curves.[72]

The chemical environment surrounding a redox system in RTILs differs greatly from that in an aqueous and organic electrolyte solution. First, RTILs are solventless environments. Ions exist as ion pairs and clusters as rather than discrete spherical charges. In conventional solutions, ions are shielded from one another by solvent molecules. However, there is no solvent in RTILs. The large asymmetric cations and small inorganic anions are surrounded by the ions with opposite

charges, not the molecules of solvent. So, there is an extended organization of anions and cations. The movement of one ion causes the reorganization of all the cationic and anionic species. The complex ionic organization around a redox system, especially one that is charged, likely requires significant energy to reorganize upon electron transfer. In addition, the viscose medium means the reorganization process would be slow.

The high viscosity of RTIL slows down the rate of electron transfer and diffusional mass transport.[26-32] The "solution dynamics" or reorganization around the redox system is slowed because of the viscosity, as mentioned above. There are several variables in the Marcus expression ([1]) that are influenced by the viscosity:

1. v_n: The nuclear frequency factor is the effective frequency of the starting materials passing through the transition state. This parameter is inversely related to viscosity.[5] A more viscose medium results in a decrease in the nuclear frequency factor, and accordingly, k^o.

2. ΔG^*: This energy is needed for the conversion of reactant to transition state and products eventually. All redox molecules are covered by the molecules of solvents in traditional environments. However, there is no solvent in RTILs. The movement of one ion causes the reorganization of all the existing ions in RTILs, which requires larger activation energy compared to organic/aqueous solutions. A larger activation energy results in slower kinetics (k^o). [72]

3. κ_{el}: The electronic transmission coefficient is determined by the number of collisions between the redox molecule and the electrode and the probability of electron transfer per collision. When a redox molecule arrives at the interface, it collides with the electrode surface, transfers an electron, and eventually wanders off into the bulk

solution.[115] The number of collisions between the redox molecule and electrode surface and the probability of electron transfer decrease in the more viscose medium, which decreases k^o.[63]

The experimental results provided here show that the apparent heterogeneous electron transfer rate constant (k^o_{app}) is inversely related to the viscosity.[5, 16] The heterogeneous electron transfer rate constants (k^o_{app}) for ferrocene derivatives in three RTILs are in order of 10^{-4} to 10^{-5} cm s^{-1}. Previous studies reported similar values for the heterogeneous electron transfer rate constant (k^o_{app}). Kim et al. reported 1.5 (±1.1) $\times 10^{-3}$ and 5.0 (±1.2) $\times 10^{-3}$ cm s^{-1} as rate constants in 1-butyl-3-methylimidazolium tetrafluoroborate for ferrocene and ferrocene carboxylic acid, respectively, at boron-doped microcrystalline diamond thin-film electrodes.[63] Jarošová et al. reported k^o value in the order of 10^{-4} cm s^{-1} for ferrocene carboxylic acid in 1-ethyl-3-methylimidazolium tetrafluoroborate and 1-butyl-3-methylimidazolium tetrafluoroborate at boron-doped diamond (BDD), nitrogen-incorporated tetrahedral carbon thin-film (t*a*-C: N), and glassy carbon electrodes (GC). Their results showed that the rate constant increases with the temperature, consistent with lowering the RTIL's viscosity. They reported that the heterogeneous electron transfer rate constants depend on RTILs' physical properties and the electrode material. The RTIL with the larger viscosity, 1-butyl-3-methylimidazolium tetrafluoroborate, showed a slower electron transfer kinetics (smaller k^o) and higher activation energy (E_a). In both RTILs, k^o_{app} for FCA decreases in the following order: BDD > t*a*-C: N > GC.[72] They believed that the difference may arise from the different organization of the ions at the electrode-electrolyte interface at the microstructurally distinct carbon electrodes. Compton et al. reported the k^o value of 0.1-0.2 cm s^{-1} for ferrocene derivatives in 1-ethyl-3-methylimidazolium bis(trifluoromethylsulfonyl) imide at a Pt microband electrode using the high-speed channel

electrode under steady-state condition.[46] Tachikawa reported the k^o value of 0.2–1.5 $\times 10^{-2}$ cm s^{-1} for ferrocene in bis(trifluoromethylsulfonyl)amide. The apparent heterogeneous rate constants in the ionic liquids were smaller than those in organic solvents because of the slower dynamics in RTILs. They reported that the k^o is inversely related to the electrolyte viscosity.[5] Hapiot et al. found k^o values for ferrocene and anthracene in RTILs with the core structure of 1-alkyl-3-methylimidazolium or quaternary ammonium cations, which are ~1-2 orders of magnitude smaller than organic solutions.[116] Fontaine et al. reported a k^o value of (2.1 ± 0.3) $\times 10^{-2}$ cm s^{-1} for ferrocene in 1-ethyl-3-methylimidazolium bis(trifluoromethylsulfonyl)imide at a Pt disk electrode using cyclic voltammetry.[102] Xiao et al. reported a k^o for ferrocene in order of 10^{-4} cm s^{-1} in 1-butyl-3-methylimidazolium hexafluorophosphate at glassy carbon and edge plane pyrolytic graphite.[117] The k^o values reported here are consistent with previous reports for ferrocene derivatives in RTILs with the same or similar viscosity at BDDs.[38, 63, 72]

The hydrodynamic radius (r) for ferrocene derivatives was obtained from the Stokes-Einstein equation using experimental diffusion coefficients calculated from cyclic voltametric data. P was either 4 or 6 depending on whether the "stick" or "slip" limits were assumed. Plots of the apparent heterogeneous electron transfer rate constant (k^o) against the hydrodynamic radius (r) for ferrocene derivatives in three probed RTILs show no apparent relationship between k^o and r. The fact that no significant trend is observed likely means that the electron transfer is orientation independent. Additionally, this suggests that, in line with previous literature reports,[46, 118, 119] the dependence of k^o on the hydrodynamic radius as predicted by the Marcus expression appears to break down in ionic liquid media as expected for an ionic rather than dipolar medium. Marcus theory is based on the reorganization of solvent dipoles, whereas RTILs are composed of pure ions. Further studies are required to understand the solvent dynamic in RTILs and the factors which

may operate. Fietkau et al. studied the heterogeneous electron transfer rate constant for the oxidation of a series of ferrocene derivatives in [C_2mim] [NTf_2] using the high-speed channel electrode system (HSChE) under steady-state conditions. They reported no correlation between the heterogeneous rate constant and the hydrodynamic radius in RTILs.[46] One study from Compton's group on the electrochemical oxidation of N,N,N′,N′-tetramethyl-p-phenylenediamine (TMPD) at 303 K in five ionic liquids ([C_2mim][NTf_2], [C_4mim][NTf_2], [C_4mpyrr][NTf_2], [C_4mim][BF_4], and [C_4mim][PF_6]) using cyclic voltammetry and potential step chronoamperometry showed no obvious relationship between k^o and the hydrodynamic radius, r.[118] Belding et al. studied the anodic oxidation of several arenes and anthracenes in room-temperature ionic liquids. They observed that the heterogeneous rate constants for several arenes and substituted anthracenes do not obey the Marcus model for the dependence of k^o on solvodynamic radius that is expected for outer-sphere electron transfers.[119]

Overall, the result indicate that the ferrocene derivatives exhibit classical "outer sphere" electron transfer behavior in the three RTILs. The viscosity of these three RTILs is the physical property controlling the rate of electron transfer. The work shows $k^o \propto \eta^{-1}$. This means the rate of electron transfer is governed by the relaxation of RTIL ionic coupled to the ET with the ferrocene derivatives. The plots of ln k^o vs. ln η was linear with a slope near -1.0. This means that the ET process is adiabatic (no energy loss or gain) and that the outer sphere activation reorganization barrier, $\Delta G_{os}^{\ddagger}$, dominates the $\Delta G^{\ddagger}$.

3.6. Conclusions

Boron-doped diamond thin films deposited on quartz (BDDOTEs) were prepared using chemical vapor deposition method (CVD). Their microstructure, morphology, and optical properties were investigated using different microscopic and spectroscopic techniques (see chapter

2). We investigated the electrochemical behavior of ferrocene derivatives in three homologous RTILs ([EMIM][BF_4], [BMIM][BF_4], [HMIM][BF_4]). The following are the key findings from this research:

1. The voltammetric background current, working potential window, and double-layer capacitance do not depend on the type of RTILs at BDDOTEs. The molecular composition and viscosity of the RTILs does not have a significant effect on the capacitance values.

2. The double-layer values are below 10 μF cm^{-2} in three RTILs at probed potentials. Flat *C-E* profiles are seen for BDDOTEs in the three used RTILs, consistent with previous reports for carbon electrodes.

3. Capacitance values are larger in KCl compared to RTILs at a particular potential. The larger capacitance in aqueous solutions is probably due to the larger dielectric constant of water, smaller size of ion and higher concentration of free ions in aqueous solutions.

4. The diffusion coefficients for ferrocene derivatives are in order of 10^{-7} to 10^{-9} cm^2 s^{-1} in three used RTILs. The diffusion coefficients for ferrocene derivatives are smaller in ionic liquids with higher viscosity as expected by the Stokes-Einstein equation.

5. The peak current is lower in RTIL with the higher viscosity because of the smaller diffusion coefficients in a more viscose medium.

6. k^o_{app} are in order of 10^{-4} to 10^{-5} cm s^{-1} in three RTILs. k^o_{app} are inversely related to the viscosity of RTILs. The smallest k^o_{app} is seen for [HMIM][BF_4] with the highest viscosity because of the lower nuclear frequency, ν_n, factor and larger outer-shell activation energy, $\Delta G^{\ddagger}_{OS}$. Similar values are obtained from digital simulation.

7. No correlation was found between k^o_{app} and hydrodynamic radius (r) in probed RTILs indicating the electron transfer is orientation independent. Other factors contribute to the electron transfer process.

REFERENCES

[1] E. J. Piechota, G. J. Meyer, 'Introduction to electron transfer: theoretical foundations and pedagogical examples', *J. Chem. Educ.* **2019**, *96*, 2450-2466.

[2] R. A. Marcus, 'On the theory of oxidation-reduction reactions involving electron transfer. I', *J. Chem. Phys.* **1956**, *24*, 966-978.

[3] R. A. Marcus, 'Tutorial on rate constants and reorganization energies', *J. Electroanal. Chem.* **2000**, *483*, 2-6.

[4] H. Gerischer, 'Messungen der Austauschstromdichte beim Gleichgewichtspotential an einer Platinelektrode in Fe^{2+}/Fe^{3+}-Lösungen', *Z. Elektrochem.* **1950**, *54*, 366-369.

[5] N. Tachikawa, Y. Katayama, T. Miura, 'Electrode kinetics of ferrocenium/ferrocene in some amide-based room-temperature ionic liquids', *Electrochem. solid-state lett.* **2009**, *12*, F39.

[6] R. A. Marcus, 'On the frequency factor in electron transfer reactions and its role in the highly exothermic regime', *Int. J. Chem. Kinet.* **1981**, *13*, 865-872.

[7] M. Opałło, 'The solvent effect on the electro-oxidation of 1,4-phenylenediamine. The influence of the solvent reorientation dynamics on the one-electron transfer rate', *J. Chem. Soc., Faraday Trans. 1***1986**, *82*, 339-347.

[8] R. A. Marcus, 'On the theory of oxidation-reduction reactions involving electron transfer. II. Applications to data on the rates of isotopic exchange reactions', *J. Chem. Phys.* **1957**, *26*, 867-871.

[9] R. A. Marcus, 'On the theory of oxidation—reduction reactions involving electron transfer. v. comparison and properties of electrochemical and chemical rate constants1', *J. Phys. Chem.* **1963**, *67*, 853-857.

[10] R. A. Marcus, 'On the theory of electron-transfer reactions. vi. unified treatment for homogeneous and electrode reactions', *J. Chem. Phys.* **1965**, *43*, 679-701.

[11] R. A. Marcus, 'Exchange reactions and electron transfer reactions including isotopic exchange. Theory of oxidation-reduction reactions involving electron transfer. Part 4.—A statistical-mechanical basis for treating contributions from solvent, ligands, and inert salt', *Discuss. Faraday Soc.* **1960**, *29*, 21-31.

[12] A. D. Clegg, N. V. Rees, O. V. Klymenko, B. A. Coles, R. G. Compton, 'Marcus theory of outer-sphere heterogeneous electron transfer reactions: dependence of the standard electrochemical rate constant on the hydrodynamic radius from high precision measurements of the oxidation of anthracene and its derivatives in nonaqueous solvents using the high-speed channel electrode', *J. Am. Chem. Soc.* **2004**, *126*, 6185-6192.

[13] A. D. Clegg, N. V. Rees, O. V. Klymenko, B. A. Coles, R. G. Compton, 'Marcus theory of outer-sphere heterogeneous electron transfer reactions: high precision steady-state measurements of the standard electrochemical rate constant for ferrocene derivatives in alkyl cyanide solvents', *J. Electroanal. Chem.* **2005**, *580*, 78-86.

[14] Y. Nagasawa, H. Miyasaka, 'Ultrafast solvation dynamics and charge transfer reactions in room temperature ionic liquids', *Phys. Chem. Chem. Phys.* **2014**, *16*, 13008-13026.

[15] A. Hamnett, 'Comprehensive chemical kinetics, vol. 27', edited by RG Compton, Elsevier Science, Oxford **1987**, 61.

[16] C. L. Bentley, J. Li, A. M. Bond, J. Zhang, 'Mass-transport and heterogeneous electron-transfer kinetics associated with the ferrocene/ferrocenium process in ionic liquids', *J. Phys. Chem. C* **2016**, *120*, 16516-16525.

[17] H. Fernández, M. A. Zón, 'Determination of the kinetic and activation parameters for the electro-oxidation of N,N,N', N'-tetramethyl-p-phenylenediamine (TMPD) in acetonitrile (ACN) by chronocoulometry and other electrochemical techniques', *J. electroanal. chem. interfacial electrochem.* **1990**, *283*, 251-270.

[18] M. B. Moressi, M. A. Zón, H. Fernández, 'Solvent effects on the heterogeneous kinetics of N,N,N′,N′-tetramethyl p-phenylendiamine (TMPD) in nonaqueous binary solvent mixtures. The role of the preferential solvation phenomenon', *Electrochim. Acta* **2000**, *45*, 1669-1682.

[19] H. Fernández, M. A. Zón, 'Solvent effects on the kinetics of heterogeneous electron transfer processes. The TMPD/$TMPD^{\cdot+}$ redox couple', *J. Electroanal. Chem.* **1992**, *332*, 237-255.

[20] W. R. Fawcett, M. Opallo, 'On the differences in the magnitude of the observed solvent effect in the kinetics of simple heterogeneous electron transfer reactions', *J. Electroanal. Chem.* **1993**, *349*, 273-284.

[21] A. Kapturkiewicz, W. Jaenicke, 'Comparison between heterogeneous and homogeneous electron transfer in p-phenylenediamine systems', *J. Chem. Soc., Faraday Trans. 1* **1987**, *83*, 2727-2734.

[22] J. O. M. Bockris, A. K. N. Reddy, 'Ion-ion interactions', *Modern Electrochemistry 1: Ionics* **1998**, 225-359.

[23] A. D. Clegg, N. V. Rees, O. V. Klymenko, B. A. Coles, R. G. Compton, 'Experimental validation of marcus theory for outer-sphere heterogeneous electron-transfer reactions: the oxidation of substituted 1,4-phenylenediamines', *ChemPhysChem* **2004**, *5*, 1234-1240.

[24] T. Tsuda, C. L. Hussey, 'Electrochemical applications of room-temperature ionic liquids', *Electrochem. Soc. Interface* **2007**, *16*, 42.

[25] M. C. Buzzeo, R. G. Evans, R. G. Compton, 'Non-haloaluminate room-temperature ionic liquids in electrochemistry—a review', *ChemPhysChem* **2004**, *5*, 1106-1120.

[26] M. Galiński, A. Lewandowski, I. Stępniak, 'Ionic liquids as electrolytes', *Electrochim. Acta* **2006**, *51*, 5567-5580.

[27] T. Torimoto, T. Tsuda, K.-i. Okazaki, S. Kuwabata, 'New frontiers in materials science opened by ionic liquids', *Adv. Mater.* **2010**, *22*, 1196-1221.

[28] D. S. Silvester, R. G. Compton, 'Electrochemistry in room temperature ionic liquids: a review and some possible applications', *Z. fur Phys. Chem.* **2006**, *220*, 1247-1274.

[29] M. A. Navarra, 'Ionic liquids as safe electrolyte components for Li-metal and Li-ion batteries', *MRS Bull.* **2013**, *38*, 548-553.

[30] P. Hapiot, C. Lagrost, 'Electrochemical reactivity in room-temperature ionic liquids', *Chem. Rev.* **2008**, *108*, 2238-2264.

[31] H. Weingärtner, P. Sasisanker, C. Daguenet, P. J. Dyson, I. Krossing, J. M. Slattery, T. Schubert, 'The dielectric response of room-temperature ionic liquids: effect of cation variation', *J. Phys. Chem. B* **2007**, *111*, 4775-4780.

[32] J. A. Widegren, A. Laesecke, J. W. Magee, 'The effect of dissolved water on the viscosities of hydrophobic room-temperature ionic liquids', *Chem. Commun.* **2005**, 1610-1612.

[33] C. Zhao, G. Burrell, A. A. J. Torriero, F. Separovic, N. F. Dunlop, D. R. MacFarlane, A. M. Bond, 'Electrochemistry of room temperature protic ionic liquids', *J. Phys. Chem. B* **2008**, *112*, 6923-6936.

[34] M. Armand, F. Endres, D. R. MacFarlane, H. Ohno, B. Scrosati, 'Ionic-liquid materials for the electrochemical challenges of the future', *Nat. Mater.* **2009**, *8*, 621-629.

[35] H. Liu, Y. Liu, J. Li, 'Ionic liquids in surface electrochemistry', *Phys. Chem. Chem. Phys.* **2010**, *12*, 1685-1697.

[36] D. R. MacFarlane, M. Forsyth, P. C. Howlett, J. M. Pringle, J. Sun, G. Annat, W. Neil, E. I. Izgorodina, 'Ionic liquids in electrochemical devices and processes: managing interfacial electrochemistry', *Acc. Chem. Res.* **2007**, *40*, 1165-1173.

[37] S. Passerini, G. B. Appetecchi, 'Toward more environmentally friendly routes to high purity ionic liquids', *MRS Bull.* **2013**, *38*, 540-547.

[38] R. Jarosova, G. M. Swain, 'Rapid preparation of room temperature ionic liquids with low water content as characterized with a t*a*-C:N electrode', *J. Electrochem. Soc.* **2015**, *162*, H507-H511.

[39] M. Gnahm, D. M. Kolb, 'The purification of an ionic liquid', *J. Electroanal. Chem.* **2011**, *651*, 250-252.

[40] U. Schröder, J. D. Wadhawan, R. G. Compton, F. Marken, P. A. Z. Suarez, C. S. Consorti, R. F. de Souza, J. Dupont, 'Water-induced accelerated ion diffusion: voltammetric studies in 1-methyl-3-[2,6-(s)-dimethylocten-2-yl]imidazolium tetrafluoroborate, 1-butyl-3-methylimidazolium tetrafluoroborate and hexafluorophosphate ionic liquids', *New J. Chem.* **2000**, *24*, 1009-1015.

[41] A. M. O'Mahony, D. S. Silvester, L. Aldous, C. Hardacre, R. G. Compton, 'Effect of water on the electrochemical window and potential limits of room-temperature ionic liquids', *J. Chem. Eng. Data.* **2008**, *53*, 2884-2891.

[42] H. Tokuda, S. Tsuzuki, M. A. Susan, K. Hayamizu, M. Watanabe, 'How ionic are room-temperature ionic liquids? An indicator of the physicochemical properties', *J Phys Chem B* **2006**, *110*, 19593-19600.

[43] D. R. MacFarlane, M. Forsyth, E. I. Izgorodina, A. P. Abbott, G. Annat, K. Fraser, 'On the concept of ionicity in ionic liquids', *Phys. Chem. Chem. Phys.* **2009**, *11*, 4962-4967.

[44] D. R. MacFarlane, J. M. Pringle, P. C. Howlett, M. Forsyth, 'Ionic liquids and reactions at the electrochemical interface', *Phys. Chem. Chem. Phys.* **2010**, *12*, 1659-1669.

[45] A. A. Kornyshev, 'Double-layer in ionic liquids: paradigm change?', *J. Phys. Chem. B* **2007**, *111*, 5545-5557.

[46] N. Fietkau, A. D. Clegg, R. G. Evans, C. Villagrán, C. Hardacre, R. G. Compton, 'Electrochemical rate constants in room temperature ionic liquids: the oxidation of a series of ferrocene derivatives', *ChemPhysChem* **2006**, *7*, 1041-1045.

[47] M. V. Fedorov, A. A. Kornyshev, 'Ionic liquids at electrified interfaces', *Chem. Rev.* **2014**, *114*, 2978-3036.

[48] L. E. Barrosse-Antle, A. M. Bond, R. G. Compton, A. M. O'Mahony, E. I. Rogers, D. S. Silvester, 'Voltammetry in room temperature ionic liquids: comparisons and contrasts with conventional electrochemical solvents', *Chem. Asian J.* **2010**, *5*, 202-230.

[49] V. V. Singh, L. K. Pandey, P. K. Sharma, U. Biswas, K. Ganesan, M. Boopathi, 'electrochemistry of ferrocene in different room temperature ionic liquids with platinum and gold electrodes', *J. Sci. Technol.* **2020***, 8*, 41-50.

[50] R. J. Bowling, R. T. Packard, R. L. McCreery, 'Activation of highly ordered pyrolytic graphite for heterogeneous electron transfer: relationship between electrochemical performance and carbon microstructure', *J. Am. Chem. Soc.* **1989**, *111*, 1217-1223.

[51] R. J. Rice, R. L. McCreery, 'Quantitative relationship between electron transfer rate and surface microstructure of laser-modified graphite electrodes', *Anal. Chem.* **1989**, *61*, 1637-1641.

[52] R. J. Rice, N. M. Pontikos, R. L. McCreery, 'Quantitative correlations of heterogeneous electron-transfer kinetics with surface properties of glassy carbon electrodes', *J. Am. Chem. Soc.* **1990**, *112*, 4617-4622.

[53] K. R. Kneten, R. L. McCreery, 'Effects of redox system structure on electron-transfer kinetics at ordered graphite and glassy carbon electrodes', *Anal. Chem.* **1992**, *64*, 2518-2524.

[54] P. Chen, M. A. Fryling, R. L. McCreery, 'Electron transfer kinetics at modified carbon electrode surfaces: the role of specific surface sites', *Anal. Chem.* **1995**, *67*, 3115-3122.

[55] P. Chen, R. L. McCreery, 'Control of electron transfer kinetics at glassy carbon electrodes by specific surface modification', *Anal. Chem.* **1996**, *68*, 3958-3965.

[56] R. L. McCreery, A. J. Bard, 'Electroanalytical chemistry', *Marcel Dekker, Inc., New York* **1991**, *17*, 221-374.

[57] I. Švancara, K. Vytřas, J. Barek, J. Zima, 'Carbon paste electrodes in modern electroanalysis', *Crit. Rev. Anal* **2001**, *31*, 311-345.

[58] C. Xu, B. Xu, Y. Gu, Z. Xiong, J. Sun, X. S. Zhao, 'Graphene-based electrodes for electrochemical energy storage', *Energy Environ. Sci.* **2013**, *6*, 1388-1414.

[59] J. K. McDonough, Y. Gogotsi, 'Carbon onions: synthesis and electrochemical applications', *Electrochem. Soc. Interface* **2013**, *22*, 61.

[60] A. C. Power, B. Gorey, S. Chandra, J. Chapman, 'Carbon nanomaterials and their application to electrochemical sensors: a review', *Nanotechnol. Rev.* **2018**, *7*, 19-41.

[61] S. Haymond, G. T. Babcock, G. M. Swain, 'Electron transfer kinetics of ferrocene at microcrystalline boron-doped diamond electrodes: effect of solvent and electrolyte', *Electroanalysis* **2003**, *15*, 249-253.

[62] S. Haymond, G. T. Babcock, G. M. Swain, 'Direct electrochemistry of Cytochrome c at nanocrystalline boron-doped diamond', *J. Am. Chem. Soc.* **2002**, *124*, 10634-10635.

[63] D. Y. Kim, J. C. Yang, H. W. Kim, G. M. Swain, 'Heterogeneous electron-transfer rate constants for ferrocene and ferrocene carboxylic acid at boron-doped diamond electrodes in a room temperature ionic liquid', *Electrochim. Acta* **2013**, *94*, 49-56.

[64] D. Y. Kim, B. Merzougui, G. M. Swain, 'Preparation and characterization of glassy carbon powder modified with a thin layer of boron-doped ultrananocrystalline diamond (B-UNCD)', *Chem. Mater.* **2009**, *21*, 2705-2713.

[65] N. Wächter, C. Munson, R. Jarošová, I. Berkun, T. Hogan, R. C. Rocha-Filho, G. M. Swain, 'Structure, electronic properties, and electrochemical behavior of a boron-doped diamond/quartz optically transparent electrode', *ACS Appl Mater Interfaces* **2016**, *8*, 28325-28337.

[66] J. K. Zak, J. E. Butler, G. M. Swain, 'Diamond optically transparent electrodes: demonstration of concept with ferri/ferrocyanide and methyl viologen', *Anal Chem* **2001**, *73*, 908-914.

[67] J. Stotter, Y. Show, S. Wang, G. Swain, 'Comparison of the electrical, optical, and electrochemical properties of diamond and indium tin oxide thin-film electrodes', *Chem. Mater.* **2005**, *17*, 4880-4888.

[68] J. Stotter, J. Zak, Z. Behler, Y. Show, G. M. Swain, 'Optical and electrochemical properties of optically transparent, boron-doped diamond thin films deposited on quartz', *Anal. Chem.* **2002**, *74*, 5924-5930.

[69] Y. Dai, D. A. Proshlyakov, J. K. Zak, G. M. Swain, 'Optically transparent diamond electrode for use in ir transmission spectroelectrochemical measurements', *Anal. Chem.* **2007**, *79*, 7526-7533.

[70] Y. Dai, Y. Zheng, G. M. Swain, D. A. Proshlyakov, 'Equilibrium and kinetic behavior of $Fe(CN)_6^{-3/-4}$ and cytochrome c in direct electrochemistry using a film electrode thin-layer transmission cell', *Anal. Chem.* **2011**, *83*, 542-548.

[71] J. Stotter, S. Haymond, J. Zak, Y. Show, Z. Cvackova, G. Swain, 'Optically transparent diamond electrodes for uv-vis and ir spectroelectrochemistry', *Electrochem. Soc. Interface* **2003**, *12*, 33-38.

[72] R. Jarošová, K. Bhardwaj, G. M. Swain, 'Temperature dependence of the heterogeneous electron-transfer rate constant for ferrocene carboxylic acid in room temperature ionic liquids at microstructurally distinct carbon electrodes', *J. Electroanal. Chem.* **2020**, *875*, 114744.

[73] M. C. Granger, M. Witek, J. Xu, J. Wang, M. Hupert, A. Hanks, M. D. Koppang, J. E. Butler, G. Lucazeau, M. Mermoux, J. W. Strojek, G. M. Swain, 'Standard electrochemical behavior of high-quality, boron-doped polycrystalline diamond thin-film electrodes', *Anal. Chem.* **2000**, *72*, 3793-3804.

[74] M. Hupert, A. Muck, J. Wang, J. Stotter, Z. Cvackova, S. Haymond, Y. Show, G. M. Swain, 'Conductive diamond thin-films in electrochemistry', *Diam. Relat. Mater.* **2003**, *12*, 1940-1949.

[75] G. M. Swain, 'Electrically conducting diamond thin films: advanced electrode materials for electrochemical technologies', *Electroanal. chem., ser. adv.***2003**, *22*, 181.

[76] J. V. Macpherson, 'A practical guide to using boron doped diamond in electrochemical research', *Phys. Chem. Chem. Phys.* **2015**, *17*, 2935-2949.

[77] N. Yang, G. M. Swain, X. Jiang, 'Nanocarbon electrochemistry and electroanalysis: current status and future perspectives', *Electroanalysis* **2016**, *28*, 27-34.

[78] K. Bhardwaj, F. Parvis, Y. Wang, G. J. Blanchard, G. M. Swain, 'Effect of surface oxygen on the wettability and electrochemical properties of boron-doped nanocrystalline diamond electrodes in room-temperature ionic liquids', *Langmuir* **2020**, *36*, 5717-5729.

[79] C. I. Pakes, J. A. Garrido, H. Kawarada, 'Diamond surface conductivity: properties, devices, and sensors', *MRS Bull.* **2014**, *39*, 542-548.

[80] Z. Futera, T. Watanabe, Y. Einaga, Y. Tateyama, 'First principles calculation study on surfaces and water interfaces of boron-doped diamond', *J. Phys. Chem. C* **2014**, *118*, 22040-22052.

[81] Y. V. Pleskov, M. D. Krotova, V. V. Elkin, E. A. Ekimov, 'Electrochemical behaviour of boron-doped diamond compacts – a new electrode material', *Electrochim. Acta* **2016**, *201*, 268-273.

[82] Y. Einaga, J. S. Foord, G. M. Swain, 'Diamond electrodes: diversity and maturity', *MRS Bull.* **2014**, *39*, 525-532.

[83] S. Wang, V. M. Swope, J. E. Butler, T. Feygelson, G. M. Swain, 'The structural and electrochemical properties of boron-doped nanocrystalline diamond thin-film electrodes grown from Ar-rich and H_2-rich source gases', *Diam. Relat. Mater.* **2009**, *18*, 669-677.

[84] M. C. Granger, J. Xu, J. W. Strojek, G. M. Swain, 'Polycrystalline diamond electrodes: basic properties and applications as amperometric detectors in flow injection analysis and liquid chromatography', *Anal. Chim. Acta* **1999**, *397*, 145-161.

[85] J. Xu, M. C. Granger, Q. Chen, J. W. Strojek, T. E. Lister, G. M. Swain, 'Peer reviewed: boron-doped diamond thin-film electrodes', *Anal. Chem.* **1997**, *69*, 591A-597A.

[86] S. J. Cobb, Z. J. Ayres, J. V. Macpherson, 'Boron doped diamond: A designer electrode material for the twenty-first century', *Annu Rev Anal Chem* **2018**, *11*, 463-484.

[87] S. Haymond, J. K. Zak, Y. Show, J. E. Butler, G. T. Babcock, G. M. Swain, 'Spectroelectrochemical responsiveness of a freestanding, boron-doped diamond, optically transparent electrode toward ferrocene', *Anal. Chim. Acta* **2003**, *500*, 137-144.

[88] R. Khalil, N. Chaabene, M. Azar, I. B. Malham, M. Turmine, 'Effect of the chain lengthening on transport properties of imidazolium-based ionic liquids', *Fluid Ph. Equilibria.* **2020**, *503*, 112316.

[89] R. S. Nicholson, 'Theory and application of cyclic voltammetry for measurement of electrode reaction kinetics', *Anal. Chem.* **1965**, *37*, 1351-1355.

[90] P. Mishra, U. Singh, C. M. Pandey, G. Pandey, 'Application of student's t-test, analysis of variance, and covariance', *Ann Card Anaesth* **2019**, *22*, 407-411.

[91] Y. Liu, Y. Zeng, R. Liu, H. Wu, G. Wang, D. Cao, 'Poisoning of acetone to Pt and Au electrodes for electrooxidation of 2-propanol in alkaline medium', *Electrochim. Acta* **2012**, *76*, 174-178.

[92] R. Jarošová, P. M. De Sousa Bezerra, C. Munson, G. M. Swain, 'Assessment of heterogeneous electron-transfer rate constants for soluble redox analytes at tetrahedral amorphous carbon, boron-doped diamond, and glassy carbon electrodes', *Phys. Status Solidi A* **2016**, *213*, 2087-2098.

[93] I. Lavagnini, R. Antiochia, F. Magno, 'An extended method for the practical evaluation of the standard rate constant from cyclic voltammetric data', *Electroanalysis* **2004**, *16*, 505-506.

[94] T. Jänsch, J. Wallauer, B. Roling, 'Influence of electrode roughness on double layer formation in ionic liquids', *J. Phys. Chem. C* **2015**, *119*, 4620-4626.

[95] B. Hirschorn, M. E. Orazem, B. Tribollet, V. Vivier, I. Frateur, M. Musiani, 'Determination of effective capacitance and film thickness from constant-phase-element parameters', *Electrochim. Acta* **2010**, *55*, 6218-6227.

[96] S. Ren, Y. Hou, W. Wu, W. Liu, 'Purification of ionic liquids: sweeping solvents by nitrogen', *J. Chem. Eng. Data.* **2010**, *55*, 5074-5077.

[97] E. L. Bennett, C. Song, Y. Huang, J. Xiao, 'Measured relative complex permittivities for multiple series of ionic liquids', *J. Mol. Liq.* **2019**, *294*, 111571.

[98] S. Ernst, L. Aldous, R. G. Compton, 'The electrochemical reduction of oxygen at boron-doped diamond and glassy carbon electrodes: A comparative study in a room-temperature ionic liquid', *J. Electroanal. Chem.* **2011**, *663*, 108-112.

[99] A. J. Lucio, S. K. Shaw, J. Zhang, A. M. Bond, 'Double-layer capacitance at ionic liquid–boron-doped diamond electrode interfaces studied by fourier transformed alternating current voltammetry', *J. Phys. Chem. C* **2018**, *122*, 11777-11788.

[100] G. Gerhardt, R. N. Adams, 'Determination of diffusion coefficients by flow injection analysis', *Anal. Chem.* **1982**, *54*, 2618-2620.

[101] D. Zigah, J. Ghilane, C. Lagrost, P. Hapiot, 'Variations of diffusion coefficients of redox active molecules in room temperature ionic liquids upon electron transfer', *J. Phys. Chem. B* **2008**, *112*, 14952-14958.

[102] O. Fontaine, C. Lagrost, J. Ghilane, P. Martin, G. Trippé, C. Fave, J. C. Lacroix, P. Hapiot, H. N. Randriamahazaka, 'Mass transport and heterogeneous electron transfer of a ferrocene derivative in a room-temperature ionic liquid', *J. Electroanal. Chem.* **2009**, *632*, 88-96.

[103] A. A. Kornyshev, N. B. Luque, W. Schmickler, 'Differential capacitance of ionic liquid interface with graphite: the story of two double layers', *J. Solid State Electrochem.* **2014**, *18*, 1345-1349.

[104] M. T. Alam, M. M. Islam, T. Okajima, T. Ohsaka, 'Capacitance measurements in a series of room-temperature ionic liquids at glassy carbon and gold electrode interfaces', *J. Phys. Chem. C* **2008**, *112*, 16600-16608.

[105] M. M. Islam, M. T. Alam, T. Okajima, T. Ohsaka, 'Electrical double layer structure in ionic liquids: an understanding of the unusual capacitance−potential curve at a nonmetallic electrode', *J. Phys. Chem. C* **2009**, *113*, 3386-3389.

[106] C. Larriba, Y. Yoshida, J. Fernández de la Mora, 'Correlation between surface tension and void fraction in ionic liquids', *J. Phys. Chem. B* **2008**, *112*, 12401-12407.

[107] M. Lozynski, J. Pernak, Z. Gdaniec, B. Gorska, F. Béguin, 'Proof of ion-pair structures in ammonium-based protic ionic liquids using combined NMR and DFT/PCM-based chemical shift calculations', *Phys. Chem. Chem. Phys.* **2017**, *19*, 25033-25043.

[108] H. Kawarada, 'Hydrogen-terminated diamond surfaces and interfaces', *Surf. Sci. Rep.* **1996**, *26*, 205-259.

[109] J. Ristein, in *Semiconductors and Semimetals, Vol. 77* (Eds.: C. E. Nebel, J. Ristein), Elsevier, **2004**, pp. 37-96.

[110] G. Janssen, W. J. P. Van Enckevort, W. Vollenberg, L. J. Giling, 'Characterization of single-crystal diamond grown by chemical vapour deposition processes', *Diam. Relat. Mater.* **1992**, *1*, 789-800.

[111] N. R. Wilson, S. L. Clewes, M. E. Newton, P. R. Unwin, J. V. Macpherson, 'Impact of grain-dependent boron uptake on the electrochemical and electrical properties of polycrystalline boron doped diamond electrodes', *J. Phys. Chem. B* **2006**, *110*, 5639-5646.

[112] B. V. Spitsyn, L. L. Bouilov, B. V. Derjaguin, 'Vapor growth of diamond on diamond and other surfaces', *J. Cryst. Growth* **1981**, *52*, 219-226.

[113] S. Wang, G. M. Swain, 'Spatially heterogeneous electrical and electrochemical properties of hydrogen-terminated boron-doped nanocrystalline diamond thin film deposited from an argon-rich $CH_4/H_2/Ar/B_2H_6$ source gas mixture', *J. Phys. Chem. C* **2007**, *111*, 3986-3995.

[114] J. Li, C. L. Bentley, S.-y. Tan, V. S. S. Mosali, M. A. Rahman, S. J. Cobb, S.-X. Guo, J. V. Macpherson, P. R. Unwin, A. M. Bond, J. Zhang, 'Impact of sp^2 carbon edge effects on the electron-transfer kinetics of the ferrocene/ferricenium process at a boron-doped diamond electrode in an ionic liquid', *J. Phys. Chem. C* **2019**, *123*, 17397-17406.

[115] 'A random walk through electron-transfer kinetics', *Anal. Chem.* **2005**, *77*, 214 A-220 A.

[116] C. Lagrost, D. Carrié, M. Vaultier, P. Hapiot, 'Reactivities of some electrogenerated organic cation radicals in room-temperature ionic liquids: toward an alternative to volatile organic solvents?', *J. Phys. Chem. A* **2003**, *107*, 745-752.

[117] L. Xiao, E. J. F. Dickinson, G. G. Wildgoose, R. G. Compton, 'A comparison of electron transfer kinetics of three common carbon electrode surfaces in acetonitrile and in room temperature ionic liquid 1-butyl-3-methylimidiazonium hexafluorophosphate: correlation to surface structure and the limit of the diffusion domain approximation', *Electroanalysis* **2010**, *22*, 269-276.

[118] J. S. Long, D. S. Silvester, A. S. Barnes, N. V. Rees, L. Aldous, C. Hardacre, R. G. Compton, 'Oxidation of several p-phenylenediamines in room temperature ionic liquids: estimation of transport and electrode kinetic parameters', *J. Phys. Chem. C* **2008**, *112*, 6993-7000.

[119] S. R. Belding, N. V. Rees, L. Aldous, C. Hardacre, R. G. Compton, 'Behavior of the heterogeneous electron-transfer rate constants of arenes and substituted anthracenes in room-temperature ionic liquids', *J. Phys. Chem. C* **2008**, *112*, 1650-1657.

CHAPTER 4. EFFECT OF ROOM TEMPERATURE IONIC LIQUID ON THE CAPACITANCE AND HETEROGENEOUS ELECTRON-TRANSFER KINETICS FOR FERROCENE DERIVATIVES AT BORON-DOPED NANOCRYSTALLINE DIAMOND THIN-FILM ELECTRODES

4.1. Abstract

Studies were performed to investigate how the room temperature ionic liquid (RTIL) composition affects the potential-dependent capacitance and heterogeneous electron-transfer rate constant for three ferrocene derivatives at boron-doped nanocrystalline diamond thin-film electrodes. The electrode morphology and microstructure were probed by scanning electron microscopy (SEM) and Raman spectroscopy, respectively. Apparent heterogeneous electron transfer rate constants (k^o_{app}) were determined for ferrocene, ferrocene methanol, and ferrocene carboxylic acid in three homologous room temperature ionic liquids: 1-ethyl-3-methylimidazolium tetrafluoroborate ([EMIM][BF_4]), 1-butyl-3-methylimidazolium tetrafluoroborate ([BMIM][BF_4]), and 1-hexyl-3-methylimidazolium tetrafluoroborate ([HMIM][BF_4]). The k^o_{app} values and diffusion coefficients both decreased with increased RTIL viscosity (η). The diffusion coefficient and k^o_{app} ranged from 10^{-7}-10^{-9} cm^2 s^{-1} and 10^{-4}-10^{-5} cm s^{-1}, respectively, for the ferrocene derivatives across the three RTILs. Capacitance values ranged from 6 to 12 μF cm^{-2} in three RTILs over a potential range from -1 and 1 V vs. Ag QRE and were independent of the ionic liquid composition indicating that changing the cation size and symmetry does not significantly affect the volume in which the counterbalancing ion excess exists on the solution side of the interface. At least for these redox systems and the three RTILs, the most important property affecting k^o_{app} is the RTIL viscosity as opposed to the molecular structure of the cation. The plot of ln k^o_{app} vs. ln η was linear with a slope of -1 indicating that solvent dynamics control the rate of electron transfer (*i.e.*, reorganization of RTIL ions around the redox molecule

upon electron transfer). Some material characterization data are presented as are some control electrochemical measurement data in an aqueous electrolyte solution.

4.2. Introduction

Carbon materials (sp^2-bonded) have been extensively studied as electrodes for electrosynthesis, electroanalysis and electrochemical energy conversion and storage over the years.[1-5] Their low cost, rich surface chemistry, chemical stability, wide potential window and compatibility with most solvents and electrolyte salts make carbon materials attractive for electrochemical applications. There are multiple variables that affect electron-transfer kinetics for soluble redox systems at these electrodes including carbon electrode type, past history of use, surface cleanliness, exposed microstructure, and surface chemistry. The structure-function relationship of sp^2 carbon electrodes has been extensively studied over the years and there is a good understanding of the relationship between the particular redox system, its redox reaction mechanism, and the electrode variables that are most influential in terms of the heterogeneous electron-transfer rate constant (k^o) in aqueous electrolyte solutions. [1,2,6-10]

Our group studies sp^3 carbon electrodes with a goal of understanding the factors that influence k^o for different redox analytes in aqueous[11-13] and organic electrolytes. [14] Boron-doped diamond and nitrogen-incorporated tetrahedral amorphous (t*a*-C:N) carbon thin-film electrodes are the two sp^3 carbon materials under study. Boron-doped diamond can be prepared as a microcrystalline, nanocrystalline, or ultrananocrystalline thin film. The former two diamond film types are prepared by microwave-assisted chemical vapor deposition using a hydrogen-rich CH_4/H_2 source gas mixture.[15-17] The ultrananocrystalline terminology is generally reserved for films prepared using an argon-rich, CH_4/Ar source gas mixture. [18-21] Generally speaking, as long as the films are highly boron doped to impart a high level of electrical conductivity (>10 S cm^{-1}),

all three exhibit similar electrochemical behavior toward soluble redox systems in aqueous electrolyte solutions. [22-24]

Boron-doped diamond (BDD) electrodes exhibit attractive properties for electrochemical applications including (i) a wide working potential window, (ii) low voltammetric background current, (iii) microstructural stability at extreme positive and negative potentials and high current densities, (iv) a low oxygen surface after preparation but one that is easily modified, (v) weak molecular adsorption, and (vi) optical transparency. [25-30] Much has been learned about structure-function relationships of these carbon electrodes for redox systems in aqueous[25-30] and non-aqueous electrolytes. [14,31,32] However, much less is known about how factors such as the electrode microstructure, surface chemistry, etc. affect k^o values for soluble redox systems in room temperature ionic liquids (RTILs). We contribute to this knowledge gap with the work reported herein.

RTILs possess a combination of properties (*e.g.*, high charge density, no solvent, electrochemical stability, low volatility) that make them interesting for fundamental study and for electrochemical applications. [33-38] The properties of RTILs, their behavior at electrified interfaces, and their role in heterogeneous redox reactions have been discussed in several recent papers. [33-38] Electrochemical applications in solar cells[39], electrochemical sensors,[40] fuel cells, [41] lithium batteries[42], and supercapacitors[43] have been reported.

Neat RTILs contain no dielectric solvent, unless one is intentionally added or water impurity is absorbed from the environment. They are salts with melting points near or below room temperature. The constituent cations are typically large, asymmetrically shaped and organic (*e.g.*, alkyl imidazolium) species while the anions are typically more symmetrically shaped and

inorganic (*e.g.,* tetrafluoroborate, BF_4^-).[33-38] The judicious choice of cation and anion can be used to tailor the viscosity or the formation of local heterogeneities in the liquid phase. [33-35]

There are two practical issues when using RTILs in electrochemical applications. First, the high viscosity and therefore the low diffusion coefficient of redox analytes reduces the rate of mass transfer. Second, the absence of a dielectric screening solvent means that there will be strong electrostatic interactions between ionic liquid cations and anions, and a charged redox system. The latter can be a cause for large reorganization energies (*i.e.*, solvent dynamics), large standard free energies of activation ($\Delta G^{\ddagger}$), and slow electron-transfer kinetics (k^o).[34] Other key issues to consider with RTILs in electrochemical applications are (i) the interfacial organization of the RTIL cation and anion excesses at a potential-controlled electrode surface that ultimately control the potential drop at the plane of closest approach or the driving force for the electron transfer, (ii) the reorganization energy, and (iii) the work terms that control the concentrations of oxidized (for the cathodic current) and reduced (for the anodic current) species at the plane of closest approach.

Herein, we report on the potential-dependent capacitance, the apparent heterogeneous electron-transfer rate constant (k^o_{app}), and diffusion coefficient (D) for ferrocene (Fc), ferrocene methanol (FcMeOH), and ferrocene carboxylic acid (FCA) in 1-ethyl-3-methylimidazolium tetrafluoroborate ([EMIM][BF_4]), 1-butyl-3-methylimidazolium tetrafluoroborate ([BMIM][BF_4]), 1-hexyl-3-methylimidazolium tetrafluoroborate ([HMIM][BF_4]) at nanocrystalline BDD electrodes. The three RTILs have cations with the same core structure but with different alkyl chain lengths. The viscosity of RTILs increases with the size of alkyl chain substituent because of the enhanced van der Waals interactions. [33-35] We selected these redox systems because they can be dissolved and undergo heterogeneous electron-transfer in RTILs. Furthermore, there is some literature reporting on k^o values for various ferrocene derivatives in a

variety of RTILs at metal and carbon electrodes including BDD.[44-56] The apparent heterogeneous electron-transfer rate constants (k^o_{app}) were determined using the cyclic voltametric peak separation-scan rate (ΔE_p-v) trends using the so-called "Nicholson method" and through computer-simulated fits of the experimental voltammetric data.

4.3. Experimental

Boron-Doped Diamond (BDD) Thin Films Deposited on Si. The BDD thin film was deposited on a boron-doped Si (111) substrate (~10^{-3} ohm-cm) by microwave-assisted chemical vapor deposition (CVD). A 1.5 kW reactor from Seki Diamond Systems (Japan) (formerly ASTeX) was used for the diamond growth. Prior to growth, the Si substrate was ultrasonically cleaned in acetone for 15 min, hand-scratched in diamond powder (100 nm diam.) slurried in ultrapure water for 3 min on a felt pad, rinsed with ultrapure water, and then ultrasonically seeded with nanodiamond particles (Opal Seed, Adamas Nanotechnologies Inc., Raleigh, NC). Opal Seed consists of nominally 30 nm nanodiamond powder particles suspended in dimethyl sulfoxide (DMSO). After seeding in a glass beaker, the substrate was rinsed with ultrapure water in the beaker and then dried with N_2 gas before placement in the CVD reactor chamber. The scratches introduced and the embedded diamond power particles serve as initial nucleation sites for diamond film growth.

For the BDD thin film growth, a 1% methane (CH_4)/hydrogen (H_2) source gas mixture was employed with 10 ppm of diborane (B_2H_6) added for boron doping. A total gas flow of 200 sccm was used (2.00 sccm CH_4, 2.00 sccm B_2H_6 in H_2, and 96.0 sccm H_2). The microwave power was 800 W and the system pressure was 35 torr. The substrate temperature during the deposition was on the order of 825 ^oC, as estimated with a disappearing-filament optical pyrometer. These deposition conditions produced a diamond film 2-4 μm thick during a growth time of 4-6 h. The

boron doping level was in the low 10^{21} cm^{-3} range, based on Raman spectroscopic and electrical measurement data for other diamond films prepared using similar conditions. [56] The electrical resistivity was ≤ 0.01 ohm-cm. The BDD films were considered to be low in surface oxygen as they were hydrogen plasma treated initially and during use.

At the end of the deposition period, the CH_4 and B_2H_6 flows were stopped while the H_2 flow continued with the plasma still ignited. The specimen was then cooled in the presence of atomic hydrogen formed in the plasma by slowly lowering the microwave power and system pressure over a 30-min period to reduce the estimated substrate temperature to below 400 °C. This post-growth cooling is essential for maintaining a hydrogen surface termination and preventing surface reconstruction from an sp^3 to sp^2 hybridization due to surface hydrogen desorption at the higher temperatures.

Visible Raman Spectroscopy. Raman spectroscopy was used to probe the microstructure of the BDD thin films deposited on Si. Raman spectra were recorded using a Renishaw inVia Reflex confocal Raman microscope equipped with a diode-pumped Nd:YAG laser with a frequency doubled excitation wavelength of 532 nm. The focus and position of the laser beam excitation was controlled using a confocal microscope with a motorized stage. The spectral data were recorded and analyzed using WiREInterface software. The parameters controlled by the software were the laser power (10 mW), integration time (3-10 s), spectral range (400-2100 cm^{-1}), and the step size for the line profiles (2 μm). Three spectra were recorded at each location on a specimen and are presented herein as an average spectrum. A Type IIa single-crystal diamond standard (one-phonon line at 1332 cm^{-1}) was used to calibrate the Raman spectrometer before each measurement.

Scanning Electron Microscopy. The BDD thin film morphology was studied using scanning electron microscopy (SEM). Electron micrographs were recorded using two different field-emission electron microscopes (JEOL 6610LV and JEOL 7500F (Ltd., Tokyo, Japan)) at the Center of Advanced Microscopy, Michigan State University. Secondary electrons from the specimen were used for imaging at magnifications from 5000-30,000x. Micrographs were generated using an accelerating voltage of 5 kV and a working distance of 4-6 mm.

Statistical Data Analysis. Electrochemical experiments were performed using at least three different BDD electrodes. The data are reported as mean ± standard deviation. The Student's t-test and one-way analysis of variance (ANOVA) were used to determine statistically significant differences among the mean values assuming the null hypothesis. p-values ≤ 0.05 were considered statistically significant.

Electrochemical Measurements in Room Temperature Ionic Liquids. All electrochemical measurements using the RTILs were performed in a continuously N_2-purged vinyl glove box (Coy Laboratories, Grass Lake, MI). The relative humidity in the box was measured to be $\leq 0.1\%$ using a hygrometer. The BDD working electrode was clamped to the bottom of a single compartment glass electrochemical cell. [12] An o-ring with an area of 0.2 cm^2 was placed between the bottom of the glass cell and the working electrode to define the geometric electrode area exposed to the solution. The backside of the conducting Si substrate was lightly scratched using a polishing pad to remove the oxide layer. A layer of graphite from a pencil was then applied to the abraded and cleaned substrate. Electrical connection was made to the substrate with a clean copper plate current collector. The BDD electrodes were pretreated before use by exposing the surface to ultraclean isopropanol (distilled and stored over activated carbon) for 20-30 min. For all electrochemical measurements in RTILs, a Pt wire was used as the counter

electrode. An Ag wire served as the quasi-reference electrode (Ag QRE). Approximately 1 mL of purified RTIL was used in an electrochemical measurement. The RTIL was additionally deaerated in the cell by argon gas purging for 10 min before each measurement. argon gas blanketed the RTIL during an electrochemical measurement in the N_2-purged glove box.

Electrochemical Measurements in Aqueous Electrolyte. Electrochemical measurements were made in the same single compartment glass cell in the laboratory ambient. A graphite rod was used as the counter electrode and a homemade Ag/AgCl electrode served as the reference. Aqueous electrolyte solutions (1 mol L^{-1}) were deaerated with nitrogen gas purging for 10-20 min before and blanketed with the gas during a measurement.

Cyclic Voltammetry Measurements. Cyclic voltammetry (CV) was performed using a computer-controlled potentiostat (Model 650B or 650A, CH Instruments Inc., Austin, TX). Voltammograms were recorded as a function of the scan rate (0.1 to 0.5 V s^{-1}). The double-layer capacitance, C_{dl} (μF cm^{-2}), was calculated from the slope of background current density (j, A cm^{-2}) *vs.* scan rate (v, V s^{-1}) plots for different applied potentials using equation [1],

$$j = C_{dl}v \quad [1]$$

The apparent heterogeneous electron transfer rate constant (k^o_{app}) was calculated from cyclic voltammetric ΔE_p-υ data, known as Nicholson method, using equation [2][57],

$$k^o = \psi \frac{[\pi D_{ox} \upsilon (nF/RT)]^{1/2}}{(D_{ox}/D_{red})^{\alpha/2}} \quad [2]$$

in which D_{ox}, D_{red}, v, n, R, T, F, α are diffusion coefficients of the oxidized and reduced species (cm^2 s^{-1}), scan rate (V s^{-1}), number of electrons transferred per molecule, ideal gas constant, temperature (T), Faraday's constant, and the transfer coefficient, respectively. ψ is the

dimensionless kinetic parameter determined from the cyclic voltametric ΔE_p and can be calculated using equation [3] in which X is the $n\Delta E_p$ value. [58]

$$\psi = \frac{(-0.6288+0.0021\,X)}{(1-0.017\,X)} \quad [3]$$

Experimental cyclic voltammetric curves were also matched with computer simulated curves using Digisim® (version 3.03) software to determine the heterogeneous electron-transfer rate constant (k^o_{sim}). The k^o and α values as well as D_{red} and D_{ox} were varied to match the simulated with the experimental curve shapes and peak currents. The ΔE_p value and peak currents were used as the main criterion for a successful fit.

Electrochemical Impedance Spectroscopy (EIS). Electrochemical impedance spectroscopy (EIS) was performed using a computer-controlled potentiostat (Model 650A or 650B, CH Instruments Inc., Austin, TX). EIS was carried out at different applied potentials from -1.0 to 1.0 V vs. Ag QRE using a range of frequencies from 10^5 to 10^{-1} Hz. Twelve data points were collected per frequency decade. A sine wave (10 mV amplitude) was co-added to each DC potential. An equilibration time of 300 s was allotted before collecting the impedance data at each applied potential. The resultant impedance data were subjected to a fitting procedure using the model equivalent circuit shown in Figure 4.1. The full frequency EIS data were fit using ZView® 3.5h software.

In the model circuit, R_s represents the combined bulk electrolyte, electrode, and electrical contact ohmic resistance. R_p is the polarization resistance. A constant phase element (CPE) was used in place of a capacitor to describe the quasi-capacitive character of the electric double layer at the heterogeneous electrode surface.[59] The impedance of the CPE is given in equation [4],

$$Z_{CPE} = \frac{1}{Q(j\omega)^n} \quad [4]$$

in which Q is the quasi-capacitance, n is the so-called homogeneity factor (n = 1 for an ideal capacitor), ω is the angular frequency, and j is the imaginary number. The quasi-capacitance, Q, has no physical meaning; however, the effective capacitance, C_{eff}, in farads may be calculated from Q using the surface distribution function proposed by Hirschorn et al. [60]

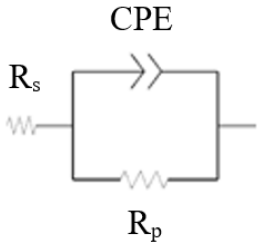

Figure 4.1. The representative model electrical equivalent circuit used to fit the full frequency impedance data.

Equation 5 was used to calculate C_{eff} at each potential.

$$C_{eff} = \left(\frac{R_s R_p}{R_s + R_p}\right)^{\frac{1-n}{n}} Q^{\frac{1}{n}} \quad [5]$$

C_{eff} was divided by the geometric area (0.2 cm^2) of the o-ring to obtain the normalized capacitance values presented in the paper.

Reagents for Electrochemical Measurements in Aqueous Electrolytes. Potassium chloride, CAS: 7447-40-7 and potassium hexacyanoferrate(II) trihydrate ($[K_4Fe(CN)_6 \cdot 3H_2O]$), CAS: 14459-95-1 were obtained from Sigma-Aldrich and used without additional purification.

Reagents for Electrochemical Measurements in RTILs. The RTILs used, 1-ethyl-3-methylimidazolium tetrafluoroborate ($[EMIM][BF_4]$), CAS: 143314-16-3, 1-butyl-3-methylimidazolium tetrafluoroborate ($[BMIM][BF_4]$), CAS: 174501-65-6, and 1-hexyl-3-methylimidazolium tetrafluoroborate ($[HMIM][BF_4]$), CAS: 244193-50-8), 1-ethyl-3-

methylimidazolium bis(trifluoromethylsulfonyl)imide ([EMIM][TFSI], CAS: 174899-82-2), 1-butyl-3-methylimidazolium bis(trifluoromethylsulfonyl)imide ([BMIM][TFSI], CAS: 174899-83-3), and 1-hexyl-3-methylimidazolium bis(trifluoromethylsulfonyl)imide ([HMIM][TFSI], CAS:382150-5-7) were purchased commercially from IoLiTec Technologies (Germany) and specified as ≥ 98% purity. Ferrocenecarboxylic acid (CAS: 1271-42-7, 97%), ferrocene (CAS: 102–54-5, 98%), and ferrocenemethanol (CAS: 1273-86-5, 97%) were purchased commercially (Sigma Aldrich), and used as received.

Purification of the RTILs. The RTILs were purified to remove water and other impurities using a pretreatment method described previously. [61-63]

1. The "as-received" RTIL was stored over activated carbon for at least 14 days. This step removes organic impurities via adsorption onto the carbon. The RTIL was then carefully removed using a syringe through a 0.45 μm Teflon filter (Millex®HA) and transferred into a clean and capped glass vial.

2. The filtered RTIL was then stored over activated molecular sieves (5Å) (ThermoFisher Scientific) in the capped glass vial for at least one week to remove water impurity. The molecular sieves were activated before use by heating at ~400 ^{o}C in a furnace for two weeks.

3. A small volume of the purified RTIL was then transferred to a clean and dry glass vial in a nitrogen-purged vinyl glove box (Coy Laboratories, Grass Lake, MI) and then was heated at ~70 ^{o}C for 50 min while being purged with ultra-high purity Ar (Airgas).

4. At this point, the RTIL was transferred to the electrochemical cell for a measurement. The heated argon gas purging of the RTIL was also sometimes performed directly in the electrochemical cell.

After this purification procedure, the water level in selected RTIL samples was found to be below 100 ppm based on thermogravimetric analysis mass loss data. The mass loss upon heating to 300 ºC was assumed to be all volatilized water impurity. All cleaned glassware was rinsed with ultrapure water, rinsed with ultrapure isopropanol, and then dried in the oven overnight before being transferred to the glove box for use in the RTIL experiments. For samples measured for water impurity content, the measurements were always made before any electrochemical measurements in the glove box. The ultrapure water used for glassware cleaning was prepared using a Barnstead E-pure System (ThermoFisher Scientific). The ultrapure water had an electrical resistivity ≥17 MΩ-cm.

A solution containing a ferrocene derivative redox system dissolved in an RTIL was prepared according to the following procedure: [62,63]

1. A solution of the redox system at the desired concentration was prepared volumetrically using ultraclean isopropanol (distilled and stored over activated carbon) (≥ 99.5, CAS No. 67-63-0, purchased from Sigma Aldrich) as the solvent.

2. A quantitative volume of this stock solution containing the dissolved redox system was then transferred to a clean 1 mL voltammetric flask.

3. The volumetric flask was then placed in the oven to completely evaporate the isopropanol (~1h, 100 ºC). The flask containing the solid residual ferrocene compound was then transferred to the vinyl glove box.

4. The desired RTIL was then added to the flask and filled to the mark to redissolve the ferrocene derivative achieving the desired concentration of 1 mmol L^{-1}.

5. The RTIL solution containing the redox system was stirred for at least 12 h before use in an electrochemical measurement.

Physical Properties of the RTILs. Figure 4.2 shows the molecular structure of three RTILs used. The physical properties of the RTILs, as specified by the supplier, are listed in Table 4.1.

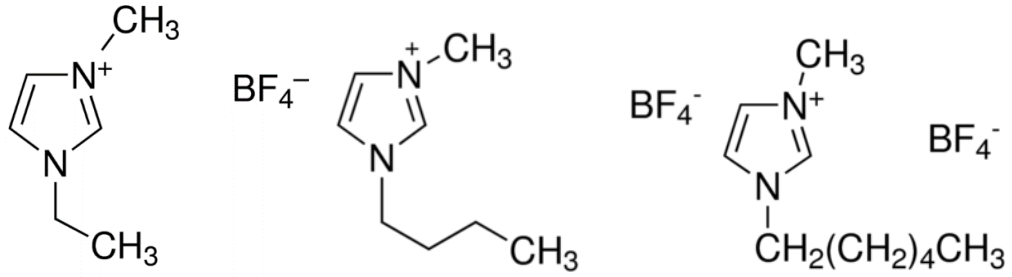

[EMIM][BF_4] [BMIM][BF_4] [HMIM][BF_4]

Figure 4.2. Molecular structures of the alkyl imidazolium RTILs used.

Table 4.1. Physical properties of water, [EMIM][BF_4], [BMIM][BF_4], and [HMIM][BF_4] at 25 °C.

Analyte	Mol. Wt. (g mol^{-1})	Viscosity (cP)	Conductivity (mS cm^{-1})	Dielectric Constant	Density (g cm^{-3})
[EMIM][BF_4]	197.97	34*	14.1*	12.9	1.28*
[BMIM][BF_4]	226.02	104*	3.2*	9.7	1.30*
[HMIM][BF_4]	254.08	288*	1.2*	8.4	1.15*

*Data were provided by the chemical supplier, IoLiTec Technologies. The reported dielectric constants for the three RTILs were obtained from ref. 64.

4.4. Results

4.4.1. Characterization of BDD Electrodes

Figure 4.3A and B show SEM micrographs of one BDD thin-film electrode used in this work. All the electrodes used possessed a similar morphology. The micrographs reveal the presence of a continuous nanocrystalline film over the substrate surface. The film consists of faceted and randomly-oriented crystallites with a size in the range of 0.5 to 1 μm. There are no voids, pinholes or other defects observed in the film.

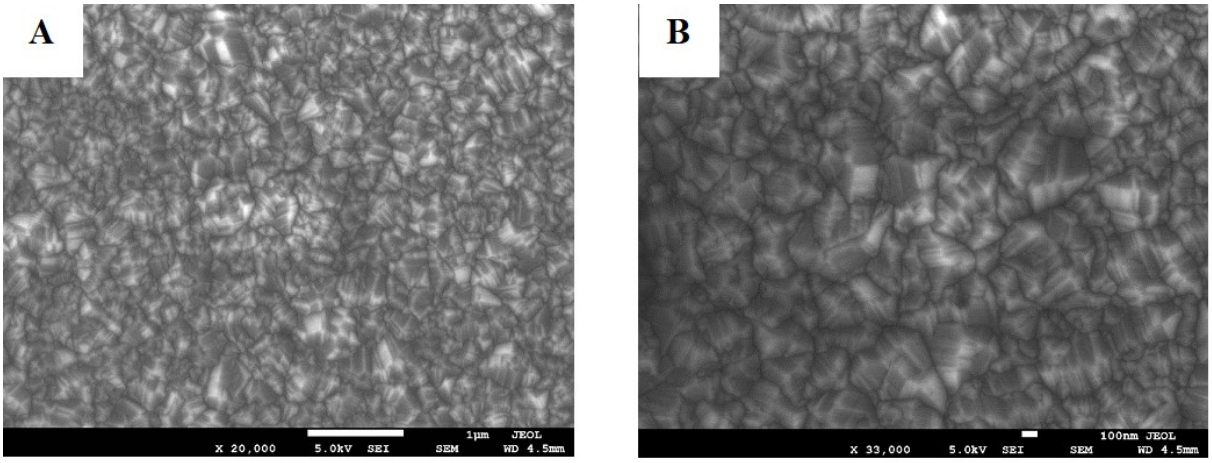

Figure 4.3. SEM micrographs of a typical BDD thin-film electrode at two different magnifications: (A) 1 μm scale bar (20,000X, 5.0 kV, and WD = 4.5 mm) and (B) 100 nm scale bar (33,000X, 5.0 kV, and WD = 4.5 mm). WD = working distance.

Figure 4.4 presents Raman spectra (visible excitation) for one BDD thin-film electrode used in this work. Similar spectra were recorded for all the electrodes used. Figure 4.4A shows an individual spectrum with peaks at 518, 1224, 1328, and 1497 cm^{-1}. [56,65,66] The peak at 1328 cm^{-1} is the first-order optical phonon of diamond. The expected position for this phonon mode is 1332 cm^{-1} as is observed for single crystal diamonds. [67] For heavily boron-doped films (> 10^{20} cm^{-3}), the peak intensity is reduced, the peak shifts toward lower wavenumbers due to the increased boron substitution within the diamond lattice, the linewidth broadens, and the peak acquires an

asymmetric Fano lineshape. [68] The Fano lineshape appears at the onset of metallic conductivity through the boron impurity band. With increased boron doping, broad peaks at 500 and 1225 cm^{-1} emerge and tend to track the doping level. [65,66] The presence of these two peaks is consistent with a heavily boron-doped film. The broad band around 500 cm^{-1} has been assigned to vibrational modes of boron dimers[66,69-73] and to clustered boron atoms in the diamond lattice. [55,56,72,74] The sharp peak at 518 cm^{-1} arises from the first-order optical phonon of the crystalline Si substrate. This peak is a component of much broader scattering intensity centered at 500 cm^{-1} arising from the boron atoms. It should be noted that the bands at 500 and 1225 cm^{-1} have been observed for both heavily boron-doped films as well as undoped nanocrystalline diamond powders, so they are not always exclusively linked to boron doping. [69] The 1224 cm^{-1} band has been attributed to a maximum in the phonon density of states arising from scattering by phonons associated with the loss of long-range order in the diamond. These could be related to smaller domains of amorphous sp^3-bonded carbon[69] or possibly high levels of boron incorporation that disrupt the lattice during growth. [70] The broad peak at 1497 cm^{-1} is assigned to scattering by localized domains of sp^2-bonded carbon in grain boundaries or at the interface between the diamond and the Si. [65,66] The weak peak at *ca.* 1000 cm^{-1} is the second-order phonon for the Si substrate. Since the diamond film is relatively thin, the laser light penetrates through to the substrate and the 518 and 1000 cm^{-1} peaks appear in the spectrum. Figure 4.4B shows a series of Raman spectra recorded along a line profile across the film. The spectral pattern is uniform across the profile indicating a uniform microstructure spatially. Similar line spectral patterns were recorded at different locations for all three BDD films used in this work. The Raman spectra provide evidence for the presence of a uniform, heavily boron-doped diamond film across the substrate with a nanocrystalline morphology. [56,69,71-73]

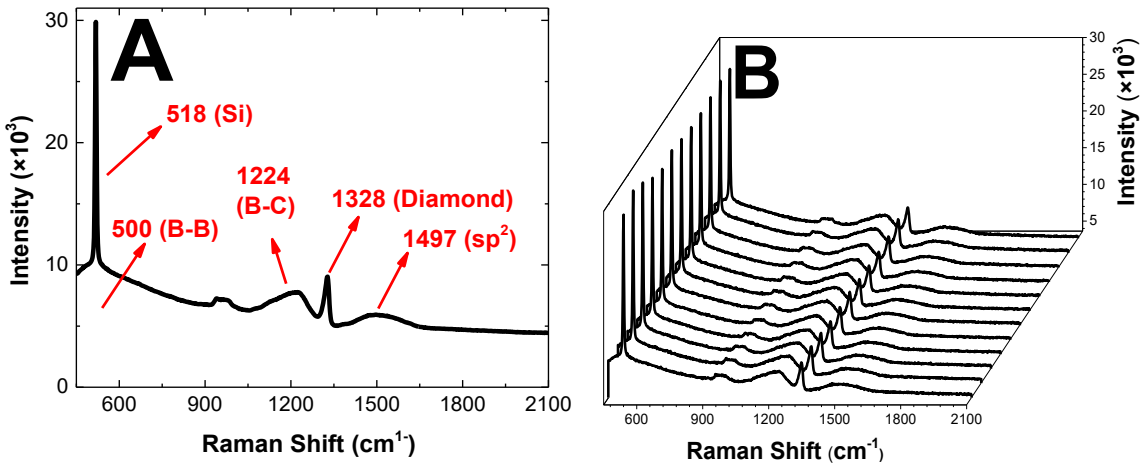

Figure 4.4. (A) An individual visible Raman spectrum for a typical nanocrystalline BDD thin-film on Si. (B) Series of visible Raman spectra recorded along a line profile across the nanocrystalline film. Integration time = 3 s. Excitation wavelength = 532 nm. Twelve spectra are presented that were recorded along the 139 μm linear distance.

4.4.2. Working Potential Window, Voltammetric Background Current, and Double-Layer Capacitance

The three RTILs consist of the same counter anion and cations with the same core structure (3-methylimidazolium), but with different substituent alkyl chain lengths (n= 2, 4, and 6). [HMIM][BF_4], [BMIM][BF_4], and [EMIM][BF_4] are about 300, 100, and 30x more viscous, respectively, than water. The dielectric constant for [EMIM][BF_4] is slightly larger than [BMIM][BF_4] and [HMIM][BF_4], and all are at least 5x lower than water. All RTILs are slightly more dense than water. [EMIM][BF_4] is the most conducting electrolyte among three RTILs due to the higher mobility of the smaller [EMIM] cation. [75,76]

The working potential window for the BDD thin-film electrodes was recorded in the three RTILs. Figure 4.5 presents cyclic voltametric *i-E* curves for a BDD thin-film electrode. It can be seen that the working potential window is in the 4.7 to 5.1 V range, generally independent of the RTIL type. A current of ± 250 μA cm^{-2} was used to determine the potential limits on the positive-

and negative-going sweeps. The working potential window is defined as the potential range between the oxidation and reduction currents resulting from the electrolysis of the RTIL cation and anion. Two small peaks were observed, one between 1 and 2 V on the positive-going sweep and the other between -1 and -2 V on the negative-going sweep, most notably in [EMIM][BF_4] and [BMIM][BF_4]. The former is attributed to the oxidation of residual water impurity, and the latter is attributed to the reduction of dissolved oxygen not removed by the argon gas purging. [62,63,77]

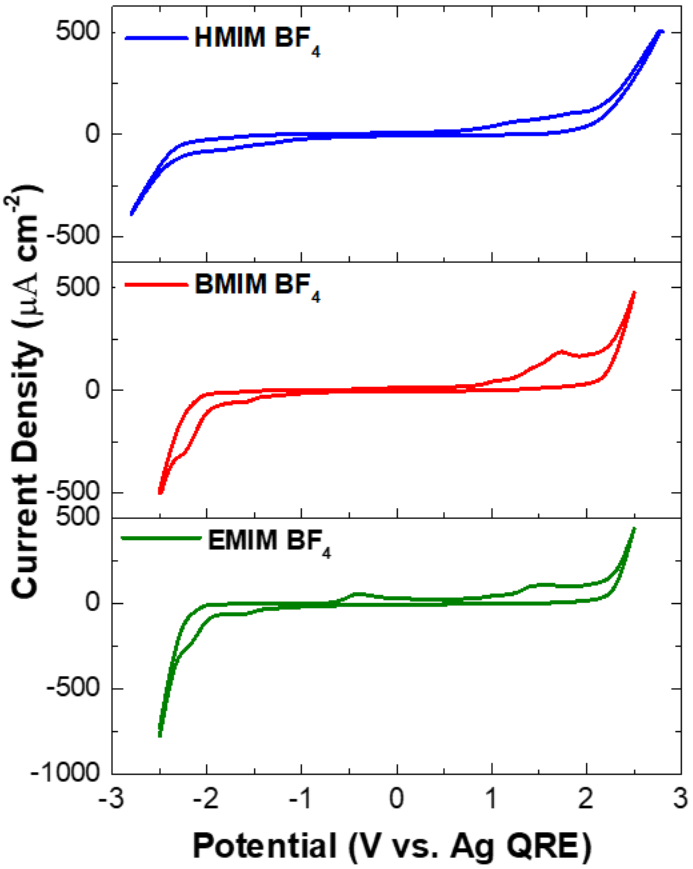

Figure 4.5. Cyclic voltammetric *i-E* curves for a typical BDD thin-film electrode revealing the working potential window in [EMIM][BF_4], [BMIM][BF_4] and [HMIM][BF_4]. Scan rate = 0.1 V s^{-1}.

Figures 4.6A, C and E. show representative cyclic voltammetric background *i-E* curves for each of the RTILs at a BDD thin-film electrode. These curves were recorded over a range of scan rates from 0.1 to 0.5 V s^{-1}. There are no oxidation or reduction peaks present in this more narrow potential range in any of the RTILs. The curve shapes are symmetric about the zero-current line and, importantly, the voltammetric current increases with the scan rate. Figures 4.6B, D, and F show plots of cyclic voltammetric background current versus scan rate recorded at 0.2 V. The currents were measured on the positive-going sweep relative to the zero current line. These plots are linear ($R^2 > 0.999$) with a near-zero y-axis extrapolated intercept, which confirms the current is capacitive in nature at this potential. Similar linear plots were obtained for background currents at multiple potentials within the working potential window. As the excess surface charge at each potential is changed at an increasing rate with scan rate, the RTIL ions on the solution side of the interface can rearrange equally as fast so as to achieve the requisite counterbalancing ion excess needed to maintain charge neutrality in the interface ($Q_{electrode}$ (E) = $-Q_{sol,RTIL}$). One would anticipate that at even higher scan rates than those used in this work, the current would no longer increase linearly with the scan rate as the viscous nature of the RTIL would limit how fast ions and ion pairs could reorient and accumulate the counterbalancing excess at the electrode-RTIL interface. This is reflected, in part, by the increased standard deviation about the mean for the data at the higher scan rates.

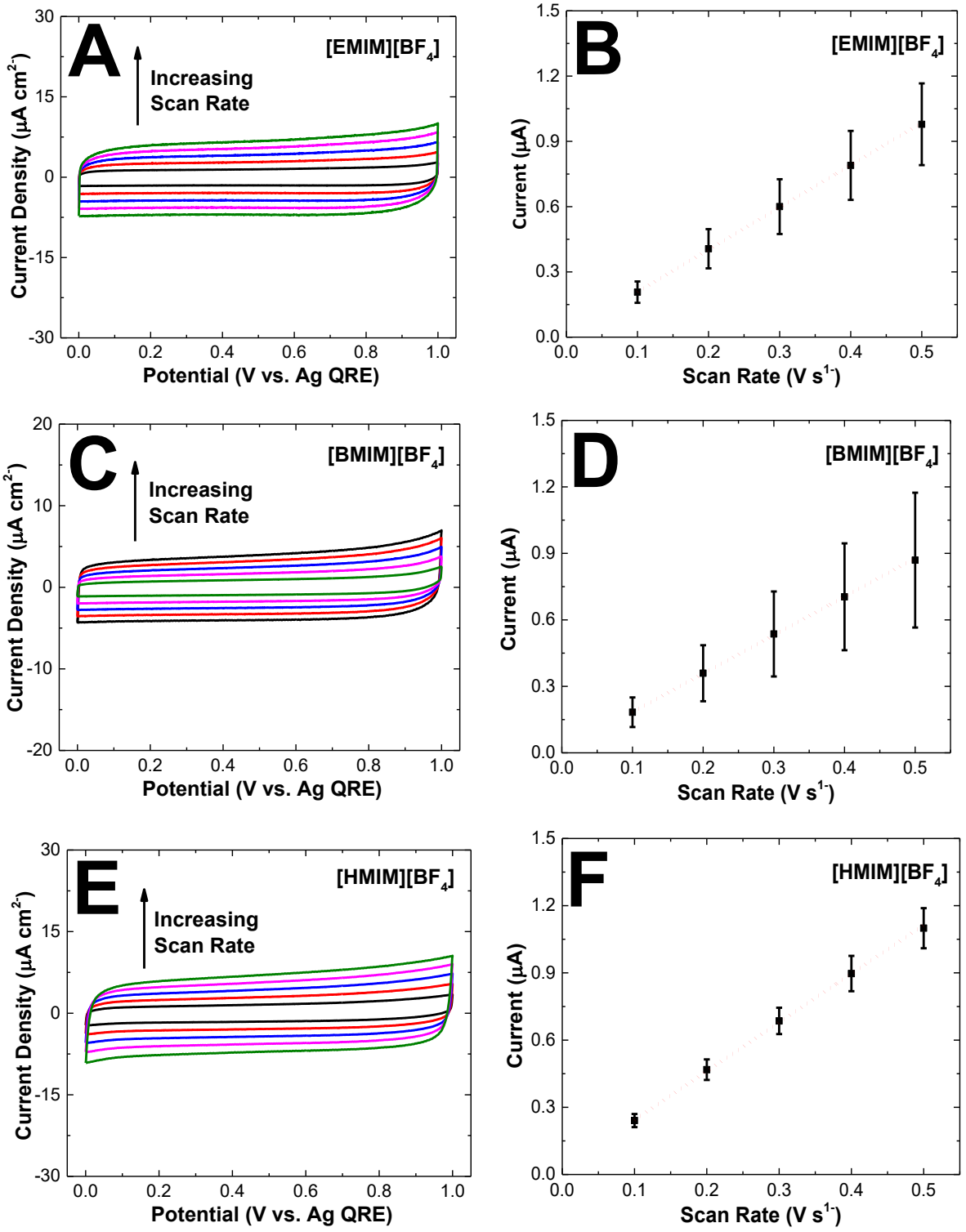

Figure 4.6. Cyclic voltammetric *i-E* curves recorded as a function of the scan rate (0.1- 0.5 V s^{-1}) for a typical BDD thin-film electrode in (A) [EMIM][BF_4], (C) [BMIM][BF_4], and (E) [HMIM][BF_4]. Plots of the cyclic voltammetric background current vs. scan rate at 0.2 V for BDD electrodes in (B) [EMIM][BF_4], (D) [BMIM][BF_4], and (F) [HMIM][BF_4]. Current values are presented as mean ± std. dev. for n = 3 BDD electrodes.

Table 4.2 presents capacitance data for the three RTILs at the BDD thin-film electrodes (N=3). Data are presented for two example potentials; 0.2 and 0.4 V. Capacitance values were calculated from the slope of the cyclic voltammetric current vs. scan rate plots according to equation [1]. The capacitance values are normalized to the geometric area of the electrode exposed to the solution. The supposition is that the background current is exclusively capacitive in nature, so these are accurate and not overestimated capacitance values. The linearity of the background charging current vs. scan rate plots (i_{ch}-υ) plots at these scan rates supports this.

Table 4.2. Capacitance values for BDD thin-film electrodes in [EMIM][BF_4], [BMIM][BF_4], and [HMIM][BF_4] at 0.2 and 0.4 V, as determined from cyclic voltametric data.

RTIL	**Capacitance (μF/cm^2)**	
	E= 0.2 V	**E= 0.4 V**
[EMIM][BF_4]	9.6 ± 1.7	10.5 ± 2.0
[BMIM][BF_4]	8.6 ± 2.9	9.4 ± 3.3
[HMIM][BF_4]	10.7 ± 0.9	12.3 ± 1.3

Data are presented as mean ± standard deviation for n=3 BDD electrodes.

The capacitance values at both potentials are similar in each of the three RTILs. For example, the nominal capacitance at 0.2 and 0.4 V for [EMIM][BF_4] is 9.6 ± 1.7 and 10.5 ± 2.0 μF/cm^2, respectively, which are statistically the same. The capacitance magnitudes for BDD in these three RTILs are consistent with values previously reported for these and other RTILs with reported values ranging from 7-13 μF/cm^2 within this potential range. [63,79-80]

C_{dl}-E data were also generated from voltammetric background charging current-scan rate (i_{ch} - υ) plots for a different set of BDD thin-film electrodes in three additional RTILs at potentials of -0.2, 0.2 and 0.4 V. In [EMIM][TFSI] (η = 39.4 cP), C_{dl} values ranged from 6.2 to 12.2 μF cm^{-}

^{2}. In [BMIM][TFSI] (η = 48.8 cP), C_{dl} values ranged from 5.9 to 9.8 μF cm^{-2}. In [HMIM][TFSI] (η = 63.2 cP), C_{dl} values ranged from 5.5 to 9.3 μF cm^{-2}. There was a general trend of slightly increasing C_{dl} value with increasing positive potential. The take-home message is that the C_{dl} values for BDD electrodes are largely independent of the RTIL composition.

Similar measurements were also performed on the same BDD thin-film electrodes in an aqueous electrolyte solution for comparison. Figure 4.7A shows representative background cyclic voltammetric *i-E* curves in 1 mol L^{-1} KCl. The curves were recorded as a function of the scan rate from 0.1 to 0.5 V s^{-1}. There are no peaks seen in the curves and the current at all potentials increases with scan rate. Plots of the anodic or positive-going current vs. scan rate at 0.2 and 0.4 V are presented in Figures 4.7B and C. The plots are linear (R^2>0.999) indicating the current is capacitive in origin. The slope of this plot was used to calculate the double-layer capacitance. The capacitance for BDD was found to be 15.1 ± 2.2 and 18.0 ± 2.4 μF/cm^2 at 0.2 and 0.4 V, respectively. The values are statistically equivalent. Importantly though, the capacitance of the electrodes in the aqueous electrolyte is 1.5-2x larger than in the RTILs. For a given potential and an excess surface charge at that potential, a greater amount of compensating solvent dipoles and ions accumulate in the interfacial region in aqueous electrolyte solutions than in RTILs due to the smaller size and more spherical shape of the solvated cations and anions. This is the cause for the greater capacitance of the same electrodes in the aqueous electrolyte solution than in the RTILs.

Electrochemical impedance spectroscopy (EIS) was also used to determine the capacitance-potential profiles for BDD thin-film electrodes in the different RTILs and in KCl. Full frequency measurements were made at potentials from -1.0 to 1.0 V vs. Ag QRE. The data were analyzed in the Nyquist format using the model equivalent circuit shown in Figure 4.1 Equation 5, described by Hirschorn *et al*., was used to calculate the effective capacitance, C_{eff}, at each

potential using values for the circuit elements (R_s, R_p and Q) determined from the curve fitting procedure. [60]

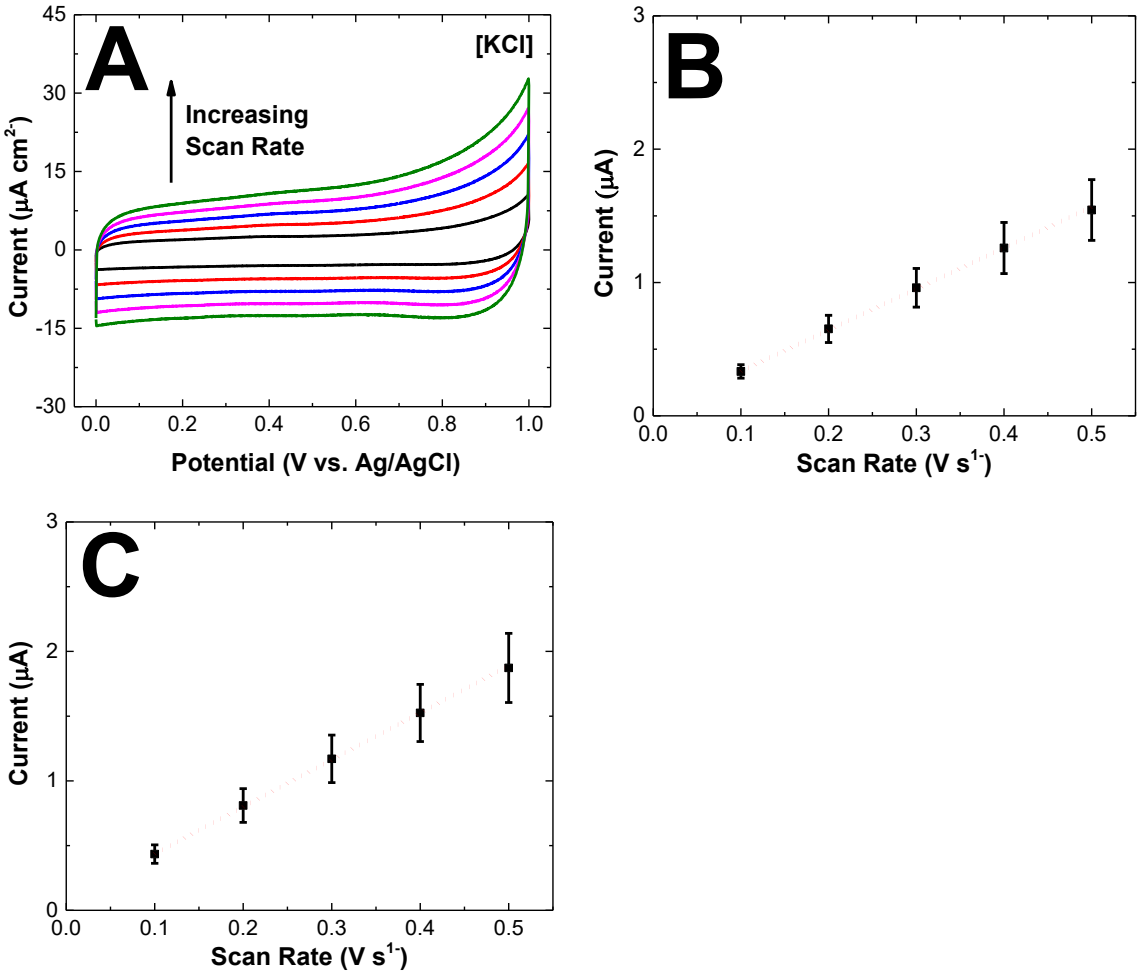

Figure 4.7. (A) Cyclic voltammetric $i-E$ curves recorded as a function of the scan rate (0.1−0.5 V s^{-1}) for BDD electrodes in 1 mol L^{-1} KCl. Plots of the background current vs. scan rate at (B) E= 0.2 V and (C) E= 0.4 V for the electrodes are also presented. Current values are presented as mean ± std. dev. for n = 3 BDD electrodes.

Figures 4.8A and B show C_{dl}-E curves for the BDD electrodes in the three RTILs and in 1 mol L^{-1} KCl, respectively. The reference electrode was Ag QRE in the RTILs and Ag/AgCl in the KCl solution measurements. The capacitance data presented are the calculated C_{eff} values that range from 5.7 to 7.4 μF cm^{-2} in [EMIM][BF_4], 6.6 to 8.4 μF cm^{-2} in [BMIM][BF_4], and 7.5 to 11.6 μF cm^{-2} in [HMIM][BF_4]. In KCl, the values are slightly larger ranging from 10.4 to 16.2 μF

cm^{-2} over the probed potential range. There is a general trend of slightly increasing capacitance with increasing positive potential particularly in [HMIM][BF_4] and KCl. Additionally, the capacitance values obtained from EIS data are in good agreement with values determined from cyclic voltammetric data. Little hysteresis was observed in the C_{dl}-E data for BDD electrodes with direction of the potential change in all three RTILs.

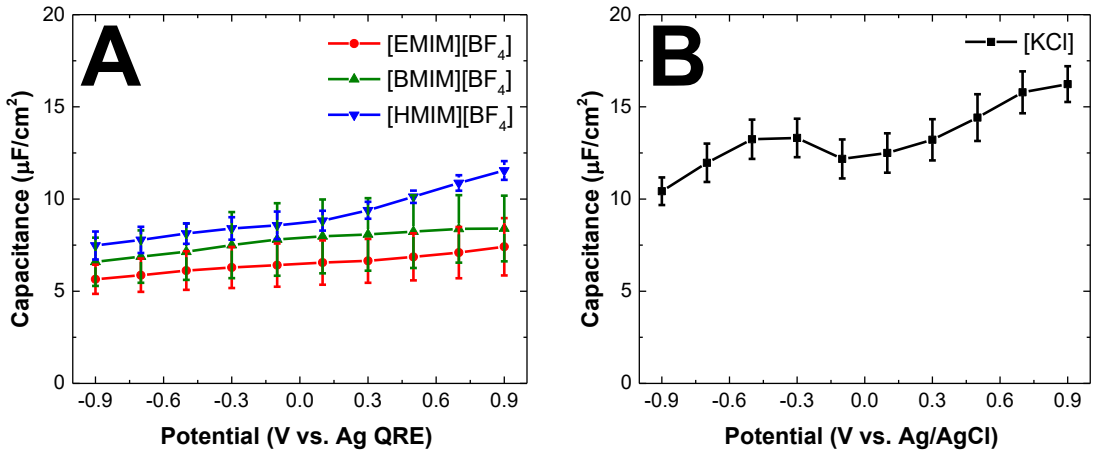

Figure 4.8. Plots capacitance (C_{eff}), calculated from the full frequency EIS data, vs. applied potential for BDD thin-film electrodes in (A) the three RTILs: (red) [EMIM][BF_4], (green) [BMIM][BF_4], and (blue) [HMIM][BF_4], and (B) 1 mol L^{-1} KCl. Data are presented as mean ± standard deviation for three BDD electrodes (n=3). Capacitance values were determined from negative toward positive DC potentials from the EIS data over a frequency range from 10^{-1} to 10^{5} Hz.

The capacitance values are higher in 1 mol L^{-1} KCl than in the three RTILs, consistent with the trends observed using the analyzed cyclic voltammetric data. ANOVA analysis indicated no statistically significant difference in the mean capacitance values in the three RTILs at any of the potentials. In other words, the capacitance magnitude as a function of potential is not affected by the RTIL type (*i.e.*, identity of the organic cation). The shape of C_{dl}-E profiles in the RTILs can vary depending on the type of electrode. For carbon electrodes, like GC and BDD, a flat or U-shape profile is typically observed, like the profiles presented herein. [63,78-83] For metal-based

electrodes, on the other hand, a bell or camel-shape (*i.e.*, curves with two maxima) profiles are routinely observed. [84-86] The flat or slightly U-shaped capacitance profile and the capacitance magnitudes obtained from EIS data are in good agreement with previous reports for BDD electrodes in these and other RTILs. [63,77,81-83] It is noteworthy that the capacitance values calculated from the EIS data are similar to the values determined from the cyclic voltammetric data. Capacitance values for carbon electrodes determined by voltammetry are often higher than the values determined from EIS data because the former is influenced by faradaic current while the latter is not. This is because carbon electrodes often have a faradic component as part of the background voltammetric current arising from the electrochemical activity of carbon-oxygen surface functional groups. [78] BDD electrodes are generally devoid of such redox-active and or ionizable carbon-oxygen functional groups.

4.4.3. Cyclic Voltammetric Behavior of $Fe(CN)_6^{-3/-4}$ in [KCl]

The electrochemical activity of the BDD thin-film electrodes was investigated using potassium ferrocyanide, $Fe(CN)_6^{-3/-4}$, in 1 mol L^{-1} KCl. [11-13,87,88] Our research has shown that even though this redox system can apparently dissolve in RTILs, there is no electrochemical activity observed at GC or BDD electrodes when the water impurity content is low (≤ 100 ppm). Similar inactivity in RTILs is observed for seemingly soluble $Ru(NH_3)_6^{+3/+2}$ and $IrCl_6^{-2/-3}$. As water impurity is titrated in; however, the redox activity of these highly charged redox systems develops in cyclic voltametric measurements. We presume this is because there is a large activation barrier for electron transfer with these redox systems in the RTILs (*e.g.*, large RTIL reorganization energy) low in water impurity due to solvation effects making the heterogeneous electron-transfer rate constant, k^o, low. In the absence of a dielectric screening solvent, a highly organized arrangement of RTIL ions and ion pairs around the $Fe(CN)_6^{-4}$ species is expected. This strong

electrostatically driven organization of RTIL ions would be expected to have a large activation barrier for reorganization around $Fe(CN)_6^{-3}$ upon oxidation.

Figure 4.9A shows representative cyclic voltametric *i-E* curves for 0.1 mmol L^{-1} $Fe(CN)_6^{-3/-4}$ in 1 mol L^{-1} KCl as a function of scan rate from 0.1 to 0.5 Vs^{-1}. This redox system is useful for probing the activity of both sp^2 and sp^3 carbon electrodes because k^o_{app} is quite sensitive to the surface cleanliness, surface chemistry, and microstructure of both sp^2 and sp^3 carbon electrodes. [6-13,87,88] Well-defined oxidation and reduction peak currents are seen at each scan rate. At 0.1 V s^{-1}, the oxidation and reduction peak potentials are 0.360 and 0.210 V vs. Ag/AgCl, respectively. The ΔE_p and midpoint potential, $E_{p/2}$, are 0.150 and 0.285 V, respectively. The oxidation and reduction peak currents are 8.3 and -8.6 μA, respectively. The ratio of oxidation-to-reduction peak currents is approximately one. The increase of ΔE_p with scan rate is consistent with quasi-reversible electron-transfer kinetics. The ΔE_p values are 0.150, 0.174, 0.203, 0.212, and 0.230 V at 0.1, 0.2, 0.3, 0.4, and 0.5 V s^{-1}, respectively. This ΔE_p is larger than the typical value of 65-75 mV seen for as-prepared (low surface oxygen) BDD thin-film electrodes. [87,88] Surface oxygen functional groups are known to inhibit the rate of electron transfer for this redox system at BDD electrodes. However, these electrodes were hydrogen plasma treated prior to the measurements so they should have been low in surface oxygen at the time of the measurements. Therefore, the relatively large 150 mV value seen for this electrode is not attributed to the presence of surface carbon-oxygen functional groups. Figure 4.9B shows plots of the oxidation and reduction peak currents vs. scan $rate^{1/2}$. The plots are linear with the regression coefficients $R^2 > 0.995$. This linearity indicates that the rate of the redox reaction is limited by semi-infinite linear diffusion of the analyte to the electrode surface.

The increase in ΔE_p with increase in scan rate can have two origins: (1) sluggish electron-transfer kinetics at the scan rates and (2) ohmic resistance arising from the equivalent series resistance of the solution, electrode, and electrical contact. Before any electron-transfer kinetic studies can be performed using voltametric data, one must confirm that ohmic resistance is not affecting the cyclic voltametric curve shapes and, therefore, the ΔE_p values. This issue is discussed in the following section.

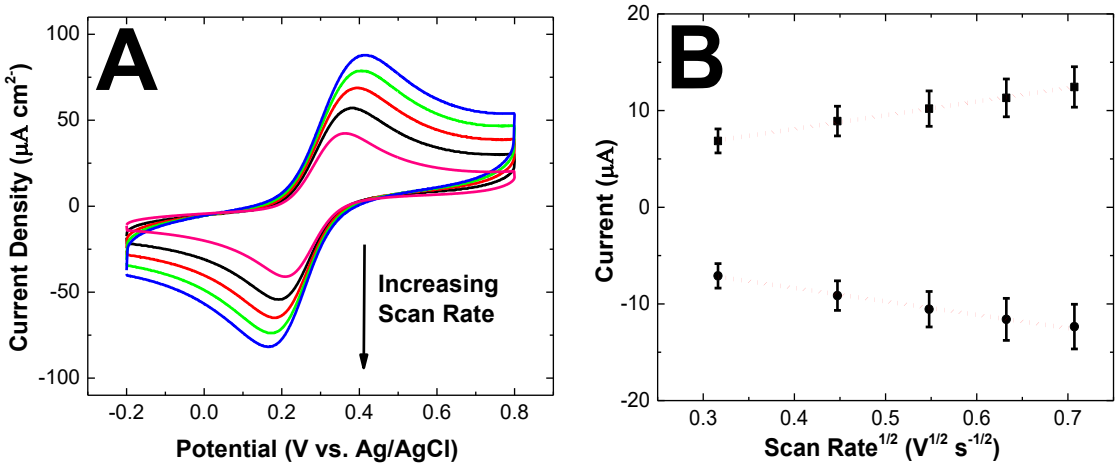

Figure 4.9. (A) Cyclic voltammetric *i-E* curves for 0.1 mmol L^{-1} $Fe(CN)_6^{-3/-4}$in 1 mol L^{-1} KCl recorded as a function of the scan rate from 0.1 to 0.5 V s^{-1} for a BDD thin-film electrode. (B) Plots of the oxidation and reduction peak currents vs. scan rate$^{1/2}$ for BDD thin-film electrodes. Current values are presented as mean ± std. dev. for n = 3 electrodes.

4.4.4. Cyclic Voltammetry of Potassium Ferrocyanide in Potassium Chloride as a Function of Concentration

To assess whether the curve shapes for the BDD electrodes were affected by ohmic resistance, cyclic voltametric *i-E* curves were recorded for $Fe(CN)_6^{-3/-4}$ in 1 mol L^{-1} KCl at various concentrations with the scan rate held constant at 0.1 V s^{-1}. Figure 4.10A shows curves for analyte concentrations of 0.1, 0.3, 0.5, 0.7, and 0.9 mmol L^{-1}. Well-defined oxidation and reduction peaks are seen for all the concentrations. The oxidation and reduction peak currents increase with the

concentration of the analyte, as expected. Importantly, a sign of contributing ohmic resistance effects is the increasing ΔE_p with increasing analyte concentration or increasing current (*i.e.*, greater *iR* curve distortion). For example, ΔE_p at 0.1 V s^{-1} is 150 mV for the 0.1 mmol L^{-1} analyte concentration and 219 mV for the 0.9 mmol L^{-1} concentration. If the equivalent series resistance is not a significant value (a few ohms to a few 10's of ohms), then ΔE_p will be invariant with the concentration at a given scan rate for a diffusion-controlled redox reaction.

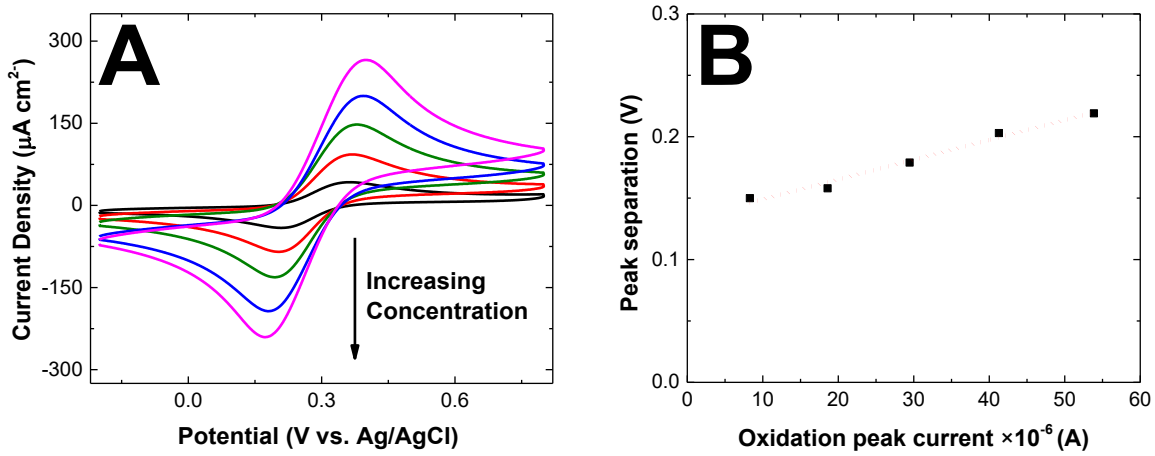

Figure 4.10. (A) Cyclic voltammetric *i*−*E* curves for various concentrations of $Fe(CN)_6^{-3/-4}$ (0.1, 0.3, 0.5, 0.7, 0.9 mmol L^{-1}) in 1 mol L^{-1} KCl recorded at a BDD thin-film electrode. (B) Plot of the peak separation vs. oxidation peak current for the same concentrations of $Fe(CN)_6^{-4}$ at a BDD thin-film electrode with the slope indicating the magnitude of the equivalent series ohmic resistance.

Figure 4.10B shows the plot of ΔE_p vs. the oxidation peak current for various analyte concentrations at a BDD electrode with the scan rate of 0.1 V s^{-1} kept constant. This plot shows good linearity with a regression coefficient of 0.9846. According to Ohm's law, the slope of this plot is the equivalent series resistance, mainly arising from the electrode ohmic resistance. For this electrode, the equivalent series resistance (diamond film + Si substrate + contact + electrolyte solution) was 1610 Ω. In the highly conducting KCl electrolyte, the dominant contributor to the series resistance is the ohmic resistance of the BDD electrode. This resistance value, determined

for the different BDD thin-film electrodes, was useful for *iR* correcting the cyclic voltametric curves for $Fe(CN)_6^{-3/-4}$ in KCl. Unfortunately, the RTILs have a higher solution resistance than the KCl electrolyte solution does. The high frequency ohmic resistance obtained from the EIS Bode plot data is a series resistance than includes the diamond film + Si substrate + contact + the RTIL resistance. On average, the values ranged from 480-764 in $[EMIM][BF_4]$, 2382-3359 in $[BMIM][BF_4]$ and 5100-6488 in $[HMIM][BF_4]$. The resistance values were used to *iR* correct the cyclic voltametric ΔE_p values for the ferrocene derivatives in the different RTILs, which were then used for the calculation of the heterogeneous electron-transfer rate constant.

4.4.5. Heterogeneous Electron Transfer Rate Constant for Potassium Ferrocyanide in [KCl]

Apparent heterogeneous electron-transfer rate constants (k^o_{app}) for the different redox systems were determined by two methods: the so-called Nicholson method[57,58] and digital simulation. In the Nicholson method, *iR* corrected cyclic voltammetric ΔE_p - scan rate data are used to determine k^o_{app}. The anodic and cathodic peak potentials can be corrected for ohmic (*iR*) curve distortion using the following equations [6] and [7],

$$E^{ox}_{p,corr} = E^{ox}_{p,org} - i^{ox}_p R \qquad [6]$$

$$E^{red}_{p,corr} = E^{red}_{p,org} - i^{red}_p R \qquad [7]$$

in which, $E^{ox}_{p,corr.}$, $E^{ox}_{p,org.}$, $E^{red}_{p,cor.}$, $E^{red}_{p,org.}$, i_p^{ox}, i_p^{red}, and *R* are the corrected (*corr*) and original (*org* or uncorrected) oxidation and reduction peak potentials, the oxidation and reduction peak currents, and the equivalent series resistance. The corrected ΔE_p was then used to calculate the k^o_{app} using Eq. 2. k^o_{app} value for $Fe(CN)_6^{-3/-4}$ was determined to be 2.28 (± 1.26) × 10^{-3} cm s^{-1}. This

nominal value is slightly lower than other values we have reported for BDD electrodes that are generally in the low 10^{-2} cm s^{-1} range. [87,88]

4.4.6. Cyclic Voltammetry of Ferrocene Derivatives in Room Temperature Ionic Liquids

The redox activity of ferrocene carboxylic acid (FCA), ferrocene methanol (FcMeOH), and ferrocene (Fc) were investigated at the BDD thin-film electrodes in the three different RTILs. Figure 4.11A-C show representative cyclic voltametric *i-E* curves (uncorrected for *iR*) for FCA in [EMIM][BF_4], [BMIM][BF_4], and [HMIM][BF_4]. The curves in each RTIL were recorded at scan rates from 0.1 – 0.5 V s^{-1}. Well-defined oxidation and reduction peaks are seen for this redox system in all three RTILs. The oxidation and reduction peak currents increase with the scan rate in all three RTILs. Figure 4.11A shows the curves for FCA in [EMIM][BF_4]. The oxidation and reduction peak currents are 9.16 and -8.01 μA, respectively, at 0.1 V s^{-1}. The ratio of oxidation to reduction peak currents is slightly greater than 1.0 suggestive of slightly different diffusion coefficients for FCA and FCA^+. The oxidation and reduction peak potentials are 0.617 and 0.475 V vs. Ag QRE. The ΔE_p value is 0.142 V and $E_{p/2}$ is 0.55 V vs. Ag QRE. The ΔE_p values, uncorrected for *iR* effects, increase with the scan rate indicating quasi-reversible electrochemical behavior, meaning that both electron-transfer and mass-transfer kinetics influence the curve shapes.

Figure 4.11B shows the cyclic voltammetric *i-E* curves (uncorrected for *iR*) for FCA in [BMIM][BF_4]. The oxidation and reduction peak currents are 5.11 and -4.40 μA, respectively, at 0.1 V s^{-1} and the ratio of oxidation and reduction peak currents is slightly greater than 1.0. The oxidation and reduction peak potentials are 0.486 and 0.289 V vs. Ag QRE. The ΔE_p is 0.197 V and $E_{p/2}$ is 0.388 V vs Ag QRE. The ΔE_p values, uncorrected for *iR* effects, increase with the scan

rate indicating quasi-reversible electrochemical behavior, meaning that both electron-transfer and mass-transfer kinetics influence the curve shapes.

Figure 4.11C shows the cyclic voltammetric *i-E* curves (uncorrected for *iR* effects) for FCA in [HMIM][BF_4]. The oxidation and reduction peak currents are 4.22 and -3.31 µA, respectively, at 0.1 V s^{-1} and the ratio of the oxidation and reduction peak currents is slightly greater than 1.0.

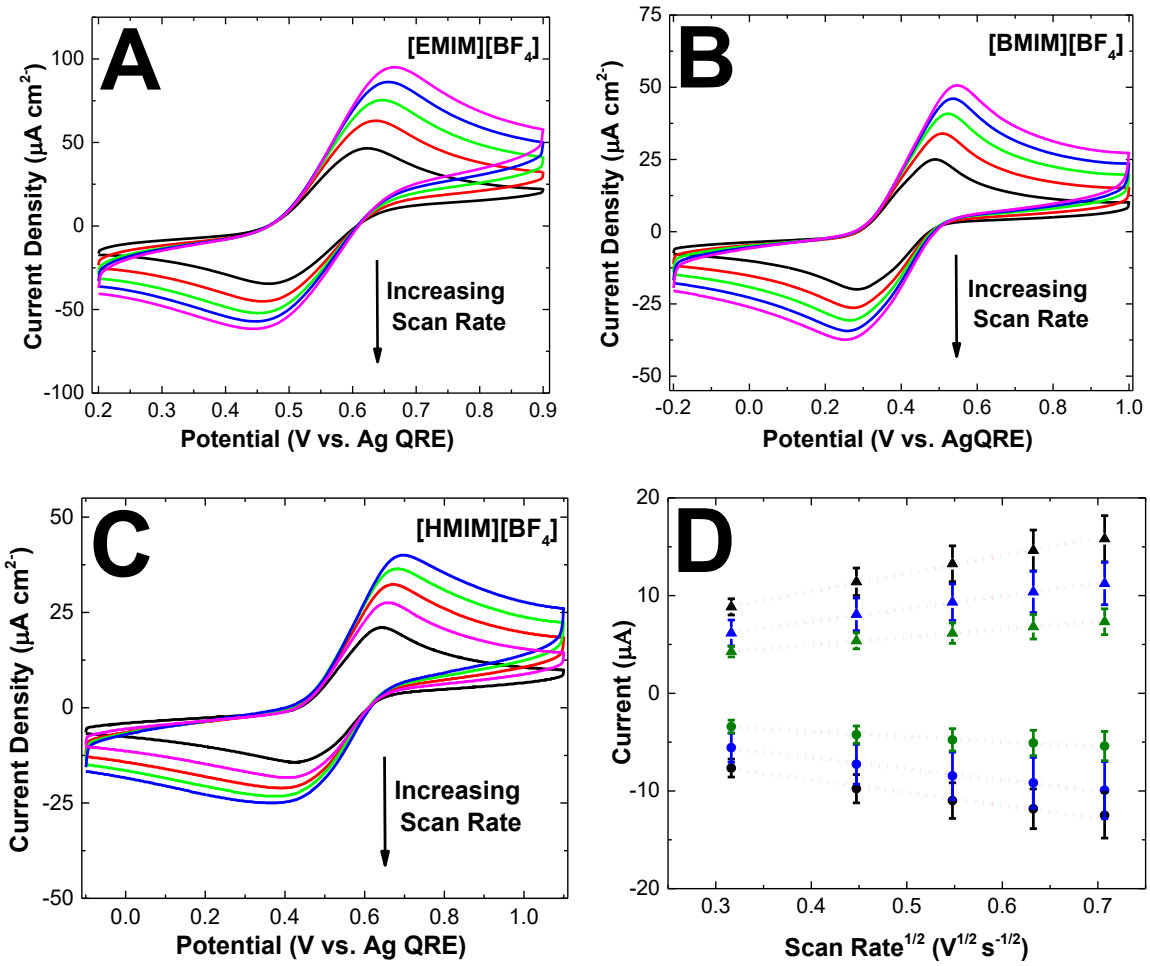

Figure 4.11. Cyclic voltammetric *i*−*E* curves for ferrocene carboxylic acid (FCA) in (A) [EMIM][BF_4], (B) [BMIM][BF_4] and (C) [HMIM][BF_4] recorded as a function of scan rate (0.1, 0.2, 0.3, 0.4, 0.5 V s^{-1}) for a BDD thin-film electrode. The FCA concentration was 1 mmol L^{-1}. (D) Plots of oxidation and reduction peak current vs. scan rate$^{1/2}$ in (black) [EMIM][BF_4], (blue) [BMIM][BF_4], and (green) [HMIM][BF_4]. (▲) oxidation peak current. (●) reduction peak current.

The oxidation and reduction peak potentials are 0.640 and 0.435 V vs. Ag QRE. The ΔE_p is 0.205 V at 0.1 V s^{-1} and $E_{p/2}$ is 0.538 V vs. Ag QRE. The ΔE_p values, uncorrected for *iR* effects, increase with the scan rate indicating quasi-reversible electrochemical behavior, meaning that both electron-transfer and mass-transfer kinetics influence the curve shapes.

The peak currents for FCA decrease in order of $[EMIM][BF_4]$ > $[BMIM][BF_4]$ > $[HMIM][BF_4]$. This is due to the viscosity increase of $[HMIM][BF_4]$ > $[BMIM][BF_4]$ > $[EMIM][BF_4]$ as D is proportional to the reciprocal of the viscosity. The ΔE_p values at a given scan rate increase in the order of $[EMIM][BF_4]$ < $[BMIM][BF_4]$ < $[HMIM][BF_4]$. In general, for quasi-reversible electrochemical systems, the peak current does not always track linearly with the scan $rate^{1/2}$, so these plots provide, at best, only an approximate value for the redox analyte diffusion coefficient. Diffusion coefficients are best determined by other methods like chronoamperometry. At the scan rates used in this work, 0.1-0.5 V s^{-1}, plots of the oxidation and reduction peak currents exhibited a degree of linearity. For example, Figure 4.11D presents plots of oxidation and reduction peak currents for FCA vs. scan $rate^{1/2}$ in the three RTILs. The plots of both peak currents are linear consistent with currents limited by semi-infinite linear diffusion of the analyte to and from the electrode surface. R^2 values were > 0.9842. The curve slopes decrease as the diffusion coefficient for the analyte decreases in the order of $[EMIM][BF_4]$ > $[BMIM][BF_4]$ > $[HMIM][BF_4]$.

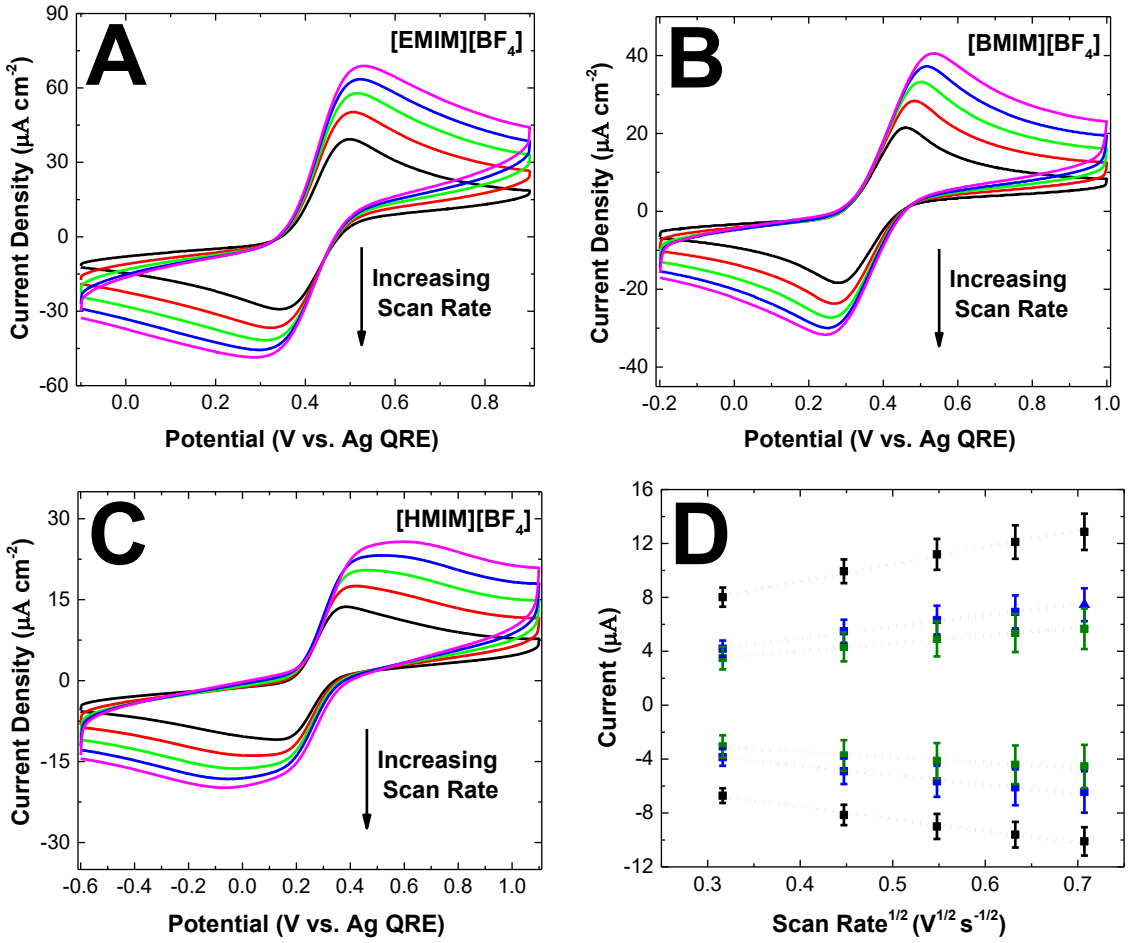

Figure 4.12. Cyclic voltammetric *i*−*E* curves for ferrocene methanol (FcMeOH) in (A) [EMIM][BF_4], (B) [BMIM][BF_4] and (C) [HMIM][BF_4] recorded as a function of scan rate (0.1, 0.2, 0.3, 0.4, 0.5 V s^{-1}) for a BDD thin-film electrode. The FcMeOH concentration was 1 mmol L^{-1}. (D) Plots of oxidation and reduction peak current vs. scan rate$^{1/2}$ in (black) [EMIM][BF_4], (blue) [BMIM][BF_4], and (green) [HMIM][BF_4]. (▲) oxidation peak current. (●) reduction peak current.

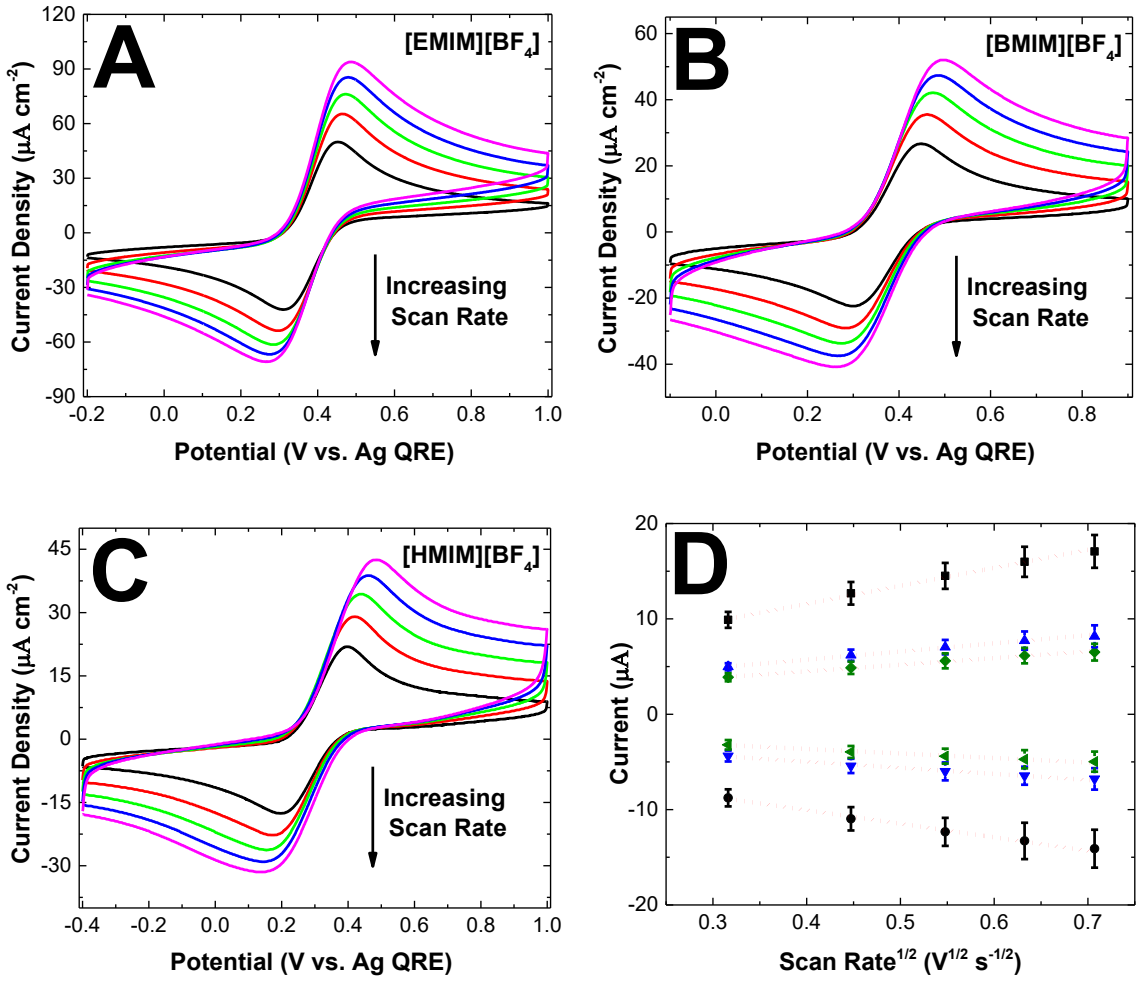

Figure 4.13. Cyclic voltammetric *i*−*E* curves for ferrocene (Fc) in (A) [EMIM][BF_4], (B) [BMIM][BF_4] and (C) [HMIM][BF_4] recorded as a function of scan rate (0.1, 0.2, 0.3, 0.4, 0.5 V s^{-1}) for a BDD thin-film electrode. The Fc concentration was 1 mmol L^{-1}. (D) Plots of oxidation and reduction peak current vs. scan $rate^{1/2}$ in (black) [EMIM][BF_4], (blue) [BMIM][BF_4], and (green) [HMIM][BF_4]. (▲) oxidation peak current. (●) reduction peak current.

Figures 4.12A-C and 4.13A-C show the representative cyclic voltametric *i*-*E* curves (uncorrected for *iR*) for ferrocene methanol (FcMeOH) and ferrocene (Fc) in [EMIM][BF_4], [BMIM][BF_4], and [HMIM][BF_4], respectively. The ΔE_p values for both redox analytes, uncorrected for *iR* effects, increase with the scan rate indicating quasi-reversible electrochemical behavior, meaning that both electron-transfer and mass-transfer kinetics influence the curve shapes. Figures 4.12D and 4.13D show plots of the oxidation and reduction peak currents for both

redox systems vs. scan rate$^{1/2}$ in the three RTILs exhibit a degree of linearity and R^2 values were > 0.9739. It is clear that in the more viscous RTIL, [HMIM][BF_4], true time dependent diffusion of FcMeOH with a growing depletion layer is not observed. The post-peak current decay does not follow a $t^{-1/2}$ profile. Rather, there appears to be some contribution of radial diffusion leading to less time dependence of the diffusion-limited current.

For the case of FcMeOH in [EMIM][BF_4], the oxidation and reduction peak currents are 7.99 and -6.78 μA, respectively, at 0.1 V s^{-1}. The ratio of oxidation to reduction peak currents is slightly greater than 1.0. The oxidation and reduction peak potentials are 0.493 and 0.346 V vs. Ag QRE. The ΔE_p value is 0.147 V at 0.1 V s^{-1} and $E_{p/2}$ is 0.420 V vs. Ag QRE. The oxidation and reduction peak currents for FcMeOH in [BMIM][BF_4] are 4.66 and -4.43 μA, respectively, at 0.1 V s^{-1} and the ratio of oxidation and reduction peak currents is slightly greater than 1.0. The oxidation and reduction peak potentials are 0.436 and 0.282 V vs. Ag QRE. The ΔE_p is 0.154 V and $E_{p/2}$ is 0.359 V vs Ag QRE. The oxidation and reduction peak currents for FcMeOH in [HMIM][BF_4] are 2.67 and -2.23 μA, respectively, at 0.1 V s^{-1} and the ratio of the oxidation and reduction peak currents is slightly greater than 1.0. The oxidation and reduction peak potentials are 0.376 and 0.146 V vs. Ag QRE. The ΔE_p is 0.230 V and $E_{p/2}$ is 0.261 V vs. Ag QRE.

For Fc in [EMIM][BF_4], the oxidation and reduction peak currents are 10.47 and -9.56 μA, respectively, at 0.1 V s^{-1}. The ratio of oxidation to reduction peak currents is slightly greater than 1.0. The oxidation and reduction peak potentials are 0.452 and 0.311 V vs. Ag QRE. The ΔE_p value is 0.141 V and $E_{p/2}$ is 0.382 V vs. Ag QRE. The oxidation and reduction peak currents for Fc in [BMIM][BF_4] are 5.38 and -4.99 μA, respectively, at 0.1 V s^{-1} and the ratio of oxidation and reduction peak currents is slightly greater than 1.0. The oxidation and reduction peak potentials are at 0.440 and 0.294 V vs. Ag QRE. The ΔE_p is 0.146 V and $E_{p/2}$ is 0.367 V vs Ag QRE. The

oxidation and reduction peak currents for Fc in [HMIM][BF_4] are 4.37 and -3.75 μA, respectively, at 0.1 V s^{-1} and the ratio of the oxidation and reduction peak currents is slightly greater than 1.0. The oxidation and reduction peak potentials are at 0.392 and 0.199 V vs. Ag QRE. The ΔE_p is 0.193 V and $E_{p/2}$ is 0.296 V vs. Ag QRE.

For all three ferrocene derivatives, the peak currents decrease in order of [EMIM][BF_4] > [BMIM][BF_4] > [HMIM][BF_4] and the uncorrected ΔE_p values increase in the order of [EMIM][BF_4] < [BMIM][BF_4] < [HMIM][BF_4]. The diffusion coefficient for all three redox systems decreases with increasing RTIL viscosity in order of [EMIM][BF_4] > [BMIM][BF_4] > [HMIM][BF_4].

Table 4.3 presents experimental voltametric data (original ΔE_p, *iR* corrected ΔE_p, oxidation peak current, i_p^{ox}, diffusion coefficient, D_{ox}, and k^o_{app}) for FCA, FcMeOH and Fc in the three RTILs. The k^o_{app} values were determined using the Nicholson method using *iR* corrected voltametric data and by digital simulation. The simulated rate constants (k^o_{sim}) are also presented in Table 4.3.

The original uncorrected and *iR* corrected ΔE_p values for the ferrocene derivatives increase with increasing RTIL viscosity. For example, the *iR* corrected ΔE_p (0.1 V s^{-1}) for FCA increase in the following order: [EMIM][BF_4] (ΔE_p = 139 ± 9 mV) < [BMIM][BF_4] (ΔE_p = 150 ± 26 mV) < [HMIM][BF_4] (ΔE_p = 167 ± 15 mV). Similar trends are seen for FcMeOH and Fc. The increase in ΔE_p is due to a decrease in k^o_{app} with increasing RTIL viscosity. The experimentally determined k^o_{app} values for FCA decrease in the following order: [EMIM][BF_4] (2.41 (± 0.70) ×10^{-4} cm s^{-1}) > [BMIM][BF_4] (1.87 (± 1.43) ×10^{-4} cm s^{-1}) > [HMIM][BF_4] (0.65 (± 0.31) ×10^{-4} cm s^{-1}).

Table 4.3. Summary of cyclic voltametric data and the experimentally determined and simulated k^o_{app} values for ferrocene carboxylic acid (FCA), ferrocene methanol (FcMeOH), and ferrocene (Fc) in [EMIM][BF_4], [BMIM][BF_4], and [HMIM][BF_4] at BDD thin-film electrodes.

Analyte	Electrolyte	$\Delta E_{p,org}$ (mV)	$\Delta E_{p,corr}$ (mV)	i_p^{ox} (µA)	D_{ox} $\times 10^{-7}$ ($cm^2\ s^{-1}$)	$k^o_{app,exp}$ $\times 10^{-4}$ ($cm\ s^{-1}$)	$k^o_{app,sim}$ $\times 10^{-4}$ ($cm\ s^{-1}$)
FCA	EMIM	150 ± 9	139 ± 9	8.85 ± 0.83	0.56 ± 0.31	2.41 ± 0.70	4.50 ± 1.32
	BMIM	181 ± 22	150 ± 26	6.17 ± 1.32	0.45 ± 0.29	1.87 ± 1.43	1.67 ± 0.72
	HMIM	212 ± 10	167 ± 15	4.26 ± 0.54	0.10 ± 0.08	0.65 ± 0.31	0.77 ± 0.30
FcMeOH	EMIM	154 ± 6	144 ± 7	8.01 ± 0.71	0.26 ± 0.08	1.53 ± 0.29	3.60 ± 1.22
	BMIM	171 ± 20	149 ± 27	4.20 ± 0.60	0.16 ± 0.11	1.18 ± 0.84	1.97 ± 0.96
	HMIM	217 ± 20	179 ± 26	3.49 ± 0.84	0.06 ± 0.05	0.45 ± 0.37	0.85 ± 0.43
Fc	EMIM	150 ± 8	137 ± 10	9.90 ± 0.84	0.66 ± 0.28	2.73 ± 0.98	5.07 ± 1.78
	BMIM	166 ± 24	140 ± 31	4.98 ± 0.37	0.13 ± 0.06	1.40 ± 1.05	2.27 ± 0.87
	HMIM	209 ± 24	167 ± 34	3.89 ± 0.43	0.08 ±0.05	0.64 ± 0.44	0.91 ± 0.29

Data are presented as mean ± standard deviation for n=3 BDD electrodes. Scan rate = 0.1 V s^{-1} for all measurement data. Diffusion coefficients were determined from the slope of i_p^{red} vs. $v^{1/2}$ plots. Experimental apparent heterogeneous electron-transfer rate constant (k^o_{app}) values determined experimentally by the Nicholson method and by digital simulation from fits of the experimental cyclic voltametric data (electrode area = 0.2 cm^2, $\alpha = 0.5$).

Similar trends are observed for FcMeOH and Fc with k^o_{app} values ranging from 10^{-5} to 10^{-4} cm s^{-1}. The k^o_{app} for all three ferrocene derivatives were similar in the different RTILs with the viscosity being the controlling factor rather than the RTIL molecular compositions. The D_{ox} values for all three ferrocene derivatives are 10^{-7} to 10^{-9} $cm^2\ s^{-1}$. These values were determined from measurements in Ar-purged solution. It should be noted that Barrosse-Antle et al. have reported

that diffusion coefficient for ferrocene is larger in Ar-purged solution than in solutions under vacuum.[50]

The cyclic voltammetric curves were fit to digitally simulated curves (DigiSim® 3.03) through adjustments in D_{red}, D_{ox}, k^o and α. The experimentally determined values of D_{red} and D_{ox} served as the starting points for adjustments in the simulated curves so as to match the peak currents and ΔE_p values. Table 4.3 presents apparent heterogeneous electron-transfer rate constant (k^o_{app}) data for the three redox systems in the different RTILs. The simulated k^o_{app} values are 10^{-4} cm s^{-1} and are 1-2 orders of magnitude lower than the k^o_{app} value for $Fe(CN)_6^{-3/-4}$ in KCl at the same electrodes. The $k^o_{app,sim}$ values decrease with increasing RTIL viscosity in the following order: $[EMIM][BF_4]$ > $[BMIM][BF_4]$ > $[HMIM][BF_4]$. There is good agreement between the k^o_{app} values determined experimentally and by simulation. Figure 4.14A-C presents overlays of the experimental and simulated cyclic voltametric *i-E* curves for FCA in the three RTILs at a BDD thin-film electrode. There is generally good agreement between the curve shapes pre and post the oxidation and reduction peaks. The best fitting was observed when an α value of 0.5 was used in the simulations. In some cases, a slight mismatch in the diffusion- limited currents was observed with the time dependence of the experimental diffusion-controlled current being different from the simulated current. This can be seen for FCA oxidation in $[EMIM][BF_4]$ and $[HMIM][BF_4]$. This is attributed to heterogeneities in the electrode surface morphology and active-site density and spacing.[89] The geometric area of the electrode, and not the true area, was used in the simulations. In the viscous RTILs, the depletion layer thickness on the time scale of the measurement (scan rate) will be far less than the thickness in aqueous electrolyte solution. For example, using ($l = 2(Dt)^{1/2}$) and the Fc oxidation reaction at 0.1 V s^{-1}, the depletion layer thickness is on the order of 90 μm in KCl and only 4 μm in $[HMIM][BF_4]$. This means that surface roughness and active

area effects will influence the voltametric curve shapes at these scan rates more so in the viscous RTILs than in the aqueous electrolyte. More work is needs to perform more detailed simulations of the experimental cyclic voltammetric curves to extract more rigorous k^o data and for assessment of whether or not the Butler-Volmer model is appropriate to describe electron-transfer kinetics in RTILs.

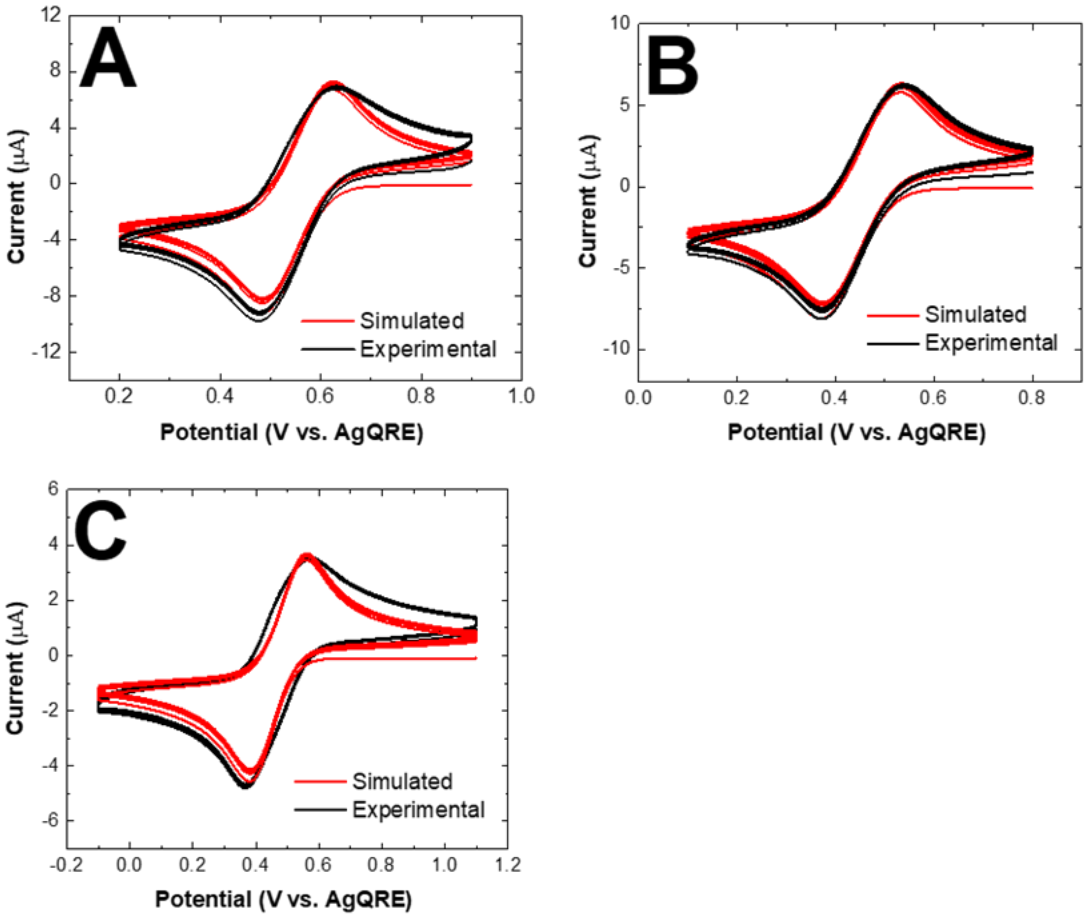

Figure 4.14. Cyclic voltammetric $i-E$ curves for 1 mmol L^{-1} FCA in (A) [EMIM][BF_4], (B) [BMIM][BF_4] and (C) [HMIM][BF_4] at a BDD thin-film electrode. Experimental (black line) and simulated (red line) curves are presented. Scan rate = 0.1 V s^{-1}. Area = 0.2 cm^2. Simulation parameters used were C_{dl} = 1 μF and α = 0.5.

A common source of error when using the Nicholson approach is the uncompensated ohmic drop which causes increased peak separation with scan rate and lower calculated k^o values than the

true values. Efforts were made to *iR* correct the ΔE_p values for the ferrocene derivatives in order to improve the accuracy of the k^o values determined from the $\Delta E_p - \upsilon$ data. A good indicator of minor ohmic potential errors is the variation in calculated k^o values with scan rate. Table 4.4 presents a summary of the data for Fc, FCA and FcMeOH in the three RTILs.

Table 4.4. Summary of the experimentally determined apparent heterogeneous electron transfer rate constant values, k^o_{app}, for ferrocene carboxylic acid (FCA), ferrocene methanol (FcMeOH), and ferrocene (Fc) in [EMIM][BF_4], [BMIM][BF_4], and [HMIM][BF_4] at BDD thin-film electrodes at various scan rates : 0.1-0.5 V s^{-1}.

Scan Rate (V s^{-1})	**k^o (cm s^{-1}) (10^{-4})**								
	Fc			**FCA**			**FcMeOH**		
	EMI BF_4	**BMI BF_4**	**HMI BF_4**	**EMI BF_4**	**BMI BF_4**	**HMI BF_4**	**EMI BF_4**	**BMI BF_4**	**HMI BF_4**
0.1	2.73 ± 0.98	1.40 ± 1.05	0.64 ± 0.44	2.41 ± 0.70	1.87 ± 1.43	0.65 ± 0.31	1.53 ± 0.29	1.18 ± 0.84	0.45 ± 0.37
0.2	2.77 ± 1.17	1.47 ± 1.14	0.52 ± 0.50	2.46 ± 0.80	1.81 ± 1.38	0.79 ± 0.46	1.39 ± 0.39	1.09 ± 0.88	0.35 ± 0.33
0.3	2.47 ± 1.26	1.30 ± 1.18	N/A	2.39 ± 0.88	1.72 ± 1.11	0.69 ± 0.44	1.21 ± 0.39	0.95 ± 0.91	0.24 ± 0.30
0.4	2.26 ± 1.23	1.22 ± 1.10	N/A	2.27 ± 0.93	1.75 ± 1.44	0.66 ± 0.45	1.12 ± 0.49	0.88 ± 0.96	N/A
0.5	1.93 ± 1.28	1.12 ± 1.16	N/A	2.29 ± 1.03	1.55 ± 1.30	0.72 ± 0.46	1.02 ± 0.54	0.75 ± 0.90	N/A

If ohmic effects have been effectively corrected for, then the calculated k^o will be similar at all scan rates. If not, then k^o will trend toward lower values with increasing scan rate. It can be seen in the data that in some cases, k^o is independent of scan rate and in other cases a slightly decreasing value is seen with increasing scan rate. For this reason, we also attempted to validate the k^o values by simulating curves and comparing them to experimental cyclic voltammograms.

4.5. Discussion

The heterogeneous electron-transfer rate constant, k^o, for some redox systems in aqueous electrolyte solutions, like $Fe(CN)_6^{-3/-4}$, is sensitive to the surface cleanliness, microstructure, and surface chemistry of carbon electrodes.[6-10] For other redox systems, such as $Ru(NH_3)_6^{+3/+2}$, these factors are much less influential. For all redox systems, the electronic properties of the electrode (*i.e.*, electrical conductivity) impact the shape of current-voltage curves used to extract k^o values. It is also established that the electrolyte composition and solvent type can influence k^o for some redox systems more so than others.[6-10,11-13,87,88] One would like to know if this same "surface sensitivity" exists for redox systems in RTIL media at carbon electrodes. It appears there is a more limited number of redox systems that can be used to probe carbon electrode surface-reactivity relationships in RTILs. This is because the redox system needs to be both soluble and have a relatively low reorganizational energy barrier for electron transfer in the RTIL. The highly charged inorganic redox systems that are commonly used to assess carbon electrode activity, at least in our hands, do not undergo electron transfer at these electrodes when dissolved in these RTILs. Two groups of redox analytes that can be used in RTILs are ferrocene and anthracene derivatives. There is some literature reporting on the electrochemical behavior of these redox systems in RTILs at different carbon electrodes including BDD. [51,62,63,76,90,91] Our objective for this work was to learn how the molecular structure of the RTIL, specifically the size and nature of the cation, affects capacitance and heterogeneous electron-transfer kinetics at BDD electrodes. Three ferrocene derivatives were used as redox probe molecules because all are dissolved and undergo relative facile electron-transfer at carbon electrodes in RTIL media.

When studying the effect of RTILs on redox reactions at solid electrodes, it is important to remember that the ionic liquid presents a heterogeneous chemical environment unlike the more

homogeneous aqueous electrolyte solution that consists of essentially spherically-shaped ions separated from one another by dielectric solvent molecules. In contrast, RTILs consist of asymmetrically shaped cations and anions with no dielectric solvent intentionally added. The cations are comprised of a highly polar and charged head group, and a non-polar tail. The weak non-polar forces between the alkyl chains induces aggregation and reverse micelle-like domains surrounded by ion-rich polar domains. [34,92] When dissolved in an RTIL, the redox molecule maybe located heterogeneously at particular positions within the RTIL phase depending on its chemical and physical properties rather than being homogenously distributed.[34,92] This heterogeneous distribution could affect the distance of closest approach with the electrode and therefore the electron-tunneling rate through the ionic liquid to and from the electrode. The existence of localized domains could also affect the concentration of redox molecules available at the electrode surface to undergo electron transfer.

Another issue to consider is the fact that the solvation environment around a redox system, especially a charged one, will necessarily be different in an RTIL than in a polar solvent/electrolyte solution. If solvent rearrangement, or the inter and intra-molecular reorganization energy, is the rate limiting step accompanying an electron transfer reaction, then these reaction rates will be much slower in the viscous RTILs than in aqueous electrolyte solution. In other words, the high viscosity of the RTILs slows down the rates of both electron transfer and diffusional mass transfer.

Background cyclic voltametric data between -1 and 1 V vs. AgQRE revealed that the current increases proportionally with the scan rate, at least up to 0.5 V s^{-1}. The linear increase in current with scan rate confirms the current at potentials within this window is capacitive in nature for BDD electrodes. BDD electrodes are generally inert and possess few electroactive and or ionizable surface carbon-oxygen functional groups when hydrogen terminated. Even with the high

viscosity of the RTILs, the ions and ion pairs that exist in these media are able to assemble excesses in the interfacial region so as to counterbalance the potential-dependent excess surface charge on the electrode as fast as the electrode surface charge is being changed (*i.e.*, different scan rates), at least up to 0.5 V s^{-1}.

The C_{dl}-E data presented for the BDD electrodes reveals that the capacitance is flat and unchanging or slightly increasing with increasing positive potential over a range of 2 V. The capacitance magnitudes are indifferent in the three RTILs indicating that a change of the alkyl substituent group on the imidazolium ring (n=2, 4 or 6), which necessarily increases the overall size and asymmetry of the cation, does not impact the interfacial excess charge density and distance away from the electrode that this excess exists to counterbalance the BDD surface charge density at each applied potential. The capacitance magnitudes in the three RTILs are 5-12 μF cm^{-2} and in the aqueous 1 M KCl solution are 1.5-2x higher at 10-18 μF cm^{-2}. Similar capacitance data have been reported for BDD electrodes in RTILs. [63,78-80,83,86] Capacitance-potential measurements directly probe the interfacial ion excesses. These data indicate the measured capacitance is dominated by the properties of the liquid phase and not by any space charge layer within the BDD electrode, at least for the highly doped electrodes used in this work. Furthermore, the data indicate that the counterbalancing excess charge density on the aqueous electrolyte solution side of the interface can be organized in less volume and with less distance from the electrode than in RTILs. The smaller ion radii and higher dielectric constant of water enables a higher volumetric charge density to be accumulated in the interfacial region of BDD electrodes in response to an electrode potential change than can be accumulated in the RTILs. In other words, the counterbalancing excess charge in the RTILs extends a greater distance from the electrode than does the excess charge layer in the aqueous electrolyte solution. Even with the different cation sizes, the

capacitance is independent of the molecular structure of these three RTILs. There is short-range order within the double layer region, as determined from the capacitance data, but also longer-range order that extends 10's to 100's of micrometers in the RTIL bulk. [93-95] The short-range order is expected to have more of an impact on the electron-transfer kinetics while the longer-range order may more affect analyte mass transfer, ion transference number, and conductance.

With no solvent added, the organization of the RTIL ions in the electrified interface is different from that in an aqueous or organic electrolyte/solvent system. The biggest difference being that the RTIL ions specifically interact (*i.e.*, adsorb) with the electrode surface. As has been summarized by Lucio et al. [79] and reviewed by Fedrov and Kornyshev[34], there are several descriptions of the organization of RTIL ions at an electrified interface. In one model, the counterbalancing ion excess is one layer thick at a highly conducting electrode comparable to a Helmholtz layer model. In this case, the capacitance would be independent of the electrode potential. Some have postulated a more traditional double layer structure with a Helmholtz layer and a diffuse layer, the so-called Gouy-Chapman-Stern model. This model predicts that the capacitance should be a minimum near the potential of zero charge (E_{pzc}) and increase at more positive and negative potentials as the electrode becomes more highly charged. The diffuse layer becomes more compact and at potentials far from E_{pzc}, the capacitance will approach a constant value. A multi-layer arrangement of alternating cations and anions in the interface to counterbalance the excess surface charge is another possible model. An accepted and experimentally tested model describing the interfacial organization of RTIL ions at an electrified interface is the mean-field lattice model by Kornyshev. [34,96-98] This model describes a highly concentrated liquid of compressible ions free of a dielectric solvent. The model predicts a bell or camel-shaped capacitance-potential profile with a capacitance maximum at E_{pzc}.

The capacitance-potential profiles for various carbon electrodes, including BDD, in RTILs are generally flat or have a "U-shape". [78-81, 86] This contrasts with the camel or bell-shaped profiles seen for metal electrodes with a capacitance maximum at E_{pzc}. It is unclear why the behavior at carbon electrodes is so much different from metal electrodes. Kornyshev suggested there are two electrical double-layers in series at the interface of a semiconducting electrode (*e.g.,* BDD) and an RTIL; one in the electrode (space charge layer) and the other in RTIL. [96] The flat capacitance-potential profile observed for BDD electrodes in this work suggests that the excess surface charge on the electrode does not change much at the different potentials and is of a magnitude that the highly charged RTIL can effectively organize to counterbalance the surface charge in the liquid layer nearest the electrode much like the compact layer in the Gouy-Chapman-Stern model.

RTILs are attractive because they can solubilize a wide range of chemical species, more so than conventional solvents, and they are unreactive leading to a wide working potential window. The BDD electrodes exhibit a 4-5 V potential window in these three imidazolium RTILs. In terms of heterogeneous electron-transfer kinetics, the reorganization energy, the work terms, and the potential drop at the plane of closest approach – the location with respect to the electrode surface where the electron transfer takes place with the soluble redox system – are all key factors. Since there is no solvent to shield the ions, one might expect larger reorganization energies for a redox analyte in RTILs than in aqueous or organic electrolyte solutions. There might be a considerable energy barrier to reorganize the RTIL ions and ion pairs around a neutral ferrocene derivative when an electron is transferred to produce the charged ferrocenium ion. A higher reorganization energy would contribute to a lower k^o value. The work terms are important because they determine the concentrations of oxidized (for the cathodic current) and reduced (for the anodic current) species at the plane of closest approach. These work terms will depend on the charge of the redox

species, the organization of the RTIL ions around the redox system to produce the "solvated" species, the electrode potential, and the viscosity of the RTIL. The potential driving force refers to how compact the localization of excess charge is on the solution side of the interface that controls the electrostatic potential drop at the plane of closest approach. All of these factors are important to consider as one tries to understand heterogeneous electron-transfer kinetics in RTILs at BDD and other carbon electrodes.

The apparent heterogeneous electron-transfer rate constant, k^o_{app}, for the three ferrocene derivatives is in the range of 10^{-4} to 10^{-5} cm s^{-1} and decreases with increasing RTIL viscosity, [EMIM][BF_4] > [BMIM][BF_4] > [HMIM][BF_4]. Good agreement was observed between the k^o_{app} values determined from ΔE_p-v analysis and digital simulation. The k^o_{app} values in the RTILs are 100-1000x lower than values for outer-sphere redox systems in aqueous electrolyte solutions[63,87,88] and organic electrolyte solutions[14] at BDD electrodes. Therefore, viscosity rather than the molecular structure of the RTIL is the dominant factor controlling the electron-transfer kinetics.

There are a couple of factors that cause the lower k^o values in RTILs as compared to aqueous electrolyte solutions. Marcus theory, which is often used to explain k^o in aqueous solutions, was used herein to describe k^o_{app} for the ferrocene derivatives in the RTILs. The equation for k^o is shown in [8] [48,55,63,99,100]

$$k^o = K_p \kappa_{el} v_n e^{\left(\frac{-\Delta G^{\ddagger}}{RT}\right)} \qquad [8]$$

in which K_p, κ_{el}, v_n are the precursor equilibrium rate constant, electronic transmission coefficient, and nuclear frequency factor, respectively. $\Delta G^{\ddagger}$ is the total activation energy. R and T are ideal gas constant and temperature, respectively. The nuclear frequency factor, v_n, is the frequency of

attempts the redox molecule makes to the transition state and this frequency is lower in the more viscous RTILs. The fact that the k^o_{app} values vary linearly with η^{-1} is consistent with v_n varying linearly with η^{-1}.

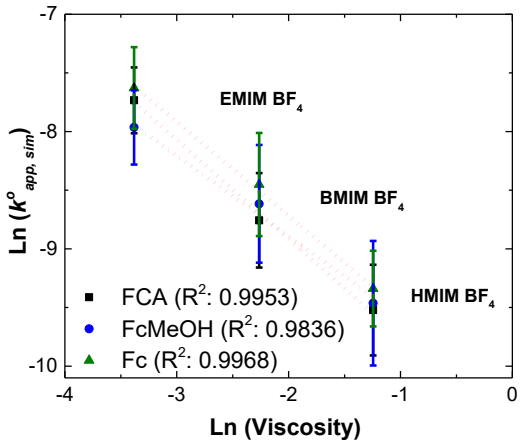

Figure 4.15. Plots of the natural log of $k^o_{app,sim}$ determined from digital simulation versus the natural log of the RTIL viscosity (η) for the three different ferrocene derivatives: Fc (ferrocene), FCA (ferrocene carboxylic acid) and FcMeOH (ferrocene methanol) at room temperature. Data are presented as mean ± std. dev. for n=3 diamond electrodes.

The second factor that makes k^o_{app} lower in the RTILs is $\Delta G^{\ddagger}$ is the total activation energy. A larger activation energy barrier exists in RTILs that in aqueous electrolyte solutions presumably because of the larger activation energy needed to reorient the RTIL ions around the redox molecule in the solvent-less liquid during electron transfer. According to Marcus Theory, $\Delta G^{\ddagger}$ can be divided into the inner shell $\Delta G^{\ddagger}_{IS}$ and outer shell $\Delta G^{\ddagger}_{OS}$ activation energies. [55,99] The former is related to changes in bond lengths or bond breakage and formation, while the latter is related to changes in the solvation (*i.e.*, reorganization of the RTIL ions around the ferrocene derivative) during electron transfer. Figure 4.15 shows that plots of ln (k^o_{app}) versus ln (η) for the three ferrocene derivatives are linear with a slope near -1.0. This suggests that $\Delta G^{\ddagger}_{OS}$ makes a dominant contribution to $\Delta G^{\ddagger}$.[55,99] In other words, RTIL ion relaxation dynamics strongly influence the electron transfer rate similarly for all three RTILs, regardless of the difference in cation molecular structure. As has

been concluded by Bentley et al., the linear relationship between implies that the influence of ion pairing and/or double layer effects on k^o are largely invariant with the RTIL molecular structure. [55]

4.6. Conclusions

The potential dependent capacitance and heterogeneous electron-transfer rate constant for ferrocene, ferrocene methanol, and ferrocene carboxylic acid were investigated in three homologous room-temperature ionic liquids ([EMIM][BF_4], [BMIM][BF_4], [HMIM][BF_4]) at heavily boron-doped, nanocrystalline diamond thin-films deposited on Si. The following is a summary of the key findings from this research:

1. The voltammetric background current, working potential window, and potential-dependent capacitance for the BDD electrodes were similar in all three RTILs, regardless of the viscosity and cation molecular structure differences.

2. The working potential window of the BDD electrodes in the three RTILs was 4 - 5 V.

3. Capacitance-potential profiles were flat or slightly increasing with increasing positive potential over a -1 to 1 V vs. AgQRE range and ranged from 5-12 $\mu F/cm^2$ for all three RTILs at BDD electrodes. Capacitance values in an aqueous electrolyte solution (1 mol L^{-1} KCl) were 1.5-2x larger at the same electrodes.

4. Similar capacitance-potential values were observed in the three RTILs indicating that changing the length of the alkyl substituent (n = 2, 4 and 6) on the imidazolium ring does not significantly alter the RTIL ions ability to accumulate excesses in the interfacial region in response to a change in excess surface charge with change in potential.

5. The diffusion coefficient for the ferrocene derivatives ranged from 10^{-7} to 10^{-9} cm^2 s^{-1} in the three RTILs and decreased linearly with increasing viscosity (D_{ox} α η^{-1}). The diffusion coefficients were determined from quasi-reversible cyclic voltammetric *i-E* curves and therefore should be considered approximate values. Future work will involve determining these values by another method such as chronoamperometry.

6. The apparent heterogeneous electron transfer rate constants (k^o_{app}) for the ferrocene derivatives in the three RTILs were similar and ranged 10^{-4} to 10^{-5} cm s^{-1} at the BDD electrodes. Similar values were obtained from the analysis of ΔE_p - v analysis and from digital simulation. k^o_{app} decreased linearly with increasing viscosity (k^o_{app} α η^{-1}).

7. For some experimental curves, the degree of fit with simulated curves on the rising part of the oxidation (forward) and reduction (reverse) peaks and the post-peak mass transport limited currents was less than desired. In some cases, experimental currents for the oxidation (forward) peak rose more steeply than did the simulated currents, and experimental currents post-peak in the diffusion-limited region decayed more slowing with time than did the simulated currents. The simulated *i-E* curves were generated using the Butler-Volmer model for electron transfer kinetics and semi-infinite linear diffusion of the analyte to and from a homogeneously active planar electrode. The differences between the experimental and simulated curves needs to be explored in more detail to verify the Butler-Volmer model is appropriate to describe electron transfer in RTILs. One reason for the differences in experimental and simulated curves could be that the BDD surface is heterogeneously active with sites where both planar and non-planar diffusion are controlling the flux of analyte to the surface.

8. Using Marcus Theory, the low k^o_{app} values in the RTILs are explained by a low nuclear frequency factor, v_n, and a high outer-shell activation energy, $\Delta G^{\ddagger}_{OS}$, caused by slow RTIL ion relaxation dynamics around the redox center during electron transfer.

REFERENCES

[1] McCreery, R. L. "Carbon electrodes: structural effects on electron transfer kinetics", *Electroanal. Chem.*, A. J. Bard, Ed.; Marcel Dekker Inc., **1991,** *17*, 221.

[2] Rice, R. J.; Pontikos, N. M.; McCreery, R. L. "Quantitative correlations of heterogeneous electron-transfer kinetics with surface properties of glassy carbon electrodes", *J. Am. Chem. Soc.* **1990**, *112*, 4617-4622.

[3] Švancara, I.; Vytřas, K.; Barek, J.; Zima, J. "Carbon paste electrodes in modern electroanalysis", *Crit. Rev. Anal. Chem.* **2001**, *31*, 311-345.

[4] Agui, L.; Yanez-Sedeno, P.; Pingarron, J. M. "Role of carbon nanotubes in electroanalytical chemistry - a review", *Anal. Chim. Acta*, **2008**, *622*, 11-47.

[5] Coroş, M.; Pruneanu, S.; Stefan-van Staden, R. "Review-recent progress in the graphene-based electrochemical sensors and biosensors", *J. Electrochem. Soc.* **2019**, *167*, 037528.

[6] Bowling, R.; Packard, R. T.; McCreery, R. L. "Mechanism of electrochemical activation of carbon electrodes: role of graphitic lattice defects", *Langmuir*, **1989**, 5, 683-688.

[7] Kneten, K. R.; McCreery, R. L. "Effects of redox system structure on electron-transfer kinetics at ordered graphite and glassy carbon electrodes", *Anal. Chem.* **1992**, *64*, 2518-2524.

[8] Kneten-Cline, K.; McDermott, M. T.; McCreery, R. L. "Anomalously slow electron transfer at ordered graphite electrodes: influence of electronic factors and reactive sites", *J. Phys. Chem*. **1994**, *98*, 5314-5319.

[9] Chen, P.; McCreery, R. L. "Control of electron transfer kinetics at glassy carbon electrodes by specific surface site modification", *Anal. Chem.* **1996**, *68*, 3958-3965.

[10] Ranganathan, S.; McCreery, R. L. "Electroanalytical performance of carbon films with near-atomic flatness", *Anal. Chem.* **2001**, *73*, 893-900.

[11] Granger, M. C.; Xu, J.; Strojek, J. W.; Swain, G. M. "Polycrystalline diamond electrodes: basic properties and applications as amperometric detectors in flow injection analysis and liquid chromatography", *Anal. Chim. Acta*, **1999**, *397*, 145-161.

[12] Granger, M. C.; Witek, M.; Xu, J.; Wang, J.; Hupert, M.; Hanks, A.; Koppang, M. D.; Butler, J. E.; Lucazeau, G.; Mermoux, M.; Strojek, J. W.; Swain, G. M. "Standard electrochemical behavior of high-quality, boron-doped polycrystalline diamond thin-film electrodes", *Anal. Chem.* **2000**, *72*, 3793-3804.

[13] Hupert, M.; Muck, A.; Wang, J.; Stotter, J.; Cvackova, Z.; Haymond, S.; Show, Y.; Swain, G. M. "Conductive diamond thin films in electrochemistry", *Diam. Rel. Mater.* **2003**, *12*, 1940-1949.

[14] Haymond, S.; Babcock, G. T.; Swain, G. M. "Electron transfer kinetics of ferrocene at microcrystalline boron-doped diamond electrodes: effect of solvent and electrolyte", *Electroanal.* **2003**, *15*, 249-253.

[15] Celii, F. G.; Butler, J. E. "Diamond chemical vapor deposition" *Ann. Rev. Phys. Chem*. **1991**, *42*, 643-684.

[16] Butler, J.E.; Sumant, A. V. "The CVD of nanodiamond materials." *Chem. Vap. Dep*. **2008**, *14*, 145-160.

[17] Jiang, M.; Chen, C.; Wang, P.; Hu, X. "Diamond formation mechanism in chemical vapor deposition.", *PNAS*, **2022**, *119*, e2201451119.

[18] Gruen, D.M. "Nanocrystalline diamond films", *Annu. Rev. Mater. Res.* **1999**, *29*, 211-259.

[19] Zhou, D.; Krauss, A. R.; Corrigan, T. D.; McCauley, T. G.; Chang, R. P. H.; Gruen, D. M. "Microstructure and field emission of nanocrystalline diamond prepared from c60 precursors", *J. Electrochem. Soc.* **1997**, *144*, L224 - L228.

[20] Zhou, D.; Gruen, D. M.; Qin, L. C.; McCauley, T. G.; Krauss, A. R. "Control of diamond film microstructure by Ar additions to CH_4/H_2 microwave plasmas", *J. Appl. Phys.* **1998**, *84*, 1981-1989.

[21] Corrigan, T. D.; Gruen, D. M.; Krauss, A. R.; Zapol, P.; Chang, R. P. H. "The effect of nitrogen addition to Ar/CH_4 plasmas on the growth. morphology and field emission of ultrananocrystalline diamond", *Diam. Rel. Mater.* **2002**, *11*, 43-48.

[22] Fausett, B.; Granger, M. C.; Hupert, M. L.; Wang, J.; Swain, G. M.; Gruen, D. M. "The electrochemical properties of nanocrystalline diamond thin-films deposited from C_{60}/argon and methane/nitrogen gas mixtures", *Electroanal.* **2000**, *12*, 7-15.

[23] Show, Y.; Witek, M. A.; Sonthalia, P.; Swain, G. M. "Characterization and electrochemical responsiveness of boron-doped nanocrystalline diamond thin-film electrodes", *Chem. Mater.* **2003**, *15*, 879-888.

[24] Wang, S.; Butler, J. E.; Swain, G. M. "The structural and electrochemical properties of boron-doped nanocrystalline diamond thin-film electrodes grown from Ar-rich and H_2-rich source gases", *Diam. Rel. Mater.* **2009**, *18*, 669-677.

[25] Luong, J. H. T.; Male, K. B.; Glennon, J. D. "Boron-doped diamond electrode: synthesis, characterization, functionalization and analytical applications", *Analyst*, **2009**, *134*, 1965-1979.

[26] Einaga, Y. “Diamond electrodes for electrochemical analysis”, *J. Appl. Electrochem.* **2010**, *40*, 1807-1816.

[27] Einaga, Y.; Foord, J. S.; Swain, G. M. “Diamond electrodes: diversity and maturity”, *MRS Bull.* **2014**, *39*, 525-532.

[28] Macpherson, J. V. “A practical guide to using boron doped diamond in electrochemical research”, *Phys. Chem. Chem. Phys.* **2015**, *17*, 2935-2949.

[29] Cobb, S. J.; Ayres, Z. J.; Macpherson, J. “Boron doped diamond: a designer electrode material for the twenty-first century”, *Annu. Rev. Anal. Chem.* **2018**, *11*, 463-484.

[30] Muzyka, K.; Sun, J.; Fereja, T. H.; Lan, Y.; Zhang, W.; Xu, G. “Boron-doped diamond: current progress and challenges in view of electroanalytical applications”, *Anal. Methods*, **2019**, *11*, 397-414.

[31] Griesbach, U.; Zollinger, D.; Pütter, H. Comninellis, C. “Evaluation of boron doped diamond electrodes for organic electrosynthesis on a preparative scale”, *J. Appl. Electrochem.* **2005**, *35*, 1265-1270.

[32] Ruther, R. E.; Cui, Q.; Hamers, R. J. “Conformational disorder enhances electron transfer through alkyl monolayers: ferrocene on conductive diamond”, *J. Am. Chem. Soc.* **2013**, *135*, 5751-5761.

[33] Hapiot, P.; Lagrost, C. “Electrochemical reactivity in room-temperature ionic liquids”, *Chem. Rev.* **2008**, *108*, 2238-2264.

[34] Federov, M. V.; Kornyshev, A. A. “Ionic liquids at electrified interfaces”, *Chem. Rev*. **2014**, *114*, 2978-3036.

[35] Uysal, A.; Zhou, H.; Feng, G.; Lee, S. S.; Li, S.; Cummings, P. T.; Fulvio, P. F.; Dai, S.; McDonough, J. K.; Gogotsi, Y.; Fenter, P. “Interfacial ionic liquids: connecting static and dynamic structures”, *J. Phys.: Condens. Matter*, **2014**, *27*, 032101.

[36] Watanabe, M; Thomas, M. L.; Zhang, S.; Ueno, K.; Yasuda, M.; Dokko, K. “Application of ionic liquids to energy storage and conversion materials and devices”, *Chem. Rev*. **2017**, *117*, 7190–7239.

[37] Paul, A.; Muthukurmar, S.; Prasad, S. “Review-room-temperature ionic liquids for electrochemical application with special focus on gas sensors”, *J. Electrochem. Soc.* **2019**, *167*, 037511.

[38] Zhou, H.; Bai, S.; Zhang, Y.; Xu, D.; Wang, M. “Recent advances in ionic liquids and ionic liquid-functionalized graphene: catalytic application and environmental remediation”, *Int. J. Environ. Res. Public Health*, **2022**, *19*, 7584.

[39] Wang, P.; Zakeeruddin, S. M.; Moser, J. E.; Grätzel, M. "A new ionic liquid electrolyte enhances the conversion efficiency of dye-sensitized solar cells", *J. Phys. Chem. B*, **2003**, *107*, 13280-13285.

[40] Buzzeo, M. C.; Hardacre, C.; Compton, R. G. "Use of room temperature ionic liquids in gas sensor design", *Anal. Chem.* **2004**, *76*, 4583-4588.

[41] Ma, C. A.; Li, M. C.; Zheng, Y. F.; Liu, B. Y. "Electro-oxidation of formaldehyde on polyaniline prepared in 1-ethylimidazolium trifluoroacetate", *Electrochem. Solid-State Lett.* **2005**, *8*, G122-G124.

[42] Howlett, P. C.; MacFarlane, D. R.; Hollenkamp, A. F. "High lithium metal cycling efficiency in a room-temperature ionic liquid", *Electrochem. Solid-State Lett.* **2004**, *7*, A97-A101.

[43] Liu, H.; Yu, H. "Ionic liquids for electrochemical energy storage devices applications", *J. Mater. Sci. Technol.* **2019**, *35*, 674-686.

[44] Chang, B. Y.; Hong, S. Y.; Yoo, J.S.; Park, S. M. "Determination of electron transfer kinetic parameters by fourier transform electrochemical impedance spectroscopic analysis", *J. Phys. Chem. B*, **2006**, *110*, 19386-19392.

[45] Fietkau, N.; Clegg, A. D.; Evans, R. G.; Villagrán, C.; Hardacre, C.; Compton, R. G. "Electrochemical rate constants in room temperature ionic liquids: the oxidation of a series of ferrocene derivatives", *ChemPhysChem,* **2006**, *7*, 1041-1045.

[46] Silvester, D. S.; Rogers, E. I.; Brosse-Antle, L. E.; Broder, T. L.; Compton, R. G. "The electrochemistry of simple inorganic molecules in room temperature ionic liquids", *J. Braz. Chem. Soc*. **2008**, *19*, 611-620.

[47] Rogers, E. I.; Silvester, D. S.; Poole, D. L.; Aldous, L.; Hardacre, C.; Compton, R. G. "Voltammetric characterization of the ferrocene/ferrocenium and cobaltocenium/cobaltocene redox couples in RTILs", *J. Phys. Chem. C*, **2008**, *112*, 2729-2735.

[48] Tachikawa, N.; Katayama, Y.; Miura, T. "Electrode kinetics of ferrocenium/ferrocene in some amine-based room temperature ionic liquids", *Electrochem. Solid-State Lett.* **2009**, *12*, F39-F41.

[49] Fontaine, O.; Lagrost, C.; Ghilane, J.; Martin, P.; Trippé, G.; Fave, C.; Lacroix, J. -C.; Hapiot, P.; Randriamahazaka, H. N. "Mass transport and heterogeneous electron transfer of a ferrocene derivative in a room temperature ionic liquid", *J. Electroanal. Chem.* **2009**, *632*, 88-96.

[50] Barrosse-Antle, L. E.; Aldous, L.; Hardacre, C.; Bond, A. M.; Compton, R. G. "Dissolved argon changes the rate of diffusion in room temperature ionic liquids: effect of the presence

and absence of argon and nitrogen on the voltammetry of ferrocene", *J. Phys. Chem. C,* **2009**, *113*, 7750-7754.

[51] Xiao, L.; Dickinson, E. J. F.; Wildgoose, G. G.; Compton, R. G. "A comparison of electron transfer kinetics of three common carbon electrode surfaces in acetonitrile and in room temperature ionic liquid 1-butyl-3-methylimidiazonium hexafluorophosphate: correlation to surface structure and the limit of the diffusion domain approximation", *Electroanal.* **2010**, *22*, 269-276.

[52] Brosse-Antle, L. E.; Bond, A. M.; Compton, R. G.; Omahoney, A. M.; Rogers, E. I.; Silvester, D. S. "Voltammetry in room temperature ionic liquids: comparisons and contrasts with conventional electrochemical solvents", *Chem. Asian J.* **2010**, *5*, 202-230.

[53] Brinis, N.; Aoudia, K.; Chaal, L.; Saidani, B.; Deslouis, C. "Heterogeneous electron transfer and diffusivities of ferrocene/ferrocenium couple in toluene/phosphonium-based ionic liquid solutions", *J. Electroanal. Chem*. **2013**, *692*, 46-52.

[54] Bahadori, L.; Chakrabati, M. H.; Hashim, M. A.; Manan, N. S. A.; Mjalli, F. S.; AlNashef, I. M.; Brandon, N. P. "Temperature effects on the kinetics of ferrocene and cobaltocenium in methyltriphenylphosphonium bromide based deep eutectic solvents", *J. Electrochem. Soc*. **2015**, *162*, H617-H624.

[55] Bentley, C. L.; Li, J.; Bond, A. M.; Zhang, J. "Mass-transport and heterogeneous electron transfer kinetics associated with the ferrocene/ferrocenium process in ionic liquids", *J. Phys. Chem. C,* **2016**, *120*, 16516-16525.

[56] Wächter, N.; Munson, C.; Jarošová, R.; Berkun, I.; Hogan, T.; Rocha-Filho, R. C.; Swain, G. M. "Structure, electronic properties, and electrochemical behavior of a boron-doped diamond/quartz optically transparent electrode", *ACS Appl. Mater. Interfaces*, **2016**, *8*, 28325-28337.

[57] Nicholson, R. S. "Theory and application of cyclic voltammetry for measurement of electrode reaction kinetics", *Anal. Chem.* **1965**, *37*, 1351-1355.

[58] Lavagnini, I.; Antiochia, R.; Magno, F. "An extended method for the practical evaluation of the standard rate constant from cyclic voltammetric data", *Electroanal.* **2004**, *16*, 505-506.

[59] Córdoba-Torres, P.; Mesquita, T. J.; Nogueira, R. P. "Relationship between the origin of constant-phase element behavior in electrochemical impedance spectroscopy and electrode surface structure", *J. Phys. Chem. C* **2015**, *119*, 4136–4147.

[60] Hirschorn, B.; Orazem, M. E.; Tribollet, B.; Vivier, V.; Frateur, I.; Musiani, M. "Determination of effective capacitance and film thickness from constant-phase-element parameters", *Electrochim. Acta,* **2010**, *55*, 6218-6227.

[61] Ren, S.; Hou, Y.; Wu, W.; Liu, W. “Purification of ionic liquids: sweeping solvents by nitrogen”, *J. Chem. Eng. Data,* **2010**, *55*, 5074-5077.

[62] Jarošová, R.; Swain, G. M. “Rapid preparation of room temperature ionic liquids with low water content as characterized with a t*a*-C:N electrode”, *J. Electrochem. Soc.* **2015**, *162*, H507-H511.

[63] Jarošová, R.; Bhardwaj, K.; Swain, G. M. “Temperature dependence of the heterogeneous electron-transfer rate constant for ferrocene carboxylic acid in room temperature ionic liquids at microstructurally distinct carbon electrodes”, *J. Electroanal. Chem.* **2020**, *875*, 114744.

[64] Bennett, E.; Song, C.; Huang, Y.; Xiao, J. “Measured relative complex permittivities for multiple series of ionic liquids”, *J. Mol. Liq.* **2019**, *294*, 111571.

[65] Szirmai, P.; Pichler, T.; Williams, O. A.; Mandal, S.; Bäuerle, C.; Simon, F. “A detailed analysis of the raman spectra in superconducting boron doped nanocrystalline diamond”, *Phys. Status Solidi B*, **2012**, *249*, 2656-2659.

[66] May, P. W.; Ludlow, W. J.; Hannaway, M.; Heard, P. J.; Smith, J. A.; Rosser, K. N. “Raman and conductivity studies of boron-doped microcrystalline diamond, facetted nanocrystalline diamond and cauliflower diamond films”, *Diam. Relat. Mater.* **2008**, *17*, 105-117.

[67] Solin, S. A.; Ramdas, A. K. “Raman spectrum of diamond”, *Phys. Rev. B*, **1970**, *1*, 1687-1698.

[68] Mortet, V.; Gregora, I.; Taylor, A.; Lambert, N.; Ashcheulov, P.; Gedeonova, Z.; Hubik, P. “New perspectives for heavily boron-doped diamond Raman spectrum analysis”, *Carbon*, **2020**, *168*, 319-327.

[69] Gonon, P.; Gheeraert, E.; Deneuville, A.; Fontaine, F.; Abello, L.; Lucazeau, G. “Characterization of heavily B-doped polycrystalline diamond films using raman spectroscopy and electron spin resonance”, *J. Appl. Phys.* **1995**, *78*, 7059-7062.

[70] Narducci, D.; Guarnieri, C. R.; Cuomo, J. J. “Defect clustering and boron electrical deactivation in p-doped polycrystalline diamond films”, *J. Electrochem. Soc.* **1991**, *138*, 2446-2451.

[71] Bourgeois, E.; Bustarret, E.; Achatz, P.; Omnès, F.; Blase, X. “Impurity dimers in superconducting B-doped diamond: experiment and first-principles calculations”, *Phys. Rev. B*, **2006**, *74*, 094509.

[72] Bernard, M.; Baron, C.; Deneuville, A. “About the origin of the low wave number structures of the Raman spectra of heavily boron doped diamond films”, *Diam. Relat. Mater.* **2004**, *13*, 896-899.

[73] Sidorov, V. A.; Ekimov, E. A. “Superconductivity in diamond”, *Diam. Relat. Mater.* **2010**, *19*, 351-357.

[74] Ferrari, A. C.; Robertson, J. “Origin of the 1150-cm^{-1} Raman mode in nanocrystalline diamond”, *Phys. Rev. B*, **2001**, *63*, 121405.

[75] Buzzeo, M. C.; Evans, R. G.; Compton, R. G. “Non-haloaluminate room-temperature ionic liquids in electrochemistry-a review”, *ChemPhysChem*, **2004**, *5*, 1106-1120.

[76] Zhao, C.; Burrell, G.; Torriero, A. A. J.; Separovic, F.; Dunlop, N. F.; MacFarlane, D. R.; Bond, A. M. “Electrochemistry of room temperature protic ionic liquids”, *J. Phys. Chem. B*, **2008**, *112*, 6923-6936.

[77] Zhao, C.; Bond, A. M.; Lu, X. “Determination of water in room temperature ionic liquids by cathodic stripping voltammetry at a gold electrode”, *Anal. Chem.* **2012**, *84*, 2784-2791.

[78] Bhardwaj, K.; Parvis, F.; Wang, Y.; Blanchard, G. J.; Swain, G. M. “Effect of surface oxygen on the wettability and electrochemical properties of boron-doped nanocrystalline diamond electrodes in room-temperature ionic liquids”, *Langmuir*, **2020**, *36*, 5717-5729.

[79] Lucio, A. J.; Shaw, S. K.; Zhang, J.; Bond, A. M. “Double-layer capacitance at ionic liquid–boron-doped diamond electrode interfaces studied by fourier transformed alternating current voltammetry”, *J. Phys. Chem. C*, **2018**, *122*, 11777-11788.

[80] Lucio, A. J.; Shaw, S. K. “Effects and controls of capacitive hysteresis in ionic liquid electrochemical measurements”, *Analyst*, **2018**, *143*, 4887-4900.

[81] Alam, M. T.; Islam, M. M.; Okajima, T.; Ohsaka, T. “Capacitance measurements in a series of room-temperature ionic liquids at glassy carbon and gold electrode interfaces”, *J. Phys. Chem. C*, **2008**, *112*, 16600-16608.

[82] Islam, M. M.; Alam, M. T.; Okajima, T.; Ohsaka, T. “Electrical double layer structure in ionic liquids: an understanding of the unusual capacitance−potential curve at a nonmetallic electrode”, *J. Phys. Chem. C*, **2009**, *113*, 3386-3389.

[83] Lockett, V.; Sedev, R.; Ralston, J.; Horne, M.; Rodopoulos, T. “Differential capacitance of the electrical double layer in imidazolium-based ionic liquids: influence of potential, cation size, and temperature”, *J. Phys. Chem. C*, **2008**, *112*, 7486-7495.

[84] Lauw, Y.; Horne, M. D.; Rodopoulos, T.; Nelson, A.; Leermakers, F. A. M. “Electrical double-layer capacitance in room temperature ionic liquids: ion-size and specific adsorption effects”, *J. Phys. Chem. B*, **2010**, *114*, 11149-11154.

[85] Gomes, C.; Costa, R.; Pereira, C. M.; Silva, A. F. “The electrical double layer at the ionic liquid/au and pt electrode interface”, *RSC Adv.* **2014**, *4*, 28914-28921.

[86] Lockett, V.; Horne, M.; Sedev, R.; Rodopoulos, T.; Ralston, J. "Differential capacitance of the double layer at the electrode/ionic liquids interface", *Phys. Chem. Chem. Phys.* **2010**, *12*, 12499-12512.

[87] Fischer, A.; Show, Y.; Swain, G. M. "electrochemical performance of diamond thin-film electrodes from different commercial sources", *Anal. Chem.* **2004**, *76*, 2553-2560.

[88] Jarošová, R.; De Sousa Bezerra, P. M.; Munson, C.; Swain, G. M. "assessment of heterogeneous electron-transfer rate constants for soluble redox analytes at tetrahedral amorphous carbon, boron-doped diamond, and glassy carbon electrodes", *Phys. Status Solidi A*, **2016**, *213*, 2087-2098.

[89] Li, J.; Bentley, C. L.; Tan, S-y.; Mosali, V. S. S.; Rahman, M.A.; Cobb, S. J.; Guo, S-X.; Macpherson, J.V.; Unwin, P. R.; Bond, A. M.; Zhang, J. "Impact of sp^2 carbon edge effects on the electron-transfer kinetics of the ferrocene/ferricenium process at a boron-doped diamond electrode in an ionic liquid", *J. Phys. Chem. C*, **2019**, *123*, 17397-17406.

[90] Kim, D. Y.; Yang, J. C.; Kim, H. W.; Swain, G. M.; "Heterogeneous electron-transfer rate constants for ferrocene and ferrocene carboxylic acid at boron-doped diamond electrodes in a room temperature ionic liquid", *Electrochim. Acta*, **2013**, *94*, 49-56.

[91] Ernst, S.; Aldous, L.; Compton, R. G. "The electrochemical reduction of oxygen at boron-doped diamond and glassy carbon electrodes: a comparative study in a room-temperature ionic liquid", *J. Electroanal. Chem.* **2011**, *663*, 108-112.

[92] Nagasawa, Y.; Miyasaka, H. "Ultrafast solvation dynamics and charge transfer reactions in room temperature ionic liquids", *Phys. Chem. Chem. Phys.* **2014**, *16*, 13008-13026.

[93] Wang, Y.; Parvis, F.; Hossain, M. I.; Ma, K.; Jarošová, R.; Swain, G. M.; Blanchard, G. J. "Local and long-range organization in room temperature ionic liquids", *Langmuir*, **2021**, *37*, 605-615.

[94] Wang, Y.; Jarošová, R.; Swain, G. M.; Blanchard, G. J. "Characterizing the magnitude and structure-dependence of free charge density gradients in room-temperature ionic liquids". *Langmuir*, **2020**, *36,* 3038-3045.

[95] Wang, Y.; Adhikari, L.; Baker, G.A.; Blanchard, G. J. "Cation structure-dependence of the induced free charge density gradient in imidazolium and pyrrolidinium ionic liquids", *Phys. Chem. Chem. Phys*. **2022**, *24*, 19314-19320.

[96] Cannes, C.; Cachet, H.; Debiemme-Chouvy, C.; Deslouis, C.; Sanoit, J. D.; Le Naour, C.; Zinovyeva, V. A. "Double layer at [BuMeIm][Tf_2N] ionic liquid–Pt or −C material interfaces", *J. Phys. Chem. C*, **2013**, *117*, 22915-22925.

[97] Pan, Y.; Cleland, W. E.; Hussey, C. L. “Heterogeneous electron transfer kinetics and diffusion of ferrocene/ferrocenium in bis-(trifluoromethylsulfonyl) imide-based ionic liquids”, *J. Electrochem. Soc.* **2012**, *159*, F125-F133.

[98] Jayachandran, K.; Gupta, R.; Vats, B. G.; Kannan, S. “Extraction and electrochemical investigations of Pu(IV) employing green solvent system containing new bifunctional ligand and Bmim [NTf_2] ionic liquid”, *J. Radioanal. Nucl. Chem.* **2018**, *318*, 1009-1014.

[99] Lagrost, C.; Preda, L.; Volanschi, E.; Hapiot, P. “Heterogeneous electron-transfer kinetics of nitro compounds in room-temperature ionic liquids”, *J. Electroanal. Chem.* **2005**, *585*, 1-7.

[100] Nagy, L.; Gyetvai, G.; Kollár, L.; Nagy, G. “Electrochemical behavior of ferrocene in ionic liquid media”, *J. Biochem. Biophys. Methods*, **2006**, *69*, 121-132.

CHAPTER 5. THE ELECTROCHEMICAL ACTIVITY OF 1-ANTHRAQUINONE AND 2-ANTHRAQUINONE-MODIFIED CARBON ELECTRODES IN ROOM TEMPERATURE IONIC LIQUIDS

5.1. Abstract

Glassy carbon and boron-doped diamond disk electrodes were functionalized with anthraquinone-1-diazonium and anthraquinone-2-diazonium admolecules. The surface modification was accomplished by an electrochemically-assisted process. Evidence is provided for the successful modification of both electrodes, regardless of their microstructural differences. The electrochemical behavior of the modified glassy carbon (GC) and boron-doped diamond (BDD) electrodes was studied in two homologous room temperature ionic liquids: 1-ethyl-3-methylimidazolium tetrafluoroborate ([EMIM][BF_4]) and 1-hexyl-3-methylimidazolium tetrafluoroborate ([HMIM][BF_4]). The major differences between the two RTILs are the length of the alkyl substituent group and the viscosity. Comparison measurements were performed in an aqueous electrolyte solution. The objective of the research was to better understand how the factors such as the type of admolecule, RTIL type, and carbon electrode microstructure influence the electrochemical behavior of modified carbon electrodes.

5.2. Introduction

The chemical modification of carbon electrodes with different functional groups and admolecules is receiving increasing interest among researchers because of a multitude of applications including model systems for understanding electron transfer,[1, 2] molecular electronics,[3, 4] bioelectronics,[5, 6] and chemical sensors[7, 8]. For the modification process, the first step is to select a suitable choice for carbon material. There are multiple carbon electrode types due to the different allotropes and are diverse in terms of their properties. Different electrodes include single and polycrystalline diamond, diamond-like carbon, glassy carbon, carbon

nanotubes, graphene and graphite.[9] Carbon electrodes differ in their density of electronic states (DOS) and surface chemistry. For example, undoped diamond is a non-conductive material with a low DOS, while nanotubes have significant DOS.[8, 9]

There are many reports describing the modification of carbon electrodes.[9-20] surface modifications are divided into two types: non-covalent and covalent approaches. Non-covalent methods include π–π staking-based surface modification[16, 19] and surfactant adsorption[21-23]. Covalent methods include the reduction of diazonium cations,[12, 24-27] oxidation of amines,[28, 29] oxidation of carboxylates,[9, 11, 30, 31] oxidation of alcohols,[32, 33] hydrogenation and halogenation reactions of carbon.[8, 34]

A common method for carbon modification is to generate a radical of a molecule followed by its attachment via an electrochemical oxidation or reduction at the surface. This is a so-called electrochemically assisted process. This generally produces a covalently bond admolecule. The electrochemical reductive grafting of aryldiazonium salts is one of the most common methods for covalent modification of not only carbon electrodes,[12, 24] but also metals[15, 35] and semiconductors.[8, 36, 37] The ad-molecules can be phenyl[38] or heteroaryl rings.[8, 39]

Aryl diazonium salts are stable in aqueous acidic solutions and acetonitrile.[8, 11-13, 40] They can easily be synthesized using a mixture of an aromatic amine with sodium nitrite ($NaNO_2$) in an ice-cold aqueous acidic solution or aprotic medium (*e.g.,* acetonitrile) in the presence of *tert*-butyl nitrite.[8, 41] A potential step or potential sweep can be applied for the modification process.[8] The cyclic voltammetric response initially shows a reduction peak current, confirming the reduction of aryl diazonium salt and generation of the radical. This reduction peak decreases in magnitude with subsequent scans because of the blockade of the surface by admolecules. In other words, the derivatization is self-limiting. This technique has many advantages. The carbon-carbon bond

formed during the modification process is stable at temperatures up to 700 ºC and over a wide potential range. It is quite fast compared to other modification methods. The deposition time can be less than 10 seconds.[8] A quick test to verify the modification has occurred is to compare the cyclic voltammograms for potassium ferrocyanide system ($[Fe(CN)_6]^{-3/-4}$) before and after modification.[8] X-ray photoelectron spectroscopy (XPS) can also be applied to verify the modification process.[8, 42]

Room temperature ionic liquids (RTILs) have many applications in various scientific fields such as fuel cells[43, 44], self-assembly of amphiphiles[45-49], catalysis[50], biological applications,[51-53] organic synthesis[54-56], and chromatography.[57, 58] RTILs have gained the attention of the scientific community because of their advantages over traditional solvents. RTILs exhibit wide working potential windows, moderate electrical conductivity, high thermal and chemical stability, and negligible vapor pressure.[57, 59, 60] The electron transfer processes in RTILs proceed differently from traditional organic/aqueous solutions. Due to their applications in various fields and fundamental differences between aqueous solutions and RTILs, it is vital to have a better understanding of the factors which can affect the electron transfer processes in RTILs.[61, 62]

In general, the electron transfer process of quinones in aqueous solutions involves a one-step, two-electron redox reaction.[63-66] The redox reaction potential shifts with the pH of the electrolyte solution. At pH < 10, the reaction involves a two-electron-two-proton process (anthraquinone to anthracenediol). At pH > 10, the reaction undergoes a two-electron-one-proton process (anthraquinone to HAQ^-anion).[63, 67] There are several reports on the electrochemistry of quinones in aqueous solutions, including solution-phase and surface-bound species.[2, 15, 63, 68-70] However, most studies on quinones in RTILs focus on solution-phase electrochemistry.[71-75] To the best of our knowledge, there has been only one study describing the electrochemical activity

of surface-bound quinone molecules in RTILs by Compton's group.[76] In their work, glassy carbon microelectrodes were modified with multilayer films of 2-anthraquinonyl groups (AQ_L). The electrodes modified with a layer of 2-anthraquinonyl groups were characterized in three different RTILs. The electroactivity of the anthraquinonyl films depended on the size of the RTIL's cations.[76] Two distinct one-electron redox waves were observed in RTILs with smaller cations. However, a single one-electron wave was seen in RTILs with larger cations. The magnitude of the second reduction step decreases with increasing the size of the cation, as the steric hindrance prevents the full reduction of AQ films. In other words, it is suggested that using larger RTIL cations cannot completely reduce the film because the film's structure prevents proper charge balancing.[2]

Herein, we report on a study of the electrochemical activity of 1-anthraquinone and 2-anthraquinone-modified glassy carbon (1-AQ-GC and 2-AQ-GC) and boron-doped diamond (1-AQ-BDD and 2-AQ-BDD) electrodes in an aqueous electrolyte solution and two RTILs. The carbon electrodes were modified with anthraquinone-1-diazonium and anthraquinone-2-diazonium salts. The electrochemical activity of the modified (electrochemically-assisted) carbon electrodes in the aqueous solution (H_2SO_4) and two RTILs ([EMIM][BF_4] and [HMIM][BF_4]) was studied to learn more about how the carbon electrode microstructure and RTIL environment affect the redox activity of surface-confined adlayer.

5.3. Experimental

General Procedure for Modification of Carbon Electrodes. The working electrode was either glassy carbon (GC, Tokai GC-30) or boron-doped diamond (BDD, the proprietary method employed at the MSU-Fraunhofer Center for Coatings and Diamond Technologies was utilized to create the commercial disk electrode)[77]. The GC working electrode was pretreated before use by

mechanical polishing with successively smaller grades of alumina powder (1.0, 0.3, and 0.05 μm diam) slurried in ultrapure water, by hand, on separate polishing pads followed by ultrasonic cleaning. After each polishing step, the electrode was rinsed with ultrapure water, and then ultrasonically cleaned for at least 20 min in ultrapure water to remove the polishing debris. The polished GC was pretreated before use by exposure in the electrochemical cell to ultraclean isopropanol (distilled and stored over activated carbon) for 20-30 min. BDD was polished with alumina powder (0.05 μm diam) slurried in ultrapure water on a felt pad. The polished BDD was rinsed with deionized water. The electrode was then ultrasonically cleaned in ultrapure water for at least 20 min. As a final cleaning step, the BDD was exposed to ultrapure isopropanol for 20-30 min.

The reference and counter electrodes for the modification step were a Ag quasi-reference electrode (Ag QRE) and a platinum wire, respectively. 1 mM amino-anthraquinone (1-aminoanthraquinone, 2-aminoanthraquinone) was dissolved in acetonitrile containing 0.1 M tetramethylammonium tetrafluoroborate, $(C_2H_5)_4N(BF_4)$ as the supporting electrolyte. Then, 3mM *tert*-butyl nitrite was added to the solution. The addition of *tert*-butylnitrite generates the diazonium salt *in situ* (see figure 5.2.) Nitrogen gas was purged through the solution for 20 min before the modification to remove dissolved oxygen. Cyclic voltammetry was then used to modify the carbon electrodes by potential cycling from -0.2 to 0.8 V vs. AgQRE (scan rate: 0.1 V s^{-1}, cycles: 10). After modification, the electrode was rinsed with acetonitrile and ultrapure water, and then ultrasonically cleaned in acetonitrile and ultrapure water for 5 min each.

Electrochemical Measurements in Room Temperature Ionic Liquids and Aqueous Electrolyte Solution. Cyclic voltammetry (CV) was performed using a computer-controlled potentiostat (Model 650B or 650A, CH Instruments Inc., Austin, TX). Voltammograms were

recorded as a function of the scan rate (0.1 to 0.5 V s^{-1}). The current data were plotted as a function of applied potential. All measurements in RTILs were prepared in an N_2-filled vinyl glove box (Coy laboratories, MI). The measurements in aqueous solution were made outside the glove box on the laboratory bench.

Room Temperature Ionic Liquids. All electrochemical measurements in RTILs were performed in a nitrogen-purged vinyl glove box. The relative humidity in the box was routinely measured to be ≤ 0.1% using a hygrometer. The reference and counter electrodes were a Ag QRE and a platinum wire, respectively. RTILs were deoxygenated with argon gas purging for ~10 min before each measurement.

Aqueous Electrolyte Solution. A graphite rod was used as the counter electrode. A homemade Ag/AgCl electrode was used as the reference. Aqueous electrolyte solutions were deaerated with N_2 gas purging for 10-20 min before each measurement. These measurements were made outside the glove box on the laboratory bench.

Reagents for the Modification of Carbon Electrodes. 1-amino-anthraquinone (CAS: 82-45-1), 2-amino-anthraquinone (CAS: 117-79-3), tetraethylammonium tetrafluoroborate (CAS: 429-06-1) and acetonitrile (CAS: 75-05-8) were purchased from Sigma-Aldrich and used without further purification. *Tert*-butyl nitrite (CAS: 540-80-7) was obtained from Thermo Scientific™.

Reagents for Electrochemical Measurements in Aqueous Electrolyte Solution. Potassium chloride (CAS: 7447-40-7), potassium hexacyanoferrate(II) trihydrate (CAS: 14459-95-1), and sulfuric acid (CAS: 7664-93-9) were obtained from Sigma-Aldrich and used without further purification.

Reagents for Electrochemical Measurements in RTILs. The RTILs, 1-ethyl-3-methylimidazolium tetrafluoroborate ([EMIM][BF_4]), (CAS: 143314-16-3) and 1-hexyl-3-methylimidazolium tetrafluoroborate ([HMIM][BF_4]) (CAS: 244193-50-8) were purchased commercially from Iolitec (Tuscaloosa, AL, specified as ≥ 98% purity).

Preparation of Room Temperature Ionic Liquids. The RTILs were purified to remove water and other impurities using a pretreatment method known as the "sweeping method".[78, 79]

1. The "as-received" RTIL was first stored over activated carbon for at least 14 days. This step removes organic impurities. The RTIL was then removed using a syringe with a 0.45 μm Teflon syringe filter (Millex®HA) and transferred into a clean glass vial.

2. The filtered RTIL was then stored over activated molecular sieves (5Å) (Fisher Scientific Company) in the glass vial for at least one week to reduce water impurity. The molecular sieves were activated before use by heating at ~400 ºC in a furnace for two weeks.

3. A small volume of the purified RTIL was then transferred to a clean and dry glass vial in the nitrogen-purged vinyl glove box (Coy Laboratories, Grass Lake, MI) and then was heated at ~70 ºC for 50 min while purged continuously with ultrahigh purity argon gas (Airgas). When finished, the RTIL was transferred to the electrochemical cell in the glove box and the electrochemical measurements were initiated.

After purification, the water level measured in selected purified RTILs was below 100 ppm, as estimated by thermogravimetric analysis (TGA).[79] All glassware was cleaned by rinsing with ultrapure water, rinsing with isopropanol, and drying in an oven overnight before transferring to the glove box for use in the RTIL experiments. The ultrapure water used for glassware cleaning

was prepared using a Barnstead E-pure System (Thermo Scientific, USA). The ultrapure water had a resistivity of ≥17 MΩ-cm.

Physical Properties of Room-Temperature Ionic Liquids. Figure 5.1 shows the chemical structure of the two RTILs used.

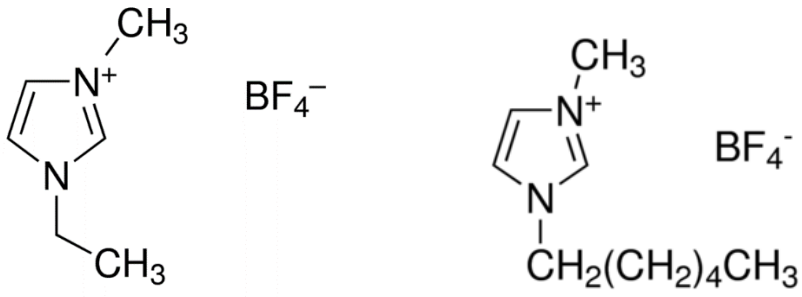

[EMIM][BF_4] **[HMIM][BF_4]**

Figure 5.1. Chemical structure of the RTILs used: ([EMIM][BF_4] and [HMIM][BF_4]).

The physical properties of water and the RTILs used in this research, as specified by the supplier, are presented in Table 5.1.

Table 5.1. Physical properties of water, [EMIM][BF_4], and [HMIM][BF_4] at 25 °C.

Analyte	Mol. Wt. (g mol^{-1})	Viscosity (cP)	Conductivity (mS cm^{-1})	Dielectric Constant	Density (g cm^{-3})
[EMIM][BF_4]	197.97	34*	14.1*	12.9[80]	1.28*
[HMIM][BF_4]	254.08	288*	1.2*	8.4[81]	1.15*

*Data were provided by the chemical supplier Iolitec.

5.4. Results

5.4.1. Modification of Carbon Electrodes

The general reaction scheme for the modification of both carbon electrodes with anthraquinone-1-diazonium (1-N_2^+-AQ) and anthraquinone-2-diazonium (2-N_2^+-AQ) is provided in Figure 5.2A and B. In general, the diazonium anthraquinone species is reduced to the aryl radical in the presence of *tert*-butylnitrite acting as an oxidizing agent in acetonitrile. The derivatization was performed directly in the electrochemical cell. The reference and counter electrodes for the modification step were a Ag quasi-reference electrode (Ag QRE) and a platinum wire, respectively. Cyclic voltammetry was used to modify the carbon electrodes by potential cycling from -0.2 to 0.8 V vs. AgQRE (scan rate: 0.1 V s^{-1}, cycles: 10). A covalent bond forms between the anthraquinone radical and a radical site on the carbon electrode. The 1-AQ and 2-AQ modified electrodes differ in the position of the bond between the anthraquinone moiety and the carbon electrode.

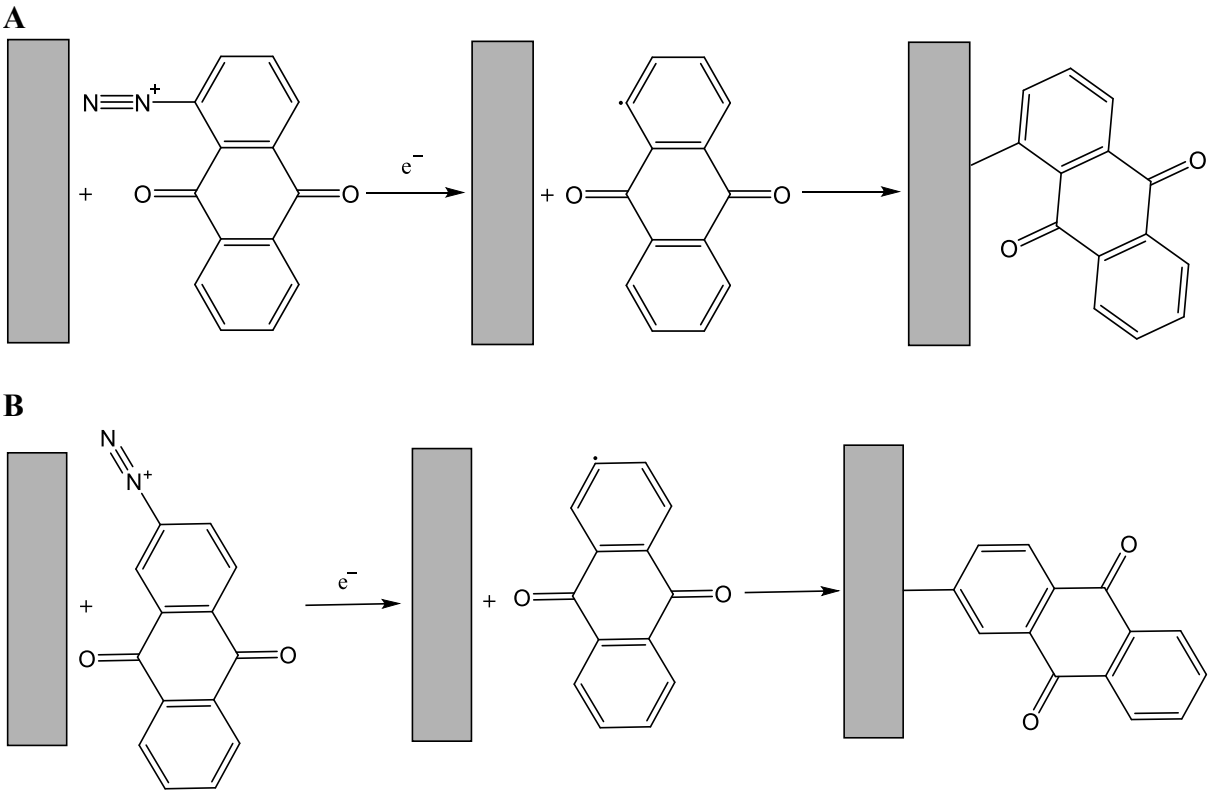

Figure 5.2. General reaction scheme for the electrochemically-assisted modification of carbon electrodes with (A) 1-N_2^+-AQ and (B) 2-N_2^+-AQ.

Figure 5.3A-D shows cyclic voltammograms during the electrochemically-assisted modification of GC (A and B) and BDD (C and D) with 1-N_2^+-AQ and 2-N_2^+-AQ in acetonitrile. The electrochemically-assisted modification was performed using a potential range of 0.8 to -0.2 V vs. Ag QRE. A reduction current is seen on the initial scan commencing at 0.5 V for GC and 0.3 V for BDD. This indicates the reduction requires a little more overpotential on BDD. The magnitude of the reduction current at both electrodes is largest on the first scan and decreases with the scan number. A reactive radical is produced by the elimination of N_2. The progressive build-up of the adlayer serves as a barrier to further electron transfer between the diazonium molecules in solution and the carbon electrode surface to produce reactive radical species in the interfacial region. In other words, the surface modification by this process is self-limiting. The modification

of carbon electrodes with anthraquinone diazonium has been reported by Kullapere et al.[82] Table 5.2 provides a summary of the onset potentials (E_{red}) for the diazonium reduction current on the two electrodes.

For the modification of GC with 1-N_2^+-AQ and 2-N_2^+-AQ, the reduction current for radical formation initiated at 0.52 ± 0.12 and 0.34 ± 0.04 V vs. Ag QRE, respectively (n=3 electrodes). These values are close to the previously reported values for the reduction of 1-N_2^+-AQ and 2-N_2^+-AQ at GC. Bélanger et al., for example, reported a reduction potential of 0.5 and 0.35 V vs Ag/AgCl for the 1-N_2^+-AQ and 2-N_2^+-AQ modification of GC, respectively.[11] Kullapere et al. reported a reduction potential of 0.28 V vs. saturated calomel electrode (SCE) for the 2-N_2^+-AQ modification at GC.[82] Baranton et al. reported a reduction potential at 0.47 V vs. Ag/AgCl for the 1-N_2^+-AQ modification at GC.[64]

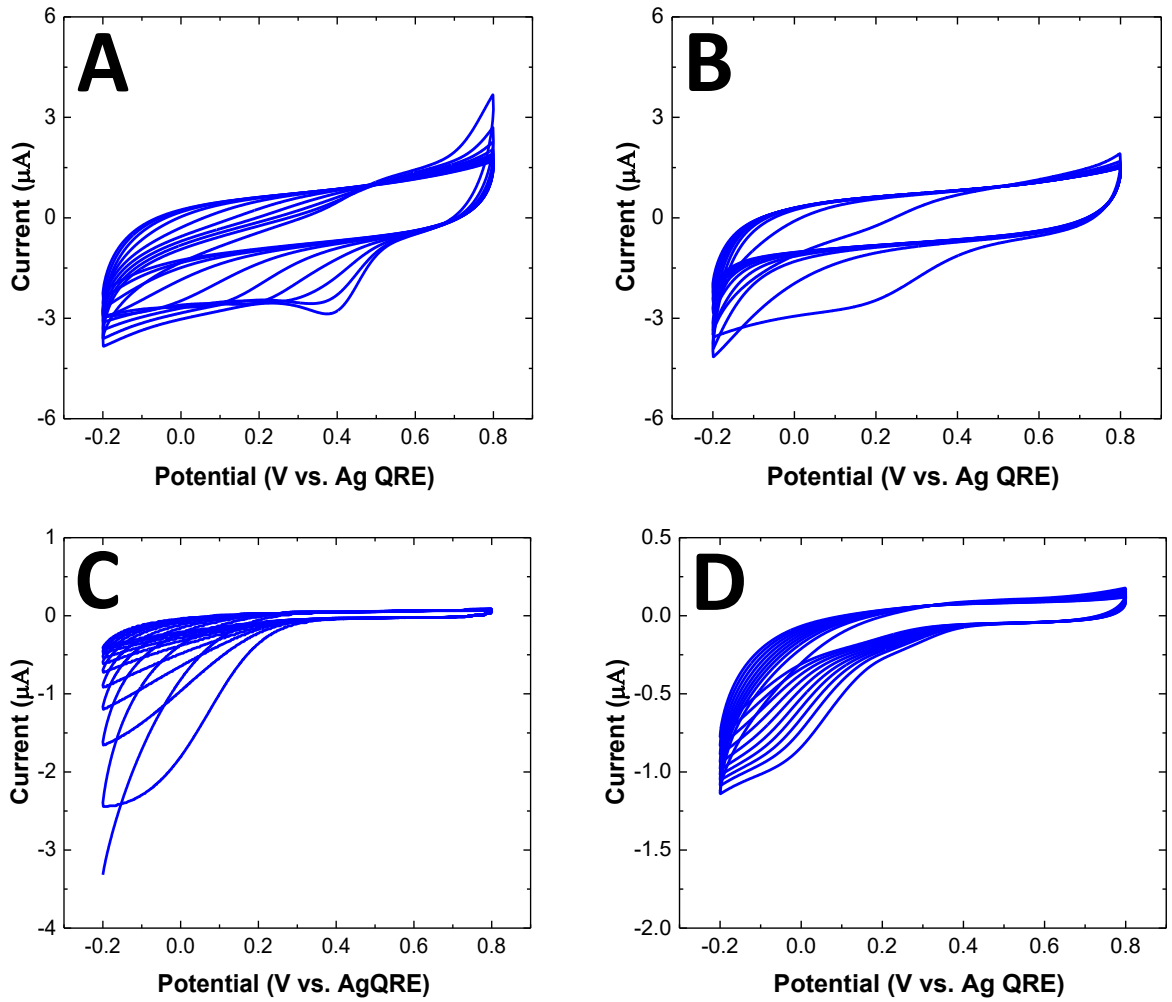

Figure 5.3. Repetitive cyclic voltammograms for the electrochemically-assisted modification of GC and BDD electrodes with 1-N_2^+-AQ and 2-N_2^+-AQ in acetonitrile containing 0.1 M tetraethylammonium tetrafluoroborate ($(C_2H_5)_4NBF_4$) electrolyte. (A) glassy carbon modified with 1-N_2^+-AQ, (B) glassy carbon modified with 2-N_2^+-AQ, (C) BDD modified with 1-N_2^+-AQ, (D) BDD modified with 2-N_2^+-AQ. Scan Rate = 0.1 V s^{-1}.

For BDD, the reduction currents for 1-N_2^+-AQ and 2-N_2^+-AQ modification start at 0.37 ± 0.17 and 0.38 ± 0.06 V vs. Ag QRE, respectively (n =3 electrodes). For GC, the required onset potential for 1-N_2^+-AQ reduction is more positive compared to that of 2-N_2^+-AQ. However, for BDD, the onset potential is approximately the same for both 1-N_2^+-AQ and 2-N_2^+-AQ. Importantly, both carbon electrode types, regardless of their microstructure, support the reduction

of both diazonium precursor molecules and both can be derivatized by this electrochemically-assisted method.

Table 5.2. Summary of the onset potentials for reduction of the diazonium precursor molecules.

Electrode	Modifying Species	E_{red} (V) *
GC	**1-N_2^+-AQ**	0.52 ± 0.12
GC	**2-N_2^+-AQ**	0.34 ± 0.04
BDD	**1-N_2^+-AQ**	0.37 ± 0.17
BDD	**2-N_2^+-AQ**	0.38 ± 0.06

Data are presented as mean ± standard deviation for n=3 measurements with each electrode type.
* E_{red} is the onset potential for the anthraquinone radical formation.

5.4.2. Evidence for Surface Modification

Blocking Effect for Potassium Ferrocyanide

Figure 5.4A-B shows cyclic voltammograms for unmodified and modified GC and BDD electrodes in the presence of 0.1 mM $Fe(CN)_6^{-3/-4}$ in 1M KCl. The blocking ability of anthraquinone adlayer toward redox probes like $Fe(CN)_6^{-3/-4}$ is well-established.[83] Well-defined oxidation and reduction peaks can be seen for $Fe(CN)_6^{-3/-4}$ at both carbon electrodes before modification (Figure 5.4A and B-black curves). The peak separation is 60 and 89 mV for GC and BDD, respectively. However, no oxidation and reduction peaks are observed for the redox probe molecule at 1-(or 2)-AQ-GC and 1-(or 2)-AQ-BDD modified electrodes (Figure 5.4A and B-blue or red curves). There is a small amount of faradic current for $Fe(CN)_6^{-3/-4}$ at 2-AQ-BDD suggesting that the adlayer may not be as completely formed (pinholes) as the 1-AQ adlayer assumes to be.

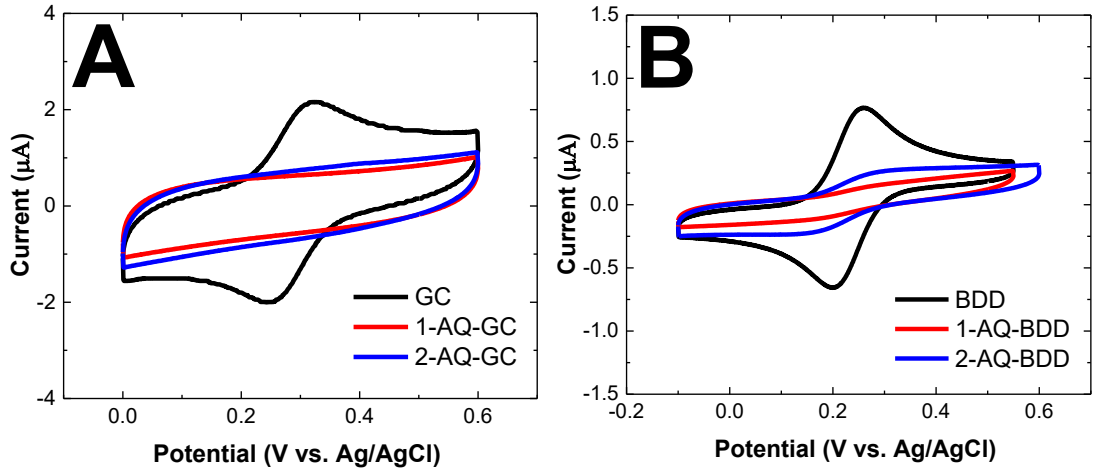

Figure 5.4. Cyclic voltametric *i-E* curves for 0.1 mM $Fe(CN)_6^{-3/-4}$ in 1 M KCl at (A) unmodified and modified GC with 1-AQ or 2-AQ and (B) unmodified and modified BDD with 1-AQ and 2-AQ. Scan rate = 0.1 V s^{-1}.

The presence of an organic adlayer at the electrode surface prevents further electron transfer with the redox system. The blocking effect is consistent with a relatively thick and insulating adlayer on both surfaces that does not support electron tunneling for this redox system. The electrochemical activity of $Fe(CN)_6^{-3/-4}$ at carbon electrodes depends on the surface chemistry, cleanliness, and microstructure.[69, 84-86] Both AQ adlayers show an equal blocking effect for this redox system on both sp^2-bonded GC and sp^3-bonded BDD. The reasons for the inhibited kinetics are supposed to be the blocking of mediating surface carbon-oxygen functional groups, specifically carbonyl groups[84], and an increased barrier to electron tunneling through the adlayer.[84-86]

Adlayer Stability Assessed Through An Ultrasonication Test

The main goal of modification is to generate a stable covalently bond organic layer on the electrode surface, not a physisorbed layer. Ultrasonication is a method for testing the stability of the diazonium adlayer on modified carbon electrodes.[12, 20, 87, 88]

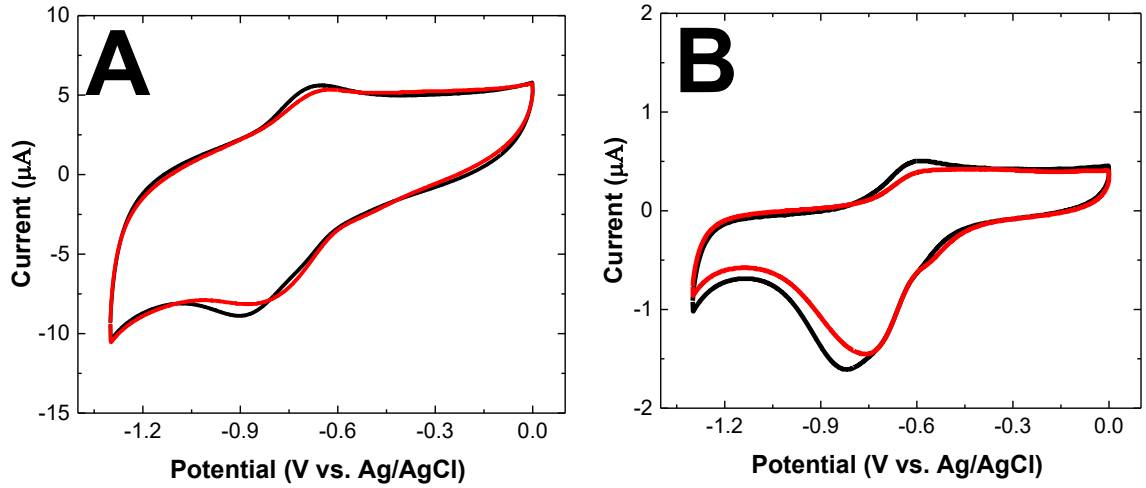

Figure 5.5. Cyclic voltammetric *i-E* curves for (A) GC and (B) BDD electrodes both modified with a 1-AQ adlayer in 1M KCl. Curves are presented for the modified electrodes before (black) and after (red) ultrasonication in acetonitrile for 20 min. Scan rate = 0.1 V s^{-1}. Electrode geometric areas for GC and BDD were 0.07 and 0.03 cm^2, respectively.

Figure 5.5A and B show cyclic voltammetric *i-E* curves for the 1-AQ adlayer on (A) GC and (B) BDD electrodes in 1M KCl, before and after ultrasonication for 20 min in acetonitrile. For GC, well-resolved reduction and oxidation peaks are seen at -0.878 V and -0.693 V vs. Ag/AgCl. At pH lower than 10, the reaction involves a two-electron-two-proton process involving the reduction of anthraquinone to anthracenediol.[63] The reduction peak current is -4.1 µA and the oxidation peak current is 1.5 µA. The ΔE_p is 185 mV (Figure 5.5A-black). The large ΔE_p indicates that even though the redox molecule is bonded to the surface, the electron-transfer kinetics are rather sluggish. After ultrasonication, the curve shape is unchanged with the reduction and oxidation peak currents remaining approximately the same. This indicates the redox-active admolecule coverage is unchanged by the ultrasonic treatment. Interestingly, ΔE_p decreases to 137 mV meaning the electron-transfer kinetics are improved by the treatment. The reason for this is not so obvious. The reduction and oxidation peak potentials for 1-AQ-GC after ultrasonication

are at -0.814 and -0.677 V vs. Ag/AgCl, respectively. The reduction and oxidation peak currents changed little with values of -2.9 and 0.88 μA, respectively.

For 1-AQ-BDD, a well-defined reduction peak is seen with a more truncated oxidation peak. The reduction peak for 1-AQ-BDD is at -0.808 V vs. Ag/AgCl. The reduction peak current is -1.3 μA. The reduction peak potential for 1-AQ-BDD after ultrasonication is at -0.748 V vs. Ag/AgCl. The reduction and oxidation peak currents are largely unchanged and indicated the stability of the adlayer. Interestingly, the curves have a very asymmetric shape with a broad reduction peak between -0.5 and -1.0 V, while there is more of a steady state curve for the oxidation rather than a peak with current flowing from -0.7 to 0 V.

The overall finding is that very small decreases in current are seen for both electrodes after ultrasonication, consistent with generally good stability of the admolecule. Hence, the majority of the adlayer molecules remain redox-active and bonded. Interestingly, the ΔE_p values decreased after the ultrasonication particularly for GC. This indicates faster redox reaction kinetics perhaps because of the removal of some impurities from the electrode surface. Impurities can slow down the electron-transfer kinetics at the surface of carbon electrodes.[89]

5.4.3. Electrochemical Activity of Modified Carbon Electrodes in RTILs

The electrochemical activity of 1-AQ and 2-AQ-modified GC and BDD in two RTILs, [EMIM][BF_4] and [HMIM][BF_4], was studied. The physical properties of two RTILs are given in Table 5.1. Representative curves for 1-AQ and 2-AQ at GC are presented in Figure 5.6 A and E (1-AQ and 2-AQ in [EMIM][BF_4]) and 5.6 C and G (1-AQ and 2-AQ in [HMIM][BF_4]). The curves were recorded at scan rates from 0.1 to 0.5 V s^{-1}. Anthraquinone has been shown to undergo

two one-electron reduction steps in aprotic room temperature ionic liquids, as previously reported:[75, 76]

$$Q^0 + e^- \rightarrow Q^{\bullet -} \qquad [1]$$

$$Q^{\bullet -} + e^- \rightarrow Q^{2-} \qquad [2]$$

The first step leads to the formation of the radical anion, $Q^{\bullet -}$. The second reduction step, the formation of dianion, Q^{2-}, occurs at more negative potentials.[75] Similarly shaped curves are seen for both 1-AQ and 2-AQ adlayers on GC in both [EMIM][BF_4] and [HMIM][BF_4], respectively. The voltammograms for both adlayers in both RTILs are characterized by two reduction peaks separated by ca. 300 mV and two oxidation peaks also separated by ca. 300 mV. The separation of the two peaks is not notable for 2-AQ. The reduction of 1-AQ and 2-AQ commences at ~ -0.6 V on GC in [EMIM][BF_4]. The reduction of 1-AQ and 2-AQ requires a more negative potential to reduce in [HMIM][BF_4] with an onset value of -0.7 V. The peak current increases with the scan rate for both 1-AQ and 2-AQ in the two RTILs (Fig. 5.6 B, D, F, H) with no shift or very small shifts in the reduction and oxidation potentials with increasing scan rate. The linearity of the peak current-scan rate relationship indicates the redox reaction for both 1-AQ and 2-AQ is occurring through an adsorbed or surface confined state.

In [EMIM][BF_4], 2-AQ undergoes an overall two-electron redox reaction with two well-delineated one-electron transfer steps. In the RTILs, unlike aqueous electrolyte solution, there is a sufficient energy difference between the two steps that can be resolved on the potential axis. The less negative reduction and oxidation peaks are assigned to the $Q^{\bullet -}$/Q redox couple, while the more negative oxidation and reduction peaks are assigned to the Q^{2-}/ $Q^{\bullet -}$ redox couple. For 1-AQ in [EMIM][BF_4] and for both 1-AQ and 2-AQ in the more viscous [HMIM][BF_4], the two stepwise,

one-electron transfer reaction is not as apparent. There are two apparent reduction peaks separated by ca. 300 mV, but the oxidation peaks collapse into one broad peak on the reverse scan.

The redox peaks for the 2-AQ-GC are better defined and distinct in [EMIM][BF_4] with a smaller cation size as compared to [HMIM][BF_4]; an observation previously reported by Compton's group.[2] The authors proposed that the ionic liquid with a larger cation inhibits the completion of the film's reduction because of the steric hindrance in terms of providing counterbalancing charge for the $Q^{\cdot-}$ and Q^{2-} species in the adlayer. In other words, a larger cation prevents a complete charge compensation.[76]

In general, the magnitude of oxidation and reduction peak currents for the first step, the formation of the radical anion, $Q^{\bullet-}$, are larger compared to the magnitude of oxidation and reduction peak currents for the second reduction step, the formation of the dianion, Q^{2-}. The peaks for the second step, as compared to the first step, are smaller in magnitude, broad, and not well-defined.[76]

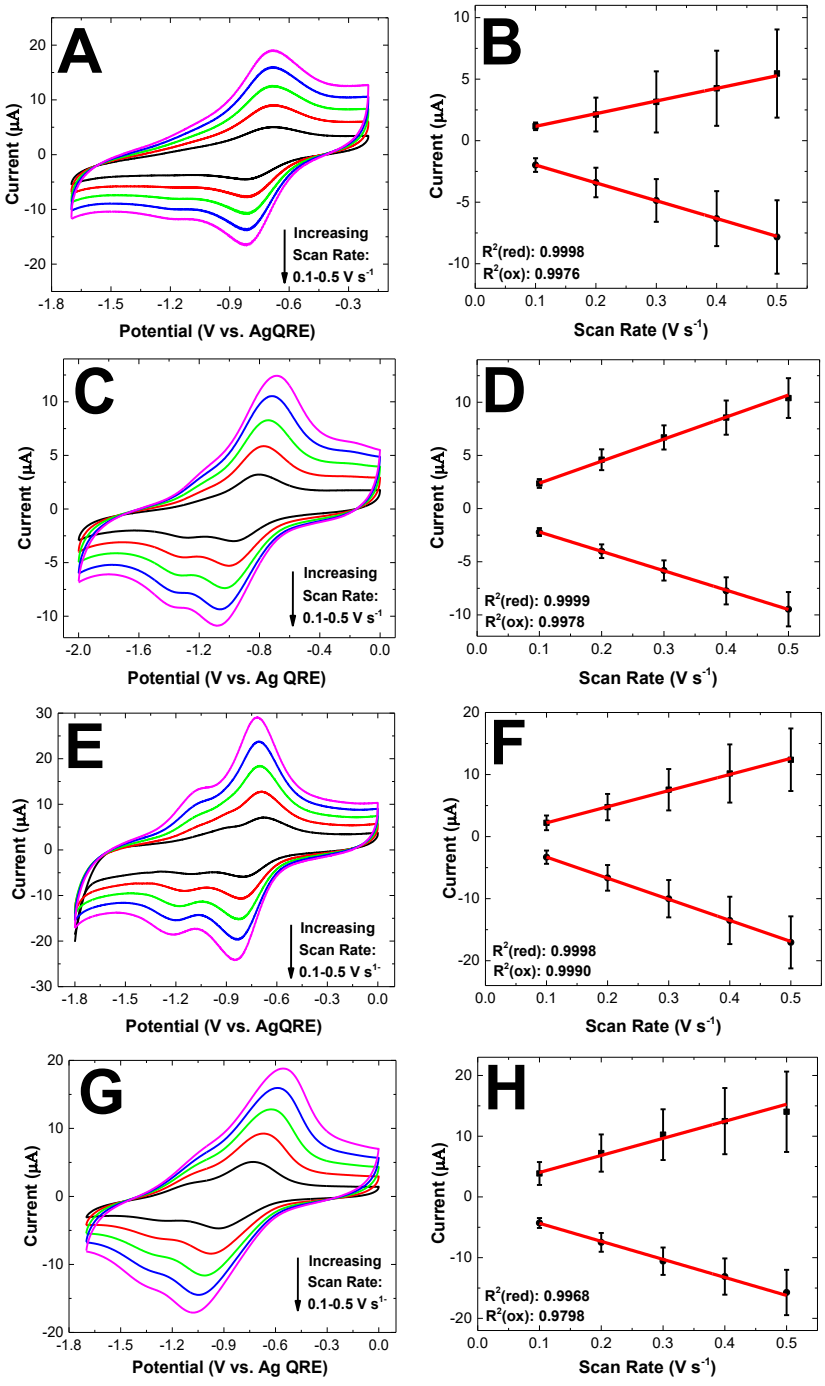

Figure 5.6. Representative cyclic voltammetric *i-E* curves for 1-AQ-GC and 2-AQ-GC in [EMIM][BF_4] and [HMIM][BF_4]. (A) 1-AQ-GC, [EMIM][BF_4], (C) 1-AQ-GC, [HMIM][BF_4], (E) 2-AQ-GC, [EMIM][BF_4], (G) 2-AQ-GC, [HMIM][BF_4]. Plots of oxidation and reduction currents vs. scan rate for the first redox reaction ($Q^0 + e^- \rightarrow Q^{\bullet -}$) at 1-AQ-GC and 2-AQ-GC in [EMIM][BF_4] and [HMIM][BF_4]. (B) 1-AQ-GC, [EMIM][BF_4], (D) 1-AQ-GC, [HMIM][BF_4], (F) 2-AQ-GC, [EMIM][BF_4], (H) 2-AQ-GC, [HMIM][BF_4]. Scan rate: 0.1-0.5 V s^{-1}. Data are provided as mean ± standard deviation for N=3 modified electrodes of each type. Linear regression was performed on the plot of the current vs. scan rate. R^2 correlation coefficient for the plots are provided.

Figure 5.6 B, D, F, and H show plots of the peak current versus the scan rate for the less negative $Q^{\bullet-}/Q$ redox reaction. The plots are linear in both RTILs with near-zero y-axis intercepts and linear regression coefficients (R^2) > 0.97 consistent with a surface-confined redox process.[76] The relationship between the peak current for an adsorbed redox species and the surface coverage, Γ, is given by [3],[76, 90]

$$i_p = \frac{n^2F^2}{4RT} A\Gamma\upsilon \qquad [3]$$

in which n, F, A, Γ, v, R, T, and i_p represent the number of transferred electrons per molecule, Faraday's constant, electrode area (cm^2), surface coverage (mol cm^{-2}), scan rate (V s^{-1}), gas constant, temperature (K), and peak current (A), respectively. Unlike the measurement in the aqueous electrolyte solution, the voltammetric response in the RTILs is consistent with two separate one-electron transfer steps. Table 5.3. shows experimental parameters determined from cyclic voltammetric data for 1-AQ-GC and 2-AQ-GC in the two RTILs.

Table 5.3. Summary of cyclic voltammetric data for 1-AQ-GC and 2-AQ-GC in [EMIM][BF_4] and [HMIM][BF_4].

Electrode	**RTILs**	**$\Delta E_{p,1}$ (V)***	**E_{mid} (V)***	**$i_{p,1}^{red}$ (µA)***	**$i_{p,1}^{red}/i_{p,1}^{ox}$ ***	**Γ (10^{-10}) (mol cm^{-2}) ** **
1-AQ-GC	**[EMIM][BF_4]**	0.07 ± 0.02	-0.75 ± 0.02	1.98 ± 0.56	1.69 ± 0.05	2.24 ± 0.69
1-AQ-GC	**[HMIM][BF_4]**	0.10 ± 0.03	-0.82 ± 0.07	2.20 ± 0.38	0.94 ± 0.10	2.79 ± 0.31
2-AQ-GC	**[EMIM][BF_4]**	0.08 ± 0.02	-0.79 ± 0.05	3.16 ± 0.94	1.53 ± 0.29	3.19 ± 0.90
2-AQ-GC	**[HMIM][BF_4]**	0.16 ± 0.001	-0.78 ± 0.08	4.18 ± 0.76	1.23 ± 0.39	5.02 ± 0.98

*Data are provided as mean ± standard deviation for N=3 and scan rate: 0.1 V s^{-1}.
**The surface coverage (Γ) is calculated for scan rate: 0.5 V s^{-1}. Surface coverage is calculated based on both reduction peak currents.

The reduction and oxidation peak potentials for the $Q^{\bullet-}$/Q redox reaction at 1-AQ-GC in [EMIM][BF_4] are at -0.79 ± 0.01 and -0.72 ± 0.03 vs. Ag QRE, respectively. The midpoint potential (E_{mid}) and peak potential separation (ΔE_p) for $Q^{\bullet-}$/Q redox reaction at 1-AQ-GC in [EMIM][BF_4] are -0.75 ± 0.02 V vs. Ag QRE and 0.07 ± 0.02 V, respectively. The reduction and oxidation peak currents for $Q^{\bullet-}$/Q redox reaction at 1-AQ-GC in [EMIM][BF_4] are -1.98 ± 0.56 and 1.17 ± 0.30 μA, respectively. The ratio of reduction to oxidation peak currents is 1.69 ± 0.05 (scan rate: 0.1 V s^{-1}).

The reduction and oxidation peak potentials for the $Q^{\bullet-}$/Q redox reaction at 1-AQ-GC in [HMIM][BF_4] are at -0.86 ± 0.08 and -0.77 ± 0.05 vs. Ag QRE, respectively. The midpoint potential (E_{mid}) and peak potential separation (ΔE_p) are -0.82 ± 0.07 V vs. Ag QRE and 0.10 ± 0.03 V, respectively. The reduction and oxidation peak currents for $Q^{\bullet-}$/Q redox reaction at 1-AQ-GC in [HMIM][BF_4] are -2.20 ± 0.38 and 2.36 ± 0.42 μA, respectively. The ratio of the reduction to oxidation peak current is 0.94 ± 0.10 (scan rate: 0.1 V s^{-1}).

The reduction and oxidation peak potentials for the $Q^{\bullet-}$/Q redox reaction at 2-AQ-GC in [EMIM][BF_4] are at -0.83 ± 0.04 and -0.75 ± 0.06 vs. Ag QRE, respectively. The midpoint potential (E_{mid}) and peak potential separation (ΔE_p) for the $Q^{\bullet-}$/Q redox reaction at 2-AQ-GC in [EMIM][BF_4] are -0.79 ± 0.05 V vs. Ag QRE and 0.08 ± 0.02 V, respectively. The reduction and oxidation peak currents are -3.16 ± 0.94 and 2.19 ± 0.93 μA, respectively. The ratio of the reduction to oxidation peak currents is 1.53 ± 0.29 (scan rate: 0.1 V s^{-1}).

The reduction and oxidation peak potentials for the $Q^{\bullet-}$/Q redox reaction at 2-AQ-GC in [HMIM][BF_4] are at -0.86 ± 0.08 and -0.70 ± 0.08 vs. Ag QRE, respectively. The midpoint potential (E_{mid}) and peak potential separation (ΔE_p) for the $Q^{\bullet-}$/Q redox reaction at 2-AQ-GC in [HMIM][BF_4] are -0.78 ± 0.08 V vs. Ag QRE and 0.16 ± 0.001 V, respectively. The reduction and

oxidation peak currents are -4.18 ± 0.76 and 3.74 ± 1.74 μA, respectively. The ratio of reduction to oxidation peak current is 1.23 ± 0.39 (scan rate: 0.1 V s^{-1}).

The electroactive surface coverage for both adlayers was determined by the integration of two reduction peak currents using Faraday's law and normalized to the geometric area of the GC electrode. The surface coverages for 1-AQ-GC in [EMIM][BF_4] and [HMIM][BF_4] are 2.24 (± 0.69) $\times 10^{-10}$ and 2.79 (± 0.31) $\times 10^{-10}$ mol cm^{-2}, respectively. The surface coverage for 2-AQ-GC in [EMIM][BF_4] and [HMIM][BF_4] is 3.19 (± 0.90) $\times 10^{-10}$ and 5.02 (± 0.98) $\times$ 10^{-10} mol cm^{-2}, respectively. There is a slightly greater surface coverage for 2-AQ-GC because of a greater presence of admolecules in the redox-active state. The Student's t-test revealed the surface coverage for each adlayer is statistically the same in both RTILs. This surface coverage is smaller than what was reported previously by Compton's group by integrating the 1st peak ($AQ_L/AQ_L^{\cdot -}$) reduction scan which were found from 1.4×10^{-9} to 2.1×10^{-9} mol cm^{-2}.

Figure 5.7 A, C, E, and G show cyclic voltammetric *i-E* curves for 1-AQ-BDD and 2-AQ-BDD in [EMIM][BF_4] and [HMIM][BF_4]. The curves were recorded at scan rates from 0.1 to 0.5 V s^{-1}. Two sets of oxidation and reduction peaks are seen for the 2-AQ-BDD electrodes in [HMIM][BF_4]. However, only one oxidation and two reduction peaks are resolved for 1-AQ-BDD electrodes in [HMIM][BF_4]. One well-shaped reduction peak with a poor-defined and broad oxidation peak can be seen for both 1-AQ-BDD and 2-AQ-BDD electrodes in [EMIM][BF_4]. In fact, the oxidation current is more of a steady state and extends from -0.6 to 0.2 V in [EMIM][BF_4]. This curve shape is distinctly different from that curve in [HMIM][BF_4]. The peak currents increase with increasing scan rate for both 1-AQ and 2-AQ, consistent with a surface-confined redox analyte.

Figure 5.7 B and F shows the plots of the reduction peak currents for both 1-AQ and 2-AQ versus the scan rate in [EMIM][BF_4]. Figure 5.7 D and H shows the plots of both the oxidation and reduction peak currents for both 1-AQ and 2-AQ versus the scan rate in [HMIM][BF_4]. The plots are linear in both RTILs with near-zero y-axis intercepts and linear regression coefficients (R^2) > 0.97 consistent with a surface-confined redox process.[76] Table 5.4. shows experimental parameters determined from cyclic voltammetric data for 1-AQ-BDD and 2-AQ-BDD in the two RTILs.

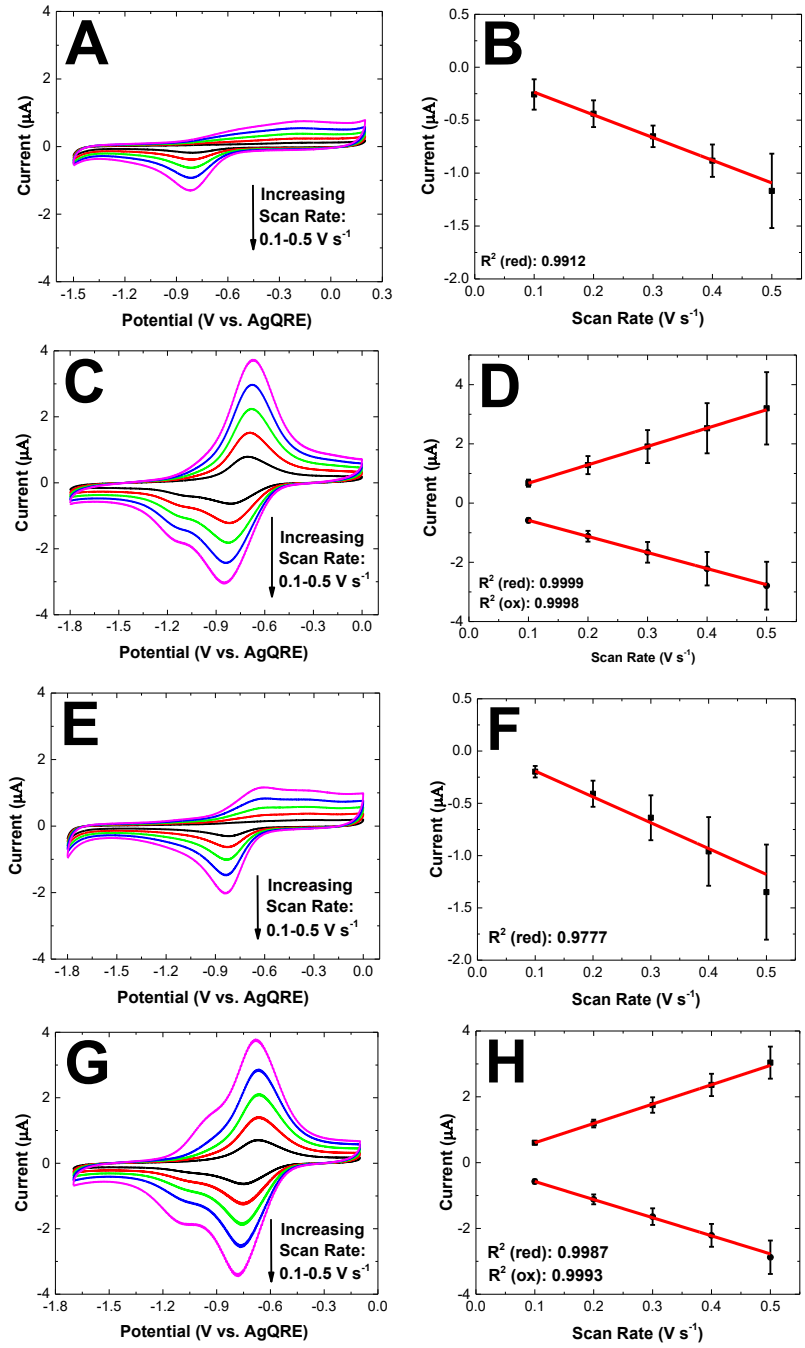

Figure 5.7. Cyclic voltammograms for 1-AQ-BDD and 2-AQ-BDD in room temperature ionic liquid ([EMIM][BF_4] and [HMIM][BF_4]), (A) WE: 1-AQ-BDD, [EMIM][BF_4], (C) WE: 1-AQ-BDD, [HMIM][BF_4], (E) WE: 2-AQ-BDD, [EMIM][BF_4], and (G) WE: 2-AQ-BDD, [HMIM][BF_4]. Plots of oxidation and reduction currents for the first redox step ($Q^0 + e^- \rightarrow Q^{\bullet -}$) vs. scan rate for 1-AQ-BDD and 2-AQ-BDD electrodes in room temperature ionic liquids. (B) WE: 1-AQ-BDD, [EMIM][BF_4], (D) WE: 1-AQ-BDD, [HMIM][BF_4], (F) WE: 2-AQ-BDD, [EMIM][BF_4], (H) WE: 2-AQ-BDD, [HMIM][BF_4]. Scan rate: 0.1-0.5 V s^{-1}. Data are provided as mean ± standard deviation for N=3 modified electrodes of each type. Linear regression was performed on the plots of current vs. scan rate. R^2 correlation coefficient for plots are provided.

The reduction peak potential and current for 1-AQ-BDD in [EMIM][BF_4] is -0.87 ± 0.07 vs. Ag QRE and -0.25 ± 0.15 μA. The reduction peak potential and current for 2-AQ-BDD in [EMIM][BF_4] is -0.89 ± 0.06 vs. Ag QRE and -0.20 ± 0.06 μA (Scan Rate: 0.1 V s^{-1}).

Table 5.4. Experimental parameters collected from cyclic voltammograms for 1-AQ-BDD and 2-AQ-BDD in [EMIM][BF_4] and [HMIM][BF_4].

Electrode	RTILs	$\Delta E_{p,1}$ (V) *	$E_{mid,1}$ (V) *	$i_{p,1}^{red}$ (μA)*	i_p^{red}/i_p^{ox} *	Γ (mol cm^{-2}) (10^{-10}) **
1-AQ-BDD	**[EMIM][BF_4]**	N/A	N/A	0.25 ± 0.15	N/A	0.55 ± 0.19
1-AQ-BDD	**[HMIM][BF_4]**	0.10 ± 0.01	-0.76 ± 0.02	0.58 ± 0.08	0.88 ± 0.05	1.64 ± 0.55
2-AQ-BDD	**[EMIM][BF_4]**	N/A	N/A	0.20 ± 0.06	N/A	0.55 ± 0.16
2-AQ-BDD	**[HMIM][BF_4]**	0.08 ± 0.01	-0.78 ± 0.09	0.58 ± 0.07	0.95 ± 0.07	1.33 ± 0.30

*****Data are provided as "mean ± standard deviation" for N=3. Scan Rate: 0.1 V s^{-1}.
****** The surface coverage (τ) is calculated for scan rate: 0.5 V s^{-1}. The surface coverage is calculated based on the reduction peak currents.

The reduction and oxidation peak potentials for the $Q^{\bullet-}$/Q redox reaction of 1-AQ-BDD in [HMIM][BF_4] are at -0.81 ± 0.01 and -0.71 ± 0.02 vs. Ag QRE, respectively. The midpoint potential (E_{mid}) and peak potential separation (ΔE_p) for the $Q^{\bullet-}$/Q redox reaction of 1-AQ-BDD in [HMIM][BF_4] are -0.76 ± 0.02 V vs. Ag QRE and 0.10 ± 0.01 V, respectively. The reduction and oxidation peak currents for 1-AQ-BDD in [HMIM][BF_4] are -0.58 ± 0.08 and 0.66 ± 0.12 μA, respectively. The ratio of the reduction to the oxidation peak current is 0.88 ± 0.05 (Scan Rate: 0.1 V s^{-1}).

The reduction and oxidation peak potentials for the $Q^{\bullet-}$/Q redox reaction of 2-AQ-BDD in [HMIM][BF_4] are at -0.82 ± 0.09 and -0.74 ± 0.09 vs. Ag QRE, respectively. The midpoint potential (E_{mid}) and peak potential separation (ΔE_p) of 2-AQ-BDD in [HMIM][BF_4] are -0.78 ±

0.09 V vs. Ag QRE and 0.08 ± 0.01 V, respectively. The reduction and oxidation peak currents of 2-AQ-BDD in [HMIM][BF_4] are -0.58 ± 0.07 and 0.61 ± 0.03 μA, respectively. The ratio of the reduction to the oxidation peak current is 0.95 ± 0.07 (Scan Rate: 0.1 V s^{-1}).

The electroactive surface coverage was determined by integration of the two reduction peak currents in [HMIM][BF_4] or the one reduction peak in [EMIM][BF_4] using Faraday's law and normalized to the geometric area of the BDD electrode. The surface coverage for 1-AQ-BDD in [EMIM][BF_4] and [HMIM][BF_4] is, as shown in table 5.4, 0.55 (± 0.19) $\times 10^{-10}$ and 1.64 (± 0.55) $\times 10^{-10}$ mol cm^{-2}, respectively. The surface coverage for 2-AQ-BDD in [EMIM][BF_4] and [HMIM][BF_4] is 0.55 (± 0.16) $\times 10^{-10}$ and 1.33 (± 0.30) $\times$ 10^{-10} mol cm^{-2}, respectively. There is greater surface coverage for both adlayers in [HMIM][BF_4] as compared to [EMIM][BF_4]. The Student's t-test revealed the surface coverage for both adlayers is statistically the same in each RTIL.

5.4.4. Electrochemical Activity of Modified Carbon Electrodes in H_2SO_4

The voltammetric behavior for 1-AQ and 2-AQ on both electrodes differs considerably in aqueous electrolyte solution. Figure 5.8 A, C, E and G presents cyclic voltammograms for 1-AQ and 2-AQ-modified GC and BDD electrodes in 0.1M H_2SO_4 as a function of scan rate from 0.1-0.5 V s^{-1}. Both electron transfers appear to happen at similar energy (concerted process) as only one reduction and oxidation peak is seen in H_2SO_4 rather than the two seen in the RTILs. The electron transfer process in acid involves two electron and two proton, Q/QH_2, redox reaction.[63, 67] In general, well-defined reduction and oxidation peaks are observed for both adlayers on both GC and BDD in 0.1M H_2SO_4. The reduction and oxidation peak currents increase with the scan rate. Figures 5.8 B, D, F and H show the plots of the reduction and oxidation peak currents vs. the

scan rate. The plots are linear indicating the presence of surface-bound AQ groups on both carbon electrodes, regardless of the microstructure.

Table 5.5 provides a summary of the cyclic voltammetric data for 1-AQ and 2-AQ-modified GC and BDD electrodes in 0.1 M H_2SO_4. The reduction and oxidation peak potentials for 1-AQ-GC are at -0.56 ± 0.03 and -0.01 ± 0.06 vs. Ag/AgCl, respectively. The midpoint potential (E_{mid}) and peak potential separation (ΔE_p) for 1-AQ-GC are -0.28 ± 0.02 V vs. Ag/AgCl and 0.55 ± 0.09 mV, respectively. The peak separation increases with the scan rate, consistent with a surface-confined redox system. The reduction and oxidation peak currents are -1.53 ± 0.23 and 1.47 ± 0.30 μA, respectively. The ratio of reduction peak current to oxidation is 1.05 ± 0.07.

The reduction and oxidation peak potentials for 2-AQ-GC are at -0.50 ± 0.03 and -0.06 ± 0.02 V vs. Ag/AgCl, respectively. The midpoint potential (E_{mid}) and peak potential separation (ΔE_p) for 2-AQ-GC are -0.28 ± 0.01 V vs. Ag/AgCl and 0.44 ± 0.04 mV, respectively. The midpoint potential is similar for 1-AQ and 2-AQ on GC, but the ΔE_p is smaller for 2-AQ indicating more rapid electron transfer kinetics. The peak separation increases with the scan rate, consistent with a surface-confined redox system. The reduction and oxidation peak currents are -1.30 ± 0.23 and 1.05 ± 0.22 μA, respectively. The ratio of reduction to oxidation peak current is 1.27 ± 0.32. The curve shape for both the oxidation and reduction currents are similar for both 1-AQ and 2-AQ. Furthermore, unlike the RTIL media, the curves do not reveal distinct electron transfer steps.

For 1-AQ-BDD, the forward reduction current is more constant with potential and only exhibits peak shape character at the higher scan rate. While the oxidation peak potential is 0.04 ± 0.03 vs. Ag/AgCl. The oxidation peak potential shifted to more positive values with the scan rate. The oxidation peak current for 1-AQ-BDD is 0.86 ± 0.11.

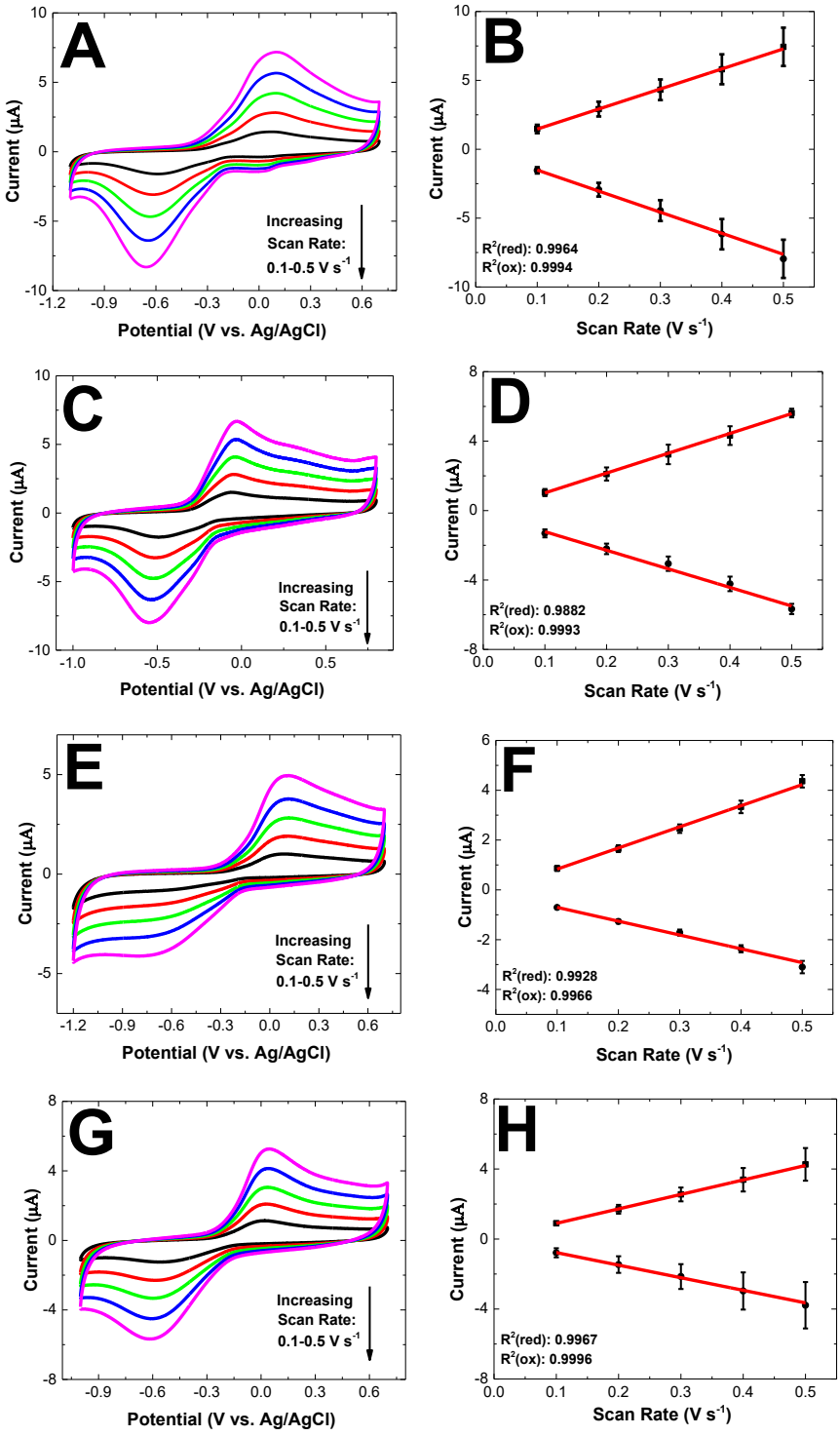

Figure 5.8. Representative background cyclic voltammetric *i-E* curves for diazonium-modified carbon electrodes in 0.1M H_2SO_4: (A) 1-AQ-GC, (C) 2-AQ-GC, (E) 1-AQ-BDD, and (G) 2-AQ-BDD. Plots of the peak currents vs. scan rate for (B) 1-AQ-GC, (D) 2-AQ-GC, (F) 1-AQ-BDD, and (H) 2-AQ-BDD. Scan rate: 0.1-0.5 V s^{-1}. Linear regressions were provided for the plot of current vs. scan rate.

For 2-AQ-BDD, the reduction and oxidation peak potentials are at -0.51 ± 0.05 and -0.01 ± 0.03 V vs. Ag/AgCl, respectively. The midpoint potential (E_{mid}) and peak separation (ΔE_p) are -0.26 ± 0.01 V vs. Ag/AgCl and 0.50 ± 0.08 V, respectively. The peak separation (ΔE_p) increases with the scan rate. The reduction and oxidation peak currents for 2-AQ-BDD are -0.79 ± 0.26 and 0.90 ± 0.11 μA, respectively. The ratio of the reduction to oxidation peak current is 0.86 ± 0.20.

Table 5.5. Experimental parameters collected from cyclic voltammograms for 1-AQ and 2-AQ-modified GC and BDD in 0.1 M H_2SO_4.

Electrode	E_{mid} (V)*	ΔE_p (V)*	i_p^{red} (μA)*	i_p^{red}/i_p^{ox} *	Γ (10^{-10}) (mol cm^{-2})**
1-AQ-GC	-0.28 ± 0.02	0.55 ± 0.09	-1.53 ± 0.23	1.05 ± 0.07	18.87 ± 2.98
2-AQ-GC	-0.28 ± 0.01	0.44 ± 0.04	-1.30 ± 0.23	1.27 ± 0.32	15.10 ± 0.87
1-AQ-BDD	N/A	N/A	N/A	N/A	6.84 ± 2.66
2-AQ-BDD	-0.26 ± 0.01	0.50 ± 0.08	-0.79 ± 0.26	0.86 ± 0.20	1.99 ± 0.84

*Data are provided as "mean ± standard deviation" for N=3. Scan Rate: 0.1 V s^{-1}.
**The surface coverage (τ) is calculated for scan rate: 0.5 V s^{-1}. The surface coverage is calculated based on the reduction peak currents.

Table 5.5 presents a summary of the electrochemical data for the 1-AQ and 2-AQ-modified GC and BDD electrodes. The most significant difference between the two electrodes is the larger electroactive surface coverage for 1-AQ-GC and 2-AQ-GC as compared to BDD. The nominal surface coverages were found to be 18.87 (± 2.98) × 10^{-10} and 15.10 (± 0.87) × 10^{-10} mol cm^{-2}, respectively. Weissmann et al. reported the value of 5.6 ×10^{-10} and 7.9 ×10^{-10} (mol cm^{-2}) for 1-AQ-GC and 2-AQ-GC, respectively, in 0.5 M H_2SO_4.[63] Kullapere et al. reported the value of 8.9 ×10^{-10} and 6.8 ×10^{-10} (mol cm^{-2}) for 1-AQ-GC and 2-AQ-GC, respectively, in Ar saturated 0.1 M

KOH.[82] The observed difference in surface coverage is probably due to the type of electrode, deposition method, and type and concentration of electrolyte.[76]

The surface coverage for 1-AQ-BDD and 2-AQ-BDD was found to be 6.84 (± 2.66) × 10^{-10} and 1.99 (± 0.84) × 10^{-10} mol cm^{-2}, respectively. The surface coverage for both adlayers at each electrode type is statistically the same. The surface coverage for both 1-AQ and 2-AQ on BDD is smaller than on GCs, probably because of the latter's larger density of electronic states. The high fraction of edge plane on GC coupled with the larger density of electronic states leads to more charge density for the diazonium adlayer formation.

5.5. Discussion

It was successfully shown that both glassy carbon (sp^2) and boron-doped diamond (sp^3) electrodes can be covalently modified with 1-AQ and 2-AQ using an electrochemically assisted technique. The electrochemical activity of the AQ-modified carbon electrodes in RTILs ([EMIM][BF_4] and [HMIM][BF_4]) was investigated and compared with the activity in H_2SO_4.

The surface modification was accomplished using an electrochemically assisted process. The reduction of diazonium salts generates the anthraquinone radical, which reacts with carbon sites on the electrode surface and to form a covalently attached admolecule.[63, 64, 82] A reduction peak is seen on the first scan of on both electrodes. The magnitude of the reduction peak current decreases, and finally disappears in the following scans. This is because less radicals are formed as the electrode gets modified. The presence of the adlayer prevents further electron transfer between the diazonium molecules in the solution and the carbon electrode. Both GC and BDD electrodes support the reduction of 1-AQ-N_2^+ and 2-AQ-N_2^+. For GC, the onset reduction potential (E_{red}) is more positive for the 1-N_2^+-AQ as compared to the 2-N_2^+-AQ modification. For BDD,

E_{red} is similar for both diazonium molecules.[63] In general, both carbon electrodes are active for the formation of the diazonium radical based on the similarity of the onset potential for the reduction reaction of ca. 0.38 V vs. Ag QRE (see table 5.1).

The presence of the AQ-adlayers was confirmed by studying their blocking effect for surface-sensitive redox system $Fe(CN)_6^{-3/-4}$ at both modified carbon electrodes.[69, 84-86, 91, 92] There are two reasons for the observed blocking effect: (1) the blockage of mediating surface carbon-oxygen functional groups, specifically carbonyl groups, and (2) the increased barrier to electron tunneling through the adlayer.[84-86] Additionally, the stability of the adlayers was verified by ultrasonication in acetonitrile. The ultrasonication did not remove any significant covalently bonded admolecules but could dislodge physiosorbed molecules.[88, 93] The ultrasonication in acetonitrile did not have a noticeable effect on the cyclic voltammetric curve shape for either AQ-modified carbon electrode.

To the best of our knowledge, there is only one publication reporting on the investigation of AQ-modified carbon electrodes in RTILs by Compton's group. They reported the cyclic voltammetric behavior of 2-AQ-modified GC depends on the size of RTIL's cation.[76] They asserted that a complete reduction of 2-AQ-adlayers cannot be achieved because of the steric hindrance of the counterbalancing cations. The same behavior was observed for 2-AQ-GC in the two RTILs used herein. In general, two distinct redox steps for both 1-AQ and 2-AQ-adlayers on GC are seen in both RTILs, but are most distinct in $[HMIM][BF_4]$. Two sets of peak-shaped curves were also seen for the 2-AQ adlayer at BDD in $[HMIM][BF_4]$. Two reduction peaks and one oxidation peak were observed for the 1-AQ adlayer at BDD in $[HMIM][BF_4]$. One reduction peak and a poorly-defined oxidation peak was seen for both adlayers at BDD in $[EMIM][BF_4]$. The

reason for the differences in the cyclic voltammograms of two adlayers at two electrode types in the probed RTILs is not clear which necessitates further studies.

The reduction peak current for the first electron transfer is larger for the 2-AQ-adlayer than 1-AQ-adlayer at GC in both RTILs. For the case of BDD, no meaningful differences were observed in the magnitude of reduction peak current for both adlayers in the two RTILs. For both AQ-modified carbon electrodes, the reduction current is slightly larger in [HMIM][BF_4] compared to [EMIM][BF_4] for both adlayers. With the present data, we do not know what causes the larger reduction peak currents in [HMIM][BF_4] compared to [EMIM][BF_4] at both modified carbon electrodes. In addition, the surface coverage is generally larger for both adlayers at GC than BDD. We presume this is due to the larger density of electronic states of GC compared to those of BDD.

Comparison measurements for AQ-modified electrodes were performed in H_2SO_4. Previous reports showed that the electrochemical activity of AQ-modified GCs highly depends on the substrate, type of electrolyte (buffered vs. unbuffered, acidic, basic, and neutral solutions), and the modification method.[11, 63, 66, 67, 94-98] In general, quinones go through a one-step, two-electron transfer redox reaction during the electron transfer process in aqueous environment.

Like the RTILs, the surface coverage is larger for GC compared to BDD in H_2SO_4. This suggests that the surface coverage depends on the nature of the electrolyte. We assume that ion-pairing and complexes, the smaller dielectric constant of RTILs, and the larger size of ions in RTILs may decrease the surface coverages in this medium compared to aqueous counterparts.

5.6. Conclusions

The electrochemical activity of anthraquinone modified carbon electrodes was studied as a function of the electrolyte (aqueous vs. RTIL), admolecule (1-AQ vs. 2-AQ), type of RTIL

([EMIM][BF_4] vs. [HMIM][BF_4]), and type of carbon electrode (GC vs. BDD). Key findings from the work can be summarized as follows.

1. The electrochemically assisted reduction of anthraquinone diazonium salts forms permanent adlayers at the surface of both GC and BDD electrodes. The blocking effect for $Fe(CN)_6^{-3/-4}$ and ultrasonication tests provide solid evidence for the successful modification with a stable adlayer.

2. The redox reactions for the surface-bound anthraquinone species at both modified carbon electrodes involve two distinct one-electron reduction steps in the RTIL and one concerted two-electron two-proton reduction step in aqueous electrolyte solution.

3. The electrochemically active surface coverage was generally larger on GC than BDD for both 1-AQ and 2-AQ in both RTILs and the aqueous electrolyte solution. The surface coverage was larger in the aqueous electrolyte than in RTILs.

4. The electrochemical behavior of the surface-bound anthraquinone species in RTILs depends on the RTIL type, carbon electrode type, and admolecule. Future research will continue to thoroughly examine how various variables may influence the electrochemical behavior of modified carbon electrodes in RTILs. The deposition process (spontaneous vs. electrochemically assisted), the type of electrode and modifiers, the optimization of the modification reaction, and the structure of RTILs are a few examples of the elements that need to be explored.

REFERENCES

[1] D. M. Adams, L. Brus, C. E. D. Chidsey, S. Creager, C. Creutz, C. R. Kagan, P. V. Kamat, M. Lieberman, S. Lindsay, R. A. Marcus, R. M. Metzger, M. E. Michel-Beyerle, J. R. Miller, M. D. Newton, D. R. Rolison, O. Sankey, K. S. Schanze, J. Yardley, X. Zhu, 'Charge transfer on the nanoscale: current status', *J. Phys. Chem. B* **2003**, *107*, 6668-6697.

[2] C. Batchelor-McAuley, B. R. Kozub, D. Menshykau, R. G. Compton, 'Voltammetric responses of surface-bound and solution-phase anthraquinone moieties in the presence of unbuffered aqueous media', *J. Phys. Chem. C* **2011**, *115*, 714-718.

[3] D. Cahen, G. Hodes, 'Molecules and electronic materials', *Adv. Mater.* **2002**, *14*, 789-798.

[4] A. Salomon, D. Cahen, S. Lindsay, J. Tomfohr, V. B. Engelkes, C. D. Frisbie, 'Comparison of electronic transport measurements on organic molecules', *Adv. Mater.* **2003**, *15*, 1881-1890.

[5] I. Willner, 'Biomaterials for sensors, fuel cells, and circuitry', *Science* **2002**, *298*, 2407-2408.

[6] I. Willner, E. Katz, 'Integration of layered redox proteins and conductive supports for bioelectronic applications', *Angew. Chem. Int. Ed.* **2000**, *39*, 1180-1218.

[7] J. J. Gooding, R. Wibowo, J. Liu, W. Yang, D. Losic, S. Orbons, F. J. Mearns, J. G. Shapter, D. B. Hibbert, 'Protein electrochemistry using aligned carbon nanotube arrays', *J. Am. Chem. Soc.* **2003**, *125*, 9006-9007.

[8] M. T. Alam, J. J. Gooding, 'Modification of carbon electrode surfaces', *Electrochemistry of Carbon Electrodes;* John Wiley and Sons: New York, NY, USA **2015**.

[9] R. L. McCreery, 'Advanced carbon electrode materials for molecular electrochemistry', *Chem. Rev.* **2008**, *108*, 2646-2687.

[10] J. J. Gooding, F. Mearns, W. Yang, J. Liu, 'Self-assembled monolayers into the 21st century: recent advances and applications', *Electroanalysis,* **2003**, *15*, 81-96.

[11] D. Belanger, J. Pinson, 'Electrografting: a powerful method for surface modification', *Chem. Soc. Rev.* **2011**, *40*, 3995-4048.

[12] A. J. Downard, 'Electrochemically assisted covalent modification of carbon electrodes', *Electroanalysis,* **2000**, *12*, 1085-1096.

[13] J. J. Gooding, 'Advances in interfacial design for electrochemical biosensors and sensors: aryl diazonium salts for modifying carbon and metal electrodes', *Electroanalysis,* **2008**, *20*, 573-582.

[14] J. Liu, J. Tang, J. J. Gooding, 'Strategies for chemical modification of graphene and applications of chemically modified graphene', *J. Mater. Chem.* **2012**, *22*, 12435-12452.

[15] J. Pinson, F. Podvorica, 'Attachment of organic layers to conductive or semiconductive surfaces by reduction of diazonium salts', *Chem. Soc. Rev.* **2005**, *34*, 429-439.

[16] K. R. Ratinac, W. Yang, J. J. Gooding, P. Thordarson, F. Braet, 'Graphene and related materials in electrochemical sensing', *Electroanalysis* **2011**, *23*, 803-826.

[17] A. Walcarius, 'Electrocatalysis, sensors and biosensors in analytical chemistry based on ordered mesoporous and macroporous carbon-modified electrodes', *TrAC - Trends Anal. Chem.* **2012**, *38*, 79-97.

[18] G. G. Wildgoose, C. E. Banks, H. C. Leventis, R. G. Compton, 'Chemically modified carbon nanotubes for use in electroanalysis', *Mikrochim Acta* **2006**, *152*, 187-214.

[19] R. J. Chen, Y. Zhang, D. Wang, H. Dai, 'Noncovalent sidewall functionalization of single-walled carbon nanotubes for protein immobilization', *J. Am. Chem. Soc.* **2001**, *123*, 3838-3839.

[20] M. Delamar, R. Hitmi, J. Pinson, J. M. Saveant, 'Covalent modification of carbon surfaces by grafting of functionalized aryl radicals produced from electrochemical reduction of diazonium salts', *J. Am. Chem. Soc.* **1992**, *114*, 5883-5884.

[21] R. Vittal, H. Gomathi, K.-J. Kim, 'Beneficial role of surfactants in electrochemistry and in the modification of electrodes', *Adv. Colloid Interface Sci.* **2006**, *119*, 55-68.

[22] E. Pajootan, M. Arami, 'Structural and electrochemical characterization of carbon electrode modified by multi-walled carbon nanotubes and surfactant', *Electrochim. Acta* **2013**, *112*, 505-514.

[23] J. Chen, T. O. Tran, M. T. Ray, D. B. Brunski, J. C. Keay, D. Hickey, M. B. Johnson, D. T. Glatzhofer, D. W. Schmidtke, 'Effect of surfactant type and redox polymer type on single-walled carbon nanotube modified electrodes', *Langmuir* **2013**, *29*, 10586-10595.

[24] C. A. Mitchell, J. L. Bahr, S. Arepalli, J. M. Tour, R. Krishnamoorti, 'Dispersion of functionalized carbon nanotubes in polystyrene', *Macromolecules* **2002**, *35*, 8825-8830.

[25] A. L. Gui, G. Liu, M. Chockalingam, G. Le Saux, J. B. Harper, J. J. Gooding, 'A comparative study of modifying gold and carbon electrode with 4-sulfophenyl diazonium salt', *Electroanalysis* **2010**, *22*, 1283-1289.

[26] G. Liu, M. Chockalingham, S. M. Khor, A. L. Gui, J. J. Gooding, 'A comparative study of the modification of gold and glassy carbon surfaces with mixed layers of in situ generated aryl diazonium compounds', *Electroanalysis,* **2010**, *22*, 918-926.

[27] G. Liu, J. Liu, T. Böcking, P. K. Eggers, J. J. Gooding, 'The modification of glassy carbon and gold electrodes with aryl diazonium salt: The impact of the electrode materials on the rate of heterogeneous electron transfer', *Chem. Phys.* **2005**, *319*, 136-146.

[28] A. Adenier, M. M. Chehimi, I. Gallardo, J. Pinson, N. Vilà, 'Electrochemical oxidation of aliphatic amines and their attachment to carbon and metal surfaces', *Langmuir* **2004**, *20*, 8243-8253.

[29] R. S. Deinhammer, M. Ho, J. W. Anderegg, M. D. Porter, 'Electrochemical oxidation of amine-containing compounds: a route to the surface modification of glassy carbon electrodes', *Langmuir* **1994**, *10*, 1306-1313.

[30] C. P. Andrieux, F. Gonzalez, J.-M. Savéant, 'Derivatization of carbon surfaces by anodic oxidation of arylacetates. Electrochemical manipulation of the grafted films', *J. Am. Chem. Soc.* **1997**, *119*, 4292-4300.

[31] C. P. Andrieux, F. Gonzalez, J. M. Savéant, 'Homolytic and heterolytic radical cleavage in the Kolbe reaction: electrochemical oxidation of arylmethyl carboxylate ions', *J. Electroanal. Chem.* **2001**, *498*, 171-180.

[32] H. Maeda, Y. Yamauchi, M. Hosoe, T.-X. Li, E. Yamaguchi, M. Kasamatsu, H. Ohmori, 'Direct covalent modification of glassy carbon surfaces with 1-alkanols by electrochemical oxidation', *Chem. Pharm. Bull.***1994**, *42*, 1870-1873.

[33] H. Maeda, T.-X. Li, M. HosoE, M. Itami, Y. Yamauchi, H. Ohmori, 'Electrochemical performance of a glassy carbon electrode anodized in 1-octanol', *Anal Sci* **1994**, *10*, 963-965.

[34] R. DeClements, G. M. Swain, T. Dallas, M. W. Holtz, R. D. Herrick, J. L. Stickney, 'Electrochemical and surface structural characterization of hydrogen plasma treated glassy carbon electrodes', *Langmuir* **1996**, *12*, 6578-6586.

[35] M.-C. Bernard, A. Chaussé, E. Cabet-Deliry, M. M. Chehimi, J. Pinson, F. Podvorica, C. Vautrin-Ul, 'Organic layers bonded to industrial, coinage, and noble metals through electrochemical reduction of aryldiazonium salts', *Chem. Mater.* **2003**, *15*, 3450-3462.

[36] P. Allongue, C. H. de Villeneuve, G. Cherouvrier, R. Cortes, M. C. Bernard, 'Phenyl layers on H–Si (111) by electrochemical reduction of diazonium salts: monolayer versus multilayer formation', *J. Electroanal. Chem.* **2003**, *550*, 161-174.

[37] M. P. Stewart, F. Maya, D. V. Kosynkin, S. M. Dirk, J. J. Stapleton, C. L. McGuiness, D. L. Allara, J. M. Tour, 'Direct covalent grafting of conjugated molecules onto Si, GaAs, and Pd surfaces from aryldiazonium salts', *J. Am. Chem. Soc.* **2004**, *126*, 370-378.

[38] S. Gam-Derouich, B. Carbonnier, M. Turmine, P. Lang, M. Jouini, D. Ben Hassen-Chehimi, M. M. Chehimi, 'Electrografted aryl diazonium initiators for surface-confined

photopolymerization: a new approach to designing functional polymer coatings', *Langmuir* **2010**, *26*, 11830-11840.

[39] V. Stockhausen, J. Ghilane, P. Martin, G. Trippé-Allard, H. Randriamahazaka, J.-C. Lacroix, 'Grafting oligothiophenes on surfaces by diazonium electroreduction: a step toward ultrathin junction with well-defined metal/oligomer interface', *J. Am. Chem. Soc.* **2009**, *131*, 14920-14927.

[40] R. Pazo-Llorente, C. Bravo-Diaz, E. Gonzalez-Romero, 'pH effects on ethanolysis of some arenediazonium ions: evidence for homolytic dediazoniation proceeding through formation of transient diazo ethers', *Eur. J. Org. Chem.* **2004**, *2004*, 3221-3226.

[41] A. I. Vogel, B. S. Furniss, A. J. Hannaford, P. W. G. Smith, A. R. Tatchell, *Vogel's textbook of practical organic chemistry, Vol. 5*, Longman Scientific & Technical London, **1989**.

[42] C. Gautier, I. López, T. Breton, 'A post-functionalization toolbox for diazonium (electro)-grafted surfaces: review of the coupling methods', *Mater. Adv.* **2021**, *2*, 2773-2810.

[43] M. A. B. H. Susan, A. Noda, S. Mitsushima, M. Watanabe, 'Brønsted acid–base ionic liquids and their use as new materials for anhydrous proton conductors', *Chem. Commun.* **2003**, 938-939.

[44] J.-P. Belieres, D. Gervasio, C. A. Angell, 'Binary inorganic salt mixtures as high conductivity liquid electrolytes for> 100 C fuel cells', *Chem. Commun.* **2006**, 4799-4801.

[45] T. L. Greaves, A. Weerawardena, C. Fong, C. J. Drummond, 'Formation of amphiphile self-assembly phases in protic ionic liquids', *J. Phys. Chem. B* **2007**, *111*, 4082-4088.

[46] J. C. Gálvez-Ruiz, G. Holl, K. Karaghiosoff, T. M. Klapötke, K. Löhnwitz, P. Mayer, H. Nöth, K. Polborn, C. J. Rohbogner, M. Suter, 'Derivatives of 1, 5-diamino-1 H-tetrazole: a new family of energetic heterocyclic-based salts', *Inorg. Chem.* **2005**, *44*, 4237-4253.

[47] W. Tamura-Lis, L. J. Lis, P. J. Quinn, 'Structures and mechanisms of lipid phase transitions in nonaqueous media. Dipalmitoylphosphatidylethanolamine in fused salt', *Biophys. J.* **1988**, *53*, 489-492.

[48] M. U. Araos, G. G. Warr, 'Self-assembly of nonionic surfactants into lyotropic liquid crystals in ethylammonium nitrate, a room-temperature ionic liquid', *J. Phys. Chem. B* **2005**, *109*, 14275-14277.

[49] R. Atkin, G. G. Warr, 'Self-assembly of a nonionic surfactant at the graphite/ionic liquid interface', *J. Am. Chem. Soc.* **2005**, *127*, 11940-11941.

[50] T. Jiang, H. Gao, B. Han, G. Zhao, Y. Chang, W. Wu, L. Gao, G. Yang, 'Ionic liquid catalyzed henry reactions', *Tetrahedron Lett.* **2004**, *45*, 2699-2701.

[51] J. Pernak, I. Goc, I. Mirska, 'Anti-microbial activities of protic ionic liquids with lactate anion', *Green Chem.* **2004**, *6*, 323-329.

[52] K. Fujita, D. R. MacFarlane, M. Forsyth, 'Protein solubilising and stabilising ionic liquids', *Chem. Commun.* **2005**, 4804-4806.

[53] K. Fujita, M. Forsyth, D. R. MacFarlane, R. W. Reid, G. D. Elliott, 'Unexpected improvement in stability and utility of Cytochrome c by solution in biocompatible ionic liquids', *Biotechnol. Bioeng.* **2006**, *94*, 1209-1213.

[54] R. V. Hangarge, D. V. Jarikote, M. S. Shingare, 'Knoevenagel condensation reactions in an ionic liquid', *Green Chem.* **2002**, *4*, 266-268.

[55] K. K. Laali, V. J. Gettwert, 'Electrophilic nitration of aromatics in ionic liquid solvents', *J. Org. Chem.* **2001**, *66*, 35-40.

[56] Y. Hu, J. Chen, Z. G. Le, Q. G. Zheng, 'Organic reactions in ionic liquids: ionic liquids ethylammonium nitrate promoted knoevenagel condensation of aromatic aldehydes with active methylene compounds', *Synth. Commun.* **2005**, *35*, 739-744.

[57] C. Zhao, G. Burrell, A. A. J. Torriero, F. Separovic, N. F. Dunlop, D. R. MacFarlane, A. M. Bond, 'Electrochemistry of room temperature protic ionic liquids', *J. Phys. Chem. B* **2008**, *112*, 6923-6936.

[58] C. F. Poole, 'Chromatographic and spectroscopic methods for the determination of solvent properties of room temperature ionic liquids', *J. Chromatogr. A* **2004**, *1037*, 49-82.

[59] M. C. Buzzeo, R. G. Evans, R. G. Compton, 'Non-haloaluminate room-temperature ionic liquids in electrochemistry—a review', *ChemPhysChem* **2004**, *5*, 1106-1120.

[60] D. S. Silvester, R. G. Compton, 'Electrochemistry in room temperature ionic liquids: a review and some possible applications', *Z. fur Phys. Chem.* **2006**, *220*, 1247-1274.

[61] K. Bhardwaj, F. Parvis, Y. Wang, G. J. Blanchard, G. M. Swain, 'Effect of surface oxygen on the wettability and electrochemical properties of boron-doped nanocrystalline diamond electrodes in room-temperature ionic liquids', *Langmuir* **2020**, *36*, 5717-5729.

[62] M. A. Bhat, P. P. Ingole, H. Randriamahazaka, 'Towards understanding the solvent-dynamic control of the transport and heterogeneous electron-transfer processes in ionic liquids', *ChemPhysChem* **2017**, *18*, 415-426.

[63] M. Weissmann, O. Crosnier, T. Brousse, D. Bélanger, 'Electrochemical study of anthraquinone groups, grafted by the diazonium chemistry, in different aqueous media-relevance for the development of aqueous hybrid electrochemical capacitor', *Electrochim. Acta* **2012**, *82*, 250-256.

[64] S. Baranton, D. Bélanger, 'In situ generation of diazonium cations in organic electrolyte for electrochemical modification of electrode surface', *Electrochim. Acta* **2008**, *53*, 6961-6967.

[65] K. Tammeveski, K. Kontturi, R. J. Nichols, R. J. Potter, D. J. Schiffrin, 'Surface redox catalysis for O_2 reduction on quinone-modified glassy carbon electrodes', *J. Electroanal. Chem.* **2001**, *515*, 101-112.

[66] J. Revenga, F. Rodríguez, J. Tijero, 'Study of the redox behavior of anthraquinone in aqueous medium', *J. Electrochem. Soc.* **1994**, *141*, 330-333.

[67] M. Quan, D. Sanchez, M. F. Wasylkiw, D. K. Smith, 'Voltammetry of quinones in unbuffered aqueous solution: reassessing the roles of proton transfer and hydrogen bonding in the aqueous electrochemistry of quinones', *J. Am. Chem. Soc.* **2007**, *129*, 12847-12856.

[68] S. H. DuVall, R. L. McCreery, 'Self-catalysis by catechols and quinones during heterogeneous electron transfer at carbon electrodes', *J. Am. Chem. Soc.* **2000**, *122*, 6759-6764.

[69] A. J. Downard, M. J. Prince, 'Barrier properties of organic monolayers on glassy carbon electrodes', *Langmuir* **2001**, *17*, 5581-5586.

[70] R. Reilson, M. Kullapere, K. Tammeveski, 'Blocking behavior of covalently attached anthraquinone towards solution-based redox probes', *Electroanalysis,* **2010**, *22*, 513-518.

[71] M. T. Carter, R. A. Osteryoung, 'Interaction of 9, 10-anthraquinone with tetrachloroaluminate and proton in basic aluminum chloride: 1-ethyl-3-methylimidazolium chloride room-temperature molten salts', *J. Electrochem. Soc.* **1992**, *139*, 1795.

[72] Y. Wang, S. R. Belding, E. I. Rogers, R. G. Compton, 'A kinetic and mechanistic study of the electrochemical oxidation of hydroquinone in 1-ethyl-3-methylimidazolium bis (trifluoromethanesulfonyl) imide,[C_2mim][NTf_2]', *J. Electroanal. Chem.* **2011**, *650*, 196-204.

[73] Y. Wang, E. I. Rogers, S. R. Belding, R. G. Compton, 'The electrochemical reduction of 1, 4-benzoquinone in 1-ethyl-3-methylimidazolium bis (trifluoromethane-sulfonyl)-imide,[C_2mim][NTf_2]: a voltammetric study of the comproportionation between benzoquinone and the benzoquinone dianion', *J. Electroanal. Chem.* **2010**, *648*, 134-142.

[74] E. O. Barnes, A. M. O'Mahony, L. Aldous, C. Hardacre, R. G. Compton, 'The electrochemical oxidation of catechol and dopamine on platinum in 1-ethyl-3-methylimidazolium bis (trifluoromethylsulfonyl) imide ([C_2mim][NTf_2]) and 1-butyl-3-methylimidazolium tetrafluoroborate ([C_4mim][BF_4]): adsorption effects in ionic liquid voltammetry', *J. Electroanal. Chem.* **2010**, *646*, 11-17.

[75] V. A. Nikitina, R. R. Nazmutdinov, G. A. Tsirlina, 'Quinones electrochemistry in room-temperature ionic liquids', *J. Phys. Chem. B* **2011**, *115*, 668-677.

[76] S. Ernst, L. Aldous, R. G. Compton, 'The voltammetry of surface bound 2-anthraquinonyl groups in room temperature ionic liquids: Cation size effects', *Chem. Phys. Lett.* **2011**, *511*, 461-465.

[77] V. Y. Maldonado, P. J. Espinoza-Montero, C. A. Rusinek, G. M. Swain, 'Analysis of Ag(I) biocide in water samples using anodic stripping voltammetry with a boron-doped diamond disk electrode', *Anal. Chem.* **2018**, *90*, 6477-6485.

[78] S. Ren, Y. Hou, W. Wu, W. Liu, 'Purification of ionic liquids: sweeping solvents by nitrogen', *J. Chem. Eng. Data.* **2010**, *55*, 5074-5077.

[79] R. Jarosova, G. M. Swain, 'Rapid preparation of room temperature ionic liquids with low water content as characterized with a t*a*-C:N electrode', *J. Electrochem. Soc.* **2015**, *162*, H507-H511.

[80] R. S. Varma, 'Solvent-free organic syntheses . using supported reagents and microwave irradiation', *Green Chem.* **1999**, *1*, 43-55.

[81] M. Gnahm, C. Müller, R. Répánszki, T. Pajkossy, D. M. Kolb, 'The interface between Au(100) and 1-butyl-3-methyl-imidazolium-hexafluorophosphate', *Phys. Chem. Chem. Phys.* **2011**, *13*, 11627-11633.

[82] M. Kullapere, J.-M. Seinberg, U. Mäeorg, G. Maia, D. J. Schiffrin, K. Tammeveski, 'Electroreduction of oxygen on glassy carbon electrodes modified with in situ generated anthraquinone diazonium cations', *Electrochim. Acta* **2009**, *54*, 1961-1969.

[83] K. H. Vase, A. H. Holm, K. Norrman, S. U. Pedersen, K. Daasbjerg, 'Covalent grafting of glassy carbon electrodes with diaryliodonium salts: New Aspects', *Langmuir* **2007**, *23*, 3786-3793.

[84] P. Chen, R. L. McCreery, 'Control of electron transfer kinetics at glassy carbon electrodes by specific surface modification', *Anal. Chem.* **1996**, *68*, 3958-3965.

[85] R. J. Bowling, R. T. Packard, R. L. McCreery, 'Activation of highly ordered pyrolytic graphite for heterogeneous electron transfer: relationship between electrochemical performance and carbon microstructure', *J. Am. Chem. Soc.* **1989**, *111*, 1217-1223.

[86] K. R. Kneten, R. L. McCreery, 'Effects of redox system structure on electron-transfer kinetics at ordered graphite and glassy carbon electrodes', *Anal. Chem.* **1992**, *64*, 2518-2524.

[87] P. Allongue, M. Delamar, B. Desbat, O. Fagebaume, R. Hitmi, J. Pinson, J.-M. Savéant, 'Covalent modification of carbon surfaces by aryl radicals generated from the electrochemical reduction of diazonium salts', *J. Am. Chem. Soc.* **1997**, *119*, 201-207.

[88] M. Delamar, G. Désarmot, O. Fagebaume, R. Hitmi, J. Pinsonc, J. M. Savéant, 'Modification of carbon fiber surfaces by electrochemical reduction of aryl diazonium salts: Application to carbon epoxy composites', *Carbon* **1997**, *35*, 801-807.

[89] S. Ranganathan, T.-C. Kuo, R. L. McCreery, 'Facile preparation of active glassy carbon electrodes with activated carbon and organic solvents', *Anal. Chem.* **1999**, *71*, 3574-3580.

[90] A. J. Bard, L. R. Faulkner, 'Electrochemical methods: fundamentals and applications' **2001**, *2*, 580-632.

[91] B. Ortiz, C. Saby, G. Y. Champagne, D. Bélanger, 'Electrochemical modification of a carbon electrode using aromatic diazonium salts. 2. electrochemistry of 4-nitrophenyl modified glassy carbon electrodes in aqueous media', *J. Electroanal. Chem.* **1998**, *455*, 75-81.

[92] C. Saby, B. Ortiz, G. Y. Champagne, D. Bélanger, 'Electrochemical modification of glassy carbon electrode using aromatic diazonium salts. 1. blocking effect of 4-nitrophenyl and 4-carboxyphenyl groups', *Langmuir* **1997**, *13*, 6805-6813.

[93] C. H. De Villeneuve, J. Pinson, M. C. Bernard, P. Allongue, 'Electrochemical formation of close-packed phenyl layers on Si (111)', *J. Phys. Chem. B* **1997**, *101*, 2415-2420.

[94] M. A. B. H. Susan, M. Begum, Y. Takeoka, M. Watanabe, 'Effect of pH and the extent of micellization on the redox behavior of non-ionic surfactants containing an anthraquinone group', *J. Electroanal. Chem.* **2000**, *481*, 192-199.

[95] M. Shamsipur, A. Salimi, S. M. Golabi, H. Sharghi, M. F. Mousavi, 'Electrochemical properties of modified carbon paste electrodes containing some amino derivatives of 9, 10-anthraquinone', *J. Solid State Electrochem.* **2001**, *5*, 68-73.

[96] C. Batchelor-McAuley, Q. Li, S. M. Dapin, R. G. Compton, 'Voltammetric characterization of DNA intercalators across the full pH range: Anthraquinone-2, 6-disulfonate and anthraquinone-2-sulfonate', *J. Phys. Chem. B* **2010**, *114*, 4094-4100.

[97] G. Pognon, T. Brousse, D. Bélanger, 'Effect of molecular grafting on the pore size distribution and the double layer capacitance of activated carbon for electrochemical double layer capacitors', *Carbon* **2011**, *49*, 1340-1348.

[98] P. Abiman, G. G. Wildgoose, R. G. Compton, 'A mechanistic investigation into the covalent chemical derivatisation of graphite and glassy carbon surfaces using aryldiazonium salts', *J. Phys. Org. Chem.* **2008**, *21*, 433-439.

CHAPTER 6. SUMMARY OF CONCLUSIONS AND POSSIBLE FUTURE WORK

The main goal of this research was to better understand how the microstructure, surface chemistry, and type of carbon electrode (glassy carbon (sp^2) and boron-doped diamond (sp^3)) affect the voltammetric background current, double-layer capacitance, working potential window, and apparent heterogeneous electron transfer rate constant (k^o) for soluble redox systems in room temperature ionic liquids (RTILs) with different physical and chemical properties.

RTILs have a multitude of applications in various scientific fields because of their physical, chemical, and electrochemical properties. For the maximum usage of RTILs, it is essential to have a better understanding of the double-layer/interfacial structure and electron- transfer kinetics in these media. Comparison measurements were made in aqueous electrolyte solutions to identify differences in the redox chemistry observed in aqueous electrolyte solution and ionic liquid environments.

In the present dissertation, the focus was mainly on boron-doped diamond electrodes because of the shortage of knowledge available about the electrochemical activity of BDDs in the novel environment of room temperature ionic liquids. BDDs have several features which make them an excellent choice to be used as a working electrode in electroanalytical chemistry, such as low background current, wide working potential window, stability, relatively fast electron transfer kinetics for various redox systems, and no requirement for conventional pretreatment.

Boron-doped nanocrystalline diamond optically transparent electrodes (BDDOTEs) were prepared by chemical vapor deposition (CVD) using a mixture of 1% CH_4/H_2 as a source gas and B_2H_6 added as the dopant. In **Chapter 2**, the morphology, microstructure, and optical properties of BDDOTEs were reported on using various techniques, such as UV/Visible absorption and

Raman spectroscopy, and scanning electron microscopy. The voltammetric background current, double-layer capacitance, working potential window for BDDOTEs were studied in three homologous room temperature ionic liquids ([EMIM][BF_4], [BMIM][BF_4], [HMIM][BF_4]). The type of RTILs exhibited no noticeable effect on the working potential window, voltammetric background current, or capacitance values. Also, the C_{dl}-E profiles for the BDDOTEs were compared with glassy carbon and metallic electrodes in the RTILs. The results revealed that the C_{dl}-E profiles for both carbon electrodes was flat or slightly increasing with positive potentials and this differed from the behavior of a Au disk electrode that exhibited a bell shaped profile. This behavior is consistent with the lattice saturation model put forward by Kornyshev. The results showed that the type of carbon electrode (GC vs. BDD) has a noticeable effect on voltammetric background current and capacitance values. Comparison measurements were made in aqueous solutions. Larger capacitance values and voltammetric background currents were observed for both types of carbon electrodes in aqueous solution as compared to RTILs.

In **Chapter 3,** the electrochemical activity of ferrocene derivatives at BDDOTEs were studied in room temperature ionic liquids ([EMIM][BF_4], [BMIM][BF_4], [HMIM][BF_4]). The apparent heterogeneous electron-transfer rate constant (k^o_{app}) was estimated from cyclic voltammetry ΔE_p-scan rate trends on (Nicholson method) and from digital simulation. The rate constant and diffusion coefficients were on the order of 10^{-4}-10^{-5} cm s^{-1} and 10^{-7}-10^{-9} cm^2 s^{-1}, respectively, depending on the viscosity of the RTIL. The results revealed that the diffusion coefficients (D) and apparent heterogeneous electron transfer rate constants (k^o_{app}) depend on the viscosity of RTILs with the largest rate constant and diffusion coefficient being observed in the RTIL with the lowest viscosity ([EMIM][BF_4]). The smallest rate constant and diffusion coefficient were observed in the RTIL with the highest viscosity ([HMIM][BF_4]). The simulated

electron transfer rate constants (k^o_{sim}) were close to the experimental values which corrected for iR effects. Comparison measurements for $Fe(CN)_6^{-3/-4}$ were made in an aqueous solution. The k^o_{app} and diffusion coefficients were in the order of 10^{-3} cm s^{-1} and 10^{-6} cm^2 s^{-1}, respectively. The larger rate constant and diffusion coefficient in aqueous solution are due to the lower viscosity as compared to the RTILs. The second goal of this research was to determine if k^o_{app} for the ferrocene derivatives depends on the reorientation dynamics of the RTIL and the hydrodynamic radius of the redox probe molecules or not. Experimental results showed that k^o_{app} depends on the reorientation dynamics, which are influenced by the viscosity (η) of three RTILs. The research showed that the electron transfer rate constant for the ferrocene redox systems does not depend on the hydrodynamic radius of the molecule in three RTILs.

In **Chapter 4,** the morphology and basic electrochemical features of boron-doped diamond thin film deposited on Si were studied. Raman spectroscopy showed the presence of a heavily boron-doped film with a nanocrystalline morphology. Further examination of the films using scanning electron microscopy and Raman spectroscopy revealed uniformity of the film coverage and microstructure across the substrate surface. The working potential window and double-layer capacitance of BDD electrodes were studied in three RTILs ([EMIM][BF_4], [BMIM][BF_4], [HMIM][BF_4]). Capacitance values ranged from 5 to 12 μF cm^{-2} in the RTILs over the probed potential range of -1 to 1 V vs. AgQRE. The electron transfer kinetics of the ferrocene derivatives were studied at BDD electrodes in three RTILs. The main goal was to understand the effect of viscosity on the electrochemical behavior of BDD electrodes in RTILs. The diffusion coefficient and apparent heterogeneous electron transfer rate constants were in the order of 10^{-7} to 10^{-9} cm^2 s^{-1} and 10^{-4} to 10^{-5} cm s^{-1}, respectively in the RTILs. The values were similar for three ferrocene derivatives (ferrocene, ferrocene methanol, ferrocene carboxylic acid) in a given RTIL. The

diffusion coefficients and apparent heterogeneous electron transfer rate constants for potassium ferrocyanide were in the order of 10^{-6} cm^2 s^{-1} and 10^{-3} cm s^{-1}, respectively. The smaller diffusion coefficient and rate constant in the RTIL arises from the higher viscosity of RTILs as compared to water. The diffusion coefficients and rate constant for the ferrocene derivatives in RTILs follow this trend: [EMIM][BF_4] (η = 34 cP) > [BMIM][BF_4] (η = 104 cP) > [HMIM][BF_4] (η = 288 cP) which reveals the diffusion and electron transfer kinetics slowdown in the more viscose medium. The theoretical rate constant values obtained from Digital simulation agree with the experimental values calculated using the Nicholson method.

In **Chapter 5,** the electrochemistry of surface-bound anthraquinone (1-AQ and 2-AQ) on glassy carbon and BDD electrodes was studied in two RTILs ([EMIM][BF_4] and [HMIM][BF_4]). Comparison measurements were performed in H_2SO_4. The blocking effect for $Fe(CN)_6^{-3/-4}$ and ultrasonication tests provided evidence for the presence of surface-bound electroactive admolecules on both GC and BDD electrodes.

The redox reactions for the surface-bound anthraquinone species at both modified carbon electrodes involve two distinct one-electron reduction steps in the RTIL and one concerted two-electron two-proton reduction step in aqueous electrolyte solution. The electrochemically active surface coverage was generally larger on GC than BDD for both 1-AQ and 2-AQ in both RTILs and the aqueous electrolyte solution. The surface coverage was larger in the aqueous electrolyte than in RTILs.

Finally, It was found that the type of RTIL, carbon electrode, and adlayer are determining factors in the electron transfer kinetics of adsorbed species.

Future work might include fully investigate how different factors can affect the electrochemical behavior of modified carbon electrodes. Examples of factors to be studied are deposition method (spontaneous vs electrochemically assisted), type of electrode and modifiers, optimization of modification reaction, and structure of RTILs.